

Electronic Theses and Dissertations, 2004-2019

2015

Nano and Nanostructured Materials for Optical Applications

Panit Chantharasupawong
University of Central Florida

 Part of the [Electromagnetics and Photonics Commons](#), and the [Optics Commons](#)
Find similar works at: <https://stars.library.ucf.edu/etd>
University of Central Florida Libraries <http://library.ucf.edu>

This Doctoral Dissertation (Open Access) is brought to you for free and open access by STARS. It has been accepted for inclusion in Electronic Theses and Dissertations, 2004-2019 by an authorized administrator of STARS. For more information, please contact STARS@ucf.edu.

STARS Citation

Chantharasupawong, Panit, "Nano and Nanostructured Materials for Optical Applications" (2015).
Electronic Theses and Dissertations, 2004-2019. 1482.
<https://stars.library.ucf.edu/etd/1482>

NANO AND NANOSTRUCTURED MATERIALS FOR OPTICAL APPLICATIONS

by

Panit Chantharasupawong
B.Eng. Chulalongkorn University, 2010
M.S. University of Central Florida, 2012

A dissertation submitted in partial fulfillment of the requirements
for the degree of Doctor of Philosophy
in the College of Optics and Photonics (CREOL)
at the University of Central Florida
Orlando, Florida

Spring Term
2015

Major Professor: Jayan Thomas

© 2015 Panit Chantharasupawong

ABSTRACT

Nano and nanostructured materials offer unique physical and chemical properties that differ considerably from their bulk counterparts. For decades, due to their fascinating properties, they have been extensively explored and found to be beneficial in numerous applications. These materials are key components in many cutting-edge optic and photonic technologies, including photovoltaics, waveguides and sensors. In this dissertation, the uses of nano and nanostructured materials for optical applications are investigated in the context of optical limiting, three dimensional displays, and optical sensing.

Nanomaterials with nonlinear optical responses are promising candidates for self-activating optical limiters. In the first part of this study, optical limiting properties of unexplored nanomaterials are investigated. A photoacoustic detection technique is developed as an alternative characterization method for studying optical nonlinearities. This was done with an indigenously developed setup for measuring the photoacoustic signals generated from samples excited with a pulse laser. A theoretical model for understanding the experimental observations is presented. In addition, the advantages of this newly developed technique over the existing methods are demonstrated.

Blending optical sensitizers with photoconducting polymers and chromophores results in a polymer composite that is able to record a light grating. This composite can be used as recording media in 3D holographic display technology. Here, 2D nano materials, like graphenes, are used as optical sensitizers to improve the response time of a photorefractive polymer. The addition of graphenes to a PATPD/ECZ/7-DCST composite results in a three-fold enhancement in response time and therefore faster recording speed of the medium. The faster build-up time is

attributed to better charge generation and mobility due to the presence of graphenes in the composite.

Lastly, a facile nanofabrication technique is developed to produce metallic nanostructures with a tunable plasmonic response. The enhancement of the light-matter interactions due to these nanostructures in sensing an analyte is demonstrated.

To my parents

ACKNOWLEDGMENTS

With deepest appreciation, I would like to acknowledge my supervisor, committee members, friends, administrative staffs and family who help and encourage me to the completion of my study.

I would like to express my deep gratitude to Prof. Jayan Thomas, my research supervisor for his mentorship, guidance, useful discussion, and encouragement for this research work. I would also like to extend a special thanks to Prof. Reji Phillip, a visiting research scientist in our group, for helping me with both of my personal and academic difficulties. I would like to thank Professor David Hagan, my committee member and an associate dean for academic programs, for helping me settling down to this research group during the first year of my study. I would also like to extend my gratitude to other committee members, Professor Pieter Kik, Professor Romain Gaume, and Professor Debashis Chanda for their time and useful discussion. With much appreciation, I would like to thank Professor Laurene Tetard for her useful teaching, discussion and guidance with my research. I would like to thank the following research collaborators for helping me with material synthesis and characterization: Professor Rongchao Jin, Professor Pulickel Ajayan and Dr. Narayanan. Also, I would like to give special thanks to Dr. Cory Christenson and Brittany Lynn for their help and useful discussion on photorefractive polymer. I also would like to thank Rachel Franzetta, CREOL senior admissions specialist, for helping me with all academic administration and documents. In addition, assistance given by all the staffs at NanoScience Technology Center has a great help in conducting my research. Moreover, I would like to thank my group members for their friendship and quality time together.

Most of all, I would like to thank my parents for always being supportive, loving and having faith in me.

TABLE OF CONTENTS

ABSTRACT.....	iii
ACKNOWLEDGMENTS	vi
TABLE OF CONTENTS.....	viii
LIST OF FIGURES	xi
LIST OF TABLES	xv
LIST OF ABBREVIATIONS.....	xvi
1. INTRODUCTION	1
1.1 Nanomaterials in laser protection	2
1.2 Nanomaterials in three dimensional display application	4
1.3 Nanomaterials in optical sensing	7
1.4 Dissertation outline	10
2. OPTICAL LIMITING PROPERTIES OF NANOMATERIALS	12
2.1 Motivation.....	12
2.2 Theoretical background	13
2.2.1 Optical processes contributing to optical limiting	13
2.2.2 Benchmark optical limiters	21
2.3 Experimental methods	33
2.3.1 Sample Characterizations.....	33
2.3.2 Optical limiting measurement.....	37
2.4 Results and discussions.....	40
2.4.1 The effect of interstitial doping on optical limiting of Zn-ferrite	40
2.4.2 Size-dependent optical limiting of gold nanoparticles.....	49
2.4.3 Optical limiting of fluorinated graphene oxide.....	58
3. PHOTOACOUSTIC DETECTION OF OPTICAL NONLINEARITIES.....	68
3.1 Motivation.....	68
3.2 Theoretical background	69
3.2.1 Direct PA generation.....	71
3.2.2 Indirect PA generation	73

3.3	Experimental methods	75
3.3.1	Simultaneous measurements	75
3.4	Results and discussion	76
3.4.1	Simultaneous Optical and Photoacoustic Measurement of Nonlinear Absorption.....	76
3.4.2	More rigorous fitting of the PAZ-scan.....	82
4	PHOTOREFRACTIVE POLYMER SENSITIZED WITH NANOMATERIALS	95
4.1	Motivation.....	95
4.2	Theoretical background	98
4.2.1	Photorefractive polymer composites.....	98
4.2.2	Fundamental of photorefractive effect.....	104
4.2.3	Theory of holographic grating	118
4.3	Experimental characterizations of PR polymer	123
4.3.1	Four wave mixing measurement	123
4.3.2	Two beam coupling measurement	128
4.3.3	Photoconductivity measurement	130
4.3.4	Transmission ellipsometry measurement.....	131
4.4	Results and discussions.....	132
4.4.1	Photorefractive performance of a graphene-doped PATPD/7-DCST/ECZ composite	132
5	FABRICATION OF TUNABLE PLASMONIC SUBSTRATES.....	152
5.1	Motivation.....	152
5.2	Theoretical background	154
5.2.1	Nanofabrication techniques	154
5.2.2	Surface plasmon.....	162
5.3	Experimental methods	169
5.3.1	Nanoimprint fabrication of tunable plasmonic substrate	169
5.4	Results and discussion	171
5.4.1	Coupling Enhancement and Giant Rabi-Splitting in Large Arrays of Tunable Plexcitonic Substrates	171
6	CONCLUSION.....	188

APPENDIX A: COPYRIGHT PERMISSIONS FOR RELEVANT PUBLICATIONS UPON WHICH THIS DISSERTATION IS BASED ON IN PART	190
APPENDIX B: STEADY STATE DIFFRACTION EFFICIENCIES OF PATPD/7-DCST/ECZ COMPOSITES.....	204
APPENDIX C: RESOLVED ABSORPTION SPECTRA OF R6G ON PLANAR SILVER SURFACE.....	206
APPENDIX D: FDTD CALCULATION OF RAMAN ENHANCEMENT FACTORS OF NANOIMPRINTED NANOHOLES.....	208
APPENDIX E: MATLAB CODES	213
APPENDIX F: LIST OF RELEVANT PUBLICATIONS.....	218
LIST OF REFERENCES	220

LIST OF FIGURES

Figure 2.1 Schematic representations of the (a) five level system, (b) simplified three level system with negligible triplet state absorption, and (c) simplified three level system with negligible excited singlet state absorption.	16
Figure 2.2 Schematic illustration of XRD setup with (a) Debye-Scherrer and (b) Bragg-Brentano configurations.	34
Figure 2.3 Schematic diagram of the Z-scan setup.....	37
Figure 2.4 An example of plots obtained from the knife edge scan. Dots are the experimental data and solid line is the theoretical fit.	39
Figure 2.5 M^2 measurement data (dots). Solid line is the theoretical fit to Equation (2.2).....	40
Figure 2.6 Schematic representation of a ferrite crystal structure.	41
Figure 2.7 SEM images of $ZnFe_2O_4$, $NiZnFe_2O_4$ and $CuZnFe_2O_4$	43
Figure 2.8 (a) Absorption spectra of the samples. Inset shows $CuZnFe_2O_4$ sample of 52% linear transmission. (b) Tauc plots for calculating the bandgap energies.	44
Figure 2.9 Open aperture z-scans of the samples. Unlike C_{60} which shows optical limiting throughout, ferrite samples exhibit absorption saturation at the lower fluences, with a relatively sharper onset of limiting in the higher fluence region. Solid lines are numerical fits to the measured data obtained using Equation 2. Inset shows photographs of (a) direct, and (b) transmitted, laser beams in the far field.....	46
Figure 2.10 Optical limiting performance of the samples. (a) Output fluence, and (b) normalized transmission, plotted against input laser fluence. Lines connecting data points are guides to the eye.	47
Figure 2.11 UV-Vis absorption spectra and Electrospray mass spectrometry (ESI-MS) data (insets) of $Au_{25}(SR)_{18}$ (counterion: tetraoctylammonium, TOA^+), charge-neutral $Au_{38}(SR)_{24}$, and charge-neutral $Au_{144}(SR)_{60}$, respectively. In all cases, $R=CH_2CH_2Ph$	51
Figure 2.12 a) Optical absorption spectrum of Au nanocrystals. Inset shows the TEM image and polydispersity histogram, b) Representative schematic of the Z-scan set-up used for nonlinear optical measurements.....	52
Figure 2.13 Open-aperture z-scans measured in the Au clusters and nanocrystals. (a) Au_{25} , (b) Au_{38} , (c) Au_{144} , and (d) Au nanocrystals (~4 nm). Samples are excited using 5 ns laser pulses at 532 nm. Linear transmission of all samples is 25% at this wavelength. As seen from the figures, optical transmission is a function of sample position with respect to the laser beam focus ($z=0$). T_{norm} is the measured transmission normalized by the linear transmission of the sample. Solid curves are numerical fits to the experimental data, obtained using Equation 4. The valley shaped curves of Au_{25} and Au_{38} indicate pure optical limiting behavior, while the humps flanking the valley in Au_{144} signify the onset of saturable absorption. Absorption saturation is significant in the Au nanocrystals, as indicated by the strong peaks.....	53
Figure 2.14 Nonlinear transmission in the Au clusters and nanocrystals, calculated from the z-scan data using Equations 1 and 2. (a) Au_{25} , (b) Au_{38} , (c) Au_{144} , and (d) Au nanocrystals (~4 nm). Saturable absorption sets in as the cluster size increases, and becomes prominent in the nanocrystals.....	55

Figure 2.15 (A) The Kohn-Sham orbital energy level diagram calculated for the model compound $\text{Au}_{25}(\text{SH})_{18}^-$, (B) The theoretical absorption spectrum of $\text{Au}_{25}(\text{SH})_{18}^{102}$	57
Figure 2.16 (a) XRD pattern of GO, F-GO and HF-GO and (b) schematic representation of F-GO.....	59
Figure 2.17 (a) UV-Vis absorption spectrum of F-GO and (b) HF-GO. The high absorbance in the short wavelength region indicates the possibility of RSA upon optical irradiation at 532 nm.	61
Figure 2.18 (a) Measured Z-scan data. All samples have the same linear transmission of 50%. (b) Variation of sample transmission with input fluence. (c) Variation of sample output fluence with input fluence (d) Variation of scattering signals with input fluence	64
Figure 2.19 XPS spectra of (a) GO, (b) F-GO, and (c) HF-GO	66
Figure 3.1 Schematic illustration of direct PA measurement	71
Figure 3.2 Schematic illustration of the thermal piston model.....	73
Figure 3.3 (a) Schematic diagram of the simultaneous optical and PA measurements (b) Photograph of the set up.	76
Figure 3.4 (a) Optical signal of PCBM in chloroform with 20% linear transmission and E_{in} of 112uJ, (b) Optical signal of DODCI in methanol with 20% linear transmission and E_{in} of 112uJ, (c) Acoustic signal of the same concentration of PCBM as in (a), and (d) Acoustic signal of the same concentration of DODCI as in (b). Optical and acoustic signals were obtained simultaneously with the OPAZ-scan configuration. The solid lines are the fitted curves.	79
Figure 3.5 (a) PA signal of a very opaque PCBM with E_{in} of 80uJ. Optical signal cannot be measured with this sample due to its opacity (b) OPAZ-scan curves of carbon-black dispersion in water with 1% transmission at 532nm and E_{in} of 103uJ. The lines are the fitted curve.	80
Figure 3.6 OPAZ-scan data. (a) optical -z-scan and its fit (b) PA z-scan with the fitting value from the curve in (a). Clearly, model 1 diverts significantly from the experimental data....	82
Figure 3.7(a) 2D-plot of a Gaussian point source initial pressure (b) X-cross section of (a).....	87
Figure 3.8 2D time evolution of pressure distribution at time t equals (a) $1\mu\text{s}$ (b) $2\mu\text{s}$ (c) $4\mu\text{s}$ and (d) $6\mu\text{s}$ for Figure 3.7	88
Figure 3.9 (a) Acoustic wave measured by a line detectors at $y=-5\text{mm}$ of the source in Figure3.7(a). (b) Acoustic wave measured by a point detector at $x=0,y=-5\text{mm}$	89
Figure 3.10 2D-plot of initial pressure distribution created by passing Gaussian beam through a thin absorbing layer.....	90
Figure 3.11 2D time evolution of pressure distribution at time t equals (a) $0\mu\text{s}$ (b) $0.25\mu\text{s}$ (c) $0.5\mu\text{s}$ and (d) $1\mu\text{s}$ for Figure 3.....	91
Figure 3.12(a) Simulation of acoustic wave measured by a line detectors at $y= -0.8\text{mm}$ of the source in Figure3.10. (b) Acoustic wave measured by a point detector at $x=0,y= -0.8\text{m}$...	91
Figure 3.13(a) Simulated acoustic signal (b) Simulated acoustic signal received by a transducer with a center frequency of 10 MHz and bandwidth of 40%	92
Figure 3.14(a) Initial pressure distribution for the k-space fitting model. The beam diameter is $80\mu\text{m}$;(b) First PA pulse simulated from the initial pressure in (a); (c) comparison between acoustic two fitting model. The fitting parameters were obtained from experimental z-scan with PCBM in a 1mm cuvette. The beam waist is $30\mu\text{m}$. The linear transmission is 0.1 and $\beta= 7\text{nm/W}$	93

Figure 3.15 Comparison of normalized PA magnitudes obtained from Model 1 and 2 for different sizes of Gaussian beam waists in the z-scan configuration.....	94
Figure 4.1 Schematic illustration of a guest host system.....	98
Figure 4.2 Chemical structures of common (i) charge transporting polymers, (ii) sensitizers, (iii) plasticizers , and (iv) chromophore.....	99
Figure 4.3 schematic illustration of the processes involved in the formation of refractive index modulation.	104
Figure 4.4 Schematic representation of charge transfer in PR polymer composites. The HOMO and LUMO levels are not drawn to scale.....	109
Figure 4.5 Schematic diagrams of (a) transmission geometry (b) reflection geometry.....	119
Figure 4.6 Schematic diagram of the two beam coupling process.	122
Figure 4.7 Geometrical representation of the FWM measurement.....	123
Figure 4.8 Schematic diagram of the optical setup for characterizing PR polymers.....	124
Figure 4.9 Steady state diffraction efficiency vs. applied voltage of PATPD/7-DCST/ECZ/PCBM fabricated in our laboratory. It has internal diffraction efficiency as high as 85% at applied voltage of 6.5kV. The sample thickness is 105 μm	126
Figure 4.10 (a) transient grating recording and (b) transient grating decaying of PATPD/7-DCST/ECZ/PCBM (our sample).	126
Figure 4.11 Steady state two beam coupling gain vs. applied voltage of PATPD/7-DCST/ECZ/PCBM	129
Figure 4.12 Schematic diagram of the optical setup for transmission ellipsometry.....	132
Figure 4.13 (a) Absorption spectra of undoped, graphene doped and PCBM doped in the film form. The inset shows the absorption of concentrated 7-DCST in THF. (b) Absorption of PR composites without chromophores (film) with (red) and without (blue) sensitizer. The addition of graphene results in broadband flat absorption in the visible wavelength range. The inset shows absorption of PCBM and graphene in THF. Axis labels of the insets are the same as of the main curves.	138
Figure 4.14 (a) Transient FWM curves (b) Photoconductivity vs. applied field and (c) Photo-charge generation efficiency of undoped, graphene doped, and PCBM doped.....	139
Figure 4.15 Γ vs. E for undoped, graphene doped and PCBM doped. Data for both s- and p-polarizations are shown.....	145
Figure 4.16 PL spectra of (a) PATPD/7-DCST composite and 7-DCST, and (b) graphene doped and undoped PR samples. The excitation wavelength was at 532nm. The composites studied here were so prepared that the % weight loading of the components in polymer matrices are the same as those of the PR samples.....	147
Figure 4.17 Molecular energetic diagram for (a) undoped and (b) graphene doped. In the undoped PR composites, a photo-generated hole is transferred from 7-DCST to PATPD. ECZ does not participate in hole transport due to its lower HOMO level of 5.92eV. These holes are the primary charge conductors in PR polymers. In the case of graphene doped, graphene may act as an electron acceptor with 7-DCST as a donor, resulting in better exciton dissociation/charge generation efficiency.	148
Figure 4.18 Dark conductivity vs applied field for undoped, graphene doped and PCBM doped.	149
Figure 5.1 Schematic representation of large area plasmonic nanostructures fabrication process by SNAP method. PAN solution is spin coated on top of a Si mold (step 1). The polymer	

film is then cured at 150°C for one minute and transferred to a glass substrate by simply peeling off the polymer film (step 2). The films are etched at variable etching time, allowing a range of the nanoholes sizes. A 35nm layer of silver (grey color) is then deposited on top of the structure (step 3). 169

Figure 5.2 AFM images of nanohole structures at etching time of (a) 0min (b) 2min(c) 3min (d) 4min and (e) 5min. Hole diameter vs etching time is plotted in (f)..... 174

Figure 5.3 (a) Normalized extinction of the plasmonic nanohole samples at different etching time as a function of illumination wavelength. (b) Extinction vs wavelength of plasmonic nanohole samples coated with 1mM of R6G..... 175

Figure 5.4 (a) AFM profile fitted with fourth order Gaussian function (b) Unit cell for simulation (c) FDTD simulated extinction spectra..... 176

Figure 5.5 Comparison between experimental and simulated plasmon peak for samples with varied etching time..... 176

Figure 5.6 (a) Evolution of absorption of 1-11mM R6G deposited on a planar silver film (b) Hybridization diagram of plexcitonic modes (c) Extinction of 5 min etched sample with increasing R6G coverage from 1mM to 11mM (d) The magnitudes of the observed Rabi splitting versus the square root of the integrated R6G extinction on glass (arbitrary unit). The dash line is a guide to the eyes..... 179

Figure 5.7 (a) Emission spectra of the samples excited with laser wavelength of 532 nm. Both Raman and fluorescence signals are present. (b) Measured and calculated enhancement factor vs. hole diameter..... 182

Figure 5.8 (a) EF profiles at different Z cross-sections. Color scales are kept uniform for better comparison (b) Schematic illustrations of the index profile of the simulated structure. (c) EF profile at the middle of the groove where two adjacent holes connect; largest EF within the R6G layer is located here. (d) EF of profile cut along x at z=32nm of the 2D profile in (c). 184

LIST OF TABLES

Table 2.1 Summary of C_{60} absorption cross-sections and life times	23
Table 2.2 Effective nonlinear absorption coefficient (β_{eff}) and saturation intensity (I_s) calculated for the samples.	55

LIST OF ABBREVIATIONS

2D	Two-Dimensional
2PA	Two Photon Absorption
3D	Three-Dimensional
AFM	Atomic Force Microscope
ATOP	Aminothiényldioxocyanopyridine
BBP	Benzyl Butyl Phthalate
CBS	Carbon Black Suspension
CNT	Carbon Nano-Tube
CRT	Cathode Ray Tube
CT	Charge-Transfer
CTP	Charge Transporting Polymer
CzEPA	Carbazolylethylpropionate.
DBOP- PPV	Poly[1,4-phenylene-1,2-di(4-benzyloxyphenyl)vinylene]
DCST	Dicyanostyrenes
DEA	N,N-diethylaniline
DEH	Diethylamino-benzaldehyde diphenylhydrazone
DFWM	Degenerate Four Wave Mixing
DiPBI	Di-perylene bisimide
DM-MNT	2,5-dimethyl-4-methoxy-48-nitro-tolane

DMA	N,N-dimethylaniline
DMNPAA	2,5-dimethyl-4-p-nitrophenylazoanisole
DODCI	3,3'-diethyloxadicarbocyanine iodide
DOP	Diethylphthalate
DPP	Diphenyl phthalate
DTNBI	1,3-dimethyl-2,2-tetramethylene-5-nitrobenzimidazoline
EBL	Electron-Beam Lithography
ECZ	9-ethyl carbazole
FDTD	Finite Difference Time Domain
FGO	Fluorinated Graphene Oxide
FIBL	Focused Ion Beam Lithography
FIT	Finite Integration Technique
FOM	Figure Of Merit
FW1/eM	Full Width at 1/e Maximum
FWHM	Full Width at Half Maximum
FWM	Four Wave Mixing
GO	Graphene Oxide
HFGO	Highly Fluorinated Graphene Oxide
HOCI	Holographic Optical Coherence Imaging
HOMO	Highest Occupied Molecular Orbital
ITO	Indium Tin Oxide
LCD	Liquid Crystal Displays

LED	Light Emitting Diode
LSPR	Localized Surface Plasmon Resonance
LUMO	Lowest Unoccupied Molecular Orbital
MNPAA	3-methoxy-4-p-nitrophenylazoanisole
MPA	Multiphoton-Absorption
MPcs	Metallophthalocyanines
MWNT	Multiwall carbon nanotubes
Ncs	Naphthalocyanines
NFWM	Non-degenerate Four Wave Mixing
NIL	Nanoimprint lithography
NIR	Near-Infrared
NMP	N-methyl-2-pyrrolidinone
NPEMI-A	3-[2-(4-nitrophenyl)ethenyl]-1-allyl-2-methylindole
NPEMI-E	3-[2-(4-nitrophenyl)ethenyl]-1-(2-ethylhexyl)-2-methylindole
OPAZ-	
scan	Optical and Photoacoustic Z-scan
PA	Photoacoustic
PAN	Polyacrylonitrile
PATPD	Poly(acrylic tetraphenyldiaminobiphenyl)
PCBM	[6,6]-phenyl C 61 -butyric acid methyl ester
PCBM	[6,6]-phenyl-C ₆₁ -butyric acid methyl ester
Pcs	Phthalocyanines

PDMS	Poly dimethylsiloxane
PF6-TPD	Poly(N ,N '-bis(4-hexylphenyl)-N'-(4-(9-phenyl-9H-fluorene-9-yl))
PMMA	Poly(methyl methacrylate)
PPV	Phenylenevinylene
PR	Photorefractive
PSP	Propagating Surface Plasmon
PSX	Polysiloxanes
PVDMI	Poly-(2,3-dimethyl-1-vinylindole)
PVI	Poly-(1-vinylindole)
PVK	Poly(vinyl carbazole)
PVNPAK	Poly (N-vinyl)-3-[p-nitrophenylazo]carbazolyl
PVP	Poly vinylpyrrolidone
R6G	Rhodamine 6G
RSA	Reverse Saturable Absorption
SC	Space Charge
SEM	Scanning Electron Microscope
SERS	Surface Enhanced Raman Scattering
SL	Soft Lithography
SNAP	Spin-on-NAano-Printing
SPR	Surface Plasmon Resonance
SWNT	Single wall carbon nanotube

TBC	Two Beam Coupling
TEM	Transmission electron microscope
TNF	2,4,7-trinitrofluorenone
TNFDM	(2,4,7- trinitrofluoren-9-ylidene)malononitrile
TNFM	(2,4,7-trinitro-9-fluorenylidene) malononitrile
TPA	Terephthalic acid
TPM	Tris(1-pyrazole) methane
UV	Ultraviolet
XPS	X-ray photoelectron spectroscopy

1. INTRODUCTION

The trend of today's technology is moving toward miniaturization. Present society wants higher resolution displays, faster computers, and more compact devices. Making things smaller and exploiting material properties at atomic scale, with the use of Nano science and technology, can serve this social demand. These disciplines involve the study of phenomena and the manipulation of material at the atomic/molecular scale, where the properties differ notably from the properties at a macroscopic scale.

The idea of exploring and manipulating material properties at an atomic scale was first proposed to the science community in 1959 by Richard Feynman. In his presentation, 'There is plenty of room at the bottom', at the American Physical Society, he proposed that many unique properties and applications could come from manipulating matters at the nanometric scale. Even though at that time, the technology that could allow such concept was not yet realized, he did not afraid to share his vision of the future. Today, with the availability of tools such as scanning electron microscopes (SEM), transmission electron microscopes (TEM), and scanning tunneling microscopes (STM), scientists are able to visualize, work and manipulate materials at the atomic level. Although the vision of Richard Feynman has been realized, the quest is still on going.

Nano-science and technology were not only aided by the availability of the tools but also the discovery of new materials. For example, R. Smalley, H. Kroto and R. Curl won the Nobel Prize in chemistry for discovering a unique carbon allotrope containing 60 carbon atoms or C_{60} , in 1986. In 1991, a Japanese scientist, S. Iijima, discovered carbon nanotubes, another form of carbon whose structure was that of a rolled-up graphite. These newly found materials at the time gained a lot of attention from the community since their physical, chemical, and mechanical

properties are so unique that they allow realization of many useful applications. Even today, research on the use of their remarkable properties in new applications is being conducted. Moreover, newer nanomaterial such as graphene (a sheet of graphite) and other 2D materials like MoS₂ have been discovered. Many research works have been conducted around them.

Interaction of light with materials has always been fascinating to scientists. In the field of optics and photonics, integration with nanoscience and nanotechnology gives rise to remarkable optical applications, for example, solar harvesting, water sanitization, displays, and sensing. The scope of this dissertation is to explore the use of nanomaterials as well as nanostructured materials in optical applications, particularly in laser protection, three dimensional displays, and optical sensing.

1.1 Nanomaterials in laser protection

Since the first realization of lasers by Maiman in 1960, the protection of human and devices against lasers has become a safety concern for those who work with the technology. In typical laboratory setting where specifications of laser output are known, safety can be simply accomplished by using conventional optical filters based on linear optical effects such as laser goggles. However, in different situation such as military defense, requirements are much more stringent. Moreover, with present day high level of globalization and market convenience of e-commerce, the availability of relatively high power commercial lasers is surprisingly high. With the advances in manufacturing of solid-state devices, compact small lasers systems are affordable for nearly everybody. With such availability, lasers threats are no longer limited to scientists and soldiers. An example of civilian laser threat is the instance where people aimed

laser at an airplane and temporarily blinded the pilots. As a result, numerous research works are focused on developing better laser protection devices.

Laser protection devices can be divided into three main categories, namely static, active and self-activating protection. In the case of static protection, optical filters including line and band filters are usually used for laser protections. With this system, laser attenuation at a particular frequency can be substantially high. However, color distortion and visibility at the protection frequency can be an issue in some applications. Active protection on the other hand, uses optical elements like shutters and spatial light modulators for blocking laser light. This type of laser protections can offer broadband response, however, with their slow response time, they are only appropriate for protection against laser dazzling with continuous laser sources. The last type of laser protections, which is self-activating, uses the concept of nonlinear optical phenomena as protection mechanisms. These phenomena include nonlinear absorption, nonlinear refraction and nonlinear scattering, which contribute to nonlinear decrease in laser light at the object plane. In literature, this self-activating light reduction is called an optical limiting process and materials that exhibit such phenomena are called optical limiters. This self-activating protection can offer fast response time but with the downfall in their relatively high activation threshold. As a result, they are only suitable for damage protection but not the laser dazzling. Optical designs can however be done for optimizing the threshold of such self-activating devices. Nonetheless, the most important part of such device lies on the material development itself. Surprisingly, most of the best performing optical limiter are nanomaterials. For example, carbon nanoparticle suspensions exhibit strong thermally induced nonlinear scattering (NLS) effects and therefore optical limiting (OL) for ns laser pulses. Fullerene shows large nonlinear absorption and has been considered as a benchmark optical limiter. Other forms of nanostructured carbon

such as carbon nanotube (CNT) also exhibit exceptional optical limiting properties. Non-carbon nanomaterials like semiconductor and metal nanoparticles also have remarkable optical limiting performance.

Therefore, the first main body of this dissertation work is to measure optical limiting properties of new functional nanomaterials with an aim to discover better materials and provide database for future development of optical limiting devices.

1.2 Nanomaterials in three dimensional display application

In the ancient time, the way for our ancestors to tell their stories was through painting on cave walls. Since the development of the first camera, actual real-life images can be recorded. By running series of the captured images, motion pictures can be produced. Displays have been used as a media for viewing stories told or recorded by the capturer. With these media, viewer's experience with the story has been much enhanced compared to the old-day static photographs. The development of display technology began with the invention of cathode ray tube (CRT) in the nineteenth century. Though the first application of CRT technology was in the radar system, it was later recognized and adopted for displaying two-dimensional images in 1928¹. Today, the old CRT technology was succeeded by new technology like plasma display, liquid crystal displays (LCD), light emitting diode (LED), and laser-based displays². These new technologies were developed with an aim of improving human experience for the users, particularly through better image and color qualities.

With rising demands for better quality and more innovative experiences with display technology from users, realization of real-world-object like dynamic three-dimensional (3D) displays has become an ultimate goal in the display development. The vision of the technology

came out in a science fiction, Star Wars in 1977. Scientists' quest for recorded 3D experiences, however, traced long back to 1838 when Charles Wheatstone proposed the concept of the stereoscope at King's College, London³. Stereopsis or the perception of 3D structure is obtained on the basis of visual information derived from binocular vision. Binocular disparity that results from two forward facing eyes seeing different viewpoints is perhaps part of animal evolution for extracting three-dimensional information about the world. Wheatstone's stereoscopes used two subtly different hand-painted pictures in combination with two tilted mirrors to send different information to each eye, creating depth sensation. Following Wheatstone's development, nowadays, the term stereoscopy refers to 3D technologies that use eyewear to present the offset views to each eye whereas the term autostereoscopy means no special eyewear is required. Autostereoscopy, however, uses special optical elements to send the offset views to each eye. Stereoscopy can be achieved through the use of, for example, color filter as in the anaglyphic images, polarizers, and interference filters, integrated to the eyewear. On the contrary, autostereoscopic displays use optical elements such as parallax barriers and lenticular elements added into the display systems. More detailed review on both stereoscopic and autostereoscopic displays can be found elsewhere⁴. One of the major problems with both stereoscopic technologies is that the perceived 3D experience is not natural. This is because the image information sent to the eyes is merely two offset images. They do not represent the real world experience. In other words, users' perceptions are fooled by receiving two offset views and as a result, fake depth sensation is created.

Another type of 3D display technology is holographic display. Hologram can provide natural depth perception. It also prompts viewers to focus on an image itself rather than on a screen^{3,5}. These advantages are due to the fact that holograms store information about both the

intensity and phase of scattered light. Upon reading the holograms, the wavefronts of that light are reconstructed making viewers perceive the image as if it were scattered from the real object. The theory of holography was first developed by Dennis Gabor in 1947. However, the first hologram was realized more than a decade later after the invention of laser. Conventional holograms are made of photosensitive materials that record permanent interference patterns between different waves. Only static images can be produced with conventional holograms. Moreover, the recorded image is permanent and the conventional holographic media is a write-once-read-many system. However, due to research endeavor of scientists in realizing a naturally 3D display technology, holographic materials that enable development of dynamic 3D display, such as photorefractive polymers, have been developed⁶⁻⁷. While some 3D stereoscopic display technologies are commercially available in the markets, the 3D holographic display technology on the other hand is still far from reaching the consumers. There are three main aspects that need to be improved before market realization of such technology. First, current optical set-up for 3D holography is bulky compared to other types of display technology. Second, generating dynamic holograms at video rate requires a lot of computational power. Lastly, the holographic materials have slow response time and relatively poor color quality.

The second main body of this work is focused on tackling the last aspect, developing newer holographic material, particularly photorefractive polymer system. The use of nanomaterials in improving the performance of the holographic media is explored and fundamental physics behind the developed systems is studied.

1.3 Nanomaterials in optical sensing

Due to unique properties of nanomaterials compared to their bulk counterparts, the applications of nanomaterials to design and fabricate sensing devices are nowadays one of the most active research subjects. Physical, chemical and biological sensors can be made with nanomaterials. For example, CNTs can be used as gas sensor by monitoring their change in electrical resistance upon exposure to chemical gases⁸⁻⁹. A mixture of liquid gallium and CNTs has a thermo-sensing property similar to mercury¹⁰. Palladium mesowires undergo structural change and resistance when exposed to hydrogen gas¹¹. Apart from sensors based on electrical/thermo-physical properties of materials, optical sensing based on changes in optical properties of materials is also a promising approach.

Due to current availability of low cost optical instrumentations such as light emitting diodes and laser diodes, optical sensors can be easily implemented. Nanomaterials have been serving important roles in developing of optical sensors¹². For instance, nano-porous silicon is used for chemical sensing since physisorbed chemicals can quench photoluminescence of the material¹³. Similarly, photoluminescence properties such as intensity and lifetime of semiconductor quantum dots are altered with the presence of adsorbates on their surfaces¹⁴. Interferometric based chemical sensors using nano-patterned porous silicon was also demonstrated¹⁵. The average refractive index of the porous silicon layer was increased due to analyte adsorption. This results in spectral shift of Fabry–Perot fringes of the device. Perhaps, one of the hottest nanomaterials that gain tremendous research activities recently in the optical sensing applications is nanostructured metal.

Metallic nanostructures exhibit interesting optical properties, some of which are not shown by their bulk counterparts. For example, metal nanoparticles show large extinction and

absorption cross-sections that are highly dependent on their size and geometry. The underlying physics behind their unique optical properties is the collective oscillation of free electrons gas near its surface or surface plasmon. The resonance condition occurs when the nanoparticles interacts with electromagnetic radiation whose energy is the same as their natural frequency of the free electron oscillation. This resonance is termed surface plasmon resonance (SPR). The first experimental observation of surface plasmon resonance was done by Robert Williams Wood in 1902 ¹⁶. He observed a peculiar diffuse dark band when investigating diffracted spectra of a metallic grating. Such phenomenon was called Wood's anomaly and was later explained by Fano anomaly in term of a forced resonance related to the leaky waves supportable by the grating ¹⁷.

Today, it is well known that those leaky waves were actually surface plasmon. When surface plasmon resonance occurs at the nanostructure interfaces, particularly nanoparticles, it is called localized surface plasmon resonance (LSPR) owing to its non-propagating nature. This surface plasmon property of metallic nanostructures are heavily utilized in making optical sensors due to two interesting consequences of the resonance. First, the resonance wavelength is dependent on the index of refraction of the environment near the metal surface. By attaching chemical probes to the surface of the metal, binding of analyte molecules to the probes results in shifting the SP extinction peak. As a result, chemical sensors, based on resonance shifting due to presence of analytes have been developed¹⁸. Another consequence is that, at the resonance, the local electromagnetic field near the metal structure is greatly enhanced. This large local electromagnetic field can be used to enhance other optical/physical phenomena like Raman scattering, fluorescence, molecular desorption and molecular ionization. Consequently, sensing technique that capitalizes on the local electromagnetic field enhancement like surface enhanced Raman spectroscopy was developed.

Surface enhanced Raman scattering (SERS) is a phenomenon in which Raman scattering signals of materials adsorbed on a small metal structure is greatly enhanced. One of the pioneering works was done by Fleischman et al. in 1974¹⁹. They observed enhanced Raman scattering signals of pyridine on a rough silver surface. Two main mechanisms are involved in signal enhancement of SERS, namely chemical mechanism and electromagnetic mechanism due to surface plasmon. However, the latter gives larger magnitude of enhancement and is considered as a dominant mechanism. The term "hot spot" has been used to generally describe the location near metallic nanostructures where there is high field intensity. Due to this field enhancement, the Raman scattering signals of molecules in the proximity of these hotspots are enhanced. Detection limit down to a few molecules has been achieved with this technique. For example, in 1977, pioneer research groups reported single molecule detection using SERS. Kneipp et al. reported the detection of single molecules of crystal violet on aggregated colloidal silver²⁰. In the same year, Nie and Emony reported single molecule detection of organic dye on the surface of a silver particle²¹. Unlike resonance-shift based sensors where information on the adsorbed species cannot be extracted, SERS provides molecular identification. However, real time detection with resonance-shift –based sensors is much easier to implement. Therefore, a complementary analytical scheme, where molecules can be first detected with LSPR-shift assays and later identified with SERS, can be used²²

In order to use surface plasmon properties in a mainstream analytics, several challenges has to be overcome. For example, more investigations need to be done on better understanding the physics of chemisorption of molecules on the metal surfaces. Also, development of reproducible plasmonic platforms has yet to achieve. Unsurprisingly, development of plasmonic substrates is one of the most prominent research activities in this field. Several fabrication

techniques have been developed for producing plasmonic substrates for sensing applications. These techniques range from simple system with metal particles dispersed on a flat surface, or in a form of solution, to complicated structure fabricated by more sophisticated tools like electron beam lithography. The former has a great disadvantage on its poor reproducibility while the latter has an issue with its associated high cost of fabrication and low throughput. Therefore, the technique for producing reliable and cost effective plasmonic substrate with exceptional quality is yet to be developed. As a result, the last main body of this work is to use the knowledge of nanofabrication in order to develop low cost plasmonic structures with an aim to provide an alternative fabrication technique to the field. The fabricated structures are used to study interesting phenomena resulting from light-matter interactions.

1.4 Dissertation outline

This dissertation work is dedicated to the use of nano and nanostructured materials for optical applications. In the beginning chapters, the application is based solely on the properties of the materials itself. In later chapters, more complex applications are introduced in which the nano/nanostructured materials are integrated with other functional materials. In chapter 2, optical limiting properties of various nanomaterials are investigated. Theoretical background as well as experimental setup for studying the materials are presented and discussed. Motivated by the work in chapter 2, a photoacoustic-based characterization technique for investigating nonlinear extinction of material is studied and discussed in chapter 3. Chapter 4 discusses the use of nanomaterials as a sensitizer in polymeric holographic media, namely photorefractive polymer. The use of 2D nanomaterials like graphenes as PR sensitizers is explored. The theoretical background for the subject is also included in this chapter. In chapter 5, the aspect of structuring

materials on a nanoscale or, in other words, nanofabrication is introduced. Commonly adopted nanofabrication techniques are briefly reviewed. The purpose of this chapter is to develop a facile fabrication technique for producing plasmonic nanostructures for enhancing light matter interaction. The use of the fabricated structures for photon-exciton coupling as well as enhancing Raman detection is investigated.

2 OPTICAL LIMITING PROPERTIES OF NANOMATERIALS*

2.1 Motivation

Lasers are indispensable for applications in a variety of fields. This includes military, telecommunications, manufacturing and medicine. Even though, laser is a very powerful source of energy, at times, it can be damaging too. These laser systems are so powerful that in industries high power laser systems are often used for cutting and drilling. For humans, unintended laser irradiations can damage eyes or other body parts. This poses serious health threat to workers who are working with such laser systems. In military applications, lasers are incorporated in many weaponries. These lasers can damage sensors or blind military personals. Therefore, there is a considerable need for a device to protect people from laser threats.

To date, laser protection devices used in real applications are non-adaptive device in which its transmission is constant regardless of incident laser power. They primarily use linear absorption of materials to reduce the transmission. Complete elimination of certain wavelengths (colors) can create serious problems in application where high visibility is required in the

* The work presented in this chapter are extensions of Chantharasupawong, P.; Philip, R.; Endo, T.; Thomas, J., Enhanced Optical Limiting in Nanosized Mixed Zinc Ferrites. *Applied Physics Letters* 2012, *100*, 221108., Philip, R.; Chantharasupawong, P.; Qian, H.; Jin, R.; Thomas, J., Evolution of Nonlinear Optical Properties: From Gold Atomic Clusters to Plasmonic Nanocrystals. *Nano letters* 2012, *12*, 4661-4667., and Chantharasupawong, P.; Philip, R.; Narayanan, N. T.; Sudeep, P. M.; Mathkar, A.; Ajayan, P. M.; Thomas, J., Optical Power Limiting in Fluorinated Graphene Oxide: An Insight into the Nonlinear Optical Properties. *The Journal of Physical Chemistry C* 2012, *116*, 25955-25961.

absence of the harmful laser radiation. One of the proposed solutions to this problem is optical limiting devices. Ideally, in such devices, instead of having intensity independent transmission, transmission decreases as the incident power increases. One of the feasible directions in realizing such adaptive devices is to use nonlinear optical materials. Surprisingly, some of the best performing nonlinear optical limiting materials are nanomaterials such as, fullerenes and carbon nanotubes²⁻³. In this chapter, optical limiting properties of interesting nanomaterials are investigated.

2.2 Theoretical background

2.2.1 Optical processes contributing to optical limiting

There are three main optical processes that can result in optical limiting behaviors of materials, namely, nonlinear absorption, nonlinear refraction and nonlinear scattering. This section will provide an introduction into such processes.

2.2.1.1 Nonlinear absorption

The simplest way for achieving passive optical limiters is through the use of nonlinear absorbing materials. In these materials, their absorption increases with increasing incident fluence or irradiance. Such nonlinear absorbers can be found in both organic and inorganic materials. Two main nonlinear absorption mechanisms are typically involved in optical limiting actions, which are (i) multiphoton-absorption (MPA) and (ii) reverse saturable absorption (RSA).

(i) *Multiphoton-absorption (MPA)*

When a medium interacts with an external electric field, its polarization can be written as²³:

$$\Delta P = K_1 \chi_{ij}^{(1)} E_j + K_2 \chi_{ijk}^{(2)} E_j E_k + K_3 \chi_{ijkl}^{(3)} E_j E_k E_l + K_4 \chi_{ijklm}^{(4)} E_j E_k E_l E_m + \dots \quad (2.1)$$

Where K's are the coefficients which depend on systems of unit and degeneracy. $\chi^{(n)}$ are optical susceptibilities in the form of n+1 rank tensor describing linear (n=1) and nonlinear processes (n>1). For example, the first term, (n=1), describes linear phenomena, i.e. index of refraction and absorption coefficient of material. The second term $\chi^{(2)}$ represents nonlinear phenomena such as second harmonic generation, sum and difference frequency generation, optical rectification, linear electro optic effect and parametric emission. The third term $\chi^{(3)}$ is responsible for 3rd harmonic generation, nonlinear refraction, two-photon absorption (2PA), stimulated Raman and Brillouin scattering, self/cross phase modulation, and four-wave mixing. These susceptibilities describe both linear and nonlinear response of the medium with electric field components of an electromagnetic radiation.

When a laser beam is propagating through a nonlinear absorbing sample, the intensity variation of a beam, traveling in the Z direction is given by:

$$\frac{dI(z)}{dz} = -\alpha^{(1)} I - \alpha^{(2)} I^2 - \alpha^{(3)} I^3 - \alpha^{(4)} I^4 - \dots \quad (2.2)$$

in which $\alpha^{(n)}$ are the absorption coefficients of simultaneous absorption of one photon (n=1), two photon (n=2), three photon (n=3), etc. $\alpha^{(n)}$ are proportional to $\chi^{(2n-1)}$

In the case of optical limiting with MPA, two photon absorption (2PA) is the dominant process since it is much more efficient and requires much lower limiting threshold than higher-order photon absorption. Therefore, Equation 2.2 is reduced to:

$$\frac{dI(z)}{dz} = -\alpha^{(1)}I - \alpha^{(2)}I^2 \quad (2.3)$$

with $\alpha^{(1)}$ and $\alpha^{(2)}$ being the linear absorption and 2PA coefficient respectively. The absorption coefficients are related to the susceptibilities through the following relations:

$$\alpha^{(1)} = 2 \text{Im}(k) = \frac{4\pi}{\lambda} \text{Im}(\sqrt{\chi^{(1)} + 1}) \quad (2.4)$$

$$\alpha^{(2)} = \frac{\omega\mu_0}{n^2} 3 \text{Im}(\chi^{(3)}(\omega, \omega, -\omega, \omega)) \quad (2.5)$$

where ω is the incident photon frequency, n is the index of refraction, k is the propagation vector, λ is the incident wavelength, μ_0 is vacuum permeability.

In general, multiphoton-absorption processes have low loss in linear regime. However, their drawback is that high irradiance is required to achieve limiting action. Therefore, optical limiters based on this principal only works well with laser pulse smaller than picoseconds. Another drawback for this type of limiters is that they usually have narrow spectral range. For example, two-photon absorbing semiconductors only work when the incident photons have their energies ranging from $E_g/2$ to E_g , where E_g is the band gap energy. One can argue that choosing large band gap semiconductor might increase the spectral range of the device. Unfortunately, the two-photon absorption coefficients of semiconductors scale inversely with the third power of the

band gap. As a result, potent semiconductor-based optical limiters are the ones that have narrow band gap and can only be used in the mid-infrared.

(ii) *Reverse saturable absorption (RSA).*

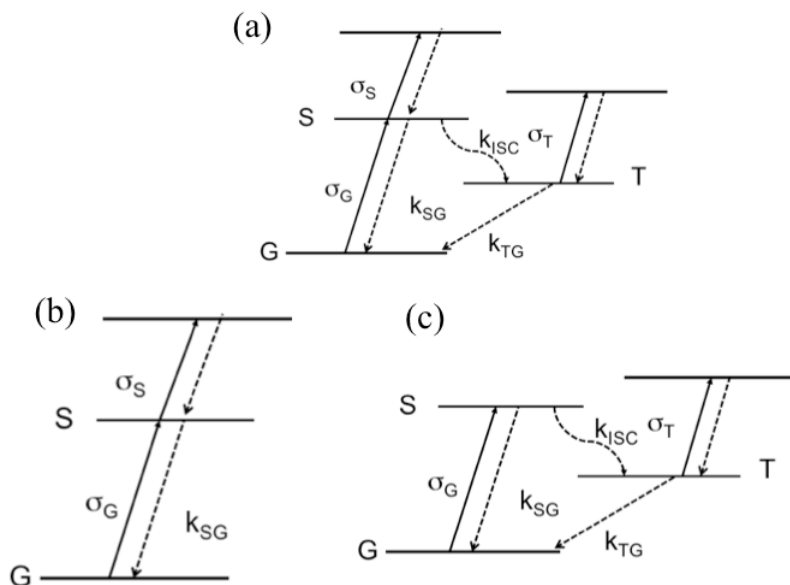


Figure 2.1 Schematic representations of the (a) five level system, (b) simplified three level system with negligible triplet state absorption, and (c) simplified three level system with negligible excited singlet state absorption.

2PA process can be significantly enhanced by a resonant one-photon absorption. Essentially, with this particular case, the absorption of two photons occurs in two-step process. First, a photon excites an electron from its ground state to the excited state. Second, another photon excites the same electron further to the higher lying excited state. To have RSA process, two requirements must be met: (1) the materials must have their excited state cross-section higher than their ground state cross-section and (2) both the ground state and the excited state can absorb photons of the same energy. In the case of organic molecules, these requirements are often met since they often have many vibronic sub-states.

Most promising reverse saturable absorbers are highly symmetric organic dyes in which low-lying excited states are weakly allowed. Since these dyes are typically polyatomic in nature, vibrational relaxation in these molecules is very rapid. Thus, even for picosecond pulse, only the fully relaxed excited states are considered for mechanistic explanation of RSA. The widely used kinetic model for RSA is five-level system, shown in Figure 2.1, described by a simple rate equation:

$$\frac{di}{dz} = -i(\sigma_G N_G + \sigma_S N_S + \sigma_T N_T) \quad (2.6)$$

where i represents the change in photon flux with distance z with the sample of length L , σ is the absorption coefficient, and N is the population of the corresponding state. The subscripts G, S, and T denote ground state, singlet state, and triplet state respectively. Under the assumption that there is negligible population in the excited state, the change of population with time can be described as follows:

$$\frac{dN_S}{dt} = \sigma_G N_G i - (k_{SG} + k_{ISC}) N_S \quad (2.7)$$

$$\frac{dN_T}{dt} = k_{ISC} N_S - k_{TG} N_T \quad (2.8)$$

$$N_0 = N_G + N_S + N_T \quad (2.9)$$

where N_0 is the total population and k is the interstate crossing rate. For short laser pulse in the order of shorter than picoseconds time scale, reverse saturable absorption will happen when the

excited singlet state absorption cross-section is higher than the ground state absorption cross section, $\sigma_S/\sigma_G > 1$, since the excited triplet population is negligible within this laser pulse duration. For such case, the five-level system (Figure 2.1(a)) can be simplified to a three-level system (Figure 2.1 (b)). On the other hand, for the laser pulse of nanoseconds or longer, the condition for having RSA is that $\sigma_{EF}/\sigma_G > 1$ where σ_{EF} is the effective weight averaged of σ_S and σ_T . This effective excited state cross-section area functions of both the intersystem crossing rate and the intersystem-crossing yield. In the limit where the intersystem-crossing rate is much shorter than the laser pulse duration, the ratio between the effective excited state cross-section and ground state cross-section can be simplified to $\Phi_{ISC}\sigma_T/\sigma_G$ where Φ_{ISC} is the intersystem crossing yield. In this case, the five level-system (Figure 2.1 (a)) can be again simplified to a three-level system (Figure 2.1(c)). In the case of the simplified three-level system, the intensity variation of a propagating laser beam traveling in the z direction is given by:

$$\frac{dI}{dz} = -\alpha I - \sigma_{EF} N I \quad (2.10)$$

By ignoring ground state depletion, the rate equation for the first excited state becomes:

$$\frac{dN}{dt} = \frac{\sigma_g N_g I}{h\omega} \quad (2.11)$$

Integrating over t results in the following expression:

$$\frac{dF}{dz} = -\alpha F - \frac{N_g \sigma_g \sigma_{ex}}{2h\omega} F^2 = -\alpha^{(1)} F - \alpha_{eff}^{(2)} F^2 \quad (2.12)$$

This equation looks like the one for 2PA but in reality it is a $\chi^{(1)}:\chi^{(1)}$ nonlinearity process.

Nonetheless, in real systems, many RSA absorbers limit nanosecond pulse or longer from both excited singlet and triplet absorptions. Ground state depletion also plays some role and will change this equation to something more complicated depending on the state lifetime. One can observe combination of both saturable absorption and excited state absorption in the real system. Even though saturable absorption is desirable in applications like laser pulse compression or passive mode locking, it is however undesirable in optical limiting. To yield a strong RSA, it is desirable to have materials with a large ratio of σ_{EF} to σ_G .

Generally, two-step two photon absorption process or reverse saturable absorption is more efficient than pure 2PA. Potent optical limiters based on nonlinear absorption usually belong to the RSA category. Centrosymmetric organic molecules, such as metallophthalocyanine and C_{60} with 2D and 3D π -electron conjugated system respectively, usually exhibit strong RSA.

2.2.1.2 Nonlinear refraction

Another optical process that can lead to reduced optical power to the device under protection is nonlinear refraction. Due to Kramer-Kronig relation, every material exhibiting nonlinear absorption also has nonlinear refraction properties. The nonlinear refraction, defined to the third order or optical Kerr effect, is described by a parameter n_2 :

$$n = n_0 + n_2 I \quad (2.13)$$

where n is the effective index of refraction of the medium and n_0 is the linear (intensity-independent) index of refraction. Due to this nonlinear effect, the central part of a laser beam induces larger refractive index change than other part of the beam. This results in the medium behaving like a lens as there is a non-uniform refractive index distribution seen by the laser beam. Depending on the sign of n_2 , this can lead to either self-focusing or self-defocusing of the

laser beam. In far field, both effects result in spreading of the beam and hence reduction in the energy density compared to the linear regime. Therefore, proper designs of an optical system, for example, placing an aperture at the pupil plane whose size corresponds to the size of the laser beam in the linear regime, can limit the total transmitted energy.

2.2.1.3 Nonlinear scattering

Optical damage in a liquid host is often desirable for obtaining better optical limiting performance. Plasma or micro bubbles that appear in a liquid host due to optical damage can cause effective scattering of the laser light. This nonlinear/intensity-dependent scattering process can provide device protection at higher input energies.

In this dissertation proposal, optical limiting actions in nanomaterials resulted from nonlinear absorption and scatterings are of interest. The reason is because aperture designs and the knowledge on the image size at the image plane are not needed when building optical limiters based on these two mechanisms. Rather, simple Keplerian telescope design can be used to build optical limiters.

2.2.2 Benchmark optical limiters

2.2.2.1 Buckminsterfullerene

Buckminsterfullerene or C_{60} belongs to the family of fullerene materials, which are composed entirely of carbons in the form of a sphere. In addition to C_{60} , other members of fullerene family are, for example, C_{70} , C_{76} , C_{78} , and C_{84} . C_{60} was first discovered in 1996 by Harald Kroto, Richard Smalley, and Robert Curl. They were awarded the Nobel Prize for the discovery. Among all fullerene materials, to date, C_{60} is by far the best optical limiter at 532nm.

In 1991, S. Kuroshima et al. studied the excited state properties of C_{60} using laser-flash photolysis²⁴. The ground state has absorption maxima around 300 and 350 nm. The excited singlet state S_1 has absorption maxima at 513, 759 and 885 nm whereas the excited triplet state T_1 has absorption maxima at 457, 509 and 747 nm. In the wavelength region greater than 400 nm, the ground state absorption is much weaker than those of the excited states S , and T_1 . These results showed the possibility of using C_{60} as a broadband optical limiter. J.W Arbogast et al. studied the photophysical properties of C_{60} and observed similar results. They found that the photoexcited triplet state absorption cross-section was stronger than that of the ground state²⁵. In 1992, L.W Tutt and A. Kost reported for the first time the optical limiting performance of C_{60} and C_{70} solution with ns pulse at 532nm²⁶. The performances of these two materials were better than other optical limiting materials previously reported. The performance of C_{60} is however better than C_{70} .

The dynamic of RSA of C_{60} in toluene solution with ns and ps pulse from 532 nm Nd:YAG laser was studied²⁷⁻²⁹. The experimental results agree well with the theoretical simulation based on the

5-level system. Y.Wang et al used the following reduced 3-level rate equations to explain their experimental data ³⁰:

$$\begin{aligned}\frac{dn_1}{dt} &= -\frac{\sigma_G I n_1}{h\nu} + \frac{n_2}{\tau_{SG}} + \frac{n_3}{\tau_{TG}}, \\ \frac{dn_2}{dt} &= \frac{\sigma_G I n_1}{h\nu} - \frac{n_2}{\tau_{SG}} - \frac{n_3}{\tau_{ISC}}, \\ \frac{dn_3}{dt} &= \frac{n_2}{\tau_{ISC}} - \frac{n_3}{\tau_{TG}},\end{aligned}\tag{2.14}$$

where n_1, n_2 and n_3 are the populations of the ground state, the first excited singlet state, and the first excited triplet state respectively. The light intensity is related to the rate equation through the following relations:

$$\frac{dI}{dz} = -\alpha I\tag{2.15}$$

$$\alpha = \alpha_0 + \alpha_s + \alpha_T = \sigma_G n_1 + \sigma_s n_2 + \sigma_T n_3$$

The boundary conditions are:

$$\begin{aligned}n_1(t = -\infty, z) &= N = n_1 + n_2 + n_3 \\ n_2(t = -\infty, z) &= 0 \\ n_3(t = -\infty, z) &= 0 \\ I(t, z = 0) &= I_0 \exp(-c(t/\Delta t)^2)\end{aligned}\tag{2.16}$$

where I_0 is the peak intensity of the incident laser assuming temporal Gaussian shape, and N is the total population. The rate parameters were taken from S. Kuroshima work, summarized in Table 2.1.

Table 2.1 Summary of C_{60} absorption cross-sections and life times

Absorption cross-section	Relaxation time
$\sigma_G=2.87 \times 10^{-18} \text{ cm}^2$	$\tau_{SG}=30\text{ns}$
$\sigma_S=1.57 \times 10^{-17} \text{ cm}^2$	$\tau_{TG}=280\mu\text{s}$
$\sigma_T=9.22 \times 10^{-18} \text{ cm}^2$	$\tau_{ISC}=1.2\text{ns}$

According to their study, the experimental results agree well with the RSA model below the light fluence of 1 J/cm^2 . The model fails to predict the experimental results beyond 1 J/cm^2 . This suggests that other processes, such as diffraction, thermal effects, and two-photon absorption, may happen. This deviation from 5-level theoretical model at higher fluence was also observed by other reports^{28, 31}. Nevertheless, their major conclusions were the following:

- (1) The laser pulse width Δt has an effect on the RSA of the C_{60} . When $\Delta t > \tau_{ISC}$, the triplet state absorption plays a dominant role. However, when $\Delta t < \tau_{ISC}$, the singlet state absorption dominates.
- (2) The optical limiting of C_{60} depends highly on the concentration of the solution. The higher the concentration the stronger the limiting. However, the transmittance is lower for a more concentrated solution.

In addition to concentration dependence of optical limiting of C_{60} , the optical limiting performance of C_{60} is also solvent dependent^{29, 32}. For example, C_{60} in N,N-diethylaniline

(DEA) or N,N-dimethylaniline (DMA) have poorer optical limiting performances with ns pulse at 532nm than C₆₀ in toluene solution. This is because the ground state absorption is higher in the case of fullerene in aromatic amine solution due to the contribution of fullerene-amine charge transfer complex. E. Koudoumas explained this solvent dependency in term of local field correction imposed by the solvent³².

Kost et. al. investigated optical limiting properties of C₆₀ in PMMA matrix³³. They found that the limiting threshold of the solid film is higher than that of C₆₀ in toluene solution. They attributed the better performance of the C₆₀/toluene to nonlinear scattering of the solvent at higher fluence. M.P. Joshi et al also studied the optical limiting of C₆₀ in toluene³¹. Since the intersystem-crossing rate is very fast compared to their ns pulse, they used 2 level systems to explain their experimental results. Discrepancy between theoretical model of RSA and the experimental data was observed at higher fluence and attributed to other nonlinear loss mechanism. Similar findings were also observed by Mc Lean et.al.²⁸ S.R. Mishra et al, later, studied the contribution of nonlinear scattering on the optical limiting performance of C₆₀ in toluene with ns pulse³⁴. They found that the RSA model fit well with the experimental results at lower fluence (~<3J/cm²). At higher fluence, however, deviation was observed. They also measured scattering signal at an angle from the sample and found that light scattering increases at the higher fluence. As a result, the scattering in C₆₀ solutions at high fluence could be due to thermally induced inhomogeneity. Several studies have investigated the effect of different functionalization to the optical limiting performance of C₆₀ molecules. Some have reported better performance such as organometallic-C₆₀ derivative³⁵, C₆₀-polycarbonate³⁶, and C₆₀-poly(vinylchloride)³⁷. Poorer performance have also been reported, for example, C₆₀-dimer,

poly-C₆₀³⁸, and C₆₀-PMMA³⁷.

While most of the optical limiting studies were done at 532nm for C₆₀, it is good to note here that the performance is also wavelength dependent. As mentioned in the beginning of the section, C₆₀ is a potential broadband optical limiter due to its wide wavelength range in which the absorption cross-section of the excited state is higher than of the ground state. However, there are still wavelengths where C₆₀ does not behave as an optical limiter. For example, J.L. Saiz et al. investigated the wavelength dependent nonlinear absorption of C₆₀³⁹. They found that at 308 and 534 nm, it behaves as reverse saturable absorber while at 337 nm the behavior changes to saturable absorber, which is undesirable for optical limiting application. Perhaps, the reason that most of optical limiting work were done with green laser (~532nm) is because the large availability of the laser. In addition, human eyes are most sensitive to green light.

2.2.2.2 Phthalocyanines and metallophthalocyanines

Phthalocyanines are aromatic macrocyclic compounds typically used as dyes. They have been used extensively in optical applications due to their large nonlinearities and fast optical response⁴⁰. Phthalocyanines (Pcs) and their central metal containing forms or metallophthalocyanines (MPcs) have shown excellent optical limiting due to their large ratio of excited state to ground state absorption. RSA is responsible for their limiting action and their behavior can be explained by the five-level system. Pcs and MPcs cannot be dissolved in common organic solvents. As a result, either alkyl or alkoxy substituents attached to their peripheral positions are usually used to improve their solubility. Perhaps, the most recognized property of Pcs in nonlinear optical applications is their so-called heavy-atom effect. Optical limiting mechanisms of Pcs and MPcs on picosecond and nanosecond time scales are different.

In picosecond time scales, the excited state absorption is dominated by the excited-singlet state, whereas in the nanosecond measurements the triplet state absorption is more prominent. This is because the lifetime of the excited-singlet state is in the order of picosecond. Nevertheless, with nanosecond pulses, the number of excited triplet populations is limited due to their slow intersystem crossing rate. It was found that the use of the heavy-atom substituents could enhance their optical limiting performance. This is because, larger the atomic number of the central metal atom, the faster the inter-system crossing rate resulting in more triplet state population⁴¹. Perry et al. investigated a series of PcMs with group 3A (Al, Ga, In) and group 4A (Si, Ge, Sn, and Pb) metal substituents. They found that the triplet quantum yield and thus optical limiting efficiency is the highest with PbPcs⁴². Shirk et al. studied the third order nonlinear susceptibility of the Pt, Pb and metal free tetrakis (cumylphenoxy) phthalocyanines using four wave mixing at the wavelength of 1064nm⁴³. They found that the third order nonlinear susceptibility was substantially higher in the case of metal substitutions. PtPc and PbPc have a number of low-lying charge transfer states not present in the metal-free compound and this contributed to such improvement. However, the Pt substitution is more effective in enhancing the third order susceptibility than the Pb substitution and this might be due to the fact that the transition metals with d-valance orbitals like Pt might introduce more low lying states than the main group metals.

MPcs generally exhibit strong absorption in the visible and in the near UV which corresponds to their Q-band (absorption at ~700 nm) and B/ Soret band (absorption at 300-400 nm) respectively⁴⁴. For the light wavelength between the B and Q bands, a photon will cause electron to make a transition from ground state to either a higher vibrational level of the first excited state or to a weakly allowed electronic state where it can later relax to lower vibrational

states of the first excited state. Within picosecond time, another photon can excite this electron further, resulting in another singlet-singlet transition. Intersystem crossing also plays its role here. It competes with fluorescence and internal conversion, resulting in electrons in the lowest triplet state. As a result, triplet-triplet absorption becomes possible. The triplet-triplet absorption spectra of MPcs are broadband and independent of the central metal atom. This absorption, centered at around 510nm, is well overlapped with the window of minimum absorption of the ground-state⁴⁵. As a result, MPcs exhibit broadband optical limiting in the range of range 450-600 nm for laser pulses whose temporal widths equal to or greater than nanosecond. The upper limit is set by the triplet lifetime. Due to poor solubility of Pcs and Mpcs, they usually form aggregates in solution. This results in fast decay of the upper triplet state due to intermolecular interactions. Yu Chen et al. synthesized axially Bridged Pcs in which two Pc molecules are joined at their central metal through an oxygen atom⁴⁶. They found that (1) axial substitution suppress aggregations of Pcs, (2) the excited singlet states lifetime was longer in the dimer than in the monomer and (3) the optical limiting efficiency was better in the dimer. Adding ligands to the central atom M of MPcs can be a method to control the nonlinear optical properties. The effect of this axial substitutions on the optical properties of indium phthalocyanines and naphthalocyanines was studied⁴⁷. It was found that, with axial ligands, optical limiting efficiency was improved. The possible reason for such enhancement might be because of the increase in dipole moment perpendicular to the macrocycle of the axially substituted Pcs. They also studied the effect of p-trifluoromethylphenyl functional group attached to the central gallium and indium atom of MPcs. They observed change in the saturation of the optical limiters and proposed that this method could be used to tailor optical limiting properties. Adding one more aromatic ring to the four peripherals of Pcs results in the extended π - conjugated forms called Naphthalocyanines

(Ncs). Expanding the ring structure from Pcs to Ncs red shift the ground state transmission window and the range of effective optical limiting⁴⁸. This method is promising for tuning the optical response of the material. The drawback of this strategy, however, is that Ncs have higher tendency to aggregate. Hanack et al. used axial as well as unsymmetrically peripheral substitutions to improve the solubility as well as the optical limiting response⁴⁹.

2.2.2.3 Carbon black suspension

Carbon black or carbon particle suspensions are polycrystalline carbon with high surface to volume ratio suspended in liquid. They can be found in common household item such as black ink. The use of carbon black suspension as optical limiter was pioneered by E.W.V. Stryland et al.⁵⁰. The mechanism behind their optical limiting action is nonlinear scattering⁵¹. The reduction in transmission with these materials is due to rapid heating of the carbon particles. This results in subsequent ionization and vaporization, which leads to the formation of rapidly expanding microplasmas. These microplasmas act as scattering centers and contributes to the optical limiting process⁵². In addition, bubble formation, also comes into play, which result in more nonlinear scattering and therefore more efficient optical limiting action. The microplasma process is solvent-independent and concentration-independent. The bubble formation, on the other hand, is very solvent-dependent and results in solvent-dependent characteristics of CBS. Thermophysical properties of the solvent plays important role in the optical limiting strength of CBS⁵³⁻⁵⁴. For example, it is found that optical limiting performance of CBS in solvent with lower boiling point is better than that of higher boiling point because of the bubble formation. The physical size of the carbon suspensions also plays an important role in their optical limiting performance. For instance, Tiwari et al found that CBS in saline has better optical limiting

performance than the one in water. They attributed their findings to larger particle size in saline⁵⁵. One of the main advantages of CBS as an optical limiter is that their limiting is extremely broadband since the carbon black has black color and the microplasma formation is initiated by linear absorption. It however has its own drawbacks. For instance, the optical limiting with CBS is only sufficient with ns time scale or longer. This is because the time required to form microplasma, which essentially is the scattering center, is in the order of ns. The process is therefore, inefficient for ps pulse or shorter. S.C Neto et al. has overcome this limitation by the use of optical design⁵⁶. They devised multipass scheme. In their set up, the short laser pulse (ps) is made to return to the same spot it previously passed, in a time late enough for the scattering centers to be formed. This results in better limiting performance of CBS with short laser pulses. Another drawback of CBS is that the material can be bleached after several pulse repetitions. This is because the limiting action arises from changes in physical state of the material. E.W.V Stryland et al used flow cell to overcome this problem. Nevertheless, CBS is still one of the most efficient optical limiters to date.

2.2.2.4 Carbon nanotubes

Carbon nanotubes are carbon allotropes with tubular shape. They are categorized as either single wall or multi wall depending on the number of carbon layers constituted the tube. Not only carbon nanotubes have unique mechanical and electrical properties, but also they possess strong nonlinear optical limiting.

In 1998, Sun *et al.* investigated optical limiting properties of multiwall carbon nanotubes (MWNT) suspended in water and dispersed poly(methyl methacrylate) (PMMA) matrix⁵⁷. Their MWNTs were prepared by an arch discharged method. They found that at 532nm with ns pulses,

optical limiting of MWNT suspended in water started at a fluence 10 times higher than that of C_{60} in toluene solution. However, their limiting properties outperformed the C_{60} solution when the fluence is in excess of 1 J/cm^2 , resulting in a smaller optical limiting threshold. The limiting performance of MWNT in PMMA was much poorer than C_{60} and MWNT in water. Sun et al. concluded that the mechanism behind the optical limiting of MWNT was nonlinear scattering since the mycoplasma formation was easier to form in liquid solution than in solid host.

At a higher wavelength of 700nm and 1064nm, optical limiting performances of MWNT both in water and host solid were better than the C_{60} solution, rendering the potential of carbon nanotubes as broadband optical limiters. The reason that C_{60} does not have optical limiting action at 1064nm is because it has no ground state absorption at that wavelength and thus excited state absorption cannot happen. Study done by Chen et al. found that optical limiting of MWNT in ethanol was also stronger than that of C_{60} in toluene and carbon black suspension (CBS) in water at both 532nm and 1064nm⁵⁸. Due to this broadband response, it was concluded that the superior optical limiting action in carbon nanotubes is resulted from nonlinear scattering. Their better performance than CBS might come from easier plasma formation and lower electron work function.

In the same year, L Vivien et al. measured optical limiting of single wall carbon nanotube (SWNT) suspended in water/surfactant solution⁵⁹. They compared its limiting performance with benchmark limiters such as C_{60} and carbon black suspension (CBS). At the wavelength of 532nm with ns pulses, SWNT, CBS and C_{60} showed similar limiting behaviors. Similar to the case of MWNT studied by Sun et. al., the onset of limiting action was lower in C_{60} than those of SWNT and CBS suspension for the 532nm wavelength. However, at the wavelength of 1064nm, C_{60}

showed no optical limiting whereas both CBS and SWNT showed optical limiting with that of SWNT being slightly better than that of CBS.

In 2000, Mishra et al. conducted a study to compare optical limiting of SWNT in three different suspension which were ethylene glycol, water and ethanol⁶⁰. They found that the SWNT in ethanol showed the best limiting performance. Since the observed optical limiting showed solvent dependency, they concluded that the main mechanism for optical limiting in SWNT suspension was micro bubble formation. Optical limiting of CNTs shows solvent dependent effect similar to that of CBS⁶¹.

Riggs and co-workers compared optical limiting performance of solubilized SWNT and MWNT and compared with their aqueous suspended counterparts⁶². The solubilized forms of the nanotubes were achieved by polymer functionalization. They found that the solubilized nanotubes have poorer optical limiting properties than nanotube in aqueous suspensions and C₆₀. They proposed that different nonlinear mechanism, i.e. nonlinear absorption, from the aqueous suspension was responsible for the observed decrease in optical limiting performance. They also found that shorter carbon nanotubes suspension had poorer optical limiting performance than longer ones and attributed this effect to bundling of the tubes. Jin et al. had observed nonlinear refraction of polymer/nanotube composite⁶³.

Vivien et al. studied the effects of pulse duration and wavelength on optical limiting properties of carbon nanotube suspensions, in 2001⁶⁴. They found that, at the same fluence, longer pulses resulted in better limiting performance and the results were explained in term of duration required to develop micro bubbles. From their study, it can be concluded that nonlinear scattering is the main mechanism for optical limiting in carbon nanotubes suspension where the

origin of scattering centers are from micro bubble formation at low fluence and carbon sublimation at high fluence.

Later, in 2002, similar to Riggs et al., Liu et al. studied optical limiting properties of solubilized MWNT solution and also proposed that optical absorption was behind the observed optical limiting with their sample instead of nonlinear scattering⁶⁵. O'Flaherty studied the nonlinear optical response of polymer-stabilized MWNT dispersion⁶⁶. They observed an evidence of electronic response of the excited state in their degenerate four wave mixing measurement.

At this point, it can be concluded that the optical limiting of carbon nanotubes depends on several factor such as the aspect ratio of the tube, the properties of the surrounding, laser wavelength and the pulse duration. Also, from various studies, it is possible that solubilized and suspended carbon nanotubes have different nonlinear mechanisms dominating their optical limiting performance. It is also possible that in the suspended forms both nonlinear scattering and nonlinear absorption exist but the former is more dominant while in the solution form the latter mechanism only exists resulting in poorer performance. Nevertheless, it is well accepted that the better performance of un-modified carbon nanotubes compared to C₆₀ is contributed by the presence of nonlinear scattering. More recent literatures are focused on modifying carbon nanotubes in order to enhance optical limiting performance of the materials. For example, Chin et al coated their carbon nanotubes with gold and silver film⁶⁷. They found that optical limiting performance was improved and attributed their observed enhancement to the surface plasmon of the metal film. Enhanced optical limiting of Boron doped MWNT when compared to the undoped was observed by Xu et al.⁶⁸. Izard et al blended carbon nanotubes with a multiphoton

absorber, Stillbebe-3, and observed slightly better optical limiting than pure carbon nanotubes⁶⁹. Webster et al. combined RSA carbocyanine dye with nitrogen-doped MWNT⁷⁰. Their mixture was able to limit laser light at 1 order of magnitude lower than unmodified carbon nanotubes. However, the limiting behavior disappeared at higher fluence due to saturable absorption. Optical limiting of covalently porphyrin-functionalized single wall carbon nanotubes was studied by Guo et al.⁷¹. They observed improved optical limiting efficiency with the materials and attributed their finding to electron donor-acceptor property of their nanohybrid system. The excited charges were separated by photo induced electron transfer from the porphyrin donor to the nanotube acceptor. Similarly, Liu et al. covalently attached single-walled carbon nanotubes with porphyrins and also observed enhanced optical limiting effects⁷².

2.3 Experimental methods

2.3.1 Sample Characterizations

2.3.1.1 X-ray diffractometer (XRD)

XRD measures the diffraction of X-rays from planes of atom within a material. Since the diffraction effect occurs when the electromagnetic wave impinges on periodic structure with geometrical variation within the same scale of the wave, X-rays ($\lambda \approx 0.01-10\text{nm}$) can give information on the interatomic distances in crystals ($\approx 0.1-0.4\text{nm}$). To observe the diffraction pattern, Bragg's law must be satisfied.

$$\lambda = 2d \sin \theta \quad (2.17)$$

Most XRD machines in universities use a monochromatic x-ray source of fixed wavelength λ . The Bragg condition is met for different plane spacing d by varying the angle of X-ray incident θ . The X-ray radiation is generated by bombarding an electron beam at a metal target. Narrow X-

ray emission lines are produced as a result. Commonly used metals are Cu K α and Mo K α emission lines with emission wavelength of 0.15 and 0.07 nm respectively. Alternatively, synchrotron can also be used to generate an X-ray continuum. X-ray diffraction data can be operated with two geometries, namely Debye-Scherrer (or transmission) geometry and Bragg-Brentano (or reflection) geometry, as illustrated in Figure 2.2.

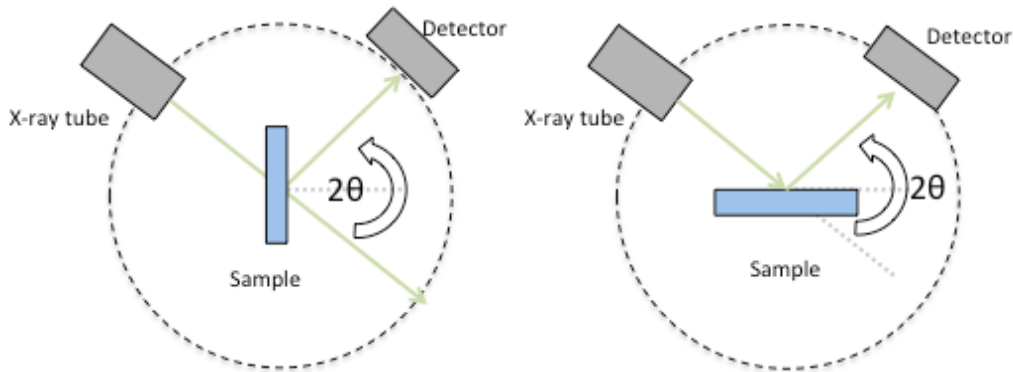


Figure 2.2 Schematic illustration of XRD setup with (a) Debye-Scherrer and (b) Bragg-Brentano configurations.

While the former configuration requires low absorbing samples and works with capillary sample, the latter can measure highly absorbing samples with relatively flat surface. The intensity of the x-ray diffraction is usually plotted against the diffraction angle 2θ . Whereas the angle that the diffraction occurs can tell the information on the atomic spacing of the sample, the width of the peak, on the other hand, can give information on the properties of the material itself. For example, sample with small crystal domains will have a border peak than the one with larger domains. Scherrer equation relates the ordered domain size with the peak width, Equation(2.18).

$$\beta_{size}(2\theta) = \frac{K\lambda}{\tau \cos\theta} \quad (2.18)$$

where β_{size} is the full width at half maximum of the peak at 2θ , K is the shape factor, and τ is the domain size.

In addition strain can also contribute to peak broadening. The peak broadening due to strain (β_{strain}) is usually assumed to be governed by the following equation.

$$\beta_{\text{strain}}(2\theta) = 4\varepsilon_0 \tan \theta \quad (2.19)$$

where ε_0 is the strain in the material. The total broadening is, therefore, the sum of instrument broadening and material broadenings (size and strain).

2.3.1.2 X-ray photoelectron spectroscopy (XPS)

XPS is surface-sensitive technique that measures intensities of photoelectrons versus its binding energy. The XPS technique is based on the photoelectric effect. Similar to the case of the XRD, X-rays are either produced with metal targets or synchrotron. When X-ray with energy $h\nu$ is incident upon the surface of the sample, its energy is absorbed by an electron. If the energy is higher than the summation of the binding energy of the electron E_b and the system work function Φ , the electron is emitted from the sample with a kinetic energy E_k , according to the well-known Einstein's formula:

$$E_k = h\nu - E_b - \phi \quad (2.20)$$

With the use of energy analyzer, emitted electrons with different kinetic energy can be counted. The system then plots the intensity of photoelectron versus the binding energy. The obtained data can be used to identify element as well as provide information on chemical state of materials, composition of the constituents, and valence band structure. XPS peaks in elemental samples, for

example metal surfaces occur at the same binding. However, in compounds where there are chemical bonds, the peak position can shift. This allows XPS to differentiate different chemical states of the sample.

2.3.1.3 Transmission electron microscope (TEM) and Scanning electron microscope (SEM)

Electron microscopy uses a beam of a high-energy electron beam created by an electron gun to generate variety of signal from a sample. The electron beam, from the electron gun, is created by applying high voltage to a filament. The higher the applied voltage, the faster the emitted electrons from the filament and therefore the shorter electron wavelength. For example, with an applied voltage of 10 KV, the wavelength of the electrons will be approximately 0.012nm, allowing virtualization of nanometer sized structure. However, the resolution of the microscope does not only depend on the wavelength of the source but also the optics. A typical TEM has a resolution as low as 0.1nm whereas the resolution of a typical SEM system is about 5nm. Imaging mechanisms in TEM and SEM are different. In TEM system, images are formed from scattered primary electron from the samples in transmission geometry. The scattered electron results in a shadow on a detecting screen, analogously to taking the X-ray images. As a result, thin sample with thickness smaller than electron penetration depth is required. On the other hand, SEM images are formed from secondary electrons. The electron beam is rapidly scanned back and forth across the specimen surface. The secondary electron is collected at the detector to produce an image. The resolution of the system is determined by the spot size of the primary electron on the surface of the sample. These two systems are powerful tools for imaging and investigating nano-meter sized samples.

2.3.2 Optical limiting measurement

Experimental set up for optical limiting characterization is simple. The main goal of the measurement is to observe optical extinction of the sample versus energy density or fluence (J/cm^2) of light excitation. One of the simple ways to do so is to irradiate a sample with a fixed laser beam size and then vary the laser energy through the use of polarizers and wave plates. However, with this technique, the energy range that can be achieved with common laboratory laser is limited and is hard to achieve high measurement resolution. Thus, another technique, where the laser energy is fixed with varied beam size, is commonly used. This can be done with either the use of telescope system or focusing lens. Perhaps, the most commonly adopted for this type of measurements is the open aperture Z-scan. This single beam measurement technique was first developed for measuring optical nonlinearities by Sheik-Bahae et al. in 1990⁷³. With this technique, the far field transmittance is measured at fixed laser energy with a varied beam diameter. The variation of the beam size and thus the fluence are achieved by using a focusing lens and moving a sample along the focusing light path. The light transmittance is recorded versus the sample position. If all transmitted light is collected, information on nonlinear extinction can be measured. Figure 2.3 illustrates the typical open-aperture Z-scan setup.

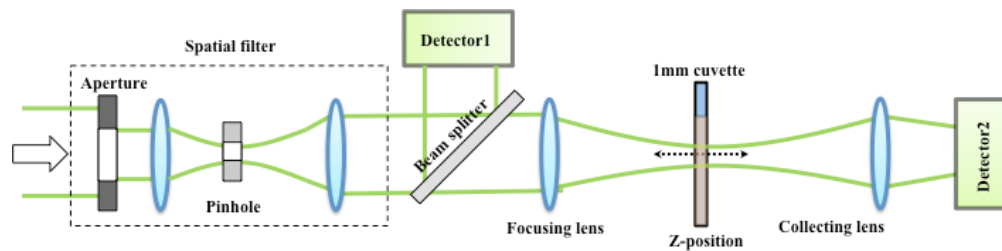


Figure 2.3 Schematic diagram of the Z-scan setup

In general, with this set up, the thin sample approximation where the sample thickness is much smaller than the Rayleigh range is used as well as a single mode Gaussian beam profile is assumed. Since the accuracy of the Z-scan experiment relies on the accurate determinations of the beam size as well as the beam profile, laser beam characterization of the employed laser system is essential.

The scanning knife-edge technique, developed by Yasuzi Suzuki and Atsushi Tachibana in 1975, is a simple way to measure the Gaussian beam diameter⁷⁴. In this technique, a razor blade is moved/scanned across the laser beam (perpendicular to the beam propagation direction). The transmittance of the laser is measured using a detector and plotted against the blade position (x). By fitting the obtained data to the following error function, the beam waist can be determined.

$$P_N(x) = \frac{1}{2} \left[1 + \operatorname{erf} \left(\frac{x-x_0}{w} \right) \right] \quad (2.21)$$

Where $P_N(x)$ is the normalized transmitted laser power, w is the beam radius measured at a position where the intensity decreases to $1/e$ times of its maximum value, and x_0 is the center position of the beam. An example of plots obtained from knife-edge scan is shown in Figure 2.4.

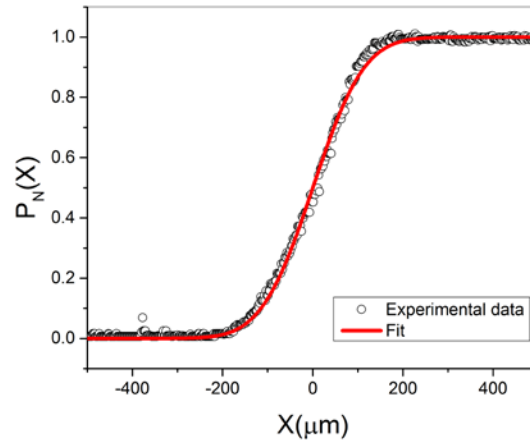


Figure 2.4 An example of plots obtained from the knife edge scan. Dots are the experimental data and solid line is the theoretical fit.

Alternatively, one can take a derivative of the function and fit the measurement data with a Gaussian profile. However, taking derivatives of data with uncertainties results in amplification of the uncertainties and, therefore, an increase in the errors⁷⁵.

To measure the beam profile quality, a M-square factor (M^2) is often used. M^2 is used to describe the deviation of the laser beam from a theoretical Gaussian. In the case of theoretical Gaussian beams, $M^2=1$. However, M^2 can be greater than 1 for actual laser systems. He-Ne laser can have $M^2\sim 1.1$ whereas M^2 of high energy laser system can be as high as 3 or 4. By performing the knife-edge scan to determine the beam waist $w(z)$ along a focusing beam path z , the M^2 can be determined from fitting the data with the following equation:

$$w(z) = w_0 \sqrt{1 + \frac{z^2 M^2}{z_0^2}} \quad (2.22)$$

where w_0 is the minimum waist and $z_0 = \pi w_0^2 / \lambda$ is the Rayleigh range.

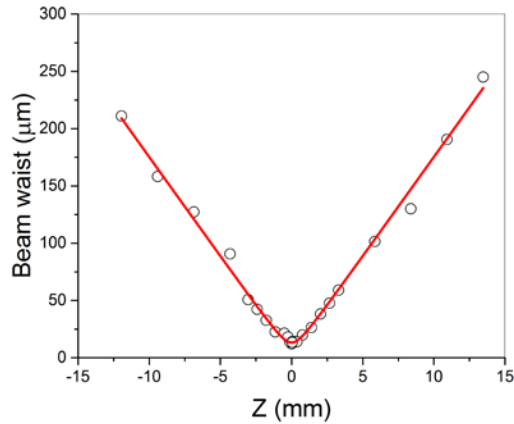


Figure 2.5 M^2 measurement data (dots). Solid line is the theoretical fit to Equation (2.2).

For our particular laser system, it was found that beam profile from the laser had M^2 much greater than one. As a result, spatial filter is inserted in the set up to clean up the beam, making the profile as close to the perfect Gaussian beam as possible. The spatial filter uses the principal of Fourier optics to alter the beam profile. In our set up, a collimated beam from the laser is expanded and passed through a circular aperture. The beam is then focused with a focusing lens. At the focal plane, an Airy beam profile is produced. A pinhole is used to allow only the central bright portion of the profile to pass. Another lens is used to reform the collimated beam. After putting the spatial filter in our set up, the beam quality was improved to $M^2 \sim 1$, Figure (2.5).

2.4 Results and discussions

2.4.1 The effect of interstitial doping on optical limiting of Zn-ferrite

Iron oxides or ferrites are non-conductive ceramic compounds derived from iron. They are magnetic in nature, and are extensively used for magnetic recording, and in the construction of inductors, permanent magnets, electrical transformers, and millimeter integrated circuits. Due

to their unique nonreciprocal and frequency-selective properties, ferrite devices have played a key role in active aperture radar, microwave, and multifunction systems on defense platforms. Recently they have been investigated for magnetic resonance imaging (MRI)⁷⁶, thermal activation therapy⁷⁷, drug delivery⁷⁸, and biosensing⁷⁹ applications

Crystal structures of ferrites can be described as a close-packed assembly of oxygen atoms with metal atoms occupying the interstitial sites⁸⁰, as shown in Figure 2.6 . Spinel ferrites are a class of ferrites of empirical formula $A^{2+}B_2^{3+}O_4^{2-}$. One unit cell of a spinel ferrite contains eight molecules with twenty-four metal positions. Of these, eight are tetrahedral sites, and the remaining sixteen are octahedral sites. In the case of Zn-ferrite tetrahedral sites are occupied by Zn^{2+} ions, and octahedral sites by Fe^{3+} ions⁶. This type of structure where divalent and trivalent cations occupy tetrahedral and octahedral sites respectively is called normal spinel.

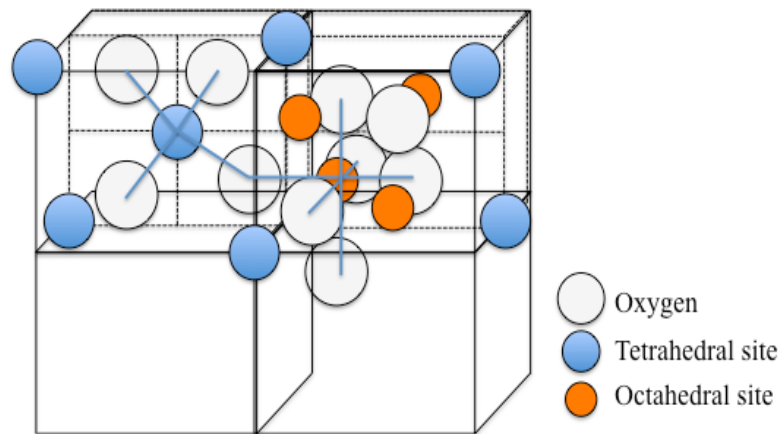


Figure 2.6 Schematic representation of a ferrite crystal structure.

The mixed forms of zinc ferrite also have spinel structure. However, the additional 3d-metal atoms interstitially replace zinc atoms. This results in perturbation in crystal field and electronic band structure of the material, which in turn can affect the material optical properties.

Optical properties of composite materials are related to local field effects. For instance, the third order nonlinear susceptibility of nanocomposites is proportional to the fourth power of the local field correction factor. Optical nonlinearities in ferrites are relatively unexplored, and reports⁸¹⁻⁸² are rare compared to organics, semiconductors and metals. Modifications in optical nonlinearity caused by the inclusion of different transition metals into a spinel ferrite system would be of considerable interest owing to applications including optical limiting. Therefore, in this section the nonlinear optical properties of nanosized spinel Zn-ferrite (ZnFe_2O_4), in comparison to its Ni and Cu mixed forms, namely, NiZn-ferrite ($\text{NiZnFe}_2\text{O}_4$) and CuZn-ferrite ($\text{CuZnFe}_2\text{O}_4$), is studied using the open-aperture z-scan technique. These results are compared to those measured in C_{60} /toluene under identical conditions. C_{60} in toluene was chosen for comparison because it is a benchmark material for optical limiting, and is extensively studied in the literatures⁸³⁻⁸⁵.

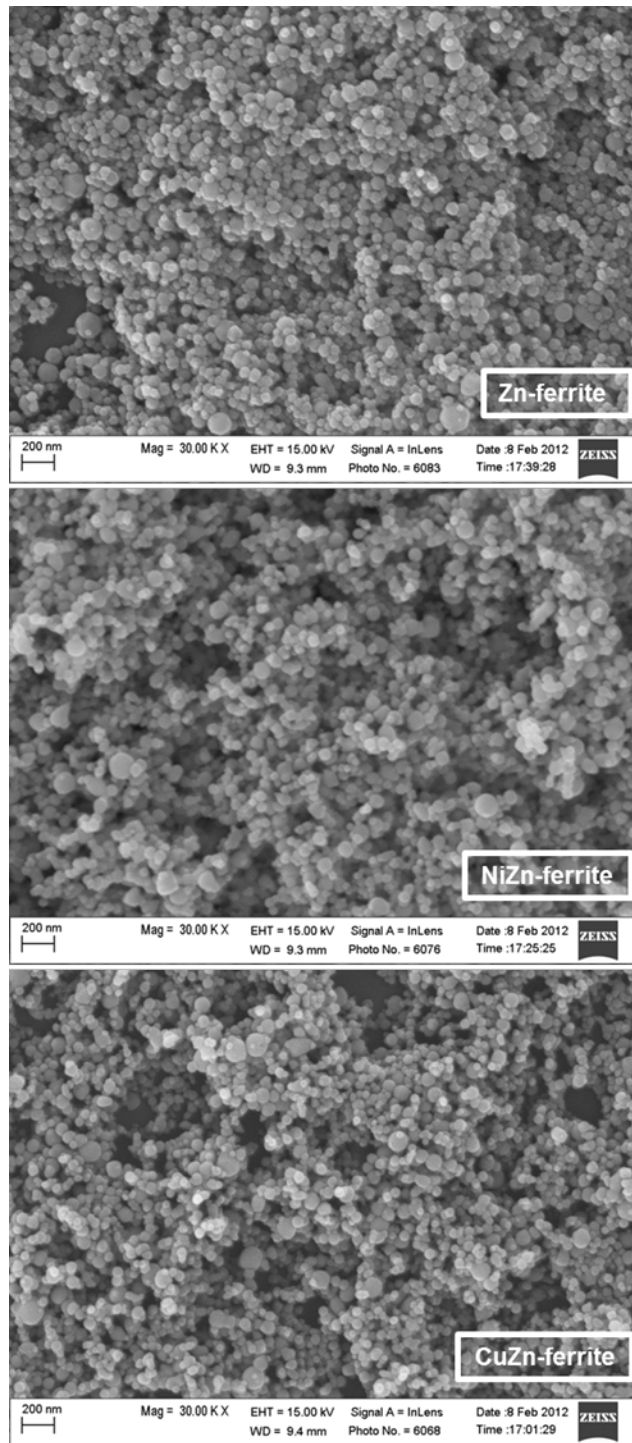


Figure 2.7 SEM images of ZnFe_2O_4 , $\text{NiZnFe}_2\text{O}_4$ and $\text{CuZnFe}_2\text{O}_4$.

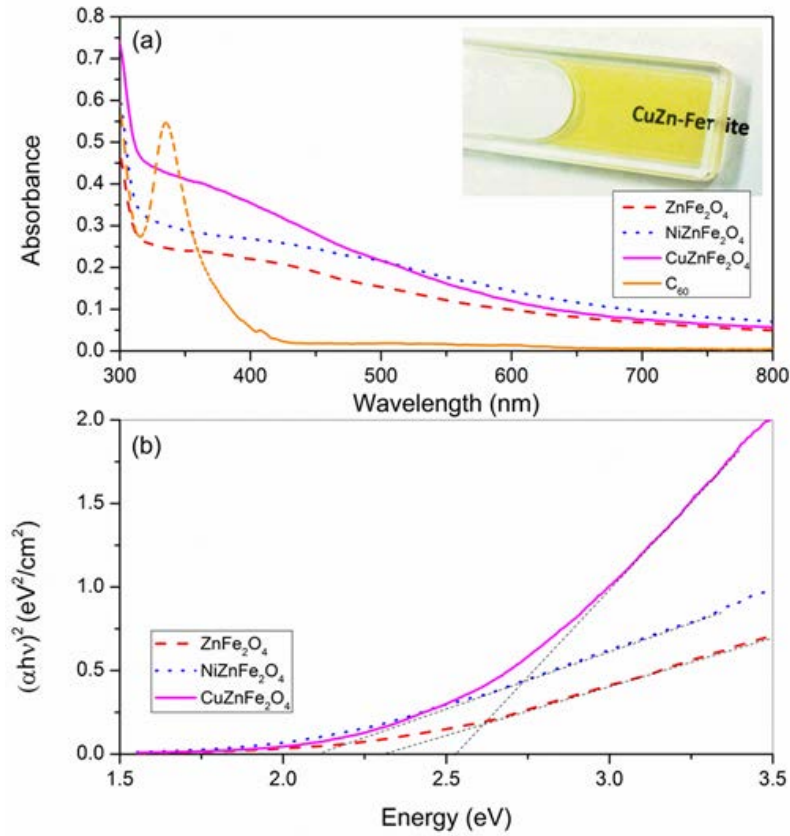


Figure 2.8 (a) Absorption spectra of the samples. Inset shows CuZnFe₂O₄ sample of 52% linear transmission. (b) Tauc plots for calculating the bandgap energies.

According to the SEM Images taken on a *Zeiss ULTRA-55 FEG SEM*, Figure 2.7, the nanoparticles are less than 100 nm in size. Linear absorption spectra of the samples were measured using a UV-VIS (Cary 300 Bio) spectrophotometer (Figure 2.8(a)). For these measurements, concentrations of approximately 1.4×10^{-4} and 1×10^{-5} mol.l⁻¹ were used for the oxide samples and C₆₀ respectively. According to the absorption spectra, ferrite samples do not show definite absorption peaks. However, assuming direct band gap, the band gap energies can be determined from the absorption coefficients (α) near the band edge by using the Tauc relation⁸⁶⁻⁸⁷

$$\alpha h\nu = A(h\nu - E_g)^{\frac{1}{2}} \quad (2.23)$$

where A is a constant that depends on the band structure and the refractive index of the material, h is the Planck's constant, ν is the frequency, and E_g is the energy gap. By plotting $(\alpha h\nu)^2$ versus $h\nu$, the band gap energy was determined by extrapolation, as shown in Figure 2.8(b). The values obtained are 2.3, 2.1, and 2.5 eV, for ZnFe_2O_4 , $\text{NiZnFe}_2\text{O}_4$, and $\text{CuZnFe}_2\text{O}_4$, respectively.

Samples for optical limiting measurements were prepared by dispersing the nanoparticles in 0.005 g.ml^{-1} solutions of Poly(methyl methacrylate) (PMMA) in toluene. The addition of PMMA helps to stabilize the dispersion. Samples were so prepared that each has the same linear transmission of approximately 52% at the excitation wavelength of 532 nm, when taken in 1 mm path length cuvettes (inset of Figure 2.8(a)). An Nd:YAG laser (*Minilite I, Continuum*) emitting 5 ns laser pulses was used as the excitation source. The laser beam was passed through an iris aperture and pinhole to obtain a clean Gaussian beam. In the open aperture Z-scan, the laser beam is focused using a lens, and the transmission of the sample is measured as a function of the relative position of the sample (z) with respect to the beam focus ($z=0$). A plano-convex lens ($f=100 \text{ mm}$) was used for focusing the beam. The beam waist at the focal point, as measured by the knife-edge method¹⁹, is $12 \pm 2 \mu\text{m}$. In the set-up, the sample taken in a 1 mm glass cuvette was mounted on a linear translation stage of 15 cm span and 1 micron resolution (Newport, ILS150PP). The incident and transmitted pulse energies were measured using pyroelectric energy probes (LaserProbe, RjP-735). Z-scans were done at three different incident laser pulse energies, viz. 5, 8 and 12 μJ . The open-aperture z-scan curves measured in the samples at the incident energy of 12 μJ are shown in Figure 2.9.

In general, the depth of the valley in the z-scan curve is a direct indication of the optical limiting efficiency of a material. From the z-scans it is clear that C_{60} exhibits the maximum dynamic range for optical limiting, as it shows a limiting effect throughout the range of

measurement. In contrast, the ferrite samples show an increase in transmission in the low and moderate fluence regions, and a deep, efficient limiting at the higher fluences. The limiting efficiency of $\text{NiZnFe}_2\text{O}_4$ and $\text{CuZnFe}_2\text{O}_4$ are better than that of C_{60} at the highest fluences. Even though C_{60} offers protection to the detector for the entire range of input fluences, this may in fact become a disadvantage because the sensitivity of the protected detector is reduced even for those input fluences which are lower than its damage threshold. Thus, from an application point of view, the ferrite samples have a unique advantage: when properly designed they can retain or even increase the sensitivity of a detector while it is in its safe operating area, and switch to sudden limiting when the input fluence exceeds the detector damage threshold.

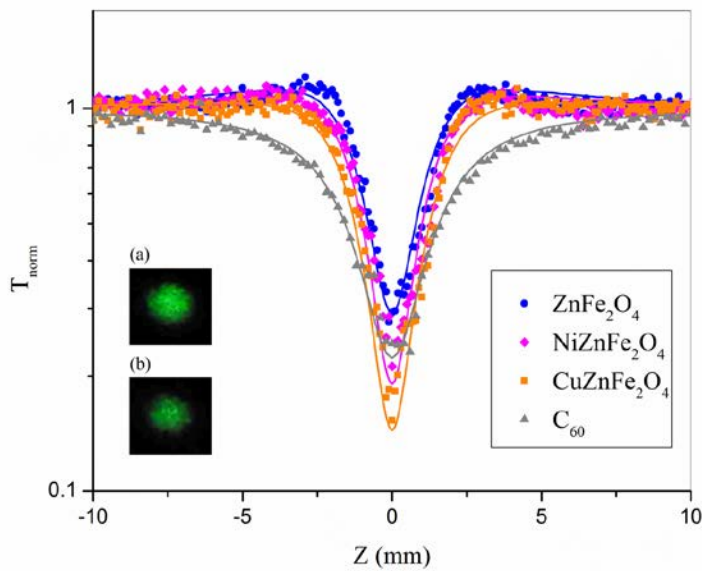


Figure 2.9 Open aperture z-scans of the samples. Unlike C_{60} which shows optical limiting throughout, ferrite samples exhibit absorption saturation at the lower fluences, with a relatively sharper onset of limiting in the higher fluence region. Solid lines are numerical fits to the measured data obtained using Equation 2. Inset shows photographs of (a) direct, and (b) transmitted, laser beams in the far field.

The normalized transmission of the samples $T(z)$ can be fit by numerically solving the following equation:

$$\frac{dI}{dz} = -\alpha I - \beta_{eff} I^2 \quad (2.24)$$

where β_{eff} is the effective nonlinear extinction coefficient. However, considering the occurrence of kinetic absorption saturation in the ferrite samples, the linear absorption α is rewritten as

$$\alpha = \frac{\alpha_0}{1 + \frac{I}{I_{sat}}} \quad (2.25)$$

where α_0 is the linear absorption coefficient and I_{sat} is the saturation intensity. Numerical fits obtained to the experimental data are shown in Figure 2.9. In the limited range of pulse energies used, there was no dependency of the nonlinear parameters on the energy.

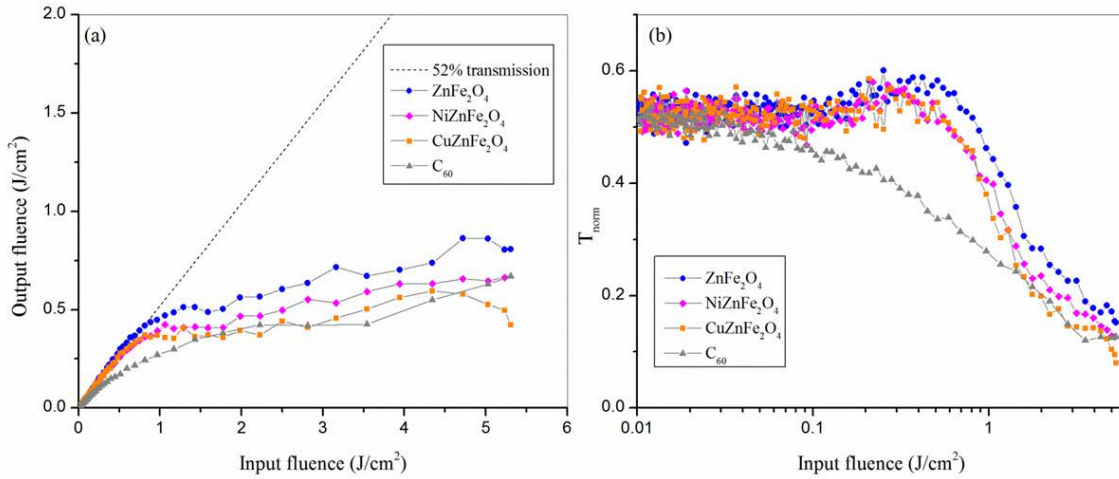


Figure 2.10 Optical limiting performance of the samples. (a) Output fluence, and (b) normalized transmission, plotted against input laser fluence. Lines connecting data points are guides to the eye.

For drawing the optical limiting curves, we note that at any given position z , the energy density (fluence) of a spatially Gaussian beam can be calculated from the laser pulse energy and

the beam radius, given in Equation (2.22). From the measured values of the energy transmitted by the samples for different values of z , the variation of the output fluence with input fluence can be determined. Figure 2.10(a) shows the output fluence, and Figure 2.10(b) shows the sample transmission, plotted against the input fluence. The optical limiting thresholds F_l (input fluence at which the transmission drops to 50% of the linear transmission) are 1.16, 1.49, 1.60 and 2.23 J.cm^{-2} for C_{60} , $\text{CuZnFe}_2\text{O}_4$, $\text{NiZnFe}_2\text{O}_4$, and ZnFe_2O_4 respectively. In comparison, the limiting thresholds of suspensions of C_{60} , carbon nanotubes and carbon black, prepared with approximately 50% linear transmission at 532 nm, for 7 ns laser pulses, are reported to be 1.0 J.cm^{-2} , 1.7 J.cm^{-2} , and 1.7 J.cm^{-2} respectively⁵⁸.

The observed enhancement in optical limiting efficiency when Cu or Ni is incorporated into Zn-ferrite can be explained using a mechanism involving self-trapping of charge transfer states. Optical response of 3d metal oxides is dominated by the charge transfer (CT) transition between 2p orbital of oxygen and 3d orbital of metal²¹. The relaxation of the optically excited CT state is governed by a cumulative effect of both electronic and ionic terms associated with the displacement of electronic shells and ionic core respectively⁸⁸. In a CT unstable system, self-trapping of the CT excited state can occur. This self-trapping mechanism is strongly governed by the lattice strain⁸⁹. In the case of nickel and copper zinc ferrite, introduction of Ni^{2+} and Cu^{2+} ion into the Zn-ferrite structure can create a distortion in the crystal field and induce strain within the structure. It may be noted that these added ions occupy either the tetrahedral site or octahedral site of the structure depending upon whether the fabrication method favors normal spinel or inverse spinel. The induced strain enhances self-trapping of the CT states, which results in an increase in excited state lifetime, and therefore the excited state absorption coefficient. Considering also the fact that thermal scattering is not significant in the samples, it can be

concluded that optical limiting observed in these ferrites is related to a reverse saturable absorption (RSA) mechanism involving excited electronic states.

2.4.2 Size-dependent optical limiting of gold nanoparticles

Metal nanoparticles have attracted considerable interest since historical time as color substances in stain glasses and art works. However, the physics behind their fascinating bright colors was only understood after the experimental observation of the surface plasmon. Today, there are numerous research activities dealing with metal nanoparticles due to their unique properties. It has been found that metal nanoparticles exhibit two interesting size regimes, namely nanoclusters and nanocrystals. While the former has their size ranging from sub-nanometer to about 2 nm, the size of the latter is from approximately 2 to 100 nm. The number density is, however, ~ 59 atoms/nm³ in both regimes for gold, owing to the similar atomic packing densities. Au clusters of the order of the de Broglie wavelength of conduction electrons (~ 0.5 nm) exhibit discrete energy levels and molecule-like HOMO-LUMO transitions, while larger Au nanoparticles (>5 nm) exhibit quasi-continuous electronic bands. In general, gold clusters of less than 3 nm size lose their bulk-like electronic properties, and are believed not to support collective plasmon excitation.⁹⁰⁻⁹¹

The evolution of the optical spectrum of gold clusters in the quantum size regime (up to ~ 300 atoms and ~ 2 nm cluster diameter) is a strong function of size, and therefore, nonlinear optical properties in this size regime are worthy of investigation. Ultra-small clusters exhibit a spectacular optical behavior that is fundamentally different from that of larger plasmonic nanocrystals. Transition from the cluster to the nano-crystalline state is significant, as it raises fundamental questions regarding the evolution of discrete electronic states towards a rather

complex band structure. Several studies have been done on the effect of varying size and shape of metal nanoparticles⁹²⁻⁹⁵. For example, it has been found that two-photon absorption at 800nm cross-section increases as the size of ultra-small gold clusters increases from 1.1 nm to 4.0 nm⁹⁶. Further studies done by the same group also show abrupt change in the optical properties (fluorescence, transient absorption, two-photon absorption) around 2.2 nm, which is close to the calculated critical size for quantization⁹⁷. As a result, it will be interesting to investigate the optical limiting of metal nanoparticles as they evolve from nanoclusters to nanocrystals. In this section, optical limiting properties of recently developed atomically precise molecular gold clusters are measured and the results are compared with that of larger Au nanocrystals of 4 nm size.

All nanoclusters used in this study were synthesized by Professor Rongchao Jin's group according to a size-focusing methodology⁹⁸. The samples under study are Au₂₅(SR)₁₈, Au₃₈(SR)₂₄, and Au₁₄₄(SR)₆₀, where R=CH₂CH₂Ph. The numbers 25, 38 and 144 represent the precise number of Au atoms in the cluster.

Electrospray mass spectrometry data of the samples (Figure 2.11) reveals that the clusters are monodispersed with high precision in the number of atoms in each cluster⁹⁹. The absorption spectra of Au₂₅ and Au₃₈ exhibit clear molecular features, while these are less distinct in Au₁₄₄. The smallest sample Au₂₅(SR)₁₈ has the metal core of approximately 0.9 nm in diameter. Absorption spectrum and a TEM image of the Au nanocrystals (purchased from Fluka) are shown in Figure 2.12. The sample exhibit SPR absorption peak at around 530nm. From its TEM image, the mean size is about 4nm.

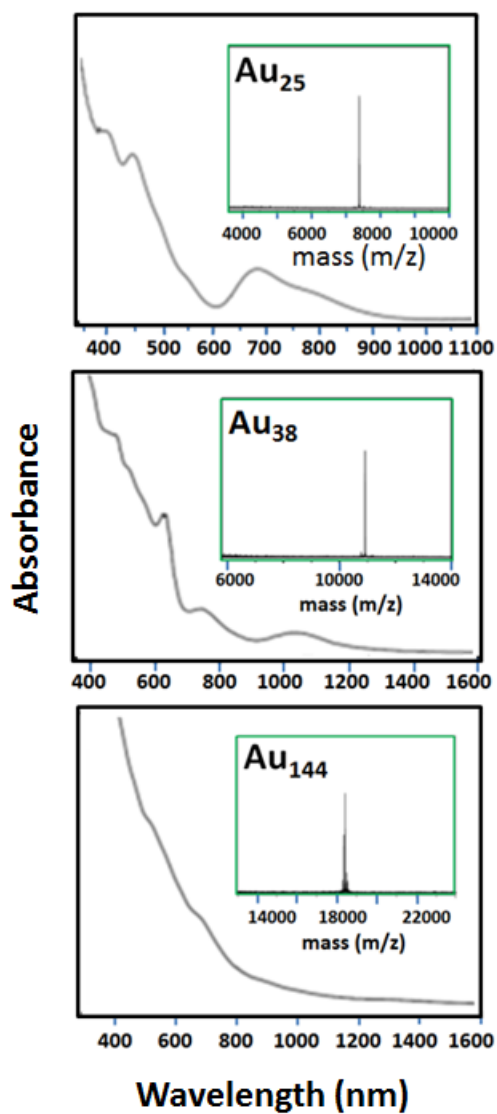


Figure 2.11 UV-Vis absorption spectra and Electrospray mass spectrometry (ESI-MS) data (insets) of $\text{Au}_{25}(\text{SR})_{18}$ (counterion: tetraoctylammonium, TOA^+), charge-neutral $\text{Au}_{38}(\text{SR})_{24}$, and charge-neutral $\text{Au}_{144}(\text{SR})_{60}$, respectively. In all cases, $\text{R}=\text{CH}_2\text{CH}_2\text{Ph}$.

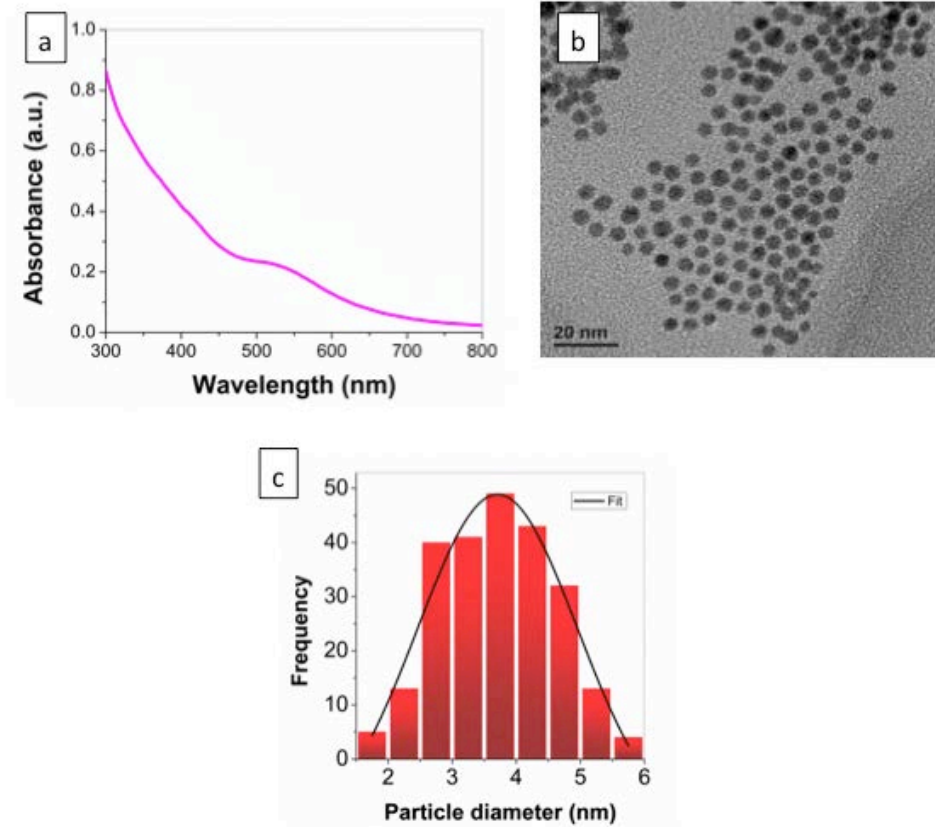


Figure 2.12 a) Optical absorption spectrum of Au nanocrystals. Inset shows the TEM image and polydispersity histogram, b) Representative schematic of the Z-scan set-up used for nonlinear optical measurements.

Nonlinear transmission measurements were carried out using the open aperture Z-scan technique. Samples for measurements were prepared by dispersing the nanoclusters and nanocrystals in toluene. A Nd:YAG laser (*Minilite I, Continuum*) emitting 5 ns laser pulses at the second harmonic wavelength (532 nm) was used for excitation. Each sample was so prepared that it had a linear transmission of 25% in a 1 mm cuvette at this wavelength. The beam was focused using a plano-convex lens ($f=100$ mm), and the beam radius at the focus (w_0) was measured to be 13 microns by using the knife-edge method. The laser pulse energy was 15 microjoules. The z-scan data are shown in Figures 2.13. The sample transmission against input laser fluence calculated from the z-scan data are presented in Figure 2.14.

According to the z-scan curves, Au₂₅ and Au₃₈ exhibit valley-shaped curves, whereas Au nanocrystals show a central valley with two symmetric peaks on the sides, with is a signature of the absorption saturation. The nanocrystals, on the other hand, show significant absorption saturation occurring in addition to nonlinear absorption.

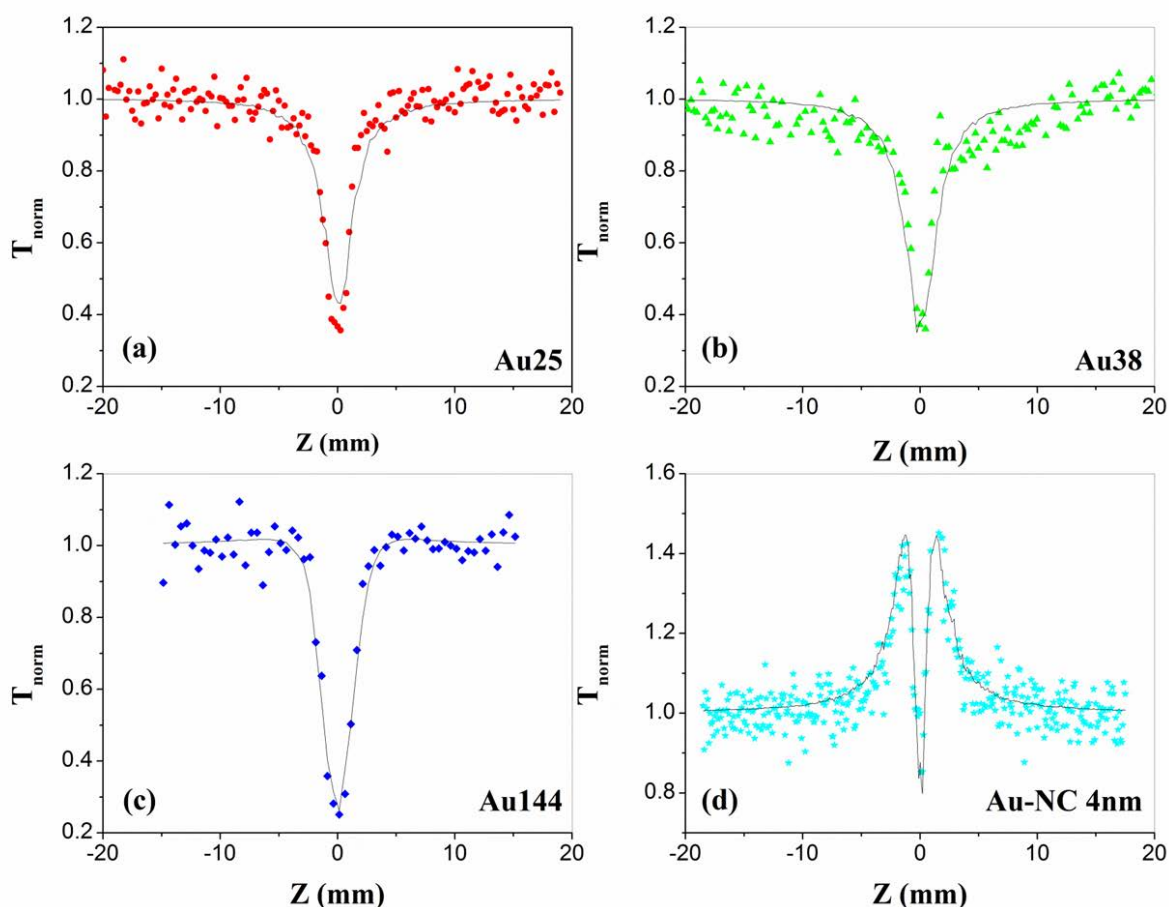


Figure 2.13 Open-aperture z-scans measured in the Au clusters and nanocrystals. (a) Au₂₅, (b) Au₃₈, (c) Au₁₄₄, and (d) Au nanocrystals (~4 nm). Samples are excited using 5 ns laser pulses at 532 nm. Linear transmission of all samples is 25% at this wavelength. As seen from the figures, optical transmission is a function of sample position with respect to the laser beam focus ($z=0$). T_{norm} is the measured transmission normalized by the linear transmission of the sample. Solid curves are numerical fits to the experimental data, obtained using Equation 4. The valley shaped curves of Au₂₅ and Au₃₈ indicate pure optical limiting behavior, while the humps flanking the valley in Au₁₄₄ signify the onset of saturable absorption. Absorption saturation is significant in the Au nanocrystals, as indicated by the strong peaks.

From Figures 2.13 and 2.14, it is obvious that in Au₂₅ and Au₃₈ an optical limiting behavior is seen throughout the incident fluence range, while in Au₁₄₄ the limiting is preceded by weak absorption saturation in the lower fluence region. On the other hand in the Au nanocrystals the limiting is preceded by prominent absorption saturation. A nonlinear absorption coefficient $\alpha(I)$ can be modelled by Equation (2.25). The transmitted intensity for a given input intensity can be calculated by numerically solving the corresponding nonlinear propagation equation of Equation (2.24).

Table 2.2 tabulates the I_s and β_{eff} For the samples. The β_{eff} increases with size in the cluster regime. While I_s is too high to be effective in Au₂₅ and Au₃₈, it has a value of 1.5×10^{12} W/m² in Au₁₄₄. In the nanocrystal regime, the I_s value is about the same but the β_{eff} value drops by a factor of 5, which results in the prominent absorption saturation exhibited by the Au nanocrystals. The optical limiting thresholds F_t (input fluence at which the transmission drops to 50% of the linear transmission) are found to be 4.0 J/cm² for Au₂₅, and 3.0 J/cm² for both Au₃₈ and Au₁₄₄. It is good to note here that optical nonlinearity in metal nanoparticles is ultrafast in nature, occurring in the range of picoseconds/femtoseconds¹⁰⁰.

Results given in Table 2.2 are in agreement with the previous study on two-photon fluorescence¹⁰¹. It was found that two-photon cross section increases with size in the cluster regime.

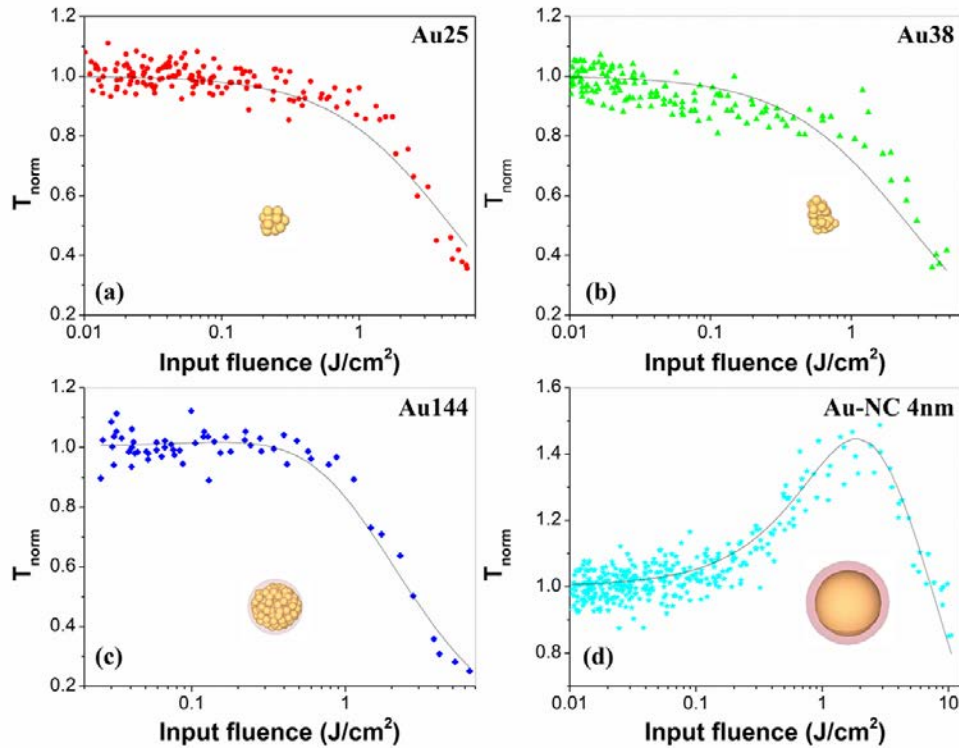


Figure 2.14 Nonlinear transmission in the Au clusters and nanocrystals, calculated from the z-scan data using Equations 1 and 2. (a) Au₂₅, (b) Au₃₈, (c) Au₁₄₄, and (d) Au nanocrystals (~4 nm). Saturable absorption sets in as the cluster size increases, and becomes prominent in the nanocrystals.

Table 2.2 Effective nonlinear absorption coefficient (β_{eff}) and saturation intensity (I_s) calculated for the samples.

Sample	Linear Transmission	I_s (W/m ²)	β_{eff} (m/W)
Au ₂₅	25%	NA	2.0×10^{-10}
Au ₃₈	25%	NA	3.5×10^{-10}
Au ₁₄₄	25%	1.5×10^{12}	7.5×10^{-10}
Au NCs (5 nm)	25%	2.2×10^{12}	1.5×10^{-10}

The Au₂₅(SR)₁₈ and Au₃₈(SR)₂₄ (R=CH₂CH₂Ph) nanoclusters exhibit unique optical properties, as manifested in their highly structured multiple-band optical absorption spectra. Unlike metallic Au nanocrystals with quasi-continuous band structure, Au₂₅(SR)₁₈ and Au₃₈(SR)₂₄ exhibit

discrete electronic energy levels and possess HOMO-LUMO. A precise correlation of the Au₂₅ structure with its calculated optical absorption properties has been obtained, with density functional theory calculation. The theoretically calculated spectrum is in well agreement with measurement¹⁰². Even though spectral structure is usually attributed to quantum confinement effects, it may be noted here that, from time-dependent DFT calculations, Aikens et al. has suggested ligand-field splitting as a cause for the multiple peaks¹⁰³. According to their study the absorption spectra are the result of complex interactions between the core and ligand and cannot be separable into two independent contributions. The Kohn-Sham orbital energy level diagram for Au₂₅ is shown in Figure 2.15. The first excited transition occurring at 1.52 eV is the LUMO ← HOMO transition, which is essentially an intraband (sp←sp) transition. The peak at 2.63 eV is caused by mixed intraband (sp←sp) and interband (sp←d) transitions, and that at 2.91 eV arises mainly from an interband transition (sp←d).

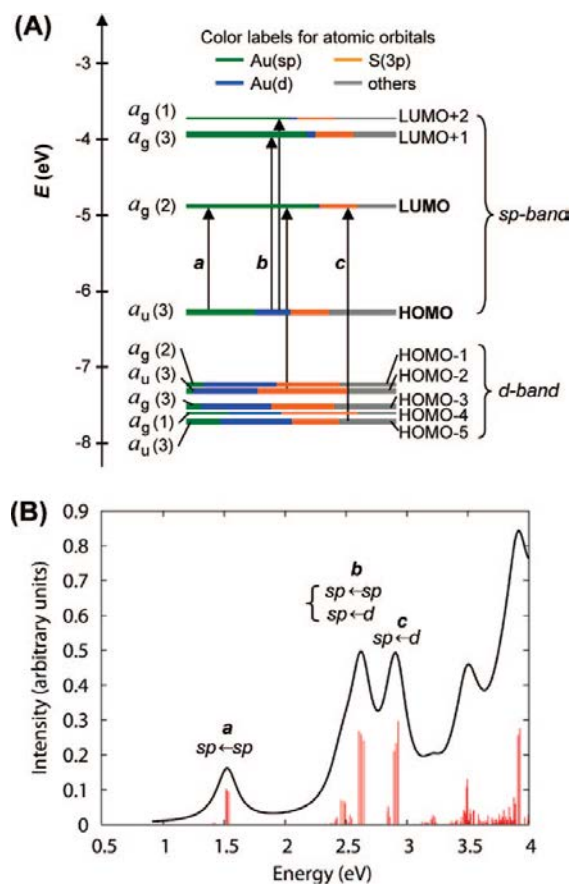


Figure 2.15 (A) The Kohn-Sham orbital energy level diagram calculated for the model compound $\text{Au}_{25}(\text{SH})_{18}^-$, (B) The theoretical absorption spectrum of $\text{Au}_{25}(\text{SH})_{18}^-$ ¹⁰²

The present results can be explained on the basis of excitation of the SPR. In one extreme or the case of nanocrystals, strong laser excitation can result in absorption saturation (or bleaching) at the SPR wavelengths¹⁰⁴. As a result, there are two competing processes in this system, namely the two-step photon absorption and plasmon excitation, which results in the observed nonlinear transmission behaviors. In another extreme or the case of small nanoclusters, the same SPR can no longer be supported by the system and therefore only nonlinear absorption exists. The sample with their size between the two extremes can show the evolution of the behavior from pure nanocluster to nanocrystal responses. In addition, Au nanocrystals show the

lowest β_{eff} value (Table 1), which indicates that the two-step absorption is weaker in the nanocrystals compared to the nanoclusters.

This study shows that ultra-small Au clusters are good optical limiters, with a limiting threshold close to that of the benchmark limiter C₆₀. This is due to the fact that unlike Au nanocrystals, the molecular Au clusters (e.g. Au₂₅ and Au₃₈) do not possess a SPR band, and therefore do not suffer absorption saturation when excited at the SPR wavelength region. Also, the nonlinear absorption coefficients are higher in the case of nanocluster. The absence of absorption saturation in the Au clusters makes them more applicable for optical power limiting applications, in comparison to the larger Au nanocrystals.

2.4.3 Optical limiting of fluorinated graphene oxide

Graphene oxide was first discovered in 1859 by Benjamin Brodie through the exfoliation of graphite oxide.¹⁰⁵ GO is an electrically hybrid material between the conducting π -states of sp² carbon sites, which contribute to the bandgap formation of the material, and the σ -states of sp³ carbon sites. The GO bandgap can be tuned by adjusting the ratio of sp² carbon atoms to sp³ carbon atoms via chemical reduction process. Chemical reduction can transform GO from an insulator to semiconductor and also to a metal-like state, in the form of graphene. While graphene possesses excellent electrical properties, mechanical flexibility, optical transparency, thermal conductivity and low thermal expansion coefficient¹⁰⁶⁻¹¹⁰, its precursor GO has interesting properties of its own. For instance, unlike graphene, GO possesses several oxygen containing hydroxyl, epoxide, diol, ketone and carboxyl functional moieties. These functional groups allow GO to interact with a wide array of materials, both organic and inorganic, which results in the high processability of GO. Due to their versatility, functionalized-GOs have

become promising candidates for various applications such as instance drug delivery¹¹¹⁻¹¹², magnetic resonance imaging (MRI)¹¹³, memory devices¹¹⁴, supercapacitor¹¹⁵⁻¹¹⁶, and optoelectronic devices¹¹⁷⁻¹¹⁸. Similarly, the optical limiting property of GO is found to be greatly enhanced with organic as well as inorganic decorations¹¹⁹⁻¹²¹.

Fluorination of carbon nanomaterials has many advantages due to the unique nature of the carbon-fluorine (C-F) bond. For instance, the C-F bond demonstrates excellent oxidative and thermal stability¹²². Due to high electronegativity of Fluorine atoms, C-F bonds have high polarity and low surface free energy. Partially fluorinated GO (F-GO) can even be paramagnetic due to the presence of localized F-bonds. F-GO will be an attractive material in many applications such as super amphiphobic surfaces, multimodality imaging and photonic devices¹²³. In this section we investigate effect of fluorination on the optical limiting performance of graphene oxide with 5 nanosecond (ns) laser pulses at the wavelength of 532 nm.

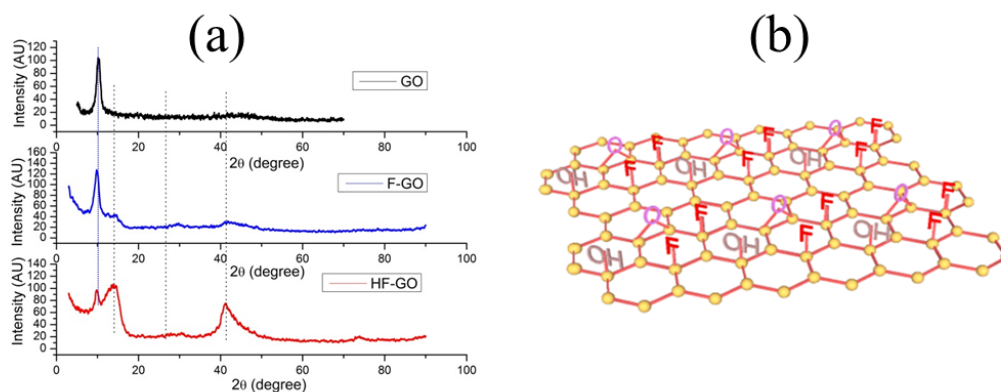


Figure 2.16 (a) XRD pattern of GO, F-GO and HF-GO and (b) schematic representation of F-GO.

All Graphene oxide (GO) based samples were synthesized using an improved synthesis route according to the literature¹²⁴. In the case of pure GO, graphite powder (Bay carbon, Inc. SP-1 grade 325 mesh) is used as a raw material, while for the synthesis of fluorinated graphene oxide, fluorinated graphite polymer (Alpha Aesar) is used as a starting raw material. Figure 2.16(a) shows the XRD of GO, F-GO and highly fluorinated graphene oxide (HF-GO). XRD pattern indicates an increased lattice spacing for GO ($\sim 6 \text{ \AA}$) compared to pristine graphite powder ($\sim 3.3 \text{ \AA}$). This observation suggests the exfoliation of graphite. F-GO is hydrophilic similar to GO, whereas highly fluorinated GO (HF-GO) is relatively hydrophobic¹²³. A schematic representation of F-GO is given in Figure 2.16(b). The increase in hydrophobicity of HF-GO can be attributed to the low surface energy of C-F bonds. Both F-GO and HF-GO have well-defined absorption peaks (Figure 2.17). The absorption spectrum of FGO is almost identical to GO, showing a peak at 225 nm which corresponds to the $\pi \rightarrow \pi^*$ transition. The weak shoulder at $\sim 300 \text{ nm}$ is due to the $n \rightarrow \pi^*$ transition of the carbonyl bonds¹²⁵. HF-GO shows no such shoulder at 300 nm, while showing a slightly less intense peak at 220 nm.

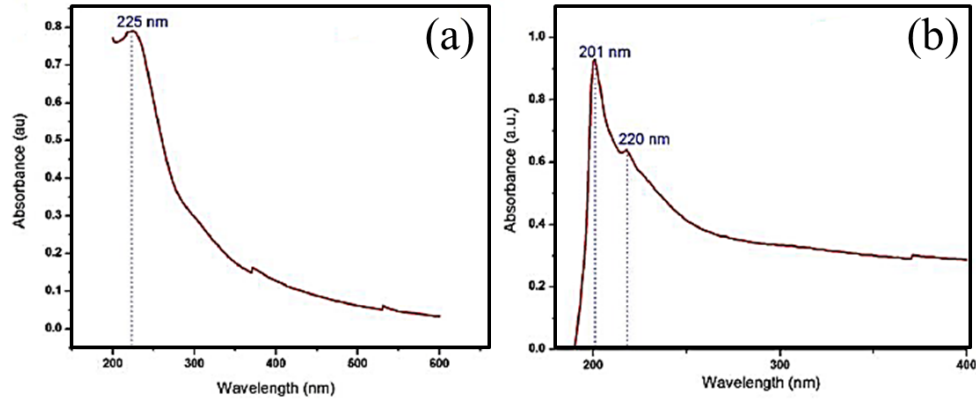


Figure 2.17 (a) UV-Vis absorption spectrum of F-GO and (b) HF-GO. The high absorbance in the short wavelength region indicates the possibility of RSA upon optical irradiation at 532 nm.

Optical limiting of GO/water, F-GO/water, and HF-GO/NMP dispersions were measured using the open aperture Z-scan technique. All samples were prepared to have a linear transmission of 50% at the excitation wavelength of 532nm. A Q-switched, frequency-doubled Nd:YAG laser (Minilite I, Continuum) was used to generate 5ns (FWHM) pulses at this wavelength. The laser output was spatially filtered to obtain a neat Gaussian beam profile, and then focused using a 200mm focal length plano-convex lens. The beam radius at the focus (w_0) was measured to be 30 ± 2 microns. The sample was taken in a 1mm path length cuvette and translated along the axis of the laser beam (z -axis) by a linear translation stage (Newport, ILS150PP). By fixing the input laser pulse energy (E_{in}) at a suitable value and translating the sample along the laser beam near the focal region, the incident laser fluence on the sample ($F_{in}(z)$) was varied. Maximum fluence is attained at the beam focus ($z=0$). The transmitted energy for different sample positions (z) was measured using a pyroelectric energy probe (LaserProbe, RjP-735). By mounting a photodiode near the sample at an angle to the beam axis,

linear and/or nonlinear light scattering was also measured. The normalized transmission ($T_{\text{norm.}}$) was then calculated by dividing the measured transmission with the linear transmission of the sample. The obtained z-scans curves for an input energy of $30 \mu\text{J}$ are shown Figure 2.18(a). All samples show an optical limiting (OL) property since the transmission decreases with increase in input fluence. The plot of sample transmission versus input fluence is shown in Figure 2.18(b), and that of output fluence versus input fluence is shown in Figure 2.18(c).

Results reveal that the optical limiting efficiencies of all fluorinated graphene samples are significantly higher than that of GO in water. The optical limiting threshold (input fluence at which transmission decreases to 50% of the linear transmission due to the nonlinearity) of F-GO/water and H-FGO/NMP are at 0.8 and 1.5 J/cm^2 respectively. The optical limiting thresholds of fluorinated GO samples are better than that of benchmark materials like C_{60} in toluene and carbon black in water⁵⁸. When comparing with the threshold values of other well-known optical limiters such as single-wall carbon nanotubes in ethanol [$\sim 1 \text{ J/cm}^2$ with 42% linear transmission]⁶⁰ and multiwall carbon nanotubes in water [$\sim 0.9 \text{ J/cm}^2$ with 50% linear transmission]⁵⁷, our F-GO/water dispersion has lower limiting threshold. The limiting threshold of GO could not be measured due to its relatively lower limiting efficiency. According to Xio-Liang et.al¹²⁶, the limiting threshold of GO/water (49% linear transmission) is at 10.2 J/cm^2 , for ns pulses at 532nm, which is an order of magnitude higher than the thresholds of fluorinated GO samples. The optical limiting properties of F-GO in N-methyl-2-pyrrolidinone (NMP) were also studied to find out the solvent contribution to the optical limiting performances when comparing F-GO/water to HF-GO/NMP dispersions. It was found that, at 50% linear transmission, F-GO in NMP also had better optical limiting efficiency than HF-GO in NMP.

The optical limiting efficiency of F-GO in NMP is lower than that in water. Such lower optical limiting efficiency can be attributed to inferior dispersibility of F-GO in NMP. Since F-GO is polar, it forms a better dispersion in water than in NMP. On the other hand, HF-GO, which is hydrophobic, only forms good dispersion in NMP. Nevertheless, FGO in NMP still has better optical limiting performance than HF-GO in the same solvent. The scattering signals are also given in Figure 2.18(d). The boiling points of water and NMP are 373K and 476K, and their enthalpies of vaporization at room temperature are 40.62 kJ/mol and 44.7 kJ/mol respectively¹²⁷. The scattering signal amplitudes are equally high in both FGO/water and FGO/NMP dispersions, indicating that solvent contribution to nonlinear scattering by thermally induced microbubbles is nearly the same in both samples.

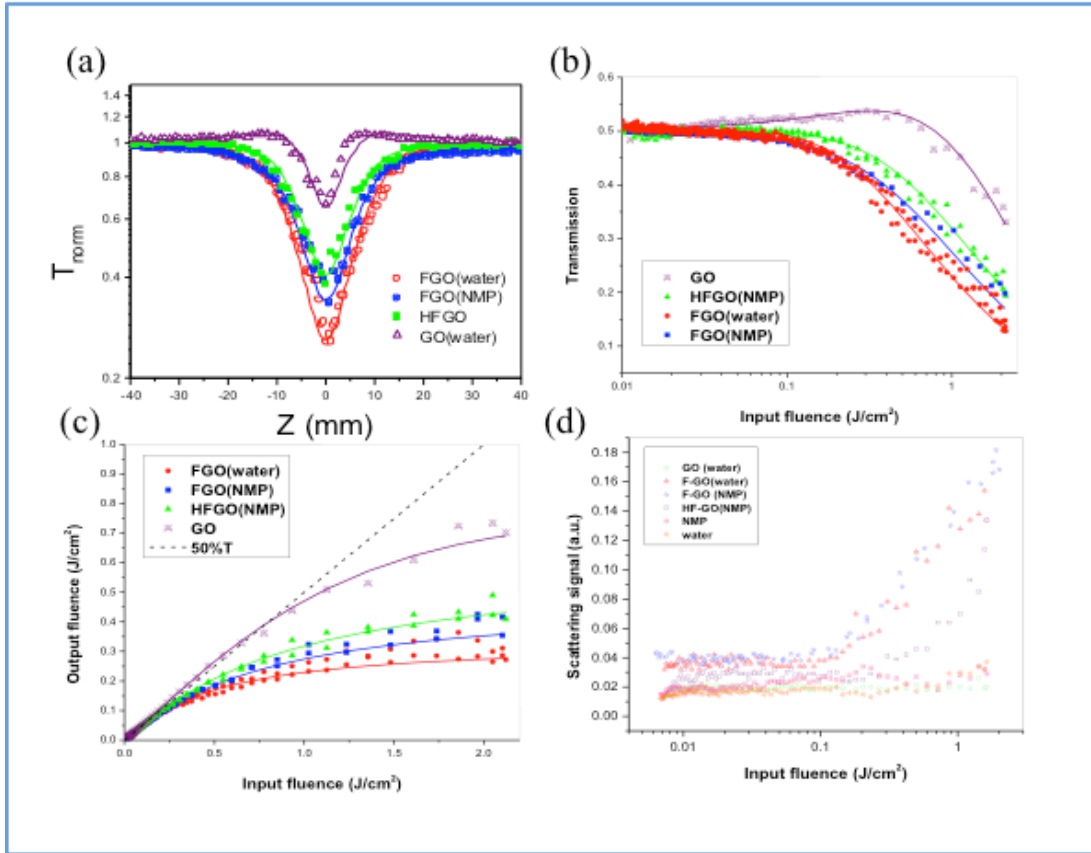


Figure 2.18 (a) Measured Z-scan data. All samples have the same linear transmission of 50%. (b) Variation of sample transmission with input fluence. (c) Variation of sample output fluence with input fluence (d) Variation of scattering signals with input fluence .

The measured open-aperture z-scan curve was fit to the Equation(2.24) and plotted in the Figure 2.18(a). The fit nonlinear absorption coefficients are, 1.40, 0.7 and 0.35 nm/W for F-GO/water, HF-GO/NMP, and GO/water respectively.

In materials, optical limiting behavior arises from nonlinear absorption and/or nonlinear scattering. Processes such as two-photon (or multi-photon) absorption and excited state absorption (also known as reverse saturable absorption - RSA) belong to the class of nonlinear absorption (NLA). Nonlinear scattering (NLS) in dispersions/solutions in the context of optical limiting refers to the scattering of photons from refractive index variations, microbubbles and

microplasma, which are caused by laser-induced heating of the medium. In absorbing media like carbon based materials optical limiting of ns laser pulses is caused mostly by RSA and/or NLS. For example, carbon particle suspensions (CS) show strong optical limiting due to NLS caused by thermally induced microplasma⁵⁰, whereas fullerenes (C₆₀) exhibit robust limiting due to large RSA^{29, 128-129}. In addition, multiwalled and single walled carbon nanotubes (CNTs) exhibit broadband optical limiting due to NLS^{57, 59} while GO exhibits limiting due to RSA¹³⁰.

By measuring the scattered light from our samples, it was found that all fluorinated graphene oxide samples exhibit strong nonlinear scattering whereas there is no nonlinear scattering present in GO. This finding suggests that there is a significant enhancement in nonlinear scattering due to the presence of C-F bonds in the fluorinated samples. This enhancement, as a result, contributes to better optical limiting properties.

Comparing the z-scan and scattering data, it can be seen that, for fluorinated graphene oxide samples, the onsets of the optical limiting start earlier than the onsets of nonlinear scattering. For example, optical limiting of F-GO in water has an onset of optical limiting at about 0.05 J/cm² whereas its nonlinear scattering appears only later, at around 0.14 J/cm². This observation suggests that the optical limiting action of fluorinated graphene oxide in the ns excitation regime is not exclusively due to nonlinear scattering but also the nonlinear absorption.

X. F. Jiang et al. reported significantly enhanced nonlinear absorption of GO upon partial reduction¹³¹. This enhancement in nonlinear absorption was attributed to localized sp² domains. Upon further reduction of GO, larger sp² domains are formed. The interconnectivity of the sp² domains results in increased nonradiative recombination rates and thus reduces its optical limiting efficiency. As-prepared GO exhibited inferior nonlinear absorption than partially reduced GO due to its lower number of localized sp² domains.

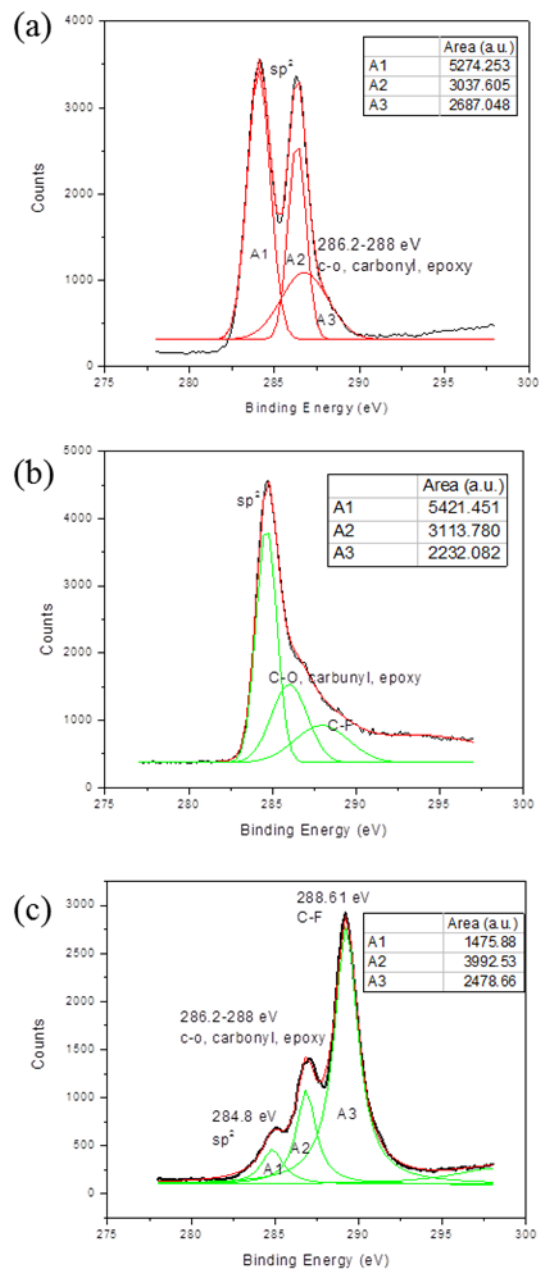


Figure 2.19 XPS spectra of (a) GO, (b) F-GO, and (c) HF-GO

In the case of fluorinated graphene oxide, the interaction of fluorine atoms with the graphene oxide layers is accomplished by covalent attachment of fluorine atoms to the layers. This interaction is accompanied by a change in the hybridization of the 2s and 2p valence

electron states of the carbon atoms from the trigonal (sp^2) to tetrahedral (sp^3) hybridization due to the formation of the additional σ bond between carbon and fluorine atom. The large difference between the local band gaps of the sp^3 and sp^2 sites creates band edge fluctuations, with the sp^3 sites acting as tunnel barriers between the π states of sp^2 clusters.⁴³ These tunnels create strongly localized isolated sp^2 domains which act as defects in the electronic band. Therefore, similar to partially reduced GO, it is possible that larger nonlinear absorption in the fluorinated samples is due to increase in the number of localized sp^2 domains, which are created by the sp^3 attachments of F atoms. However, XPS analyses, Figure 2.19, revealed that the ratios of number of sp^2 carbons to sp^3 carbons in our GO and F-GO are similar, suggesting that there are similar numbers of sp^2 domains in both samples. This finding suggests that the presence of sp^3 defects created by highly electronegative atom such as fluorine promotes larger nonlinear absorption and better optical limiting than the sp^3 sites formed with other functional groups in GO. On the other hand, the ratio of sp^2 to sp^3 carbons of HF-GO is much lower than both of FGO and GO. The lower nonlinear absorption of HF-GO when compared to F-GO can be attributed to the decrease in number of localized sp^2 domains. This is analogous to the case of inferior nonlinear absorption of as prepared GO compared to partially reduced GO reported previously¹³¹. Furthermore, the fact that HF-GO is a stronger nonlinear absorber than GO, even though it has lower number of sp^2 to sp^3 carbons, confirms the significance of fluorine sp^3 sites in the enhancement of nonlinear absorption and thus optical limiting.

3 PHOTOACOUSTIC DETECTION OF OPTICAL NONLINEARITIES[†]

3.1 Motivation

It has been evident in Chapter 2 that when a material contains both nonlinear scattering and nonlinear absorption, performing only conventional Z-scan measurement could not separate or differentiate the two contributions. This is because, transmission-based measurements, like Z-scan, both nonlinear absorption and scattering contribute to reduced transmission. In the case of F-GO, another photodetector mounted at an angle to the sample was needed to detect the scattering signal and the difference in the onsets was used as an evidence of the presence of the two mechanisms. However, what if the sample under consideration had the same onsets of both contributions? It would be impossible to make any conclusion regarding the underlying mechanism for the sample's optical limiting action. Resorting to performing additional measurements with shorter laser pulse or transient measurement might be able to draw some conclusions. Unfortunately, not every lab is equipped with required components to set up the measurements and their setups are not quite simple. In this section, another detection scheme, namely photoacoustic technique, for detecting optical nonlinearities is studied. The focus of the study is to observe the signal characteristics obtain with acoustic transducer integrated with a conventional Z-scan measurement. The system will be tested with nonlinear absorbing as well as nonlinear scattering samples.

[†] The work presented in this chapter are extensions of Chantharasupawong, P.; Philip, R.; Thomas, J., Simultaneous Optical and Photoacoustic Measurement of Nonlinear Absorption. *Applied Physics Letters* 2013, 102, 041116.

3.2 Theoretical background

Photoacoustic (PA) or optoacoustic effect was first discovered by Alexander Graham Bell in 1880, when he observed an audible sound from a tube attached to a cell enclosing a solid sample that was irradiated with modulated sunlight. The PA effect has found applications in various fields of physics, chemistry and biology. Those applications include material characterizations, spectroscopy, sensing, and imaging. In PA spectroscopy, similar spectral profile to optical absorption spectrum is obtained. However, unlike the optical method, the PA-based technique allows measurement of any type of samples whether it is crystalline, amorphous, or powder. This is because the technique is based on the fact that the absorbed light is converted to sound. While scattering samples are problematic with conventional spectroscopic techniques, PA spectroscopy has no difficulties in measuring such samples. In addition, it has been shown that optical absorption data can be obtained with PA spectroscopy even with opaque samples.

PA generation is generally due to photothermal heating effect. After optical absorption, whole or in part of absorbed light is converted to heat in the sample through nonradiative deexcitation. Other deexcitation mechanisms are also possible namely luminescence, photochemistry and photoelectricity. These deexcitation branches complement the heating branch such that the sum of their ratio equals to unity. The most common mechanism PA generation is by thermal expansion of the sample. However, other mechanism is also possible such as electrostriction, photochemical changes, gas evolution or boiling, and plasma formation. PA generation efficiency in the case of electrostriction is usually small and negligible in the order of 10^{-12} , whereas breakdown mechanism can be as large as 30%. However, for stable and chemically inactive samples, thermal expansion is the dominant mechanism.

To generate PA signal, which is essentially a longitudinal wave, intensity modulation of the light source is required to propagate sound. This requirement can either be achieved by the use of frequency -chopped continuous or pulse laser source. In the case of chopped continuous laser source, the modulation frequency is in the range of 1-1000 Hz, and the acoustic propagation distance is much larger than the sample cell. As a result, boundary conditions such as boundary reflection and thermal diffusion effect are important and cannot be neglected when analyzing PA signal. On the other hand, in the case of pulse laser source or pulse PA generation, the acoustic propagation distance is much smaller than the sample and therefore, in most cases, PA pulse is independent of the boundary reflections. Here, we limit our discussion to only the pulse PA generation since ns laser will be used as a light source.

PA generation can be classified as either direct or indirect. In the former, acoustic wave is generated in the sample where the excitation is absorbed. In the latter, however, wave is generated in the coupling media due to acoustic transmission from the sample. Theories for PA generation are briefly presented in the following section. More detailed discussion can be found in the literatures¹³²⁻¹³⁵.

3.2.1 Direct PA generation

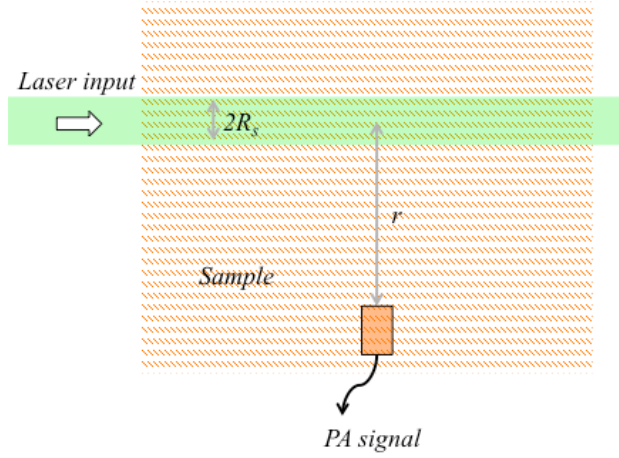


Figure 3.1 Schematic illustration of direct PA measurement

3.2.1.1 Semi-quantitative theory for small laser radius ($R_s < v\tau_L$)

The geometry of direct PA generation is illustrated in Figure 3.1. The laser radius R_s is considered small when it is smaller than the acoustic propagation distance $v\tau_L$ where v is the sound velocity and τ_L is the temporal width of the laser. In this limit, the acoustic source has a radius $R = v\tau_L$ which is larger than R_s . The source expansion immediately after the laser pulse is given by the following thermal expansion equation:

$$\pi(R + \Delta R)^2 l - \pi R^2 l = \beta \pi R^2 l \Delta T \quad (3.1)$$

where l is the length of the PA source, ΔT is the change in temperature due to non-radiative decay, and β is the thermal expansion coefficient. The temperature rise due to laser pulse is governed by the following heat capacity equation:

$$\Delta T = \frac{\alpha E}{\rho \pi R^2 C_p} \quad (3.2)$$

where C_p is the specific heat, α is the absorption coefficient, E is the laser energy, and ρ is the density. In the case of cylindrical acoustic wave, the peak displacement $U_s(r)$ at a distance r away from the source is given by:

$$U_s(R) = \Delta R (R/r)^{1/2} \quad (3.3)$$

and the PA peak pressure at position r is related to the peak displacement by:

$$P(r) \approx v \rho U_s(r) / \tau_L \quad (3.4)$$

Combining equation (3.1)-(3.4) gives the following equation for the peak pressure amplitude at the detector with the distance r away from the source.

$$P(r) \approx \frac{\beta E \alpha v^2}{2 \pi C_p (v \tau_L)^{3/2} r^{1/2}} \quad (3.5)$$

3.2.1.2 Semiquantitative theory for large laser radius ($R_s > v \tau_L$)

In this case, it means that the source does not have time to expand isobarically after the laser pulse. As a result, the pressure increase near the source surface is governed by the following bulk modulus equation:

$$\Delta P = K \beta \Delta T = \frac{K \beta E \alpha}{\pi R_s^2 \rho C_p} \quad (3.6)$$

where K is the bulk modulus. Again, the peak acoustic response at the distance r away from the source is given by.

$$P = \Delta P(R_s / r)^{1/2} = \frac{K\beta E\alpha}{\pi R_s^{3/2} r^{1/2} \rho C_p} \quad (3.7)$$

3.2.2 Indirect PA generation

In the case of the indirect generation, coupling liquid or gas is used and the detector is positioned to monitor acoustic in the coupling media. A thermal piston model is used to describe this indirect PA generation. The model geometry is illustrated in Figure 3.2.

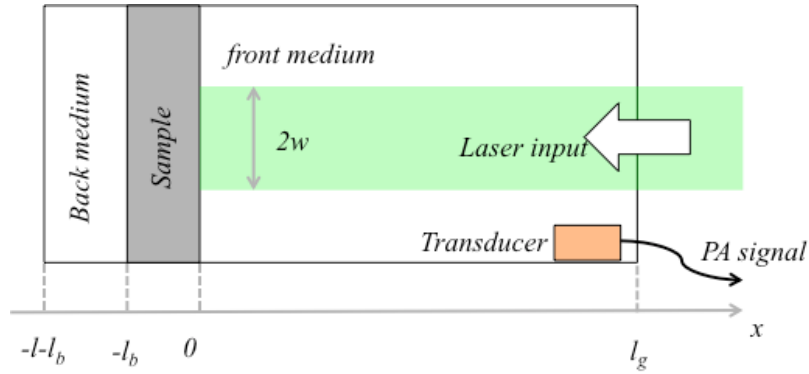


Figure 3.2 Schematic illustration of the thermal piston model

The distributed heat is governed by the thermal diffusion equations¹³⁵:

$$\frac{\partial^2 T}{\partial x^2} = \frac{1}{\alpha_s} \frac{\partial T}{\partial t} - \frac{1}{2k_s} \alpha \eta \exp(\alpha x) I(t) \text{ for } -l < x < 0 \quad (3.8)$$

$$\frac{\partial^2 T}{\partial x^2} = \frac{1}{\alpha_b} \frac{\partial T}{\partial t} \text{ for } -l-l_b < x < -l \quad (3.9)$$

$$\frac{\partial^2 T}{\partial x^2} = \frac{1}{\alpha_f} \frac{\partial T}{\partial t} \text{ for } 0 < x < l_f \quad (3.10)$$

where T is the temperature; $I(t)$ is the modulated light intensity; η is the nonradiative decay

efficiency and α_i s the thermal diffusivity of the sample ($i=s$), front material ($i=f$) and back material ($i=b$). By solving equations (3.8)-(3.10), temperature profile $T(x,t)$ can be obtained. By relating the heat change with appropriate thermodynamic equations, one can derive pressure wave distribution. Empirical estimation of the peak pressure can also be done. If we assume that there is communication layer between the sample and its coupling medium within a heat diffusion length of μ_s . The absorbed light energy can be converted to temperature rise at the surface through a heat conduction equation of the form:

$$\frac{k_s \Delta T}{\mu_s} \approx \alpha I_0 \mu_s \quad (3.11)$$

where I_0 is the peak intensity of $I(t)$. The produced heat is then coupled to an adjacent volume of liquid with an active volume of :

$$V_a = \pi w^2 s_g \quad (3.12)$$

where w is the laser beam waist and s_g is the effective thermal length of the coupling medium. Using an ideal gas law, the change in the active volume due to temperature is:

$$\frac{\Delta V_a}{V_a} = \frac{\Delta T}{T} \quad (3.13)$$

This volume fluctuation can cause a pressure fluctuation at the detector. Assuming the process is adiabatic, the pressure change is given by:

$$\Delta P = \gamma P \Delta V_a / V_0 \quad (3.14)$$

where γ is the adiabatic index and V_0 is the total coupling medium volume. Combining Equations

(3.11)-(3.14), the PA amplitude ΔP can be obtained as:

$$\Delta P = \frac{\gamma P_s w^2 I_0}{TV_0} \frac{\alpha \mu_s^2}{k_s} \quad (3.15)$$

From Equation (3.15), the normalized PA signal $\Delta P/I_0$ is proportional to the sample absorption coefficient α . Thus, determining absorption coefficient from PA detection is possible.

3.3 Experimental methods

3.3.1 Simultaneous measurements

From section 3.2, it has been found that PA generation is proportional to the absorption coefficient. Therefore, extracting absorption properties of material by detecting generated PA signal is theoretically possible. The goal of this setup is to compare signal characteristics obtained from conventional optical technique like Z-scan to what received from PA detections. The PA detection will be combined to a conventional Z-scan setup. The data obtained from both detection schemes will be from a single experimental run in order to avoid uncertainties and achieve the highest correlation as possible. Indirect PA measurement with the use of coupling medium will be employed since sample is usually taken in a cuvettes for the conventional Z-scan.

To combine PA detection with the conventional Z-scan, a PA cell is introduced into the setup. The PA cell is made from brass due to its excellent corrosion resistance and electromagnetic interference shielding. The cell is integrated to a conventional Z-scan setup by mounting it on a linear translation stage (Newport, ILS150PP). The cell has a diameter of 8 cm

and height of 5 cm. An ultrasonic transducer (Olympus NDT, model A315-SU) and glass windows are fixed on the circular cell wall as shown in Figure 3.3(a). The cell has a brass lid with a slotted teflon cap in the center, through which a 1mm path length cuvette containing the sample can be inserted. The cuvette is positioned at an angle such that its front surface is facing the transducer for better acoustic detection. The cell is filled with water as a coupling medium between the sample and the transducer. The acoustic signals are collected by the transducer that is connected to an oscilloscope. Photograph of the set-up is shown in Figure 3.3(b).

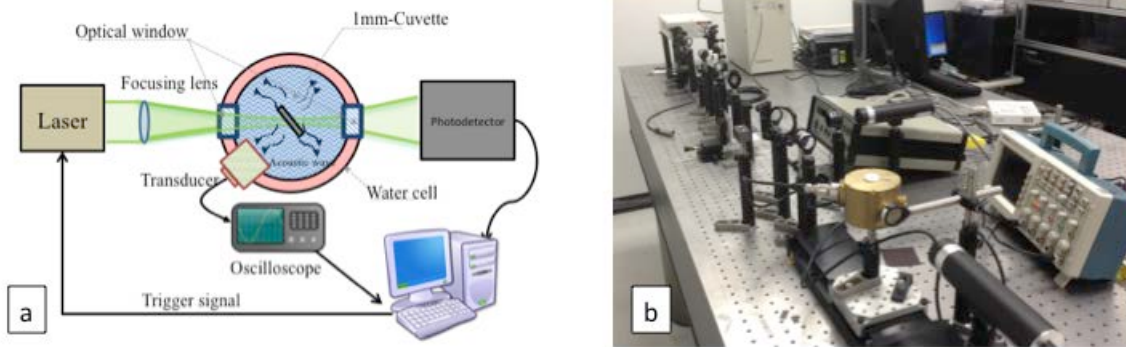


Figure 3.3 (a) Schematic diagram of the simultaneous optical and PA measurements (b) Photograph of the set up.

3.4 Results and discussion

3.4.1 Simultaneous Optical and Photoacoustic Measurement of Nonlinear Absorption

In this section, a new technique, which combines the photoacoustic technique with the conventional optical Z-scan into a single measurement, is developed. Photoacoustic and optical transmission signal are measured and obtained simultaneously in one experimental run. This combined optical and photo acoustic Z-scan technique will be called OPAZ-scan.

The first sample to study with this OPAZ-scan technique is the functionalized-C60([6,6]-phenyl-C₆₁-butyric acid methyl ester : PCBM) in chloroform. PCBM is a reverse saturable absorber/ optical limiter. As a result, since PA is proportional to the sample absorption, increase in PA generation should be observed with this sample when the material absorption starts to increase with light intensity due to RSA process. The second sample under study is 3,3'-diethyloxadicyanone iodide (DODCI) in methanol which is a saturable absorber. Increase in sample transmission and decrease in PA signal with increase in light intensity are expected with this sample due to saturable absorption (SA) process.

Normalized transmission and peak PA signals from the first acoustic pulse are plotted against sample positions for these two samples as shown in Figure 3.4. In the case of reverse saturable absorbers, Figure 3.4(a), light absorption increases as the incident intensity increases. This gives rise to decrease in transmission and hence the optical Z-scan signal as the sample is moved toward the focal point. The PA signal, Figure 3.4(c), on the other hand, show a peak since the acoustic generation is proportional to the absorbed energy. On the contrary, DODCI, Figure 3.4 (b) and (d), have reverse characteristics, as expected, because light absorption is less near the focal point.

In order to find nonlinear coefficients from transmission signals, the following differential equation for optical intensity loss in thin sample is considered.

$$\frac{dI}{dz} = -\mu_a I \quad (3.16)$$

where I is the optical intensity, z is the propagation distance, and μ_a is the absorption coefficient described by Equation (3.17) and (3.18) for reverse saturable absorber¹³⁶ and saturable absorber¹³⁷ respectively :

$$\mu_a = (\alpha_0 + \beta_{eff} I) \quad (3.17)$$

$$\mu_a = \alpha_0 (1 + I / I_{sat}) \quad (3.18)$$

where β_{eff} is the effective nonlinear absorption coefficient for reverse saturable absorbers and I_{sat} is the saturation intensity of saturable absorbers. The intensity for a TEM₀₀ Gaussian beam propagating through a sample along the +z direction is of the form:

$$I(z, t) = \left[\frac{w_0^2 I_0(x, t)}{w^2(z)} \right] \exp\left(-\frac{2r^2}{w^2(z)} \right) \quad (3.19)$$

where $w^2(z) = w_0^2 (1 + z^2 / z_0^2)$, z is the sample position relative to the focus, w_0 is the radius of the beam waist, and $z_0 = \pi w_0^2 / \lambda$ is the Rayleigh length. By integrating Equation (3.16) over sample length L , the optical intensity transmitted through a sample can be found. For a temporally Gaussian pulse, the normalized transmission of the sample is given by:

$$T_{norm}(z) = \frac{1}{\sqrt{\pi}} \int_{-\infty}^{\infty} T(z, t) dt \quad (3.20)$$

with

$$T(z, t) = \frac{\int_0^{\infty} I_{out} r dr}{e^{-\alpha_0 L} \int_0^{\infty} I_{in} r dr} \quad (3.21)$$

where α_0 is the linear absorption coefficient of the sample. Thus, by numerically solving Equation (3.16-3.21) and fitting to the experimental transmission data, the nonlinear absorption parameters β_{eff} and I_{sat} of the reverse saturable and saturable absorbers can be respectively determined. The fitting values are $\beta_{eff} = 2.2 \text{ nm/W}$ and $I_{sat} = 0.25 \text{ TW/m}^2$ for PCBM and DODCI

respectively. Analytical forms of the transmission can be found in the literatures for both saturable¹³⁷ and reverse saturable¹³⁸ absorbers.

In determining the nonlinear absorption parameters from PA signals, the Tam's indirect PA generation model¹³⁹, Equation(3.15), which describes the peak PA amplitude δP was used together with Equation (3.17-3.18). The fitting values are $\beta_{eff} = 1 \text{ nm/W}$ and $I_{sat} = 0.6 \text{ TW/m}^2$ for PCBM and DODCI respectively. These fitting parameters are comparable to what obtained from optical transmission.

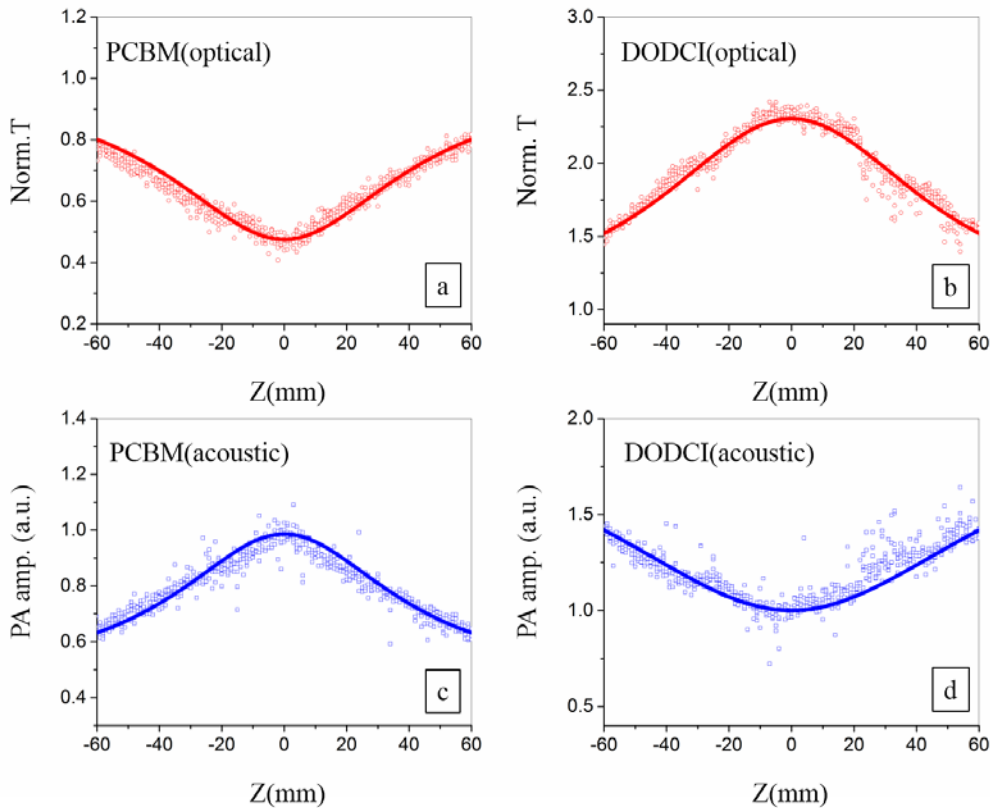


Figure 3.4 (a) Optical signal of PCBM in chloroform with 20% linear transmission and E_{in} of 112uJ, (b) Optical signal of DODCI in methanol with 20% linear transmission and E_{in} of 112uJ, (c) Acoustic signal of the same concentration of PCBM as in (a), and (d) Acoustic signal of the same concentration of DODCI as in (b). Optical and acoustic signals were obtained simultaneously with the OPAZ-scan configuration. The solid lines are the fitted curves.

In addition, we carried out an OPAZ-scan measurement of a very opaque solution of PCBM in chloroform. Due to the opacity of the sample, the transmitted energy was below the sensitivity of our energy meter and could not be measured. However, unlike the optical technique, it is possible to obtain information about the sample absorption with PA signal, as shown in Figs. 3.5(a). The data was also fit with Equation (3.15). The fitting is $\beta_{eff} = 5 \text{ nm/W}$. The fit parameter is higher than what obtained from the transparent sample. This is in agreement with previous study on C_{60} , which found that the effective nonlinear absorption coefficient of C_{60} in toluene increases with concentration^{84, 140}. This measurement clearly demonstrates the advantage of photoacoustic method over transmission method in determining the nonlinear optical coefficients of non-transparent samples.

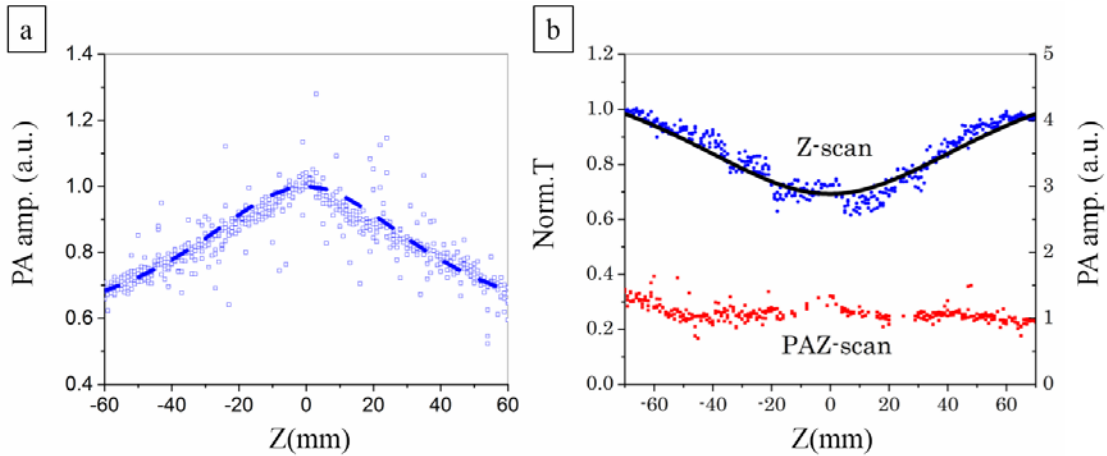


Figure 3.5 (a) PA signal of a very opaque PCBM with E_{in} of 80uJ. Optical signal cannot be measured with this sample due to its opacity (b) OPAZ-scan curves of carbon-black dispersion in water with 1% transmission at 532nm and E_{in} of 103uJ. The lines are the fitted curve.

To further demonstrate the relative advantage of the OPAZ-scan (i.e., measuring both transmission and photoacoustic data simultaneously), OPAZ-scan measurement on carbon-black suspension, which is a nonlinearly scattering sample, was carried out (Figure 3.5(b)). Interestingly, comparing Figure 3.5(b) and Figure 3.4, OPAZ curves of carbon-black suspension

(CBS) reveals a different characteristic than what is expected from reverse saturable and saturable absorbers. The former shows decrease in transmission and increase in acoustic signal as the sample moves toward the focal point, while the latter shows the opposite trend. Carbon black suspension, however, shows a decrease in the transmission and non-characteristic acoustic signals, as it is moved closer to the focal point. This observation suggests that the well-known optical limiting found in carbon-black suspensions does not originate primarily from nonlinear absorption. In fact, it has been shown that the nonlinear transmission of CBS for nanosecond pulses arises mostly from nonlinear scattering¹⁴¹. It is obvious from Figure 3.5(b) that the Z-scan curve alone is insufficient to determine the mechanisms behind the nonlinear reduction in transmission. For instance, an incorrect conclusion could be drawn because the Z-scan curves obtained from nonlinear scattering samples are similar to that obtained from reverse saturable absorbers. On the other hand, measuring the photoacoustic signal alone also is not possible to draw any conclusions. The fluctuation in the acoustic signal can be attributed to background noise in the acoustic detection created by nonlinear scattering process. Nevertheless, because the PAZ-scan curve does not show any characteristic sign of nonlinear absorption, the nonlinear transmission seen with the optical signal can be mostly attributed to a nonlinear scattering process.

3.4.2 More rigorous fitting of the PAZ-scan

From the previous section, we have found that PA can give information about nonlinear absorption and the signal is complementary to the conventional optical z-scan technique. However, so far, only semi-quantitative model have been used in fitting the nonlinear coefficient from the PA z-scan data. In this particular model, the beam profile and distribution across the sample are ignored. Only the peak intensity of the light is taken into account. It is obvious that this fitting formula is not a true representation of the system. To check this aspect, PAZ-scan as well as optical Z-scan of a nonlinear absorbing sample, PCBM in toluene were performed with a small laser beam waist of $30\ \mu\text{m}$. A small beam waist was used since light distribution within the sample change significantly from one z position to another in the case of tight focus geometry as opposed to the loose focus case. It was found that the semi-quantitative model (Model 1), Equation (3.15), failed to fit the acoustic data when the same fitting parameter from optical z-scan was used (Figure 3.6). As a result, in this section, more rigorous formulation for fitting PA data is developed.

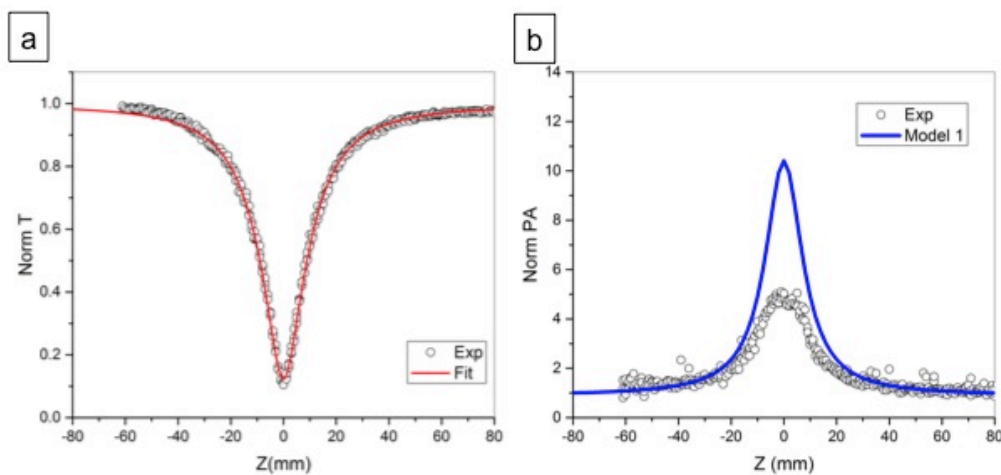


Figure 3.6 OPAZ-scan data. (a) optical $-z$ -scan and its fit (b) PA z-scan with the fitting value from the curve in (a). Clearly, model 1 deviates significantly from the experimental data.

3.4.2.1 Photoacoustic calculation with a frequency- wavenumber method

Calculation based on the frequency-wavenumber (k-space) method¹⁴² is used to simulate our experimental observations. The formulation of such calculation technique is discussed here in this section.

A sound wave is generated when absorbing fluid is heated with a laser pulse. The following pair of coupled differential equations, obtained from linearized equations of fluid dynamics, for the temperature T and pressure p can be used to determine the temperature and pressure variations:

$$\frac{\partial}{\partial t} \left(T - \frac{\gamma-1}{\gamma\alpha} p \right) = \frac{K}{\rho C_p} \nabla^2 T + \frac{H}{\rho C_p} \quad (3.22)$$

$$\left(\nabla^2 - \frac{\gamma}{v_s^2} \frac{\partial^2}{\partial t^2} \right) p = -\frac{\alpha\gamma}{v_s^2} \frac{\partial^2}{\partial t^2} T \quad (3.23)$$

where γ is the specific heat ratio, α is the pressure expansion coefficient defined by $\alpha = (\partial p / \partial T)_v$, K is the thermal conductivity, ρ is the density, v_s is the speed of sound, and the heating function H is the rate of energy density deposited by the optical radiation. Under the condition whereby the sound generation is thermoelastic, in which the heat generated by absorption of light is confined in the irradiated volume during the laser pulse (thermal confinement), the term containing thermal conductivity becomes negligible and the acoustic pressure can be expressed with the following wave equation:

$$\left(\nabla^2 - \frac{1}{v_s^2} \frac{\partial^2}{\partial t^2} \right) p = -\frac{\beta}{C_p} \frac{\partial H}{\partial t} \quad (3.24)$$

where β is the thermal expansion coefficient, $\beta = (1/V)(\partial V / \partial T)_p = \alpha\gamma / \rho v_s^2$, and V is the volume. If the light fluence distribution in the sample is given by $F(x,t)$, the heating function $H = \mu_a(x)F(x,t)$, where $\mu_a(x)$ is the absorption distribution.

The heating function can be assumed instantaneous when the laser temporal width is fast. This instantaneous condition is satisfied when the laser pulse is much faster than the time required for sound wave to propagate across the heated region, i.e. stress confinement condition. In this regime, the heating function is of the form:

$$H(x,t) = H(x)\delta(t) \quad (3.25)$$

Change in temperature is related to the absorbed energy by

$$\Delta T = H / (\rho C_v) \quad (3.26)$$

Using the thermodynamic relation:

$$\Delta \rho = \rho \kappa_T \Delta p - \beta \rho \Delta T \quad (3.27)$$

with the assumption that there is no change in the density, the change in pressure can be governed by :

$$\Delta p = (\beta / \kappa_T) \Delta T \quad (3.28)$$

Using Equation(3.26) and (3.28) with $\kappa_T = \gamma / \rho c^2$, the instantaneous increase in pressure and thus initial pressure distribution due to absorption of laser pulse is written as:

$$p_0(x) = \frac{\beta c^2}{C_p} H(x) = \Gamma H(x) \quad (3.29)$$

where Γ is the Gruneisen parameter, a lump constant associating with the heat-to-pressure conversion efficiency. With the instantaneous heating function of Equation (3.25), the solution to Equation(3.24) in the absence of boundaries can be written as:

$$p(x, t) = \frac{\beta}{C_p} \int_0^x \int_0^t G(x, t; x', t') H(x') \delta'(t') dx' dt' \quad (3.30)$$

where δ' is the first derivative of the delta function, and G is the free-space Green's function:

$$\nabla^2 G - \frac{1}{c^2} \frac{\partial^2 G}{\partial t^2} = -\delta(x-x')\delta(t-t') \quad (3.31)$$

Using the property of δ' where $\int \delta'(t-t_0) f(t) dt = -f'(t_0)$ and $\partial G / \partial t' = -\partial G / \partial t$,

Equation(3.30) becomes:

$$p(x, t) = \frac{\beta}{C_p} \int \frac{\partial G}{\partial t}(x, t; x', t') H(x') dx' \quad (3.32)$$

with Equation (3.29), Equation(3.32) can be rewritten as:

$$p(x, t) = \frac{1}{c^2} \int \frac{\partial G}{\partial t}(x, t; x', t') p_0(x') dx' \quad (3.33)$$

By taking Fourier transform of Equation (3.31) with respect to x and t, the Green's function can be expressed in term of frequency.

$$-k^2 G(\omega, \mathbf{k}) + \frac{\omega^2}{c^2} G(\omega, \mathbf{k}) = -e^{-i\mathbf{k}x'} e^{i\omega t'} \quad (3.34)$$

It can then be written in term of wavenumber vector \mathbf{k} as:

$$G(x, t, x', t') = \frac{1}{(2\pi)^4} \iint \frac{e^{i\mathbf{k}(x-x')} e^{-i\omega(t-t')}}{k^2 - (\omega/c)^2} d\omega d\mathbf{k} \quad (3.35)$$

where $k = |\mathbf{k}|$. In this equation, the spherical wave green function is written as a sum of plane wave. Using Equation (3.33) and (3.35), pressure distribution at time t can be calculated from the initial pressure distribution $p_0(x)$. First, the integrand in Equation (3.35) can be evaluated using Cauchy's residue theorem with t' set to zero. This gives the solution for $t > 0$ as:

$$G(x, t, x') = \frac{c}{(2\pi)^3} \int \frac{\sin(ckt)}{k} e^{i\mathbf{k}(x-x')} d\mathbf{k} \quad (3.36)$$

The time derivative of this function is:

$$\frac{\partial G}{\partial t} = \frac{c^2}{(2\pi)^3} \int \cos(ckt) e^{i\mathbf{k}(x-x')} d\mathbf{k} \quad (3.37)$$

Substituting Equation (3.37) in (3.33) gives

$$p(x, t) = \frac{1}{(2\pi)^3} \iint \cos(ckt) e^{i\mathbf{k}(x-x')} p_0(x') dx' d\mathbf{k} \quad (3.38)$$

By changing the order of the integrand, Equation (3.38) can be viewed as a two-step calculation.

First, the following Fourier transform has to be evaluated

$$p_0(\mathbf{k}) = \int p_0(x) e^{-i\mathbf{k}x} dx \quad (3.39)$$

Second, using the result from the first step, time evolution of pressure can be determined

$$p(x, t) = \frac{1}{(2\pi)^3} \int p_0(\mathbf{k}) \cos(ckt) e^{i\mathbf{k}x} d\mathbf{k} \quad (3.40)$$

Therefore, acoustic pressure at all position can then be calculated using Equation (3.39) and (3.40) with a known initial condition of $H(x)$.

3.4.2.2 Acoustic field time snapshots of a point source

In this section, the acoustic field propagation of an instantaneous point source is simulated. In this model, the heating function $H(x)$ is assumed to have a Gaussian profile, Figure 3.7(a). The initial pressure $p_0(x)$ is calculated from Equation(3.29) with the assumption of $\Gamma=1$. The temporal evolution of the acoustic field is then calculated from Equation (3.39) and (3.40). Figure 3.8 shows time snap shots of the acoustic fields. Simulation of acoustic wave measured by a line detectors at $y=-5\text{mm}$ is shown in Figure 3.9(a). Figure 3.9(b) shows the simulated acoustic wave measured from a point detector at $x=0$ and $y=-5\text{mm}$.

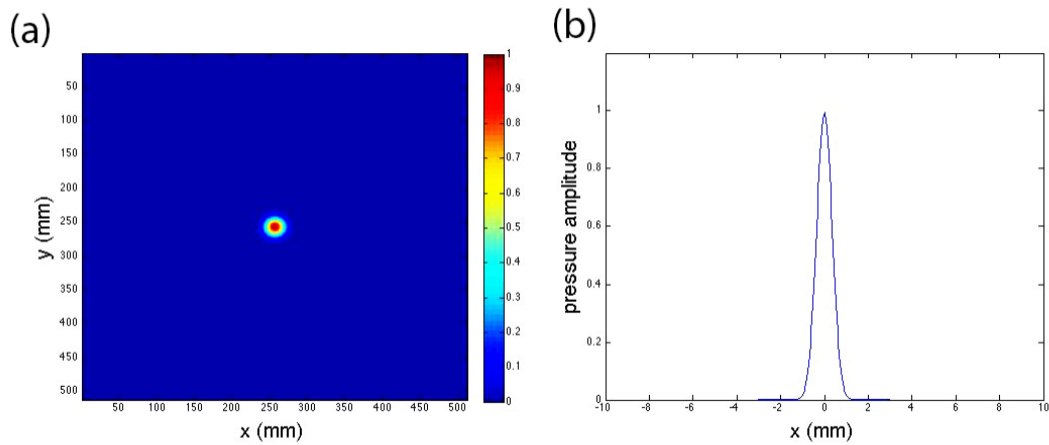


Figure 3.7(a) 2D-plot of a Gaussian point source initial pressure (b) X-cross section of (a)

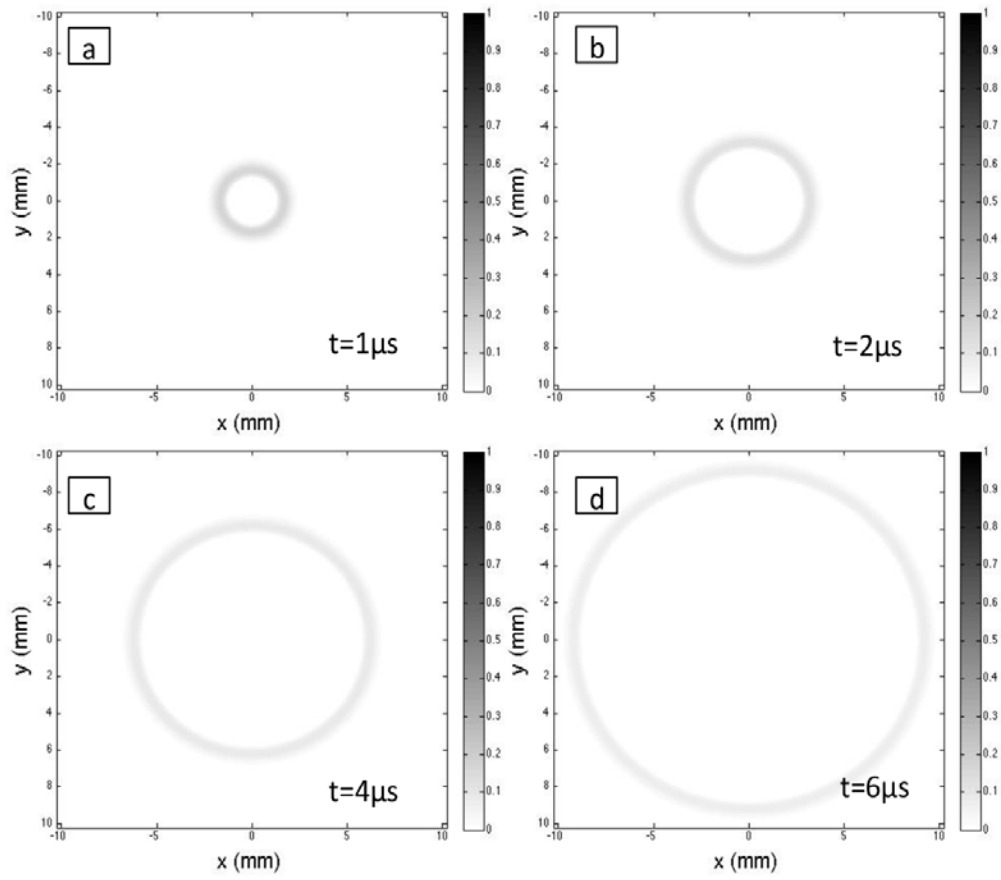


Figure 3.8 2D time evolution of pressure distribution at time t equals (a) $1\mu\text{s}$ (b) $2\mu\text{s}$ (c) $4\mu\text{s}$ and (d) $6\mu\text{s}$ for Figure 3.7

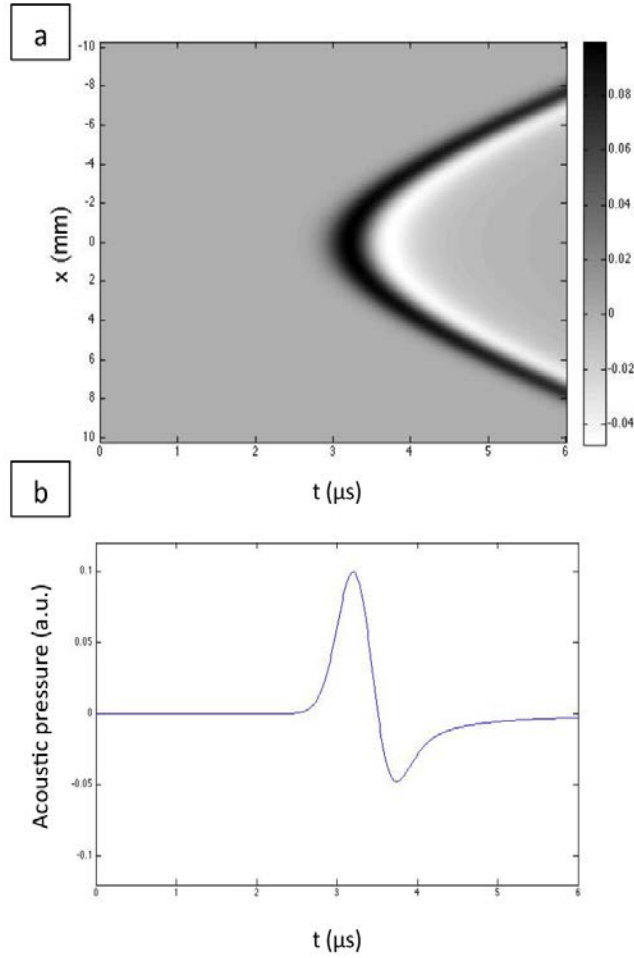


Figure 3.9 (a) Acoustic wave measured by a line detectors at $y=-5\text{mm}$ of the source in Figure3.7(a). (b) Acoustic wave measured by a point detector at $x=0,y=-5\text{mm}$

3.4.2.3 Acoustic field time snapshots of a thin absorbing sample

In this section, we expand the above simulation to the case of thin absorbing sample excited with a pulse Gaussian beam with a width of w_0 . First, the initial pressure distribution of the sample can be obtained by solving the following equation:

$$\frac{dI(x,y)}{dz} = -\mu_a I(x,y) \quad (3.41)$$

where μ_a is the absorption coefficient and z is the propagation direction. In the case of linear sample, $\mu_a = \alpha$. For samples with third order nonlinearity $\mu_a = \alpha + \beta I$. The $p_0(x,y)$ is then calculated from Equation (3.29) with $H(x,y) = \mu_a(x,y)F(x,y)$. Figure 3.10 shows the calculated initial pressure distribution of a thin linear absorbing sample with thickness $t = 1\text{mm}$, $\mu_a = 3\text{mm}^{-1}$, $w_0 = 80\mu\text{m}$, and $\Gamma = 1$. From this initial pressure distribution, the temporal evolution of the acoustic field is calculated and shown in Figure 3.11. Simulation of acoustic wave measured by a line detectors at $y = -0.8\text{mm}$ is shown in Figure 3.12(a). Figure 3.12(b) shows the simulated acoustic wave measured from a point detector at $x = 0$ and $y = -0.8\text{mm}$. Up to this point, the simulated acoustic signals were done with the assumption that the sensor has a wide frequency response. Since, transducer has a limited bandwidth response, the signal collected by the transducer can be modeled as a product of the simulated pressure signal multiplied by the transducer bandwidth in the frequency domain. Figure 3.13 shows the simulated signal collected by a transducer with a central frequency at 10MHz and a Gaussian bandwidth of 40%.

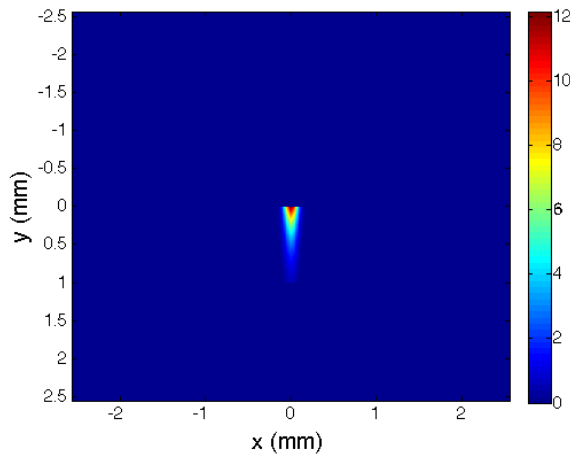


Figure 3.10 2D-plot of initial pressure distribution created by passing Gaussian beam through a thin absorbing layer

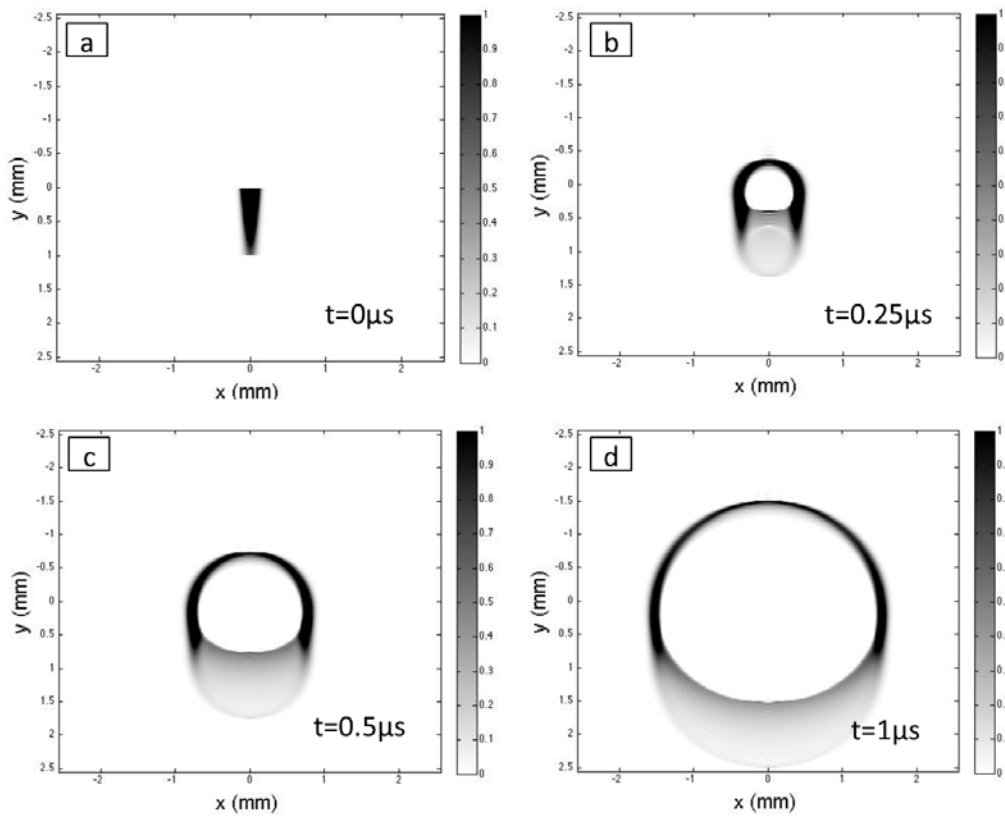


Figure 3.11 2D time evolution of pressure distribution at time t equals (a) $0\mu\text{s}$ (b) $0.25\mu\text{s}$ (c) $0.5\mu\text{s}$ and (d) $1\mu\text{s}$ for Figure 3

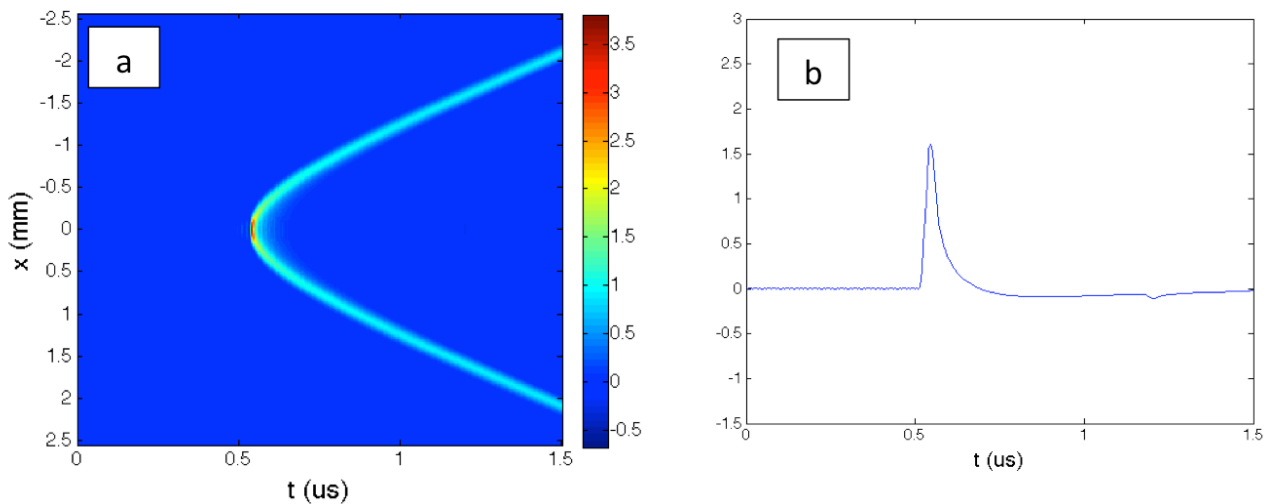


Figure 3.12(a) Simulation of acoustic wave measured by a line detectors at $y = -0.8\text{mm}$ of the source in Figure 3.10. (b) Acoustic wave measured by a point detector at $x=0, y = -0.8\text{mm}$

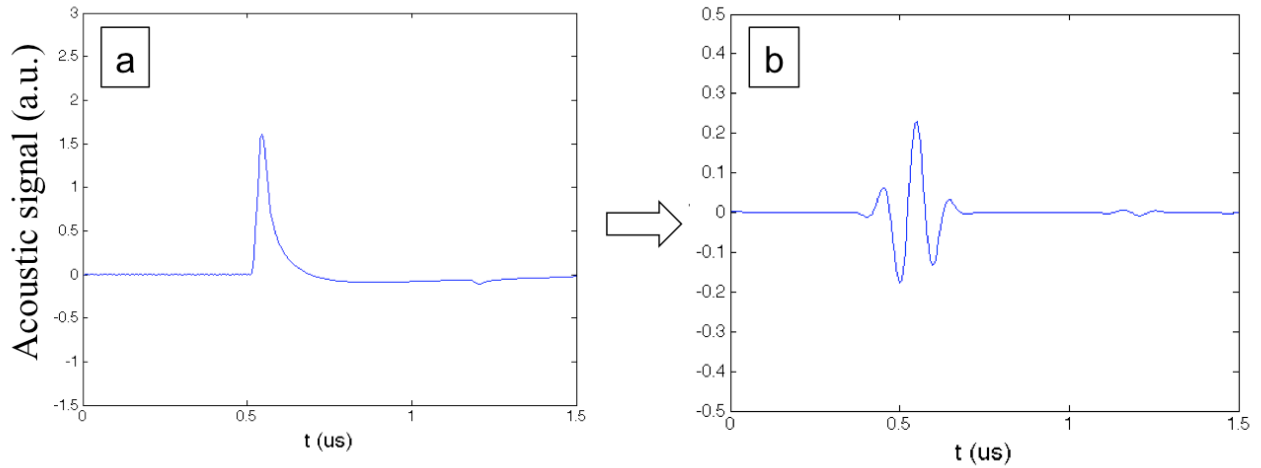


Figure 3.13(a) Simulated acoustic signal (b) Simulated acoustic signal received by a transducer with a center frequency of 10 MHz and bandwidth of 40%

3.4.2.4 PAZ-scan fitting with k-space simulation

In this section, the k-space simulation is used to fit the collected PAZ-scan data for the tight focus case. The orientation of the cuvette in the experimental setup was taken into account in finding the initial pressure distribution, Figure 3.14(a). The simulation was looped for different laser beam size at a fixed excitation energy following the nature of Z-scan setup. The acoustic signal magnitude was collected for each beam size and plotted against the Z-position. The simulated signal was collected away from the source with a line detector. The distance between the sensor and the source was shorter in the simulation to reduce the simulation time. In the actual experiment, a water delay line adds time delay to the signal. Since, when collecting the experimental data, only the magnitude of the first PA pulse was collected, therefore, in the simulation, only the first pulse, Figure 3.14(b), was simulated and the boundaries were ignored for simplicity. MATLAB code for this fitting algorithm can be found in Appendix E. In brief, the fitting program does the following:

- (1) Calculate initial pressure distribution from a given excitation, beam size at the corresponding z position, linear absorption and nonlinear absorption parameter
- (2) Calculate time evolution of the acoustic signal and measure its peak-to-peak magnitude.
Record the PA magnitude and its corresponding z-position
- (3) Repeat (1) and (2) for the whole scanning range (z axis)

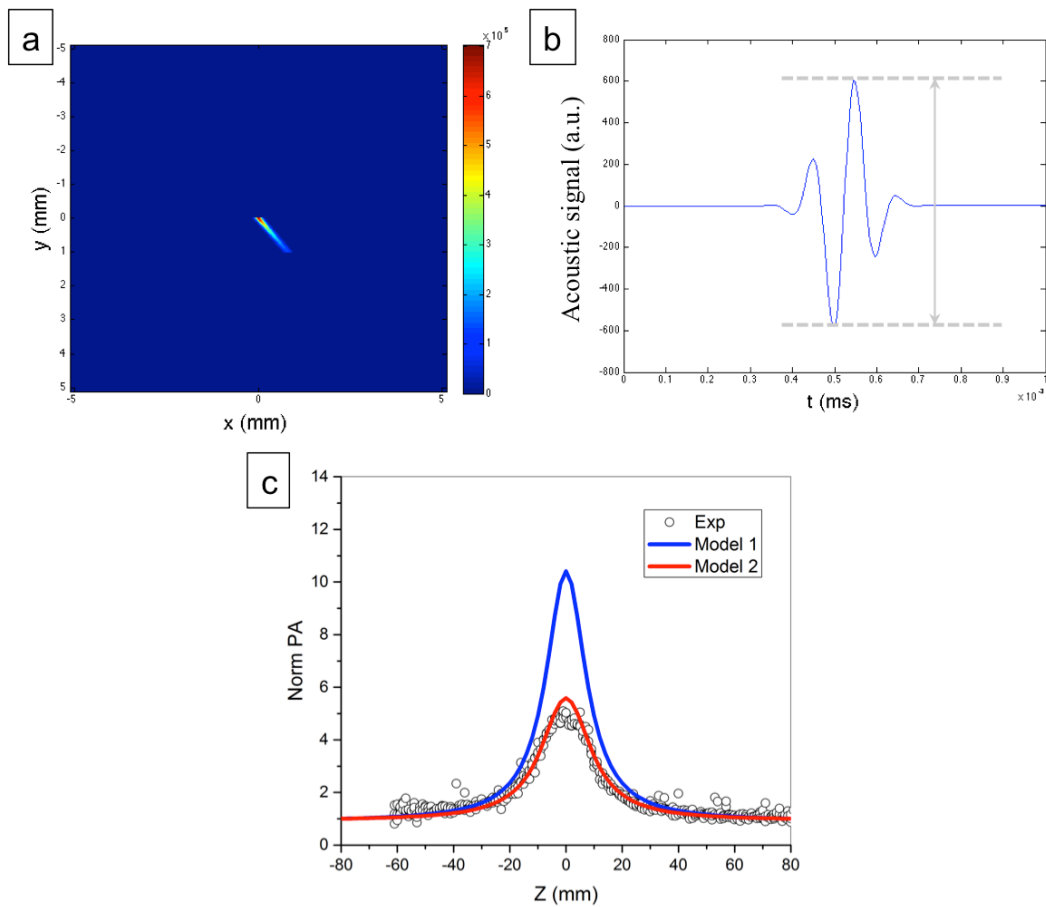


Figure 3.14(a) Initial pressure distribution for the k-space fitting model. The beam diameter is $80\mu\text{m}$; (b) First PA pulse simulated from the initial pressure in (a); (c) comparison between acoustic two fitting model. The fitting parameters were obtained from experimental z-scan with PCBM in a 1mm cuvette. The beam waist is $30\mu\text{m}$. The linear transmission is 0.1 and $\beta = 7\text{nm/W}$.

Figure 3.14(c) compares the k-space fitting formulation to the semi-quantitative formula. The parameter used was obtained from fitting the optical Z-scan. It is clear this k-space technique gives a better fit to the experimental data. The difference between the two model, namely the semi-quantitative model (Model1) and the k-space model (Model2) for different beam sizes and nonlinear parameter was also investigated, Figure 3.15. It is clear that these two model diverge significantly for small beam waist while they give similar behaviors for large beam waist which is in agreement with what have been observed experimentally.

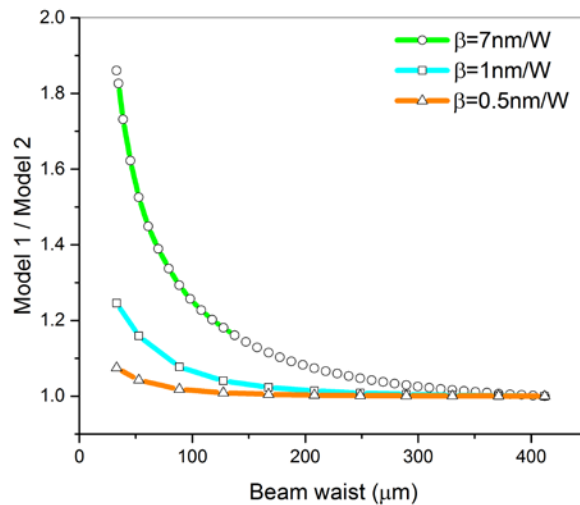


Figure 3.15 Comparison of normalized PA magnitudes obtained from Model 1 and 2 for different sizes of Gaussian beam waists in the z-scan configuration.

4 PHOTOREFRACTIVE POLYMER SENSITIZED WITH NANOMATERIALS[‡]

4.1 Motivation

The photorefractive (PR) effect is a spatial modulation of the refractive index generated by photo-charge redistribution in a material. This effect occurs when charge carriers are generated by spatially modulated light, usually from interference of two beams. The charge generation is followed by charge separation due to drift and/or diffusion processes. When these charges are trapped by defects, they create inhomogeneous space-charge distribution. In the case of inorganic crystals, the resulting electric field modulates the refractive index by a second order nonlinear effect i.e. electro-optic effect, creating an refractive index grating inside the material. In the case of PR polymers, another effect called orientational enhancement also plays significant role in creating the index modulation. The generated grating has a phase shift with respect to the modulated light intensity. This phase shift, which sometimes referred to as a nonlocal nature of the PR effect, is a distinctive characteristic of the PR effect. There are many applications associated with PR effect, for instance, high-density optical data storage¹⁴³, image processing¹⁴⁴⁻¹⁴⁵, 3D holographic display¹⁴⁶, tunable filter¹⁴⁷⁻¹⁴⁸ and bio-imaging¹⁴⁹.

The photorefractive effect was first discovered in 1966 in Lithium niobate (LiNbO₃) by Ashkin et al at Bell Lab. The effect was first called optically induced refractive index

[‡] The work presented in this chapter are extensions of Chantharasupawong, P.; Christenson, C. W.; Philip, R.; Zhai, L.; Winiarz, J.; Yamamoto, M.; Tetard, L.; Nair, R. R.; Thomas, J., Photorefractive Performances of a Graphene-Doped Patpd/7-Dcst/Ecz Composite. *Journal of Materials Chemistry C* 2014, 2, 7639-7647.

inhomogeneities. During the time of the first discovery, the effect was considered as undesirable in electro-optic and nonlinear optical application as it limited the usefulness of crystals with large electro-optic and nonlinear optical coefficient such as LiNbO_3 . This was because the index change gave rise to de-collimation and scattering of the light beams¹⁵⁰. It was later realized by Chen and his colleagues at Bell Lab that this effect is useful in holographic recording applications where materials that can modulate the refractive index upon irradiation are desirable¹⁵¹. Chen later described that this “optically induced refractive index change” phenomena, which at that time known as “optical damage”, is due to the drifting of excited electrons out of the illumination region followed by re-trapping¹⁵². His explanation laid the foundation for the present understanding of the photorefractive effect. After the discovery of the effect in LiNbO_3 , other inorganic crystals, such as BaTiO_3 ¹⁵³, KNbO_3 ¹⁵⁴, $\text{Bi}_{12}\text{SiO}_{20}$ ¹⁵⁵, and GaAs ¹⁵⁶, also showed similar properties.

In 1990, Sutter, Hulliger and Günter grew organic crystal of 2-cyclooctylamino-5-nitropyridine (COANP) single crystals doped with 7,7,8,8-tetracyanoquinodimethane (TCNQ)¹⁵⁷. They observed photorefractive effect in their crystal. The growth of doped organic crystals, however, is not an easy task because most dopants are expelled during the crystal preparation by self-purification process. In 1991, the PR effect was observed for the first time in an amorphous polymer by Ducharme et al. who worked at IBM¹⁵⁸. Their PR polymer composite was a partially cross-linked epoxy polymer (bisA-NPDA) composed of bisphenol-A-diglycidylether (bisA) attached to the nonlinear chromophore 4-nitro-1, 2-phenylenediamine (NPDA). The glass transition temperature (T_g) of the material was 65°C. Even though the performance of this polymer PR material was poor when compared to today's PR polymer materials, this discovery opened the new field of PR polymers.

PR polymer composites gained considerable attention for its advantage of large PR effect, structural flexibility, low cost, and good processability when compared to the inorganic crystal. Since large diffraction efficiency can be obtained in PR polymer composite with several microns thick sample (as opposed to a few cm thick in the case of inorganic crystals), they are interesting choices in large area and compact applications. For example, Salvador et al. used a near-infrared (NIR) sensitized PR polymer composite as recording media in holographic optical coherence imaging (HOI).¹⁵⁹ They successfully imaged tumor spheroids with their system. Perhaps, one of the most fascinating applications of PR polymer materials is the refreshable holographic 3D-display concept developed by the University of Arizona¹⁶⁰. However, in order to transform this concept to real world applications, key performances such as sensitivity, transparency and response time in PR polymer materials have to be substantially improved.

The writing speed of the PR materials depends on two major factors: (1) formation of the space charge field i.e. charge generation, transfer, transport and trapping; and (2) the reorientation dynamics of the chromophores. It is generally accepted that the former contributes to the fast time constant of the PR composite and the latter governs the slow time constant. Even though the limiting time factor for reaching the steady state in the PR polymers is the slow time constant, diffraction efficiencies smaller than the steady state diffraction value are sufficient for most practical dynamic holographic applications. As a result, sensitizers play an important role in improving the temporal dynamics of hologram creation. It was found that by the use of proper sensitizers, for example buckminster fullerene (C_{60}) and tetranitroflurone (TNF), the writing dynamics of PR polymers were substantially improved¹⁶¹⁻¹⁶². In this chapter, the use of unexplored nanomaterials as PR sensitizer will be investigated with an aim to improve the speed of the PR polymer.

4.2 Theoretical background

4.2.1 Photorefractive polymer composites

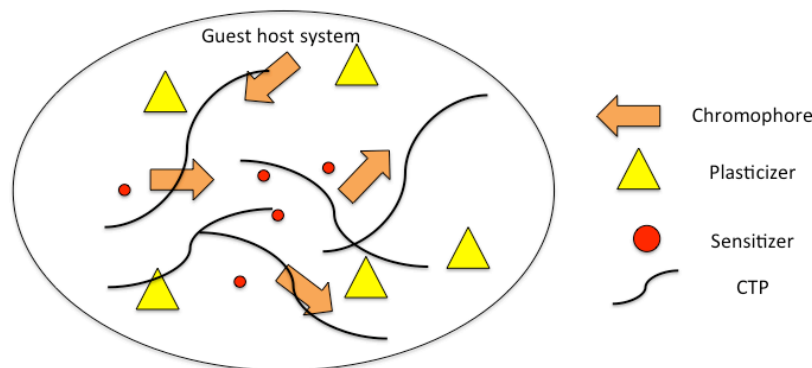


Figure 4.1 Schematic illustration of a guest host system.

PR effect can be observed in materials, which exhibit second order optical nonlinearity and charge redistribution upon light irradiation. However, unlike in crystalline inorganic PR materials where the size is limited and their second order nonlinearity is relative small, amorphous organic PR materials have attracted significant attention due to its low cost, high second order effect, ease in processibility, design flexibility and wide range of properties which can be achieved by concocting different polymers. However, one drawback of the organic PR materials is that they have low dielectric constant. This causes the redistribution of the charge to be highly electric field dependent. In practice, to have PR effect in the organic PR material, an external electric field is required to create space charge field modulation inside the material. In organic PR polymers, the properties required for PR effect to occur in organic PR polymer systems are provided by different molecules inside a composite, so called the “guest-host system” as illustrated in Figure 4.1. Those functions include photosensitivity, photoconductivity and electro-optic effect. Since these mechanisms are given by different molecules, they can be separately optimized. This is one of the advantages of the organic PR polymer system over the

inorganic crystals. In the organic PR polymer system, there are four main components i.e. charge transporting polymer (CTP), sensitizer (charge generator), plasticizer and chromophores. Sensitizer is responsible for generating charges by photo-absorption. These charges then drift with an applied field or diffuse inside the charge-transporting polymer. The non-uniform charge distribution is created because of the difference in electron and hole mobility. Trapping sites may be introduced to enhance the non-uniform charge distribution. By electro-optic effect and molecular reorientation of the chromophores, an index modulation is created from this non-uniform charge-distribution. Plasticizer is added to lower T_g , thereby assisting molecular reorientation and enhancing refractive index modulation. Each of these components is discussed in the following section.

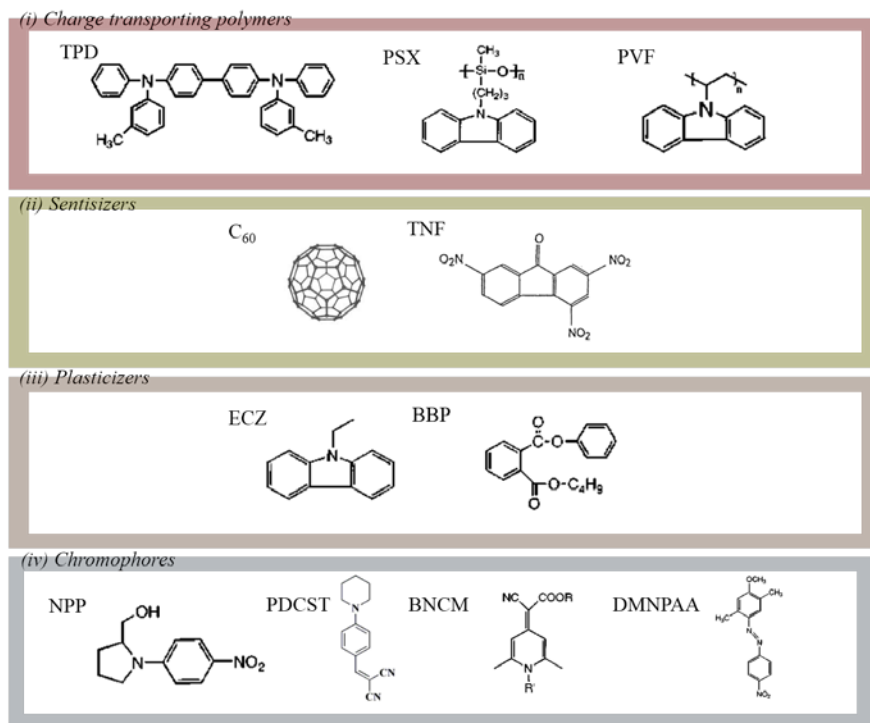


Figure 4.2 Chemical structures of common (i) charge transporting polymers, (ii) sensitizers, (iii) plasticizers, and (iv) chromophore

(i) Charge transporting polymer (CTP)

The charge-transporting polymer is an oxidizable host polymer that can transport charges. This transport process eventually leads to the nonlocal nature of the PR effect. In PR samples, holes are the majority charge carriers due to its higher mobility than electrons. The HOMO level is usually between -5.5 eV and -6.0 eV for common CTPs. It is desirable that CTPs are highly conjugated with delocalized π -electrons. They should also have appropriate energy level such that holes can be transferred from the sensitizer molecule. This means that the HOMO level of the CTP should be higher in energy (less negative) than that of the sensitizer for charge transfer to happen. Typical loading of the CTPs in the composite is at least 50% by weight to ensure that the charge transport occurs via hopping process. When CTPs are doped into an inert matrix at very low percentage, there is very limited electrical conduction. This is because CTPs are too far apart for the charge hopping to take place. The value at which this happens is usually in the range of 5–10 wt.% loading for common CTPs such as carbazole, diethylamino-benzaldehyde diphenylhydrazone (DEH), or terephthalic acid (TPA) derivatives. Above this loading value, charge transport can occur. The charge-carrier mobility increases with CTP concentration and saturates at the concentration somewhere below 100 wt.%¹⁶³

Commonly used transporting polymers are shown in 4.2 (d). Carbazole-containing polymers are the most studied CTPs. Poly(vinyl carbazole) (PVK) is the first high performing composite utilized for making PR devices with nearly 100% diffraction efficiency¹⁶². However, PVK systems have a high tendency to be phase separated because of the difference in the polarity of the component. Moreover, the response time of PVK system is rather slow.

Other CTPs have drawn considerable attention due to their high drift mobility and lower T_g . PR composites containing polymers with triarylamine side chain, such as poly(acrylic

tetraphenyldiaminobiphenyl) (PATPD), have shown high diffraction efficiency, comparable to the PVK based composite without exhibiting dependency on the illumination history¹⁶⁴⁻¹⁶⁵. Composite with poly(phenylene vinylene) derivative (poly[1,4-phenylene-1,2-di(4-benzyloxyphenyl)vinylene] (DBOP-PPV) with diphenyl phthalate (DPP) as a plasticizers, has better steady-state characteristics compared to PVK/ECZ systems¹⁶⁶. This observed better performance was attributed to (i) the reduction in polarity of the DBOP-PPV/DPP matrix, (ii) increased trap density, and (iii) improved degree of chromophore reorientation in DBOP-PPV/DPP system. While the charge transport in PVK/ECZ system is mainly from hopping, delocalized pi-conjugation play an important role in the DBOP-PPV system.

(ii) Charge generator

Generation of charges at the wavelength of interest in the PR composite is accomplished by using charges generators (also known as sensitizers). These charge generators are basically photosensitizers. They can form a charge transfer complex with the CTP, resulting in efficient charge transfer process. In the case of PR polymer composites with hole as primary conductors, photo-excited holes in the charge generator is transferred from the HOMO of the charge generator to the HOMO of the CTP. The charge generator accepts an electron from the HOMO of the CTP and becomes reduced. One of the important requirements in choosing a charge generator for a PR polymer composite is that the HOMO level of the charge generator has to be below that of the CTP. According to Marcus' theory, the larger difference between the ionization potential of the donor and acceptor results in better photogeneration efficiency. C₆₀ and TNF are the most commonly used sensitizer in the visible wavelength (4.2(a)). These molecules can often form a CT complex with donor molecules.

(iii) Plasticizer

In general, the T_g of the PR composites is much higher than room temperature. However, for high index modulation, it is imperative that the T_g of the composite is in the same range of the operating temperature. Such low T_g will result in efficient reorientation of the nonlinear chromophores. In order to lower the T_g of the PR composite, plasticizer is added to the composite. These plasticizers are typically inert with respect to charge generation and trapping. In PVK-based PR composite, Benzyl butyl phthalate (BBP) at a loading level of 10-15 wt.% is used as the plasticizer.¹⁶⁷⁻¹⁶⁸ The monomer, 9-ethyl carbazole (ECZ), has also been used¹⁶⁹.

(iv) *Chromophore*

The refractive index modulation in the PR effect is provided by chromophores interacting with the non-uniform space-charge field (SC-field). It is necessary that the chromophores possess orientational birefringence and/or the linear Pockels electro-optic properties for high refractive index modulation. Therefore, a large linear polarizability anisotropy (birefringence) and/or first hyperpolarizability (electro-optic) are desirable. In both cases, a large ground state dipole moment is required. R. Wortmann et al. has given an expression for quantifying the chromophore quality¹⁷⁰. Their figure of merit (FOM) represents the combined effect of linear birefringence and electro-optics:

$$FOM = \frac{1}{M} \left[9\mu\beta + \frac{2\mu^2\Delta\alpha}{k_B T} \right] \quad (4.1)$$

where M is the molecular weight, μ is the dipole moment, β is the first hyperpolarizability, $\Delta\alpha$ is the birefringence, and T is the temperature.

It was found that the contribution from the linear polarizability anisotropy through a process called “orientational enhancement” is higher than that from the first hyperpolarizability.¹⁷¹ For one dimensional chromophores consisting of a donor–acceptor

substituted π -electron system, greater than 75% of the contributions to the index modulation originates from the polarizability anisotropy term (birefringence contribution).¹⁷²

Optimizing the dipole moment of the chromophores is one of the important parameters in optimizing the chromophore properties. The dipole moment does not only affect the refractive index modulation, but also, the molecular aggregation, charge transport, and trapping in PR composite.

Strong donor-acceptor termination groups can be used to create electron separation across the π -conjugate bridge, thus a permanent dipole moment. In the presence of an applied electric field, delocalization along a π -conjugated bridge allows fast electronic redistribution. These molecules are called push-pull molecules. Tailoring the length of the bridge has an effect on the dipole moment of the chromophore. Too long bridge lengths may result in restricted orientational freedom. Even though, larger dipole moments can increase the figure of merit, phase instability becomes an issue when highly polar chromophores are incorporated into other non-polar molecules. As a result, an optimum chromophore density has to be determined. In addition, chromophores with high dipole moment can negatively affect the charge mobility of the PR composite due to the energetic disorder¹⁷³.

In addition, chromophores can also act as sensitizers¹⁷⁴ if their energy levels are appropriate at the operational wavelength. For this to be effective, the HOMO level of the chromophores must be lower than that of the CTP. At the same time, the chromophores can also act as hole traps if their HOMO level is higher than that of the CTP. Because of these reasons, the energy of the chromophore HOMO level relative to the HOMO of CTP is an important parameter. It not only affect chromophores performance but also the charge mobility and the photoconductivity of a PR polymer system.¹⁷⁵

As a result,, when choosing a chromophore, its effects on the index modulation, charge generation, transport, and trapping must be taken into account. Examples of high performing chromophores are dicyanostyrenes (DCST), azo-dye derivatives (DMNPAA), and oxypyridine dyes (ATOP). Chemical structures of some of the commonly used chromophores are shown in 4.2(c).

4.2.2 Fundamental of photorefractive effect

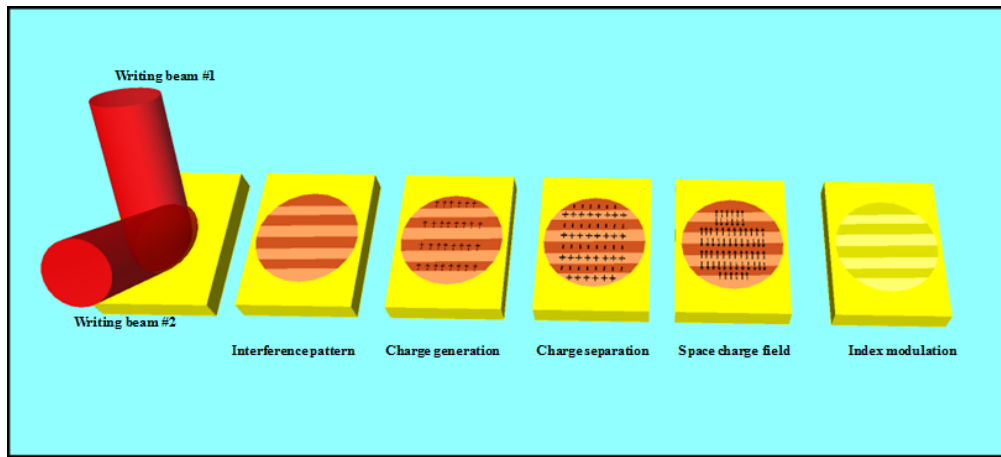


Figure 4.3 schematic illustration of the processes involved in the formation of refractive index modulation.

The photorefractive (PR) effect is a spatial modulation of the index of refraction generated by light induced charge redistribution in a material. This effect occurs when charge carriers are generated by spatially modulated light intensity usually formed by the interference of two coherent beams. For the case of plane wave, two beam interference results in intensity modulation given by:

$$I(x) = I_0(1 + m \cos(2\pi / \Lambda)) \quad (4.2)$$

where $I_0=I_1+I_2$ is the total incident intensity, $m=2(I_1I_2)^{1/2}/(I_1+I_2)$ is the fringe visibility, and Λ is the spatial wavelength (grating spacing). In a tilted transmission geometry, the spatial wavelength is:

$$\Lambda = \frac{\lambda}{2n \sin((\alpha_2 - \alpha_1)/2)} \quad (4.3)$$

where n is refractive index of the material; λ the optical wavelength in vacuum; and α_1 and α_2 are the incident internal angles of the two writing beams with respect to the sample normal. For the visible wavelength, the spatial wavelength can vary from sub-microns to a few tens of microns depending on the writing angles and wavelength.

The generated charge is then separated by drift or diffusion processes and become trapped, creating non-uniform space-charge distribution. The resulting internal electric field then modulates the refractive index by an electro-optic effect, creating an index grating inside the material. The generated grating has a phase shift with respect to the modulated light intensity. This phase shift is a distinctive characteristic of the PR effect. The process is summarized in Figure 4.3. There are four main processes that lead to the index modulation, namely 1) photogeneration of charges, 2) charge transport, 3) charge trapping and formation of SC-field and 4) index modulation in response to the SC- field.

(i) Photogeneration of charge

After having the intensity modulation in the sample, the PR process starts with absorption of photon in the bright regions. Upon absorption, electrons are excited from the highest occupied molecular orbital (HOMO) to the lowest unoccupied molecular orbital (LUMO) of the sensitizer. This absorption occurs in the molecules with proper band gap to the incident photon frequency. The sensitizer is a strong electron acceptor, and forms a charge-transfer (CT) complex with an

electron donor molecule, typically the CTP. When an electron is excited to the LUMO level of the sensitizer, the opposite charge carrier or hole is left in the HOMO level. Through the charge transfer complex, electron is transferred from the HOMO of the sensitizer to the HOMO of the CTP, resulting in a sensitizer anion.

Two critical processes during the SC-field formation are generation and separation of charges. The quantum efficiency, defined as the ratio of the number of generated electron hole pairs to the number of absorbed photons, is used to characterize the effectiveness of charge generation process. Using more sensitizers can result in larger number of generated charges. However, higher density of sensitizers will cause larger absorption, which has detrimental effect to the diffraction performance of the PR composite. Charge separation depends highly on the relative position of the HOMO and LUMO level of the donor and the acceptor. For the case of the sensitizer being an acceptor, the HOMO level of the sensitizer should be lower than the HOMO level of the donor (CTP in this case) so that the electron can be efficiently transferred from the donor to the acceptor. The LUMO of the sensitizer, on the other hand, has to be lower than that of the donor in order to facilitate the exciton dissociation. In the organic PR materials, due to the low dielectric constant of the composite, the Coulomb attraction between electron hole pair is relatively high. In order to facilitate charge separation, electric field is usually applied.

The Onsager model¹⁷⁶⁻¹⁷⁷ can be used to describe the thermal and electrical dependence of the photogeneration efficiency in some organic photoconductors. In this model, it is assumed that the formation of an electron-hole pair is followed by the formation of an intermediate charge-transfer state in which the electron and the hole are separated by an average distance of r_0 . The charge dissociation can happen with a given probability when the separation is equal to or higher than the Coulomb radius given by:

$$r_c = e^2 / 4\pi\epsilon_0 \epsilon k_B T \quad (4.4)$$

where ϵ is the relative permittivity, e is the elementary charge constant, k_B is the Boltzman constant and T is the absolute temperature. The photogeneration efficiency can be expressed as:

$$\phi(E) = \phi_0 (1 - \zeta^{-1} \sum_{n=0}^{\infty} A_n(\kappa) A_n(\zeta)) \quad (4.5)$$

with

$$\phi(E) = \phi_0 (1 - \zeta^{-1} \sum_{n=0}^{\infty} A_n(\kappa) A_n(\zeta)) \quad (4.6)$$

where $A_0(x) = 1 - \exp(-x)$, $\zeta = eEr_0/k_B T$, and $\kappa = r_c/r_0$. E is the applied electric field and ϕ_0 is the quantum efficiency. From this model, it can be seen that as the applied electric field increases the photo generation efficiency also increases. In the limiting case where E approaches infinity, the photo generation efficiency approaches the intrinsic quantum efficiency of the material.

In addition, the intermolecular interaction between the donor and the acceptor can lead to a new absorption band that does not appear in the spectrum of either component. This absorption band is called charge transfer (CT) complex band. For example the interaction between poly(*N*-vinylcarbazole) (PVK) polymer and (2,4,7-trinitro-9-fluorenylidene) malononitrile (TNFM) molecule creates CT band absorption with a tail up to 900nm. ¹⁷⁸(2,4,7- trinitrofluoren-9-ylidene)malononitrile (TNFDM) can form CT complex with PVK , resulting in a redshift in the absorption compared to the individual molecules.¹⁷⁹

(ii) Charge transport

Charge transport in PR composites, which is an amorphous polymeric system, is different from the mechanism governing the transport in crystalline materials. Periodic crystals have well-defined energy levels and the charges are transported in the valence and conduction bands.

When defects are present, hopping (the process in which a localized charge tunnels between defects when the wavefunctions overlap) can take place¹⁸⁰. In amorphous polymer, charge transport occurs successively from one polymer moiety to another. For the case of hole transport, when the electronic wavefunction of the neighboring neutral site of the donor overlaps with the wavefunction of the charged site, charge transport can take place. These transporting molecules are usually conjugated polymers with alternating π bonds that allow delocalization of the electronic wavefunctions. In this manner, the hole is transferred from one site to another, or from one molecule to another, in a similar manner to the hopping process between defects.¹⁸¹ Every transport event between two molecules must be considered as a discrete event. Similar to the valence and conduction bands in crystals, in organic materials, electron transport occurs within the LUMO levels, whereas hole transport takes place in the HOMO levels. One of the important parameters that have a significant influence on the PR performance is the mobility of the generated charges. Several parameters can affect the charge mobility within the PR composites. For example, the energetic disorder resulting from dipole-dipole interaction between the host and the dopants can decrease the charge mobility^{173, 182}. Larger concentration of the charge transport moiety results in better charge mobility. Dopants have effects on the charge transport and cause either increase or decrease in the charge mobility, depending on the energy level. Therefore, engineering and selecting the ionization potential (HOMO/LUMO level) of the components of PR samples are very important in improving the PR performance. Higher charge mobility / transport usually results in faster PR performance.

(iii) Charge trapping and development of SC-field

Charge trapping

Trapping sites are the regions where the transporting charges are trapped from participating in the transport process. The trapping mechanism is mainly determined by the energy levels of the traps relative to that of the charge transport polymer. Traps can be intentionally added molecules, intrinsic defects, or ionized acceptors. Depending on the trapping/de-trapping rates and the energy level of the trap, they can be categorized as either shallow or deep traps. The process of trapping is a dynamic process in which the charges are trapped and de-trapped. The rate, at which these processes occur, and the density of the trap will determine the rate of the SC-field formation and the magnitude of the SC-field.

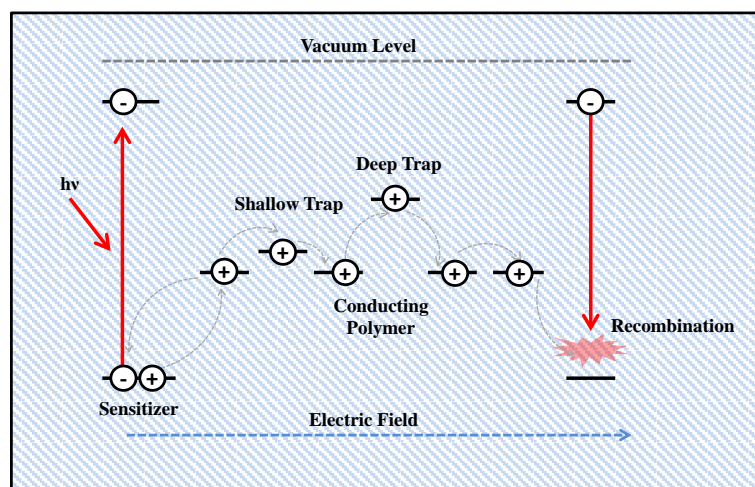


Figure 4.4 Schematic representation of charge transfer in PR polymer composites. The HOMO and LUMO levels are not drawn to scale.

Low trap densities will yield a small steady-state SC field magnitude, but result in large mobility.

High trap densities, on the other hand, will reduce the speed of the SC-field formation since longer time is required establish the SC field. However, for large trap densities, the steady state

SC-field magnitude may be larger than for smaller trap densities. In PR composites, it is not trivial to independently engineer the trap mechanism because trappings may come from different components such as the sensitizers, the chromophores, or the transport molecules.

SC-field formation

The space charge in PR composite is formed as a result of non-uniform distribution of positive and negative charges induced by interference fringes. The process of forming SC-field involves charge generation, diffusion, drift, trapping, and recombination. In the beginning of the development of the theoretical foundations of holographic storage problem in electro-optic crystal, the charge transport equation was solved to determine diffraction efficiency of the holographic media¹⁸³⁻¹⁸⁴. In this treatment, neither the influence of building space charge field nor the self-diffraction effect was taken into account. However, it was shown that, in this approximation, the diffraction efficiency was independent of the writing intensity in the case of diffusion process and it increased as an inverse square of the fringe spacing. The holographic grating was shifted by a quarter of a period from the fringe pattern. On the other hand, for the drift process, such shift did not occur according to this prediction. Later, it was shown that for the drift process the shift could be observed if the carrier transport range was comparable or larger than the fringe spacing. Kukhtarev and coworkers developed a theory of saturated holograms in electro-optic crystal¹⁸⁵. Regarding their theoretical treatment of the SC-field formation, a set of material equations based on the photoionization, thermal generation, recombination and carrier concentration was used. From their calculation, it is found that the $\pi/2$ phase shift of the holographic grating can occur when the fringe spacing is small enough and/or when the electric field is large enough. In the case of constant applied voltage, the phase shift is a function of both applied field and material parameters.

Schildkraut et al. ¹⁸⁶⁻¹⁸⁷ included the effect of traps and their dependency on the charge mobility and electric field in their model to describe space-charge field in amorphous organic solids. Unlike inorganic systems, hole transport is supported by organic systems. Holes are generated by photoexcitation of sensitizers. In polymer PR composite, excited electrons are assumed not to participate in charge transport due too small loading of the sensitizer to form charge transport manifold. Only holes are conducted through the transport manifold of CTPs. Charged sensitizer moieties can serve as recombination centers for mobile holes. In Schildkraut's model, an additional trap level is introduced. Through the use of zero and first order approximations, they derived analytical expression for SC-field for the case of deep trap and the case no traps in steady state. The first order approximation of the SC-field in the case of deep trap is of the form:

$$E_{sc} = A \frac{mE_q (iE_D - E_0)}{B_1 + iB_2} \quad (4.7)$$

with

$$A = \frac{sI_0 (N_i - T_i - \rho_0)}{\mu_0 \rho_0 (T_i + \rho_0)} \quad (4.8)$$

$$B_1 = E_D + (1 + \eta)E_q + (1 + E_m / E_0)E_t \quad (4.9)$$

$$B_2 = E_0 + \frac{E_D E_q}{E_0} (E_m / E_0 - \eta) \quad (4.10)$$

$$E_D = \xi K \quad (4.11)$$

$$E_q = \frac{\mu_0 \rho_0 (T_i + \rho_0)}{K (sI_0 + \mu_0 \rho_0)} \quad (4.12)$$

$$E_i = \rho_0 / K \quad (4.13)$$

$$E_m = \frac{1}{2} C E_0^{3/2} \quad (4.14)$$

$$\eta = A p E^p / \phi_0 \quad (4.15)$$

$$\xi = k_B T / e E_0 L \quad (4.16)$$

$$s = g \phi_0 / N_i \quad (4.17)$$

where E_0 is the projected applied field along grating vector K , C is a constant relating mobility to the electric field, μ_0 is the charge mobility, ρ_0 is the hole density, I_0 is the illumination intensity, T is the initial trap density, N_i is the initial acceptor density, ϕ_0 is the field dependent quantum efficiency, and g is the generation of hole per unit time at the initial acceptor concentration (N_i). In the case of no trap, the initial trap density T_i becomes 0 and the constant A is reduced to 1 (also assuming low light intensity).

While Schildkraut's approximation only describes the steady state value of SC-field, a later model developed by Ostroverkhova contains transient information¹⁸⁸. In addition to the Schildkraut's model, Ostroverkhova et al. introduced two trap levels. These two trap levels can be emptied thermally. Fourier decomposition was used to find the solution. Numerical calculation has to be used in order to solve for the solution.

It is good to note that all of these models require significant knowledge of the material to yield results applicable to real experiments. They are semi-quantitatively useful in understanding the SC-field formation. However, there is much physics left unaddressed. For example, the role of chromophore orientation in trapping and charge transport is ignored. The material is assumed

to be infinite with ideal ohmic contacts. The dynamic change in the beam condition once the grating is formed is neglected.

(iv) Creating of index modulation in response to the SC- field

The final step in the PR process is to form phase grating induced by the SC- field. In inorganic PR crystals, the mechanism responsible for a refractive index modulation is the linear electro-optics effect or Pockels effect. The index modulation is given by¹⁶³:

$$\Delta n = -\frac{n^3}{2} r_{eff} |E_{sc}| \quad (4.18)$$

where r_{eff} is the effective electro-optic coefficient and n is the refractive index of the crystal.

On the contrary, in amorphous organic PR materials, linear birefringence, Pockels effect , and Kerr effect are involved¹⁸⁹. For the first reported organic PR polymer, the presence of the PR effect was mainly due to the linear EO effect resulted from poling the polymer¹⁵⁷. This linear effect arises from the second-order susceptibility. In order to introduce the EO effect into materials, noncentrosymmetric dipolar compounds (chromophores) are incorporated in the PR composites. In order to achieve macroscopic anisotropy, an external electric field is required to pole the chromophores. The oriented gas model can be used to theoretically calculate the polarization properties of a bulk material based upon an ensemble of molecules with a distribution of orientations and their own molecular polarization¹⁹⁰. For a uniaxial anisotropic molecule with a permanent dipole moment μ lying along the optic axis, the linear polarizabilities in the principal axes are:

$$\alpha_{11}(\omega) = \alpha_{22}(\omega) = \alpha_{\perp}(\omega) \text{ and } \alpha_{33}(\omega) = \alpha_{\parallel}(\omega) \quad (4.19)$$

The induced molecular polarization is given by:

$$P_i^\omega = \alpha_{ii}^\omega E_i^\omega \quad (4.20)$$

The macroscopic polarization (dipole moment per unit volume) induced by an external optical field along the z-direction can be calculated by the linear summation of polarizations:

$$\begin{aligned} P_z^\omega &= 4\pi N \int [P_3^\omega \cos(3,z) + P_1^\omega \cos(1,z) + P_2^\omega \cos(2,z)] f(\Omega) d\Omega \\ &= 4\pi \{N \int [\alpha_\perp^\omega + (\alpha_\parallel^\omega - \alpha_\perp^\omega) \cos^2(3,z)] f_0(\Omega) d\Omega\} E_z^\omega \\ &= \chi_{zz}^{(1)} E_z^\omega \end{aligned} \quad (4.21)$$

where the cosine terms are the projection cosine and $f_0(\Omega)$ is an angular distribution function.

Through electromagnetic relations:

$$D = \epsilon_0 E + P \quad P = \epsilon_0 \chi^{(1)} E \quad n_{ii}^2 = (1 + \chi_{ii}^{(1)}) \quad (4.22)$$

the microscopic refractive indices along different axes can be calculated. When an electric field is applied, the molecules are poled and this changes the angular distribution function $f_0(\Omega)$ to a particular anisotropic function $f(\Omega)$. As a result, the refractive indices are changed. For example, for the light polarized along the z-axis, the change in the refractive index is given by:

$$\Delta[n_z^2(\omega)] = 4\pi N (\alpha_\parallel^\omega - \alpha_\perp^\omega) \left\{ \int \cos^2(3,z) f(\Omega) d\Omega - \int \cos^2(3,z) f_0(\Omega) d\Omega \right\} \quad (4.23)$$

If we assume isotropic distribution of molecules before applying the electric field, the above expression is reduced to:

$$\Delta[n_z^2(\omega)] = 4\pi N (\alpha_\parallel^\omega - \alpha_\perp^\omega) \left\{ \langle \cos^2 \theta_z \rangle - \frac{1}{3} \right\} \quad (4.24)$$

Similarly, for the light polarized along the x-direction:

$$\Delta[n_x^2(\omega)] = 4\pi N (\alpha_\parallel^\omega - \alpha_\perp^\omega) \left\{ \langle \cos^2 \theta_x \rangle - \frac{1}{3} \right\} = -\frac{1}{2} 4\pi N (\alpha_\parallel^\omega - \alpha_\perp^\omega) \left\{ \langle \cos^2 \theta_z \rangle - \frac{1}{3} \right\} \quad (4.25)$$

From these relations, it can be seen that the index change parallel to the poling field is 2 times larger than the one perpendicular to the field. For the spatial case of high temperature, the distribution function can be assumed to follow Maxwell-Boltzman distribution:

$$f(\Omega) \propto \exp\left(-\frac{U}{kT}\right) \quad (4.26)$$

where the interaction dipole energy of the polarizable dipole with poling electric field E_p in the z-direction is given by:

$$U(\theta) = -\mu \cdot E_p - \frac{1}{2} p \cdot E_p \quad (4.27)$$

For the case where the interaction of the permanent dipole is stronger than the induced dipole, the distribution function becomes:

$$f(\Omega) \propto \exp\left(-\frac{\mu E_p \cos \theta}{kT}\right) \quad (4.28)$$

By using this distribution function in Equation (4.23), expressions for refractive index changes can be realized. These expressions represent the dependence of the change in the index of refraction on the molecular linear polarizability and a uniform poling field along a particular laboratory axis. It is applicable to the steady state case. As mentioned earlier, in most of the organic PR polymers, linear birefringence, Pockels effect, and Kerr effect are involved. By extending this model by taking into account the higher order susceptibilities, similar formulations can be obtained with higher order contributions¹⁹¹. However, since in the PR polymer materials, the birefringence is the most dominant contribution, this development with only the first order linear susceptibility is still a good approximation. Binks et al. further developed this oriented gas model by taking in to account the time dependent rotational orientation¹⁹². Detailed formulations can be found in their report.

The followings summarize the steady state first-order and second-order changes in refractive index derived from the oriented gas model, assuming that the change in refractive index is small when compared to the index of the material ¹⁶³ .

$$\Delta n_z^{(1)}(\omega) = \frac{2B}{n} \quad (4.29)$$

$$\Delta n_{x,y}^{(1)}(\omega) = -\frac{1}{2} \Delta n_z^{(1)}(\omega) \quad (4.30)$$

$$\Delta n_z^{(2)}(\omega) = \frac{3C}{2n} \quad (4.31)$$

$$\Delta n_{x,y}^{(2)}(\omega) = -\frac{1}{3} \Delta n_z^{(2)}(\omega) \quad (4.32)$$

with

$$B = \frac{2NF_\infty}{45} \Delta\alpha u^2 \quad (4.33)$$

and

$$C = \frac{NF_\infty^2 F_0}{15} \beta u \quad (4.34)$$

where $\Delta\alpha$ is the linear birefringence, β is the first hyperpolarizability, u is the interaction energy given by $u = \mu \cdot E / k_B T$ and F_0 and F_∞ are the field correction factors taking into account the polymer matrix contribution, given by:

$$F_0 = \varepsilon_{static} (\varepsilon_{optic} + 2) / (2\varepsilon_{static} + \varepsilon_{optic}) \quad (4.35)$$

$$F_\infty = (\varepsilon_{optic} + 2) / 3 \quad (4.36)$$

where ϵ_{static} is the static dielectric constant and ϵ_{optic} is the dielectric constant at the operational wavelength. Note that the total refractive index change is $\Delta n = \Delta n^{(1)} + \Delta n^{(2)}$.

Later, in 1993, Moerner et al.¹⁷¹ published a paper showing that the performance of recent PR polymers is too high to explain by the electro-optics effect alone, even if it is assumed that the SC-field approaches that of the applied electric field. They proposed a mechanism called orientational enhancement, which is responsible for the enhancement of properties in organic PR sample. According to their model, the total internal electric field inside the polymer is given by:

$$E_T(\mathbf{r}) = [E_{sc}(\mathbf{r}) \sin \theta_G] \hat{x} + [E_{ext} + E_{sc}(\mathbf{r}) \cos \theta_G] \hat{z} \quad (4.37)$$

where $E_{sc}(\mathbf{r}) = E_{sc} \exp(iK_G \cdot \mathbf{r})$ is the modulating SC-field with wave number K_G and in the r direction. The total susceptibility change is the sum of the contribution from birefringence and electro optic effect and is given by:

$$\Delta\chi = \begin{bmatrix} A & 0 & 0 \\ 0 & A & 0 \\ 0 & 0 & C \end{bmatrix} E_T^2 \quad (4.38)$$

with

$$C = C_{BR} + C_{EO} = \frac{2NF_\infty}{45} \Delta\alpha \left(\frac{\mu}{k_B T} \right)^2 + \frac{NF_\infty^2 F_0}{15} \beta \frac{\mu}{k_B T} \quad (4.39)$$

and

$$A = A_{BR} + A_{EO} = \left(-\frac{1}{2}\right)C_{BR} + \left(\frac{1}{3}\right)C_{EO} \quad (4.40)$$

The susceptibility matrix can be transformed to the experimental geometry using the transformation $\Delta\chi_{lab} = U^T \Delta\chi U$, where U is the rotation matrix for the tilt configuration the diffraction efficiency of the sample with thickness d can then be calculated using:

$$\eta = \left| H(\hat{e}_4^* \cdot \hat{e}_3)(\hat{e}_4^* \cdot \Delta\chi_{lab} \cdot \hat{e}_3) \right| \quad (4.41)$$

where $H = (\pi d) / (2n\lambda_0(\cos\theta_1\cos\theta_2)^{1/2})$, with θ_1 and θ_2 being the angles of the writing beams with respect to the sample normal. \hat{e}_4 and \hat{e}_3 is the polarization vector of the reading and writing beams respectively.

Even though the PR process seems like a step-by-step process, in reality, all the mechanisms mentioned occur simultaneously and are dynamically coupled in many ways. Nevertheless, the explanation portrayed here is very useful for understanding the mechanisms and applicable in the case of the steady state. Next the theory of the holographic grating is discussed.

4.2.3 Theory of holographic grating

Up to this point, the mechanisms involved in the formation of phase grating have been discussed. In this section, fascinating phenomena resulted from the interaction of light with the grating are presented.

(i) Bragg vs. Raman-Nath diffraction grating

Holographic grating can be either thick or thin, and amplitude or phase; the recorded combination depends on the material. Amplitude holograms have the grating in the form of an amplitude or absorption coefficient modulation. Phase holograms have the grating formed by an optical path length or refractive index modulation. A grating is characterized into either Bragg (Thick) grating or Raman Nath (Thin) grating, depending on their interaction with light. Bragg grating only diffracts light into a single first order whereas multiple orders exist in the Raman-Nath grating. Kogelnik studied diffraction of light from a thick grating, using coupled wave

theory¹⁹³. In his formulation, he separated thin and thick regimes using a quality factor defined by:

$$Q = 2\pi\lambda d / n\Lambda^2 \quad (4.42)$$

where λ is the vacuum wavelength, d is the thickness of the film, n is the refractive index and Λ is the grating spacing. The grating can be categorized as thick grating when $Q \gg 10$ and thin when $Q < 10$. For the development of PR polymer composite, theory of thick hologram is usually used for simplification. The performance is characterized in terms of device perspectives. More rigorous analysis of coupled wave theory that applies to both thick and thin holographic grating and gives more accurate results can be found in the paper by Moharam and Gaylord¹⁹⁴. In the following sections the theories of light diffraction from thick holographic PR materials for transmission and reflection geometries are discussed.

(ii) Diffraction in transmission geometry

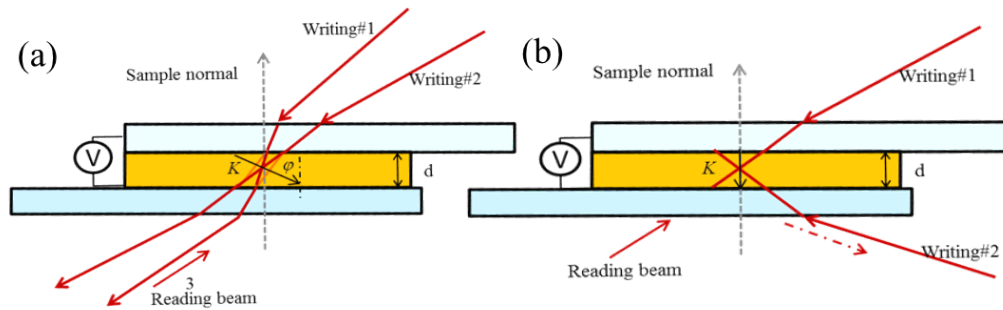


Figure 4.5 Schematic diagrams of (a) transmission geometry (b) reflection geometry

Transmission geometry is defined as a situation in which both of the writing beams are incident on one side of the sample, Figure 4.5(a). Typically, the PR composite is sandwiched between two transparent electrodes. An external electric field is applied perpendicular to the sample normal. The sample is tilted so that the applied field has a component along the grating

vector, which will assist the carrier drift. In this geometry, the grating spacing resulted from interfering two writing beams is given by:

$$\Lambda = \frac{\lambda}{2n \sin[(\alpha_1 - \alpha_2)]} \quad (4.43)$$

The slant angle of the grating inside of the material is given by:

$$\varphi = \frac{\pi}{2} - \frac{(\alpha_1 + \alpha_2)}{2} \quad (4.44)$$

The diffraction efficiency can then be calculated from the thick grating theory by Kogelnik. The signal amplitude of phase grating in transmission geometry is given by:

$$S = -j \left(\frac{c_R}{c_s} \right)^{1/2} e^{-\alpha d / c_R} e^{\xi} \frac{\sin^2 \sqrt{\nu^2 - \xi^2}}{(1 - \frac{\xi^2}{\nu^2})} \quad (4.45)$$

with

$$\nu = \frac{\kappa d}{\sqrt{c_R c_s}} \quad \text{and} \quad \xi = \frac{1}{2} d \left(\frac{\alpha}{c_R} - \frac{\alpha}{c_s} - j \frac{\nu}{c_s} \right) \quad (4.46)$$

where $\kappa = \pi \Delta n / \lambda$; $\nu = \Delta \theta K \sin(\varphi - \theta) - \Delta \lambda K^2 / 4\pi n$ with $K = \frac{2\pi}{\Lambda}$; $c_R = \cos \theta$; and

$c_s = \cos \theta - \frac{K\lambda}{2\pi n} \cos \varphi$. α is the absorption loss of the sample. θ is the angle of the reading beam

with respect to the sample normal. $\Delta \theta$ and $\Delta \lambda$ are the deviations in the reading angle and wavelength respectively. The diffraction efficiency is then given by:

$$\eta = \frac{|c_s|}{c_R} S S^* \quad (4.47)$$

For the PR material, in most of the cases, the wavelength of investigation is generated from a monochromatic light source. If we assume that $\Delta\lambda \approx 0$ and consider a special case where there is no absorption loss, the diffraction efficiency becomes:

$$\eta = \frac{\sin^2 \sqrt{\nu^2 + \xi'^2}}{\left(1 + \frac{\xi'^2}{\nu^2}\right)} \quad \text{where} \quad \xi' = \left(\frac{d}{2c_s}\right) (\Delta\theta K \sin(\phi - \theta) - \Delta\lambda K^2 / 4\pi n) \quad (4.48)$$

(iii) Diffraction in reflection geometry

The advantage of the reflection geometry is that the applied field can be in the same direction as the grating. This results in larger SC-field when compared to the transmission geometry. In the reflection geometry, Figure 4.5(b), the grating spacing and the slant angle are:

$$\Lambda = \frac{\lambda}{2n \sin[(\pi - (\alpha_1 + \alpha_2)) / 2]} \quad (4.49)$$

$$\varphi = \frac{(\alpha_1 - \alpha_2)}{2} \quad (4.50)$$

For the special case of loss-less grating, the diffraction efficiency of the reflection geometry is given by:

$$\eta_R = \frac{1}{1 + \left(\left(1 - \frac{\xi'^2}{\nu'^2}\right) / \sinh^2 \sqrt{\nu'^2 + \xi'^2}\right)} \quad \text{where} \quad \nu' = \frac{i\pi\Delta nd}{\lambda\sqrt{c_s c_R}} \quad (4.51)$$

Since the angles of incident of the writing beam in the reflection geometry is larger than those of the transmission geometry, the grating spacing for the reflection case is smaller. This results in much larger Q factor of the grating.

(iv) Two beam coupling phenomenon

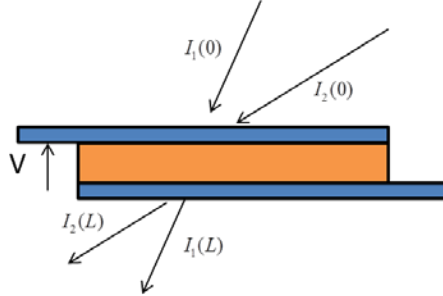


Figure 4.6 Schematic diagram of the two beam coupling process.

Due to the phase shift of the grating with respect to the interference pattern of two interfering beams, there exists a nonreciprocal steady state transfer of energy between the beams. By using slowly-varying envelope approximation and solving wave equations, the steady state intensities of the two interfering beams can be determined¹⁹⁵:

$$I_1(z) = I_1(0) \frac{1 + m^{-1}}{1 + m^{-1} \exp(\Gamma z)} e^{-\alpha z} \quad (4.52)$$

$$I_2(z) = I_2(0) \frac{1 + m^{-1}}{1 + m^{-1} \exp(\Gamma z)} e^{-\alpha z} \quad (4.53)$$

where $m = I_1(0)/I_2(0)$ is the ratio between the input energies, and Γ is the gain coefficient, given by:

$$\Gamma = \frac{2\pi\Delta n}{\lambda \cos(\theta/2)} \sin \Theta \quad (4.54)$$

where θ is the angle between the two beams inside the medium, and Θ is the phase shift of the grating which has a maximum of $\pi/2$. When $\Gamma > 0$, beam #2 gains energy. The geometry for two-beam coupling is illustrated in Figure 4.6.

4.3 Experimental characterizations of PR polymer

4.3.1 Four wave mixing measurement

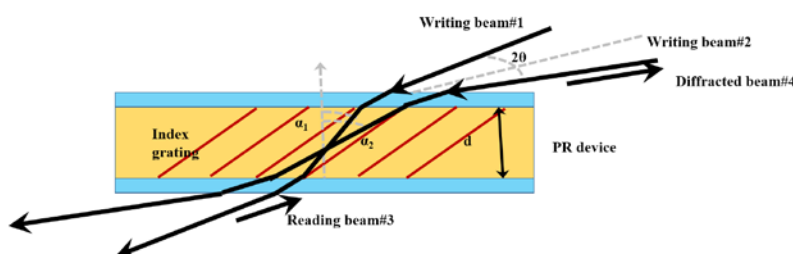


Figure 4.7 Geometrical representation of the FWM measurement

The four wave mixing measurement is used to probe the quality and the dynamic of grating formation. The geometry of four wave mixing (FWM) measurement is shown in Figure 4.7. In this experiment, the index grating by the PR effect is induced inside the material by interference of two writing beams i.e. beam#1 and beam#2. The writing beam intensity is in the range of 30-1000 mW/cm^2 . Voltage is applied across the sample to create electric field that assists charge drifting inside the sample. The quality of the index grating is then measured on the basis of diffraction of the reading beam; beam#3. The intensity of the reading beam is usually ~1-5% of the writing beam. If the same wavelength is used for reading and writing, the measurement is called degenerate four wave mixing (DFWM). If the wavelength of the reading beam is different from that of the writing beams, the measurement is called non-degenerate four wave mixing (NFWM). The NFWM is advantageous due to the absence of cross talk between reading and writing beams. Ideally, one would want the grating wave vector K_G to be in the same direction as the applied field. However, it is geometrically unrealizable because the sample is usually sandwiched between ITO electrodes; on the top and bottom. Therefore, in practice, the sample is tilted at an oblique angle so that there is no zero component of an applied external field

along the grating vector. Thus, index modulation can be created which will be seen as index grating by beam#3. The writing beams are often s-polarized to reduce unwanted effects, for example beam fanning and self-diffraction. On the contrary, the reading beam is p-polarized to increase the effective index modulation seen by the beam. The schematic of the setup is shown in Figure 4.8.

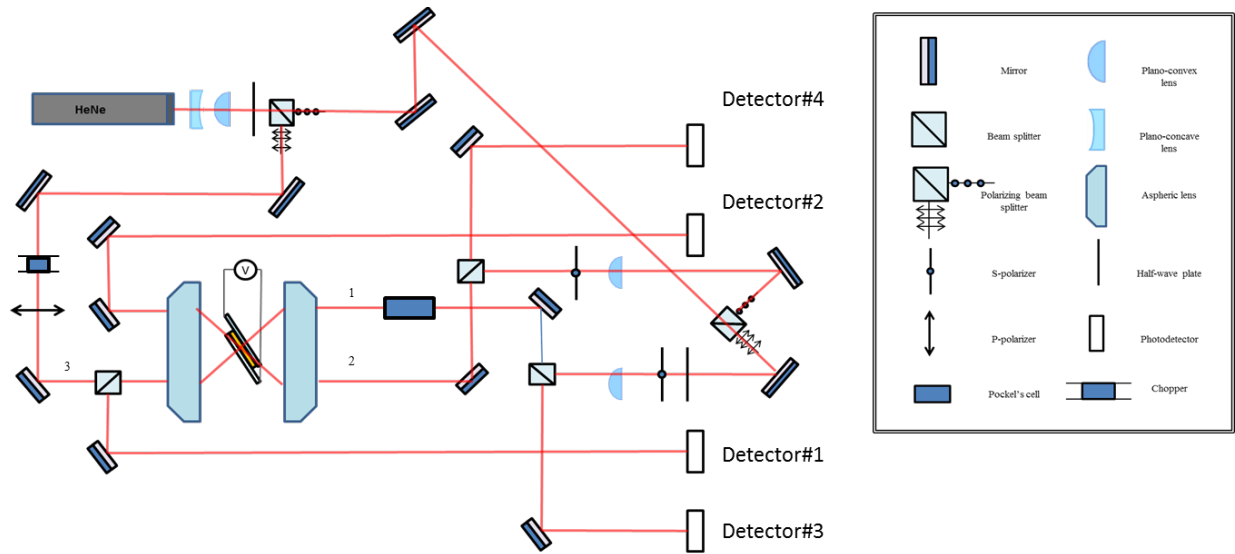


Figure 4.8 Schematic diagram of the optical setup for characterizing PR polymers.

In this setup, first, the laser beam is divided into two beams using a polarizing beam splitter (PBS). The p-polarized beam is used as a reading beam. The s-polarized beam is split further to form two s-polarized writing beams through the use of PBS, polarizers, and half wave plate. The intensities of the three beams are adjusted by using combinations of half-wave plates, polarizers and neutral density filters. Plano convex lens are used to adjust the beam sizes. Large aspheric lens in confocal geometry are used to focus the beams where the sample is mounted. With combination of translating stages, this lens system allows changing the writing and reading beam angles with simplicity and without affecting the location of the sample. The transmitted and diffracted beams pass through non-polarizing beam splitters (NPBS). Their intensities can be

monitored by using high-speed photodetectors, which are connected to a data acquisition (DAQ) unit.

(i) Steady state FWM experiment

Steady-state-four-wave mixing is the standard method for characterizing the PR performance. In this experiment, the steady state diffraction efficiency is monitored as a function of applied voltage. The internal diffraction efficiency can be calculated by:

$$\eta_{\text{int}} = \frac{I_d(V)}{I_d(V) + I_t(V)} \quad (4.55)$$

where $I_d(V)$ and $I_t(V)$ are the diffracted and transmitted intensity as a function of voltage V respectively. If losses (absorption, scattering, and reflection) are taken into account, one can calculate the external diffraction efficiency by:

$$\eta_{\text{ext}} = \frac{I_d(V)}{I_{\text{inc}}} \quad (4.56)$$

where I_{inc} is the intensity of the reading beam incident on the sample. Typical data obtained from steady state FWM is shown in Figure 4.9.

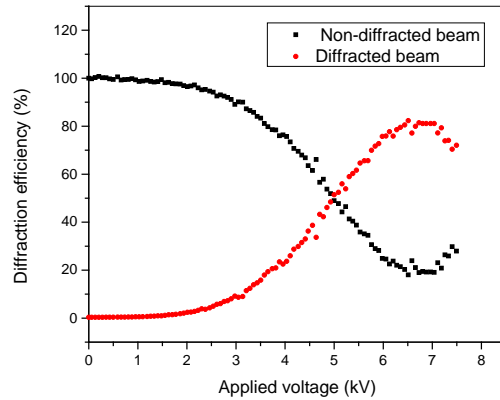


Figure 4.9 Steady state diffraction efficiency vs. applied voltage of PATPD/7-DCST/ECZ/PCBM fabricated in our laboratory. It has internal diffraction efficiency as high as 85% at applied voltage of 6.5kV. The sample thickness is 105 μm .

(ii) *Transient FWM experiment*

Transient FWM measurements monitor the grating formation dynamic at a constant applied voltage. In this experiment, the photorefractive process is initiated by turning on the writing beams using either a mechanical shutter or an optical shutter (Pockels cell). The temporal evolution of the diffraction is measured with a DAQ unit. Typical data obtained from transient FWM measurement are shown in Figure 4.10.

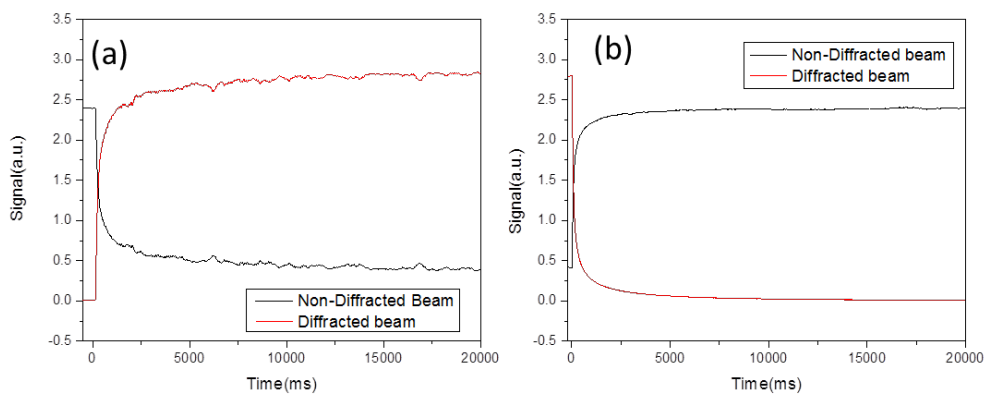


Figure 4.10 (a) transient grating recording and (b) transient grating decaying of PATPD/7-DCST/ECZ/PCBM (our sample).

To analyze this data, Bragg-equation with temporal dependent index modulation can be used:

$$\eta \propto \sin^2[B\Delta n(t)] \quad (4.57)$$

where B is a constant. It can be seen that the speed of the PR diffraction is strongly dependent on the dynamic of the index grating formation. Bi-exponential function can be used to fit the temporal dependent of the index modulation¹⁹⁶:

$$\Delta n(t) \propto [1 - m \exp(-t/t_1) - (1 - m) \exp(-t/t_2)] \quad (4.58)$$

where t_1 and t_2 are the slow and fast time constant, and m is the weighting factor. In general, at least two time constants are used for PR composites. This is because, unlike in the case of crystals where the transient is limited by the carrier transport, the time dynamic in PR composite involves many contributions such as trapping, conduction, orientation, etc.¹⁹² Stretched exponential form can also be used¹⁹⁷⁻¹⁹⁸.

$$\Delta n(t) \propto [1 - \exp(-(t/t_s)^\beta)] \quad (4.59)$$

where t_s is the time constant and β is a parameter that determines how the rate evolves with time. The stretched exponential behavior can arise when a phenomenon is governed by the convolution of a distribution of time constants¹⁹⁸. This is often the case for inhomogeneous media such as polymer composites. The β parameter is inversely related to the width of the time constant distribution. Nevertheless, quite often for the PR composites, the data curves are fitted to a biexponential form and the early time constant is reported.

It is possible to derive the sensitivity of the PR materials using the transient FWM information. The sensitivity S is defined as¹⁹⁹:

$$S(t) = \frac{\sqrt{\eta_{ext}(t)}}{I_{WB} \cdot t_{exp}} \quad (4.60)$$

where I_{WB} the writing is beam intensity and t_{exp} is the exposure time. High sensitivity means a hologram is written with sufficiently large diffraction efficiency at low light level and short exposure time. In polymeric PR composite, a high sensitivity can be realized by: (1) generating large space-charge field; (2) optimizing the chromophores; (3) reducing the losses; and (4) decreasing the required exposure.

4.3.2 Two beam coupling measurement

The geometry of two beam coupling measurement is similar to the FWM measurement except in this measurement there is no reading beam. Instead, this measurement monitors the change in relative energy between the two writing beams. This measurement is the decisive experimental proof of photo-refractivity since the phase shift of the index grating from the interference pattern of the two beams is required in order to have energy coupling between beam#1 and beam#2. The same experimental setup as in Figure 4.8 is used. However, for TBC measurement, the intensities of the beam#1 and beam#2 are monitored whereas the beam#3 is blocked. In the case of the steady state TBC measurements, the steady state intensities are monitored as a function of applied voltage. The quantifying parameter for energy coupling between the two beams in this measurement is the gain coefficient Γ . By simply solving the coupling equation, the relation between the two writing beams can be determined by the expression¹⁹⁵:

$$I_2(L) = \frac{I_1(0)+I_2(0)}{1+\frac{I_1(0)}{I_2(0)}\exp(-\Gamma L)} \quad (4.61)$$

where I_1 and I_2 is the intensity of the beam 1 and 2 respectively, and L is the sample thickness. The gain coefficient can be calculated from the measured intensities by²⁰⁰:

$$\Gamma = \frac{1}{L} [\ln(\gamma b) - \ln(b + 1 - \gamma)] \quad (4.62)$$

where $\gamma = I_2(I_1 \neq 0) / I_2(I_1 = 0)$ and $b = I_1(0) / I_2(0)$. Since the sample is slanted in typical TBC measurements of PR polymers, the set-up condition may be taken into account in the calculation of the gain coefficient:

$$\Gamma = \frac{1}{L} [\cos \alpha_1 \ln \gamma_1 - \cos \alpha_2 \ln \gamma_2] \quad (4.63)$$

where α_1 and α_2 are the beam angles relative to the sample normal; and γ_1 and γ_2 are defined as:

$$\gamma_1 = \frac{I_1(I_2 \neq 0)}{I_1(I_2 = 0)} \quad (4.64)$$

$$\gamma_2 = \frac{I_2(I_1 \neq 0)}{I_2(I_1 = 0)} \quad (4.65)$$

Figure 4.11 shows a typical steady state gain coefficient plot.

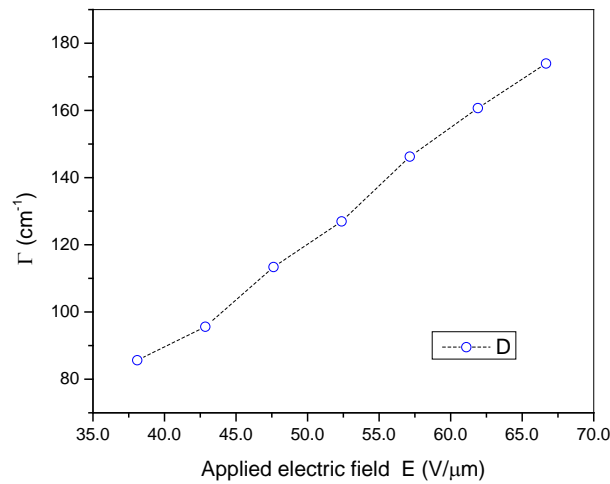


Figure 4.11 Steady state two beam coupling gain vs. applied voltage of PATPD/7-DCST/ECZ/PCBM

4.3.3 Photoconductivity measurement

Photoconductivity measurements evaluate the conductivity of the sample in presence of light. It can be measured either as a function of voltage in a steady state (fixed illumination intensity) or as a function of illumination intensity (fixed bias voltage). Transient measurements can also be done. The conductivity without illumination is called dark conductivity. The amount of current measured is a combined manifestation of several effects i.e trapping, detrapping, photo-generation efficiency and charge mobility. A great amount of information can be obtained by this simple measurement.

In a typical steady state photoconductivity measurement, the current going through the sample is measured at different applied voltage over time. The first step is to apply DC voltage without illumination and let the dark current reach the steady state. The transient behavior of the dark current can be caused by charge injection from the electrode. Once steady state in the dark is achieved, the sample is illuminated with a laser beam. The current is then measured over time until it reaches equilibrium. The rise time of the current is dependent on the trapping and mobility of the charges. The dark conductivity can be calculated by using the following expression:

$$\sigma_{dark} = \frac{i_{dark}}{EA_{elec}} \quad (4.66)$$

where i_{dark} is the measured dark current, E is the applied field, and A_{elec} is the overlap area between the electrodes and the sample. The photoconductivity can be calculated from the following expression:

$$\sigma_{photo} = \frac{i_{tot}}{EA_{beam}} - \sigma_{dark} \left(\frac{A_{elec}}{A_{beam}} - 1 \right) \quad (4.67)$$

where i_{tot} is the measured current under illumination, and A_{beam} is the laser spot size. Significant information can also be obtained from the transient photoconductivity. For instance, shallow traps will affect the behavior of the current on short time scales. Deep traps, however, will affect the behavior on longer time scales.

4.3.4 Transmission ellipsometry measurement

A key mechanism responsible for refractive index modulation in PR composite is the reorientation effect in the SC-field.¹⁷¹ The ability and speed of the chromophores to reorient are important parameters contributing to the overall PR performance.

Chromophores are often poled polymer with uniaxial birefringence. They have two indices of refraction namely ordinary index (n_o) and extraordinary index (n_e). Depending on the polarization direction of the incident light relative to the chromophore optic axis, the probe beam will see different effective index of refraction.

In this ellipsometry measurement²⁰¹, the phase retardation is measured after the beam passes through the sample. This allows calculation of birefringence of the material under applied DC field. The light used is in the wavelength range where no light absorption takes place. The change in the intensity due to phase retardation is monitored using a crossed analyzer. The light intensity behind the analyzer is of the form:

$$I = I_0 \sin^2\left(\frac{\Delta\phi}{2}\right) \quad (4.68)$$

where I_0 is the intensity of the case of parallel polarizer, and $\Delta\phi$ is the phase retardation given by:

$$|\Delta\phi| = \frac{2\pi L \sin^2 \varphi}{\lambda \cos \varphi} |n_e - n_o| \quad (4.69)$$

where L is the sample thickness and φ is the internal incident angle. Figure 4.12 illustrates the schematic diagram of the setup.

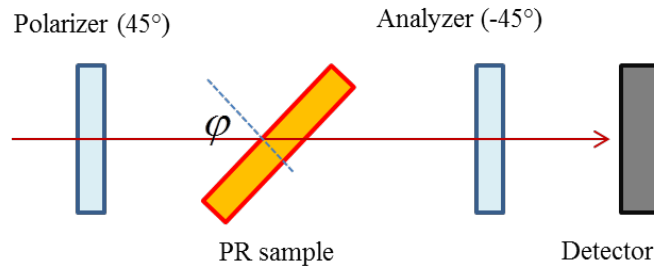


Figure 4.12 Schematic diagram of the optical setup for transmission ellipsometry

Transient ellipsometry measurements will give information about the orientation speed of the chromophores. The steady-state measurement will give an idea about the magnitude of the index modulation with a given applied field. Transient ellipsometry data can be compared to that of the transient photoconductivity to determine whether the conduction of charges or the orientation of the chromophores is the limiting factor in the PR grating formation speed.

4.4 Results and discussions

4.4.1 Photorefractive performance of a graphene-doped PATPD/7-DCST/ECZ composite

In the carbon nanostructure family, buckyballs (C_{60}) and carbon nanotubes have been used and studied as charge sensitizers in PR composites. C_{60} and its derivatives have become benchmark materials for charge generators. CNTs, on the other hand, not only serve as charge generator but also are found to help charge transport in the composite²⁰². The last member of this family that has not been well studied as a sensitizer in the PR composite is graphene.

Nanomaterials can be categorized by their dimensionality, which ranges from zero dimension (0D) to three dimension (3D). In the case of carbon the common structures are, for example, 0D fullerene, 1D carbon nanotube, 2D graphene, and 3D graphite. Interestingly, one can think of 2D graphene as a building block to form the other dimensional structures of carbon allotropes. Graphene is a monolayer of carbon atoms densely packed into a two-dimensional honeycomb lattice. Graphene can be wrapped up to form 0D fullerene, rolled to form 1D nanotube, and stacked to form 3D graphite²⁰³. In a sense, one can regard graphene as the parent of C₆₀ and CNTs. Graphene possesses excellent electrical properties, mechanical flexibility, optical transparency, thermal conductivity and low thermal expansion coefficient^{107, 110, 204-206}. Unlike semiconductors, the valence and conduction bands of graphene touch each other at a point, called a Dirac point. This results in metallic like properties in graphene with no energy bandgap, making graphene an interesting optoelectronic material. Graphene can absorb and convert light into photocurrent over a broad electromagnetic spectral range. Under an applied electric field, photocurrent generation in graphene can occur under several processes such as Seebeck effect, photovoltaic effect, and bolometric effect²⁰⁷⁻²⁰⁸. It has been found by many investigators that electrical conductivity and photo-charge transport of polymer composites are improved with graphene doping²⁰⁹⁻²¹³

For example, N. Yang et al. found that by incorporating graphene into dye sensitized solar cell, charge transport can be improved and the charge recombination can be reduced. The transport property was substantially better than using 1D material like CNTs²¹². Improved charge transport will result in faster dynamic formation as previously discussed (Section 4.2). This is apparent when hole traps were introduced to a PR composite. The reduced hole mobility

due to the traps results in slower rise time. Therefore, better charge mobility in the composite may result in faster dynamic of the device and increased sensitivity.

In photovoltaic community, graphenes have attracted considerable attention due to their unique properties. Among their unique properties, the size-dependent bandgap of graphenes and their large optical absorptivity are particularly interesting for light harvesting applications. In addition, their electronic levels and charge transfer processes can both be modified with well-developed carbon chemistry²¹⁴. The term “ graphene quantum dots” are used for graphene sheets with nanoscale dimensions since their band gap properties resemble those of semiconductor quantum dots. Yan et al. reported that highly dispersible 13nm graphene quantum dots can be used as efficient charge sensitizers in organic solar harvesting devices²¹⁵. Due to the similarity in photochemistry of organic solar cells and PR devices, graphene is a very interesting material for charge sensitization in organic PR devices.

The writing speed of the PR materials depends on two major factors: (1) formation of the space charge field which depends on the charge generation, transfer, transport and trapping processes; and (2) the reorientation dynamics of the chromophores. It is generally accepted that the former contributes to the fast time constant of the PR composite and the latter governs the slow time constant^{188, 216}. Even though the limiting time factor for reaching the steady state in the PR polymers is the slow time constant, diffraction efficiencies smaller than the steady state diffraction value are sufficient for most practical dynamic holographic applications. For instance, an updatable hologram that can be viewed under ambient light condition with only 0.5% diffraction efficiency was recently demonstrated⁶. As a result, charge generation plays an important role in improving the temporal dynamics of hologram generation. It was found that,

using proper charge generation moieties or sensitizers, like buckminster fullerene (C_{60}) or tetranitroflurinine (TNF), can substantially improve the writing dynamics of PR polymers¹⁶¹⁻¹⁶².

As a result, C_{60} has become one of the most commonly used, well-performing sensitizers in PR composites²¹⁷ and a benchmark sensitizer in the literature²¹⁸⁻²²¹. A more soluble derivative of C_{60} , [6,6]-phenyl C 61 -butyric acid methyl ester (PCBM)^{166, 222}, has also been used recently, provides similar PR performance and easier material processing. However, while carbon nano-materials, particularly C_{60} and its derivatives, have proven to be efficient charge generators in PR composites, other carbon nano-materials within the same family of carbon allotropes, like single wall carbon nanotubes (CNTs) and multiwall carbon nanotubes, can also enhance the performance of PR composites²²³⁻²²⁶. Phase separation constitutes one of the processing challenges when dealing with CNT sensitizers. Recently, Lingam et al.²²⁷ have bonded PVK polymer to CNTs. It was found that the charge-transfer process was improved through the intimate contact between the sensitizer and CTP. This grafted polymer system (PVK/7-DCST/TCP/PVK grafted CNT) showed internal diffraction efficiency as high as ~60% and two beam coupling gain of $\sim 78 \text{ cm}^{-1}$ at 633nm. Furthermore, CNTs are involved not only in the charge generation but also in charge transport, which can occur along the tube. The photoconductivity of polymer composites with CNT was found to increase significantly compared to composites without CNTs^{202, 228}.

Recently, Grishina et al. reported on the beam coupling properties of poly(N-vinylcarbazole)/ graphene composites at visible and infrared wavelengths²²⁹⁻²³⁰. Neither plasticizers nor NLO chromophores were added in their system. The two beam coupling gain of the system was measured to be 50 cm^{-1} at an applied field of $150 \text{ V}/\mu\text{m}$ and wavelength of 532nm. However, their composite does not represent a real PR sample since it lacks NLO

chromophore which is necessary for a PR system. Nevertheless, it is highly interesting to examine the use of graphene as a sensitizer in a real PR polymer composite. As a result, in this section, study on the performance of the PR polymer composite of PATPD/7-DCST/ECZ sensitized at 633nm with graphene is studied.

4.4.1.1 Effect of graphene on optical absorption of the PR composite

Graphene used in this experiment was synthesized by chemical exfoliation according to previous reports²³¹⁻²³². Briefly, graphene samples were prepared by ultrasonic cleavage of high purity HOPG in an organic solvent, N-methylpyrrolidone. The resulting solutions were centrifuged to obtain a stable dispersion. This dispersion contains 10-50 nm graphene crystallites, predominantly mono and bilayers. These dispersions were filtered through alumina filters to obtain μm thick free standing graphene laminates. These graphene laminates were re-dispersed in THF to produce PR samples.

All samples were prepared by melt processing. First, the chemicals were mixed with the designated composition in a common solvent, THF. The solution was then dried at 55 °C under vacuum for 24hr. The mixture solid was placed between two indium-tin-oxide (ITO) and melt processed at 165 °C. Polystyrene glass beads of 105 μm diameter were used as a spacer to control the thickness of the samples. Three types of PR samples were prepared for the study. The first sample (“undoped”) is an undoped sample consisting of PATPD/ECZ/7-DCST with 49.74/15.08/35.18wt%. The second sample (“graphene doped”) is graphene doped and the loading of graphene is about 0.03 wt.% (graphene doped to “undoped”). The third sample (“PCBM doped”) is a PR composite doped with the same wt.% (0.03) loading of a benchmark PR sensitizer, PCBM for comparison. PCBM is selected as a standard sample for comparison

here, since recent novel applications like updatable photorefractive 3D displays and 3D telepresence were demonstrated using samples sensitized with PCBM⁶, although at different concentration. In the present work, we study the performance of a system similar to the one developed by P.A. Blanche et al ⁶ but using graphene additives. Since our graphene is not functionalized, maximum loading of 0.03% was used in our study to avoid graphene agglomeration. Decrease in rise time would be expected for higher weight percent, due to the subsequent larger number of photogenerated charges. Optical absorption spectra of these samples are shown in Figure 4.13(a). All samples show large absorption in the green region of the spectra. These large green absorptions are due to chromophore absorption. In order for PR effects to take place, light absorption is essential: this means that all PR samples will work well in the green region. However, since the light absorption is small in the red region, the addition of the sensitizers to the system is necessary. While the undoped and PCBM doped have similar absorption spectra, the graphene doped sample shows a longer absorption tail at longer wavelengths. The optical absorption of graphene dispersed in tetrahydrofuran (THF) shown in the inset of Figure 4.13(a) is in agreement with previous reports²³³. Therefore, improvement in the PR performances in the red region with the addition of graphene is expected. Comparing absorption spectra of the PR samples with their individual components, we found that the observed absorption profiles cannot be accounted for by simple superposition of the absorptions of the individual components. We have also measured absorption spectra of both undoped and graphene-doped composites without chromophores (Figure 4.13(b)). Both samples have high absorption at ~400 nm due to absorption of the polymers. The graphene-doped sample, however, exhibits higher residual absorption throughout the visible range. This higher residual absorption can be attributed to frequency-independent absorption of graphene²³⁴⁻²³⁵. The existence of an

absorption shoulder, only when chromophores are present in the graphene doped composite, suggests an interaction between the chromophores and graphene.

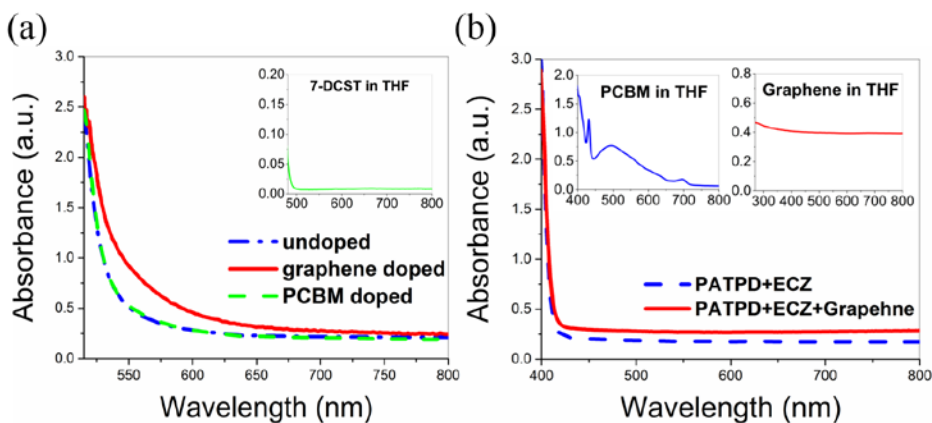


Figure 4.13 (a) Absorption spectra of undoped, graphene doped and PCBM doped in the film form. The inset shows the absorption of concentrated 7-DCST in THF. (b) Absorption of PR composites without chromophores (film) with (red) and without (blue) sensitizer. The addition of graphene results in broadband flat absorption in the visible wavelength range. The inset shows absorption of PCBM and graphene in THF. Axis labels of the insets are the same as of the main curves.

4.4.1.2 Studies on photorefractive performances of the graphene-doped PR composite

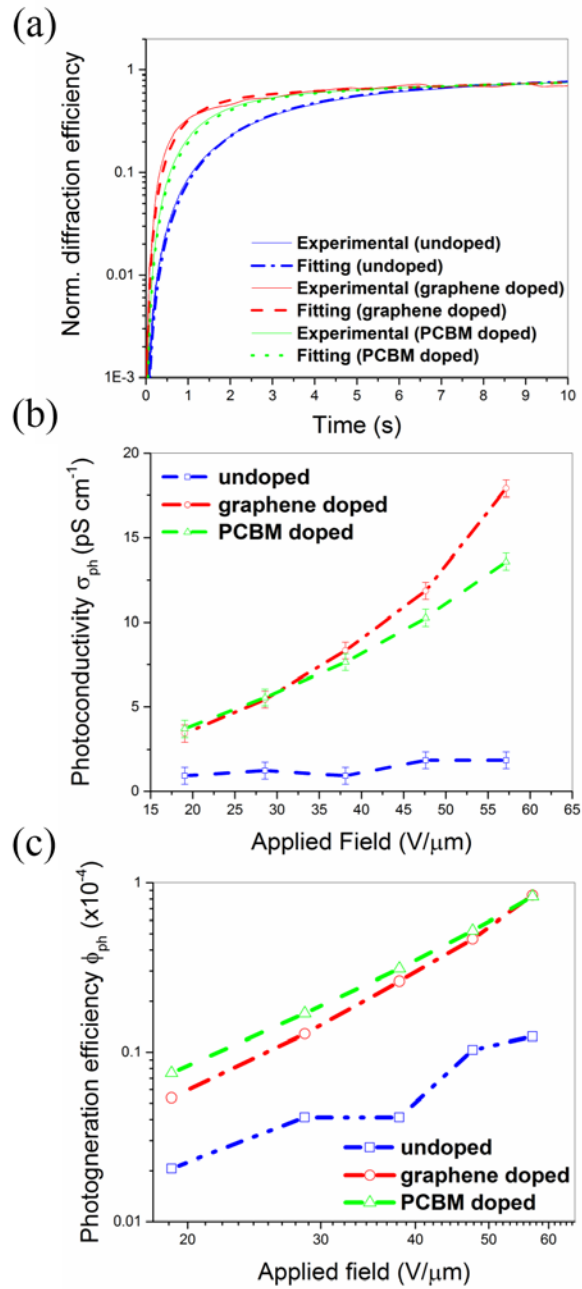


Figure 4.14 (a) Transient FWM curves (b) Photoconductivity vs. applied field and (c) Photocharge generation efficiency of undoped, graphene doped, and PCBM doped.

To measure the speed of refractive index grating formation in the PR process, we performed a transient four-wave-mixing (FWM) experiment. In this measurement, two writing beams of equal intensities of 400mW/cm^2 were used. The wavelength was 633nm generated from a HeNe laser. The intensity of the reading beam was 21mW/cm^2 . The tilt angle between the sample normal and bisect of the two writing beams was fixed at 55° . The angle between two writing beams was fixed at 24° for all measurements. Photodiodes connected to a digital oscilloscope were used to measure the transient behaviors. The transient measurements were done by blocking and un-blocking one of the writing beams using a mechanical shutter. The intensity of the diffracted beam was monitored once the shutter was open. The internal diffraction efficiencies, η_{int} , were calculated using Equation (4.55). It is to be noted that, in all of our experiments, the samples are pre-illuminated to avoid a history-dependent effect²³⁶⁻²³⁷. In a typical FWM experiment, two coherent writing beams interfere inside the sample, resulting in an intensity modulation. This modulated intensity generates photo-generated charges which then drift and diffuse to form a space-charge (SC) field. The resulting SC field modulates the refractive index by electro-optic and reorientational effects, creating an index grating inside the material. To probe the formation dynamics of such gratings, another counter propagating beam or reading beam is used. Due to the index grating, the reading beam is diffracted and the transient behavior of the grating formation can be probed. The diffraction efficiency of this transmission grating depends on the strength of the grating according to the equation:

$$\eta \propto \sin^2(S) \quad (4.70)$$

where S is the grating strength given by :

$$S = \frac{\pi \Delta n d}{\lambda \sqrt{\cos \alpha_1 \cos \alpha_2}} \cos(\alpha_1 - \alpha_2) \quad (4.71)$$

with Δn being the magnitude of the index modulation, λ is the wavelength of the reading beam, and α_1 and α_2 are the angles of the writing beams with respect to the sample normal. Due to small dielectric screening in PR polymer, an external field is applied to facilitate charge separation and the sample is tilted to project an effective electric field along the grating vector. As a result, in the case of PR polymers, Δn is a function of applied field and SC-field dependent birefringence and the electro-optic effect of the chromophore. Since the generation of SC-field and thus the index grating are dynamic in nature, Δn is a function of both time and voltage. In transient FWM measurements, we monitored the temporal behavior of the diffracted beam at a constant applied field of $64 \text{ V}/\mu\text{m}$ as one of the writing beams is blocked and then opened. The total writing intensity used was $800 \text{ mW}/\text{cm}^2$. From these measurements, shown in Figure 4.14(a), we found that the graphene doped sample showed faster dynamics than the other samples. Such observation indicates a faster formation of the refractive index grating. We have also measured the steady-state FWM properties of the samples [AppendixB, FigureB1]. All three samples showed comparable diffraction efficiency. At the applied field of $64\text{V}/\mu\text{m}$, the undoped, graphene doped and PCBM doped samples have internal diffraction efficiency of 69%, 62%, and 53% respectively.

In general, the speed of the formation of the index grating depends on two contributions, (1) speed of SC-field formation and (2) chromophore reorientation time. The first contribution is largely affected by the charge generation efficiency of the sensitizers while the second contribution depends on the properties of the chromophore and the T_g of the composite. In fitting the transient data, the assumption of bi-exponential character in the transient behavior of the index modulation, $\Delta n(t)$, results in two time constant, i.e. the fast time constant t_1 and the slow time constant t_2 , as seen in Equation (4.58).

Since the SC-field formation is much faster than the reorientation of the chromophores, t_1 can be mainly attributed to the speed of the SC-field formation. On the other hand, t_2 mostly reflects the chromophore reorientation kinetics¹⁸⁸. By fitting our data with Equation (4.58), t_1 and t_2 , for graphene doped are determined to be 0.8 s and 25 s respectively. In contrast, for undoped, $t_1 = 2.5$ s and $t_2 = 25$ s, and for PCBM doped $t_1 = 1.8$ s and $t_2 = 38$ s. The weighting factor m used for fitting undoped, graphene doped and PCBM doped data are 0.51, 0.51, and 0.65s respectively. When compared to its undoped counterpart, the graphene doped sample has approximately 3 times faster t_1 while their t_2 values are the same. Such reduction in the fast time constant, i.e. the faster SC-field formation can be attributed to the improved charge generation and transport due to the presence of graphene. In order to verify this assumption, we performed photoconductivity measurements (Figure 4.14(b)). The total light intensity used for all measurements was 400mW/cm². The speed of the SC-field formation and the value of the magnitude of the t_1 value are largely governed by the photogeneration efficiency. We found that our graphene-doped sample exhibits significantly larger photoconductivity, σ_{ph} , than the undoped sample. Its photoconductivity also is larger than that of PCBM-doped sample when applied field is larger than 30V/ μ m. This larger photoconductivity in the graphene-doped sample means, given the same irradiation, more charges (larger photocurrent) are generated in the sample. By the definition of electric current, a larger current is the manifestation of a greater number of charges flowing through the sample per time interval. In the case of the PR polymer, this enhanced charge flow will result in a faster formation of a steady state SC-field. Therefore, the observed largest photoconductivity in the graphene-doped sample explains its fastest t_1 . We also calculated the photo-charge generation efficiency, ϕ_{ph} , of the samples according to the equation

$$\varphi_{ph} = \frac{\sigma_{ph} E h \nu}{e I_a} \quad (4.72)$$

where E is the applied electric field, I_a is the absorbed light intensity, h is Planck's constant, ν is the light frequency, and e is the elemental charge constant. It is found that the photogeneration efficiencies of all samples increase with E , as depicted in Figure 4.14(c). Such field dependent efficiency suggests the electric field assisted dissociation of excitons²³⁸⁻²³⁹. In other words, holes and electrons are generated at the interface between two species (donor and acceptor). From the experimental data, the rate of increase of the efficiency with applied field is higher in the case of the graphene-doped sample compared to that of the undoped sample. This higher rate is an indication of a smaller initial electron-hole separation, or exciton thermalization length, in the graphene-doped sample²⁴⁰. Such reduction in the initial thermalization length may be explained by the small loading of the graphene. The number of participating charge generators can significantly affect the interfacial area between donor and acceptor species and the thermalization length is highly dependent upon the interfacial areas²⁴¹. Larger loadings of both species can result in continuous pathways available to both electrons and holes and thus a longer thermalization length. On the other hand, the absence of such pathways in either one of the charge species causes a reduction in the thermalization length. The undoped sample has a large initial thermalization length (smaller slope) because the charge generation and separation occurs between two species with large loadings which are, in this case, the chromophores and the charge transporting polymers. From the experiments, we found that the graphene-doped sample had much larger photo-charge generation than its undoped counterpart. It becomes obvious that the additional charges are generated by the presence of graphene. The observed reduction in the

initial thermalization length in the graphene-doped sample further confirms that such increase in photogeneration involves the species with smaller loading, i.e. graphene.

Since any species added to the PR polymer composites can also act as charge traps^{165, 242}, it is interesting to investigate this aspect. We performed two beam coupling (TBC) measurements with our sample (Figure 4.15). In this experiment, the energy exchange between two overlapping laser beams was monitored. Two interacting beams with a 1:1 intensity ratio were used. The magnitude of the energy exchange is expressed in the form of the gain coefficient, Γ , determined from Equation (4.62). This gain coefficient depends not only on the magnitude of the SC-field but also on the phase shift between the light interference pattern and the index modulation¹⁹⁵. Charge trapping can affect both the magnitude and the phase of the SC-field, resulting in changes in the magnitude of Γ ²⁴³. Not only that, TBC measurement implicitly gives information about the trapping mechanisms, the non-zero TBC gain coefficient is a proof of the PR effect in the system due to the nonlocal nature of the PR effect. We found that the gain coefficients of our graphene-doped sample are comparable to those of the undoped sample. This observation indicates that the addition of graphene neither affect the magnitude nor the phase of the SC-field, possibly due to the absence of new favorable charge traps (otherwise, very shallow traps) generated with graphene. Both samples showed large gains with p-polarized beams. This is because the index modulation seen by p-polarized light is stronger than by s-polarized light. It is to be noted here that both samples showed reversed direction of energy transfer as the incident beams were changed from s-polarization to p-polarization. This effect has previously been observed²⁴⁴.

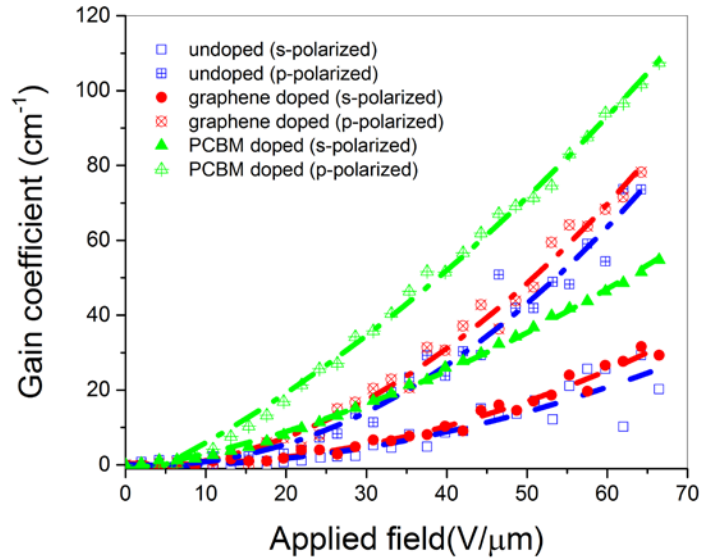


Figure 4.15 Γ vs. E for undoped, graphene doped and PCBM doped. Data for both s- and p-polarizations are shown.

When the performance of the graphene-doped sample was compared with a PR polymer doped with the benchmark sensitizers, like in the PCBM doped, we found that t_l of the graphene-doped sample is shorter than that of the PCBM-doped sample at an applied voltage of $64\text{V}/\mu\text{m}$. The shorter time constant in this graphene-doped sample is in accordance with its higher photoconductivity when compared to the PCBM-doped sample. However, the linear absorption of the graphene-doped sample is higher than that of the PCBM-doped sample at similar loading levels. The rate of increase in the photo-charge generation efficiency of the graphene-doped sample, however, is larger than that of the PCBM-doped sample. We also found that the TBC gain coefficient is much higher in the case of the PCBM-doped sample. The larger TBC gain in the PCBM-doped sample can be attributed to traps generated from ionized sensitizers²⁴⁵. In the PCBM system, the majority of charges are generated from photoexcitation of PCBM molecules. By transferring holes to the transport polymer, ionized PCBMs are created. These species act as

electron traps that increase the separation between positive and negative charges, resulting in large TBC gain. On the other hand, graphene-doped sample and undoped sample have similar gain coefficients, suggesting the lack of such trapping mechanism. This implicates that charge sensitization processes in PCBM-doped and graphene-doped samples are different. In the former, PCBM acts as independent charge sensitizers and ionized species are the results of photoexcitation. In the latter, however, graphene helps separation and transport of charges created from photoexcitation of the nonlinear chromophores as evident by photocurrent, absorption and PL measurements (discussed in the following section).

4.4.1.3 Effect of graphene on photoluminescence of the PR composite

From the TBC measurements, it is clear that the PR effect can take place in the PATPD/ECZ/7-DCST system, without the use of additional sensitizer, i.e. the case of the undoped sample. However, we found that the absorption profile of the composite is not a simple superposition of the component's profiles. This finding suggests electronic interactions between the components. To have an insight into this aspect, we performed photoluminescence (PL) measurements with 532 nm laser excitation (Figure 4.16) using a Raman confocal microscope (Witec Alpha 300 RA Raman system). First, we investigated the PL of the PATPD /7-DCST composite to observe the interaction between PATPD and 7-DCST. The PL of the PATPD/7-DCST composite has a peak at ~ 610 nm which is red-shifted compared with the PL of 7-DCST (Figure 4.16(a)). These results suggest that excited 7-DCST electronically interacts with the PATPD host polymer. The PL spectra of thin layers of undoped and graphene doped samples are shown in Figure 4(b). The undoped sample has a PL peak at 610 nm which is same as the PL peak of the PATPD/7-DCST composite. The observed peak at 610nm in the undoped PR

composite may be attributed to the radiative recombination between electron in the LUMO level of 7DCST and hole in the HOMO level of PATPD as illustrated in Figure 4.17(a). However, according to our previous optical measurements, the photo-charge generation efficiency of this system is relatively small which results in a slow formation of the SC-field.

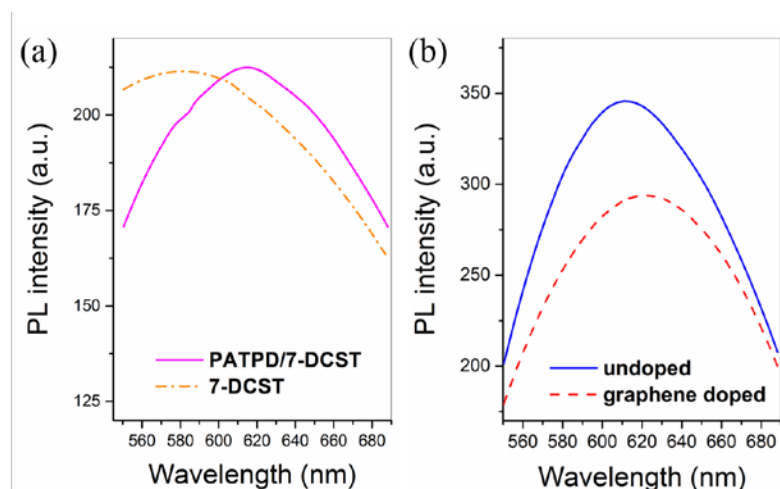


Figure 4.16 PL spectra of (a) PATPD/7-DCST composite and 7-DCST, and (b) graphene doped and undoped PR samples. The excitation wavelength was at 532nm. The composites studied here were so prepared that the % weight loading of the components in polymer matrices are the same as those of the PR samples.

By adding graphene to the system, the efficiency can be improved. This improvement in the efficiency results in faster formation of a SC-field and shorter t_f . Here, we found that graphene can be used to improve the photo-charge generation efficiency of the PR system. Even without optimization and functionalization, the photo-charge generation efficiency of the graphene sensitizers is similar to benchmark materials like PCBM. We also found that the absorption of the graphene doped sample has a longer tail in the red region than those of the undoped and PCBM doped. The PL spectrum of the graphene doped PR is also slightly red-shifted compared to that of the undoped. Considering the energy level of graphene (Figure 4.17(b)), it is possible that graphene interacts electronically with the LUMO level of 7-DCST,

resulting in the slight red-shift in the PL spectrum and better charge generation efficiency. In fact, electronic interactions between graphene and π -conjugated polymers has been observed in the case of photonic and optoelectronic devices^{117, 246-249}. It has also been found that electron transfer occurs between poly(3-octylthiophene) and graphene where graphene acts as an acceptor¹¹⁷. In addition, blending conjugated polymers with graphene-based materials can result in effective electron-hole separation and charge transport. It also provides a continuous pathway for charge transfer²⁴⁹.

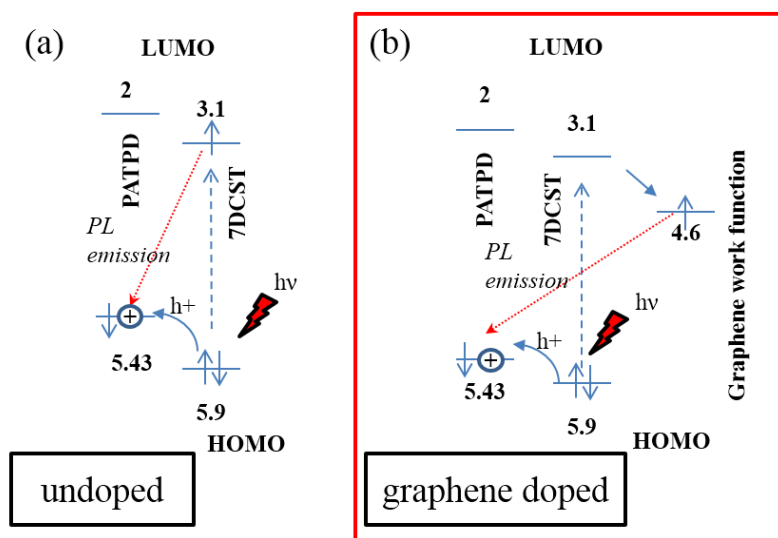


Figure 4.17 Molecular energetic diagram for (a) undoped and (b) graphene doped. In the undoped PR composites, a photo-generated hole is transferred from 7-DCST to PATPD. ECZ does not participate in hole transport due to its lower HOMO level of 5.92eV. These holes are the primary charge conductors in PR polymers. In the case of graphene doped, graphene may act as an electron acceptor with 7-DCST as a donor, resulting in better exciton dissociation/charge generation efficiency.

4.4.1.4 The role of charge trapping in the graphene-doped PR composite.

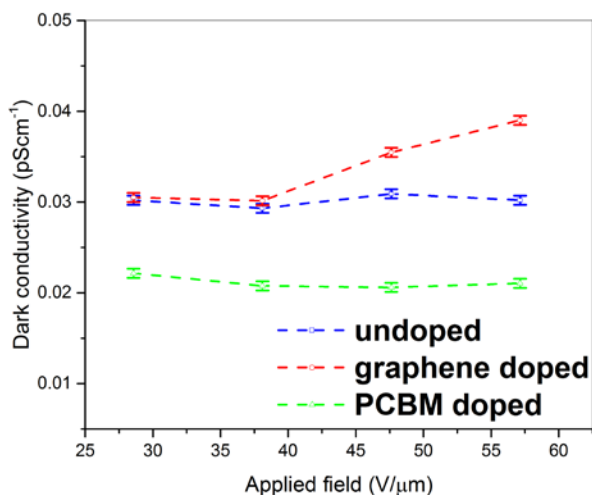


Figure 4.18 Dark conductivity vs applied field for undoped, graphene doped and PCBM doped.

While both graphene-doped and PCBM-doped samples have similar charge generation efficiency, the latter shows much stronger TBC gain. This finding can be explained in terms of charge trapping in the composites. In the PCBM-doped system, the generated charges are transferred to the conducting polymer, resulting in ionized PCBMs. The ionized PCBMs act as hole traps. However, in the case of the graphene-doped sample, the presence of graphene in the system does not significantly affect the magnitude of the TBC gain, suggesting the lack of a trapping mechanism.

An increase in the speed of the SC-field formation can be the manifestation of two phenomena, namely more efficient photo-charge generation and better charge transport. Since we observed an increase in photo-charge generation efficiency, we conclude that better charge generation process due to the interaction between graphenes and the complex is responsible for the improvement. However, it is also possible that the addition of graphene helps transporting the photo-generated charges, possibly by improving overall electrical conductivity of the composite.

Enhancement in electrical conductivity of graphene-doped composites has been observed previously²⁵⁰. In order to investigate this aspect, we looked at the dark-conductivity of the samples (Figure 4.18). The dark conductivity was measured at the steady state after pre-illumination. We found that both undoped and graphene doped have similar dark-conductivity at low voltages. However, graphene doping showed slightly higher conductivity at larger fields. It is possible that the addition of graphene leads to such voltage dependent enhancement of the dark conductivity. This aspect is the subject of future study. However, it can be concluded that, in our graphene-doped PR composite, the graphene dopants do not negatively affect the charge transport mechanism. In other words, charge trapping is absent in the graphene-doped sample. On the contrary, The PCBM doped samples show a reduction in dark-conductivity when compared with the undoped samples. This can be attributed to the trapping mechanism previously discussed.

All in all, in this section, the performance of PR composites doped with graphene was studied. It was found that, in the undoped system of PATPD/ECZ/7-DCST, charge sensitization occurs via nonlinear chromophores. Nonetheless, the addition of graphenes to the system results in shorter SC-field build-up time. The faster build-up time is attributed to larger charge generation due to the electronic interaction between graphenes and chromophores. Photocurrent studies on our samples confirm the enhancement in charge generation with the addition of graphene. From the energy levels of the component and our luminescence study, it is likely that the improved charge generation is due to the efficient exciton separation at the 7DCST-graphene interface. The PR performance of the graphene-doped sample is comparable with the PCBM-doped sample with the same (wt. %) loading. We found that the graphene-doped sample exhibits faster SC-field build up time and larger photoconductivity at high applied field ($>50\text{V}/\mu\text{m}$). The

steady state TBC gain of the sample doped with the benchmark sensitizer PCBM is larger than that of the graphene-doped PR composite. However, the TBC gains of the graphene-doped sample are comparable with the undoped composite. The absence of improvement in the TBC gains of the graphene-doped sample compared with PCBM-doped sample may be attributed to the lack of charge trapping in the graphene-doped sample. This study has revealed the potential of using graphene-based materials to improve the speed of PR polymer composites. Future work will focus on further enhancement of the PR speed by increasing the loading of graphene by suitable functionalization.

5 FABRICATION OF TUNABLE PLASMONIC SUBSTRATES[§]

5.1 Motivation

Collective oscillation of conducting electrons or plasmon has attracted significant research interest for the past decade. The unique properties of this physical phenomenon are proved to be useful in many applications, for example, bio-sensing²⁵¹⁻²⁵², cancer-therapy²⁵³⁻²⁵⁴, solar-harvesting²⁵⁵⁻²⁵⁶, and wave guiding²⁵⁷. When the frequency of the incident electromagnetic wave is in resonance with the localized surface plasmon resonance (LSPR) of a metal nanostructure, the local field strength around the structure can be enhanced by several orders of magnitudes. This field enhancement is found to be beneficial in a variety of applications such as surface enhanced Raman scattering (SERS)²¹, photoluminescence²⁵⁸⁻²⁵⁹, photo-detection²⁶⁰, photo-charge generations²⁶¹⁻²⁶², photo-catalysis²⁶³⁻²⁶⁴, nonlinear optical properties²⁶⁵⁻²⁶⁶ and surface plasmon enhanced Faraday rotation²⁶⁷.

Large-scale fabrication of patterned plasmonic nanostructures is a challenging quest. Nevertheless, it is necessary for transitioning plasmonic devices from laboratories to industries. Methods like electron-beam lithography (EBL)²⁶⁸ and focused ion beam lithography (FIBL)²⁶⁹ are commonly used for fabricating high quality nanostructures as it can circumvent the resolution limit of conventional photolithography. Fabrication of nanostructures using these techniques is, however, time consuming and expensive. One of the alternatives is to use nanotemplate

[§] The work presented in this chapter are extensions Chantharasupawong, P.; Tetard, L.; Thomas, J., Coupling Enhancement and Giant Rabi-Splitting in Large Arrays of Tunable Plexcitonic Substrates. *The Journal of Physical Chemistry C* 2014, 118, 23954-23962.

approaches such as using anodized alumina oxide²⁷⁰ or nanospheres²⁷¹⁻²⁷² as templates. These techniques provide relatively poor quality nanostructures and the templates used are sacrificial in nature. Moreover, the flexibility in designing the shape of nanostructures is limited.

Nanostructures fabricated by nanoimprinting lithography with high quality master mold as a precursor have been demonstrated to provide large area of well-ordered nanostructures with high resolution²⁷³. With this technique, the shape of the nanostructure can be designed and fabricated on the master mold using EBL or FBIL. The negative replica of the master mold can be transferred to a polymer substrate. Even though this approach also involves fabrication techniques like EBL or FIBL, it uniquely offers the ability to fabricate large number of replicas with a single master mold, keeping the cost per structure very low. Nonetheless, the shape and size of the imprinted nanostructure is fixed by the pattern on the master mold. This nanopattern can be directly used for fabricating plasmonic devices or as a second-generation mold for creating the positive replica of the designed nanostructure.

A key aspect of plasmonic nanostructures is the strong dependence of their LSPR wavelength on the shape, size, and environment. For instance, in the case of metal nanospheres, the resonance peak is red-shifted as the size of the sphere increases²⁷⁴. Anisotropic shapes like metal nano-ellipsoids have their plasmon resonance peaks dependent on the orientation of the structure relative to the incident light polarization²⁷⁵.

Unfortunately, plasmonic structures fabricated by the nanoimprinting methods have limited flexibility in changing their size and shape as it is restricted by the pattern on the master mold. Hence, the ability to tune the resonance peak using a given master mold is limited. Typical methods for tuning the resonance of patterned plasmonic structures include changing the polarization of the incident light²⁷⁶, rotating the sample relative to the light propagation axis²⁷⁷,

and increase the thickness of the deposited metal²⁷⁸⁻²⁷⁹. Nevertheless, these approaches have their own constraints. For instance, changing the polarization of the incident sources is not suitable in applications where the source is unpolarized. On the other hand, rotating the sample relative to the incident light propagation axis is not appropriate for space limited application. Changing the thickness of the deposited metal requires more than one deposition process.

In this chapter, a quick and high throughput nanofabrication technique for making tunable plasmonic substrates is presented. The use of the fabricated structures for enhancing light matter interactions is investigated.

5.2 Theoretical background

5.2.1 Nanofabrication techniques

In order to study and understand the optical properties of metal nanostructures, it is imperative that we have the ability to produce them. In this section, common fabrication techniques for producing nanostructures, not exclusively to metal, are briefly discussed. More comprehensive review can be found elsewhere²⁸⁰⁻²⁸³.

(i) Photolithography and scanning lithography

Lithography technique has been around since the advent of integrated circuit technology. The mainstream lithography used in the industry is called photolithography. In this technique, masking materials known as resists are used. These resist materials are sensitive to the electromagnetic source used in developing desired patterns. There are two kinds of resists, which are positive and negative resist. Positive resists reacts with the EM wave in such a way that a developer can remove it chemically after exposing the material with the radiation. Negative resists, on the other hand, can always be removed with a developer unless it is exposed to the

radiation. The pattern is projected on to the resist with the use of a photo-mask. Photomasks are typically made of quartz with metal of a desired pattern on them. The resolution of lithography techniques highly depends on two main factors that are the EM source and the optics of the system. The most common wavelength for the source is UV radiation. Smaller wavelength source such as extreme UV and X-ray are also used. However, higher radiation frequency poses challenges in designing the optics of the system. Another direction to improve the resolution of the system is to use higher numerical aperture optics. Improving the resolution of photolithography techniques is a subject of ongoing research and it is guided by Moore's law.

Another school of lithography is called scanning beam lithography. Unlike in the case of photolithography where the pattern is cast on a sample with only one exposure, this technique uses a scanning beam to write a pattern on a sample by a point-by-point fashion. The beam used can be laser beam (laser scanning lithography (LSL)), electron beam (electron beam lithography (EBL)) or ion beam (focused ion beam lithography (IBL)). In the case of LSL, laser wavelengths in the UV region are typically used as the source. LSL is the least expensive among the three scanning lithography techniques. EBL and IBL, on the other hand, offer higher resolution since the wavelength of electrons and physical size of the ions are much smaller than diffraction limit of the UV radiation.

LBL and EBL require a resist layer for patterning. In LBL, photoresists similar to conventional photolithography can be used. However, with the use of two-photon absorption, resolution can be further improved. With a thick resist, 3D complex structures can be made with LBL. In EBL, the most common polymer is PMMA. It is a positive resist. Electron beam breaks the polymer chains and make it removable by a developer. IBL, on the other hand, is considered as a primary writing method since the pattern can be written directly on the sample without using

a resist. Nevertheless, since the point-by-point writing scheme is very time consuming, writing large-scale patterns are challenging with these beam-scanning techniques.

To develop metal structures with lithography techniques, the desired pattern is lithographically developed on the resist material, which is coated on a substrate. Metal nanostructures are realized by depositing the metal onto the sample and then lift off the resist. Alternatively, metal layer can be deposited on the substrate before the resist is applied. Various etching processes can then be used to pattern the metal with the resist acting like a stencil.

(ii) Colloidal synthesis

History of the colloidal metal nanoparticle synthesis can be traced back to the medieval period when glass artisan used metal salts as coloring agents in producing stained glass. Back then; they did not know that the observed colors after adding gold chloride and silver nitrate to their glass are actually from gold and silver nanoparticles created during the making process. Currently, researchers use this metal salt reduction technique to produce metal particle with various shapes and sizes. For example, quasi-spherical gold particle can be produced by adding chloroauric acid with sodium citrate²⁸⁴. Au(III) ion from the acid is reduced by the negatively charge citrate ion, producing neutral Au capped with citrate group. The presence of the negatively charged citrate-capping group prevents particles from aggregation and controls the rate of the particle growth. Therefore, the size of the final product can be controlled by manipulating the nucleation and growth process through the adjustment of the reagent concentration and the reaction conditions. However, since the citrate ions are weakly absorbed onto the surface, change in temperature, pH, and concentration can destabilize the solution. To address this issue, organic capping ligand such as a long chain alkanethiol can be used to improve the stability.

Gold and silver particles are never a perfect sphere. Instead, they have irregular shapes with their surfaces determined by the facets of face center cubic (fcc) crystal structures. As a result, due to these facets, the smaller the particle is, the more its appearance deviates from being a sphere. However, by selectively controlling the growth of particular facets, anisotropic nanoparticles such as pyramids, octahedrons, cubes and rods can be produced²⁸⁵⁻²⁸⁶. An example of such process is the following. First, quasi-spherical silver seeds are produced by mixing silver nitrate and ethylene glycol. Then, by adding a capping agent such as poly vinylpyrrolidone (PVP) to the mixture, anisotropic silver particles are produced. PVP is believed to selectively interact with various crystallographic planes of the fcc silver. As a result, with the presence of PVP during the growth process, the growth rate along $\langle 100 \rangle$ direction is greatly reduced and/or growth rate along $\langle 111 \rangle$ direction is greatly enhanced. Wang showed that the shape of an fcc nanocrystal could be determined by the ratio (R) between the growth rates along $\langle 100 \rangle$ and $\langle 111 \rangle$ directions²⁸⁷. For instance, octahedron and tetrahedron are formed when $R = 1.73$. Cube, which are bounded by the less stable $\{100\}$ planes, are formed when $R=0.58$. Hence, by careful selection of the capping agent and adjustment of the reaction conditions, various particle shapes can be realized.

Core shell structures can also be produced by this chemical reduction technique. For instance, one metal can be grown on another metal seeds producing core shell structures. It is also possible to remove the core material by selective oxidation, resulting in a hollow structure²⁸⁸. In addition, dielectric core-metal shell structure can also be synthesized by chemical reduction. For example, silica nanoparticles can be used as the dielectric core²⁸⁹. Organosilane molecules are then used to modify the surface of the core. These molecules bond to the surface of the silica nanoparticles with their amine groups extending outward. When colloidal gold

solution is added, the organosilane molecules make covalent bonds with the gold particles through the amine groups with about 30 percent coverage. Complete coverage of the core with the gold shell is then achieved by reducing an aged mixture of chloroauric acid and potassium carbonate by a sodium borohydride solution. During the reduction process, the gold-decorated silica nanoparticles act as seeds or nucleation sites.

Due to the immense interest in unique properties of metal nanoparticles, other methods have also been developed for synthesizing colloidal metal nanoparticles. For example, electrical arc discharges²⁹⁰, laser ablation²⁹¹, and electrochemical reactions²⁹². However, thus far, this metal salt reduction technique is the most successful and flexible.

(iii) Self-assembly based approach

Self-assembly techniques can also be used to produce large two-dimensional arrays of metal nanostructures or even three-dimensional superlattices. One approach is to use Langmuir-Blodgett technique²⁹³⁻²⁹⁴. This technique has been developed for assembling a monolayer of organic molecules on a solid surface. The resulting film is called Langmuir-Blodgett film. The films are formed when small amount of solvent containing amphiphilic organic molecules, which consist of a hydrophilic head group and a hydrophobic tail, is dropped on water surface in a container. The solvent is chosen such that it is immiscible in water. After the solvent is evaporated off, it leaves behind the molecules with their head group immersed in the water and tail groups sticking out. The container used has movable sidewalls such that the surface tension, layer formation, packing density as well as thickness of the film can be controlled. The film can be easily transferred to a solid substrate by a simple dipping process and drawing it out under a constant surface pressure. Array of metal nanoparticle can be produced with this technique by

capping them with hydrophobic tails such as alkanethiol. The solution of the capped nanoparticles in a nonpolar organic solvent is then dispersed on the water surface.

Alternatively, array of metal nanoparticles can also be produced by controlled evaporation of organic solvent containing them on a substrate²⁹⁵⁻²⁹⁶. As the solvent evaporates, the liquid air interface moves down and intercept with the nanoparticles. These particles are trapped at the interface between air and liquid. They can only diffuse along the two-dimensional surface. As more of the solvent dries, more particles are trapped. By controlling the evaporating conditions, concentrations and the size of particles, monolayers or even superlattices of the particles can be produced. For both Langmuir-Blodgett and controlled evaporation techniques, the lattice spacing and inter particle distance are determined by the size of the capping agents.

Instead of assembling the metal nanoparticles themselves into 2D or even 3D nanostructures, hybrid methods, in which non-metal self-assembled structures (or self-organized templates) are used as a template for metal deposition, have also been developed. The most common self-assembled templates are self-assembled nanosphere^{271, 297} and anodized aluminum oxide templates²⁹⁸⁻³⁰⁰. The former is an ordered two-dimensional hexagonal array of silica or polymer nanospheres produced by controlled evaporation. Depositing metal on the structure and subsequently removing the nanosphere template can produce metal nanostructures. Such process of making nanostructures is referred to as nanosphere lithography. Since in this technique, metal is deposited between the gaps of closed packed spheres, the size of the metal structures can be much smaller than the spheres themselves. In general, nanosphere lithography produced metal nanostructures with a triangular shape of the inter-sphere gaps. However, modification of this techniques such as changing deposition angle³⁰¹, can allow fabrication of other geometries. Also, the template can also be used as an etch mask. In this case, metal is deposited on the substrate

before the sphere layer is assembled. Portions of metal film that is not covered by the spheres can be etched out with etching process like ion beam etching, leaving behind nanodisk structures.

In the second case, anodized aluminum oxide template is produced by controlled anodization of an aluminum film. Anodization can be considered as a reversed electroplating. Instead of putting metal at the cathode, the aluminum film is placed at the anode where it is oxidized. Hydrogen is produced at the cathode electrode. When aluminum is anodized in an acidic solution, the acid dissolves the oxide as it forms. By balancing the dissolving and oxidation rates, a hexagonal array of cylindrical pores is formed on the film. The pore size can be controlled by adjusting the anodization voltage. Similar to the case of the nanosphere, this nanostructured film can then be used as a template for metal deposition, hence, producing metal nanostructures.

There are also other variants of self-assembly based techniques. For example, atomic force microscope is used for guiding self-assembly of metal nanoparticles³⁰²⁻³⁰³. DNAs are also used to produce intriguing self-assembled metal structures³⁰⁴⁻³⁰⁵. Nevertheless, the main problem with the self-assembly based techniques is their uniformity. The produced structures tend to only have short-range order but lacking the long-range order.

(iv) Nanoimprint lithography and soft lithography

Nanoimprint lithography (NIL) was developed by Chou et al. in 1995 as a solution for achieving low cost and high throughput nanofabrication³⁰⁶. In the NIL process, a pre-fabricated hard mold, typically from conventional lithography such as EBL, is pressed on a resist-coated substrate. The pattern on the mold is an inverse of what produced on the sample. NIL technique is based on physical deformation of the resist. Resists used in this technique are usually polymers. The most common types of resists used are either thermoplastic polymer resists or

photopolymer resists. In the former case, the method is called thermal NIL or hot embossing since the sample has to be heated above the glass transition temperature (T_g) of the resist while pressing the mold onto the sample. The resist is then cured by cooling the sample to below T_g . In the latter case, pre-exposed resist is in a liquid phase. The mold is then pressed onto a layer of liquid polymer and UV radiation is used to harden the polymer by cross-linking process. NIL that involves UV-curing is termed UV NIL. One of the difficulties with using a hard mold is that a flat substrate is required. The quality of the pattern depends heavily on the mechanical contact between the mold and the substrate and can be greatly affected when the two surfaces are not parallel or there is any contamination between the two pressing surfaces. Soft lithography (SL) was invented to overcome the problem as it uses a soft elastomer as a mold. The most common material for the soft mold is poly dimethylsiloxane (PDMS). This soft mold is generally made by forming a template out of a rigid substrate such as silicon, using conventional lithography. An anti-sticking layer is spin coated on the rigid substrate before a liquid elastomer precursor is spread over the substrate. The precursor is then cured, peeled off and ready to be used as a stamp. Nonetheless, in general, NIL and SL are inherently similar in which a master mold or stamp is used for nano-patterning. Since many replicas can be produced with a single mold, high throughput fabrication can be easily achieved with these techniques.

Similar to conventional lithography, metal nanostructures can be fabricated with these techniques simply by either depositing metal onto a stamped pattern or using the stamped layer as an etching mask. One of the challenges with this technique is that a thinning process for the resist, such as plasma etch, is required to remove a residual resist layer²⁷⁸. The quality of the pattern is usually compromised after etching. Therefore, sometimes, metal nanostructure is achieved by depositing metal directly onto a resist layer without removing them³⁰⁷. NIL and SL

technique have advantages over other techniques in term of low cost, high throughout and the quality of produced structures.

5.2.2 Surface plasmon

Plasmons are collective oscillation of conduction band electrons. In general, there are two types of plasmons, namely propagating surface plasmon (PSP) and localized surface plasmon (LSP). PSP is surface electromagnetic wave, which is coupled to conduction band electrons, at metal dielectric surface. PSP has its wave vector parallel to the metal/dielectric interface and the field perpendicular to the interface decays evanescently. PSP was first discovered experimentally by Wood¹⁶. It was once called Wood's anomaly. LSP, on the other hand, does not propagate. They occur in metallic nanostructure whose sizes are comparable to or less than the skin depth of the excitation wavelength. The most common structures exhibiting LSP properties is metallic nanoparticle made of silver or gold. Their history can be traced back to medieval period when artisans used them to produce colors in stain glasses. Plasmons have attracted immense research interest because of the fact that, at their resonance, electromagnetic field can be squeezed smaller than their diffraction limit resulting in enormous field enhancement. Moreover, the resonance conditions of plasmonic structures are highly dependent on the structure's geometries, materials, and their surroundings. Owing to their unique properties, plasmonic structures have been proven to be very beneficial in many applications, for example, sensing, imaging, nonlinear optic and light harvesting.

Different theoretical calculations have been developed in lieu of understanding the nature of plasmonic nanostructures. For simple geometries like spherical and ellipsoidal nanoparticles, analytical based solutions can be used. For more complex structures, one needs to resort to

numerical techniques, for example finite Integration technique (FIT) and finite difference time domain (FDTD).

(i) *Analytical-based calculation*

A theory to understand the absorption and scattering of colloidal of metal nanoparticles was developed by Gustav Mie developed in 1908³⁰⁸. He solved Maxwell's equation in spherical coordinate for a plane wave interacting with a small sphere. By expanding the electromagnetic fields in an infinite series of vector spherical harmonics with appropriate boundary conditions, scattering field can be solved. Calculating the net rate at which the sphere scatters and absorbs light at the far field, one can arrive at the following expressions for the extinction σ_{ext} and scattering σ_{sca} cross-section³⁰⁹:

$$\sigma_{ext} = \frac{2\pi}{|k^2|} \sum_{n=1}^{\infty} (2n+1) \text{Re}(a_n + b_n) \quad (5.1)$$

$$\sigma_{sca} = \frac{2\pi}{|k^2|} \sum_{n=1}^{\infty} (2n+1) (|a_n|^2 + |b_n|^2) \quad (5.2)$$

with

$$a_n = \frac{\mu m^2 j_n(mx) [xj_n(x)]' - \mu_p j_n(mx) [mxj_n(x)]'}{\mu m^2 j_n(mx) [xh_n^{(0)}(x)]' - \mu_p h_n^{(0)}(mx) [mxj_n(x)]'}, b_n = \frac{\mu_p j_n(mx) [xj_n(x)]' - \mu j_n(mx) [mxj_n(x)]'}{\mu_p j_n(mx) [xh_n^{(0)}(x)]' - \mu h_n^{(0)}(mx) [mxj_n(x)]'} \quad (5.3)$$

where μ is the permeability, $m=N_1/N$ is the refractive index ratio, $x=ka=2\pi na/\lambda$, j is the spherical Bessel function, and h is the spherical Hankel function respectively. The material parameters without subscript denote those of the surrounding and with the subscript p are for the sphere. The absorption cross-section σ_{abs} can be calculated from $\sigma_{ext} = \sigma_{sca} + \sigma_{abs}$. The summation index n

corresponds to the mode of oscillation. For example, $n=1$ is the dipole oscillation and $n=2$ is the quadrupole oscillation. In the case where the nanoparticle is much smaller than the wavelength of light ($2a \ll \lambda$), the dipole term dominates the summation. In the dipole approximation, the Mie coefficients a and b are then reduced to the following relationship³¹⁰:

$$a_n \approx a_1 = -i \frac{2x^3}{3} \frac{\epsilon_p - \epsilon}{\epsilon_p + 2\epsilon} + O(x^5) \quad (5.4)$$

$$b_n \approx b_1 = -i \frac{2x^3}{3} \frac{\mu_p - \mu}{\mu_p + 2\mu} + O(x^5) \quad (5.5)$$

As a result, the cross-sections, in this dipole limit with μ and $\mu_p=1$, are of the form:

$$\sigma_{sca} = \frac{8\pi}{3} k^4 a^6 \left| \frac{\epsilon_p - \epsilon}{\epsilon_p + 2\epsilon} \right|^2 \quad (5.6)$$

$$\sigma_{ext} = 9 \frac{\omega}{c} \epsilon^{3/2} V \frac{\epsilon_2}{[\epsilon_1 + 2\epsilon]^2 + \epsilon_2^2} \quad \text{with } \epsilon_p = \epsilon_1 + i\epsilon_2 \quad (5.7)$$

where V is the volume of the particle.

In the case of metal nanoparticle, the particle is assumed to have the same frequency- dependent permittivity as the bulk metal. The metal permittivity can be approximated by the following Drude model:

$$\epsilon_p(\omega) = 1 - \frac{\omega_p^2}{\omega^2 + i\gamma\omega} \quad (5.8)$$

where ω_p is the bulk plasmon frequency and γ is the damping constant related to electron scattering processes. Substituting Equation 5.8 into Equation 5.7, frequency dependent extinction of a metal particle can be plotted.

Nevertheless, most of the synthesized metal nanoparticle are not perfect sphere but rather ellipsoidal. In this case, an extension of Mie theory, namely Gans theory, can be used. The theory was developed by Richard Gans. With the small particle approximation, the extinction of a collection of randomly oriented gold nanorods with aspect ratio R can be modeled as ³¹¹:

$$\sigma_{ext} = \frac{\omega}{3c} \varepsilon^{3/2} V \sum_j \frac{(1/P_j^2) \varepsilon_2}{\{\varepsilon_1 + [(1-P_j)/P_j] \varepsilon\}^2 + \varepsilon_2^2} \quad (5.9)$$

where P_j is the shape factors determined by the geometry of the three axes $j = A, B$ and C with length L_A, L_B and L_C respectively. For the case of prolate spheroid ($L_A > L_B = L_C$), the shape factors as a function of the aspect ratio $R = L_A/L_B$ is given by:

$$\begin{aligned} P_A &= \frac{1-e^2}{e^2} \left(\frac{1}{2e} \ln \left(\frac{1+e}{1-e} \right) - 1 \right) \\ P_B &= P_C = \frac{1-P_A}{2} \\ e &= \sqrt{1 - \frac{1}{R^2}} \end{aligned} \quad (5.10)$$

Analytical solutions for other particle geometries such as core-shell and multi shell particles can also be derived by extending the Mie theory.³¹²

(ii) Numerical based calculation

Instead of analytically solving Maxwell's equations, numerical techniques can be used. Examples of numerical-based calculations are FIT and FDTD. FIT was developed by Weiland in 1976³¹³. This numerical method utilizes special discretization schemes. It solves the Maxwell's equations by discretizing the following set of integral equations:

$$\begin{aligned}\oint_{\partial A} \vec{E} \cdot d\vec{s} &= -\oint_A \frac{\partial \vec{B}}{\partial t} \cdot d\vec{A} \\ \oint_{\partial A} \vec{H} \cdot d\vec{s} &= \oint_A \left(\frac{\partial \vec{D}}{\partial t} + \vec{J} \right) \cdot d\vec{A} \\ \oint_{\partial V} \vec{D} \cdot d\vec{A} &= \oint_V \rho \cdot dV \\ \oint_{\partial V} \vec{B} \cdot d\vec{A} &= 0\end{aligned}\tag{5.11}$$

In order to numerically solve these equations, a finite calculation domain has to be defined. Then the calculation domain is split into small sub-elements or grid cells by meshing. The Maxwell's equations are then applied and solved for each grid cells. The resolution of the result are dependent on how well refined the grid cells are.

FDTD was first established by Yee³¹⁴ as a three dimensional solution of Maxwell's curl equations:

$$\begin{aligned}\varepsilon \frac{\partial \vec{E}}{\partial t} &= \nabla \times \vec{H} \\ \mu \frac{\partial \vec{H}}{\partial t} &= -\nabla \times \vec{E}\end{aligned}\tag{5.12}$$

The above Maxwell equations in the Cartesian coordinate are given by:

$$\begin{aligned}
\varepsilon_x \frac{\partial E_x}{\partial t} &= \frac{\partial H_z}{\partial y} - \frac{\partial H_y}{\partial z} & \mu_x \frac{\partial H_x}{\partial t} &= \frac{\partial E_y}{\partial z} - \frac{\partial E_z}{\partial y} \\
\varepsilon_y \frac{\partial E_y}{\partial t} &= \frac{\partial H_x}{\partial z} - \frac{\partial H_z}{\partial x} & \mu_y \frac{\partial H_y}{\partial t} &= \frac{\partial E_z}{\partial x} - \frac{\partial E_x}{\partial z} \\
\varepsilon_z \frac{\partial E_z}{\partial t} &= \frac{\partial H_y}{\partial x} - \frac{\partial H_x}{\partial y} & \mu_z \frac{\partial H_z}{\partial t} &= \frac{\partial E_x}{\partial y} - \frac{\partial E_y}{\partial x}
\end{aligned} \tag{5.13}$$

In this technique, the problem space is meshed into Yee cell. Two-point centered difference method is used to calculate the space and time derivatives. For example, the derivative in the z direction of field E at time $n\Delta t$ and the mesh point (i, j, k) is given as³¹⁵:

$$\left. \frac{\partial E}{\partial z} \right|_{i,j,k}^n = \frac{E_{i,j,k+1/2}^n - E_{i,j,k-1/2}^n}{\Delta z} \tag{5.14}$$

The derivatives in time are also discretized but the updating of E and H are staggered in time by one half time step:

$$\left. \frac{\partial E}{\partial t} \right|^{n+1/2} \approx \frac{\bar{E}^{-n+1} - \bar{E}^{-n}}{\Delta t} = \frac{1}{\varepsilon} [\nabla \times \bar{H}]^{n+1/2} \tag{5.15}$$

$$\left. \frac{\partial H}{\partial t} \right|^{n+1} \approx \frac{\bar{H}^{-n+3/2} - \bar{H}^{-n+1/2}}{\Delta t} = -\frac{1}{\mu} [\nabla \times \bar{E}]^{n+1} \tag{5.16}$$

Rearranging the terms, we arrive at the leapfrog-updating algorithm:

$$\bar{E}^{n+1} = \bar{E}^n + \frac{\Delta t}{\epsilon} [\nabla \times \bar{H}]^{n+1/2} \quad (5.17)$$

$$\bar{H}^{n+3/2} = \bar{H}^{n+1/2} - \frac{\Delta t}{\mu} [\nabla \times \bar{E}]^{n+1} \quad (5.18)$$

Using this updating scheme with appropriate boundary and initial conditions, one can arrive at time domain solutions. Frequency domain solutions can be derived by performing Fourier transform. Other numeral techniques such as finite volume time domain (FVTD), finite element method (FEM) and discrete dipole approximation (DDA) can also be used for solving electromagnetic solutions pertaining metal nanostructures.

5.3 Experimental methods

5.3.1 Nanoimprint fabrication of tunable plasmonic substrate

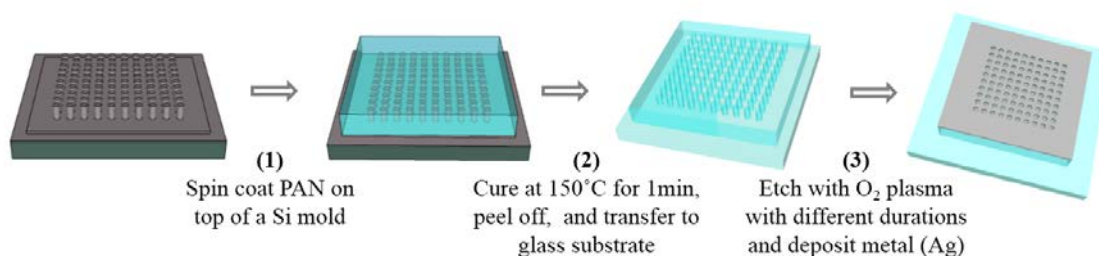


Figure 5.1 Schematic representation of large area plasmonic nanostructures fabrication process by SNAP method. PAN solution is spin coated on top of a Si mold (step 1). The polymer film is then cured at 150°C for one minute and transferred to a glass substrate by simply peeling off the polymer film (step 2). The films are etched at variable etching time, allowing a range of the nano-holes sizes. A 35nm layer of silver (grey color) is then deposited on top of the structure (step 3).

A simple nanofabrication technique, called SNAP technique (a simple spin coating technique), is developed. Large area of nano-patterns can be made from a pre-patterned mold (master mold) by a few simple fabrication steps. In the first step, polymer solution is spun on top of the mold to form a thin film of the polymer. Then, the polymer film is cured and peeled off from the mold. A glass slide with a sticking layer is prepared in advance by spinning a wet layer of the same polymer on top. The peeled film is then transferred to the glass slide by laminating the film on top of the sticking layer. With this technique, the master mold can be made of different materials such as silicon, ceramic, or carbon and can also be fabricated from various types of techniques, for example, electron beam lithography, nanoimprint, and self-assembly. Moreover, nanostructures can be formed on various type of polymers, for instance, polyvinyl alcohol, polysilazane, poly(3,4-ethylenedioxythiophene) polystyrene sulfonate, and polyacrylonitrile. However, the choices of both the master mold and the polymer depend on the surface properties of the two. In this work, electron beam lithographed Si wafer is used as the

master mold due to its high feature qualities. Polyacrylonitrile (PAN) is selected as a material for our imprinted structure owing to its good temperature stability, appropriate surface properties and high elasticity.

The square lattice nanohole arrays of PAN were fabricated using a Si mold with an array of cylindrical pillars, following the SNAP technique, as illustrated in Figure 5.1. First, 8 wt.% solution of PAN was prepared by stirring 4.8g of PAN in 60ml of dimethylformamide at 150 °C. The PAN solution was then spin-coated on the mold at 3000 rpm for 10 seconds. This resulted in nano-hole pattern on top of a $\sim 2\mu\text{m}$ PAN film. The film was cured at 150°C for a minute and transferred to a glass substrate by simply peeling off the polymer film and cementing it on the substrate with the help of thin adhesion layer of the same polymer. With this technique, nano-patterns were created within a few minutes. To further demonstrate, the simplicity of this technique in manipulating the geometries of the fabricated structures, additional fabrication step with common laboratory equipment such as plasma-cleaner was introduced. The hole diameters of fabricated nanohole samples were tuned by the use of, O₂ Plasma (PE50, PlasmaEtch) with different etch time. The plasma power and RF-frequency were set at 20 Watt and 13.56 MHz, respectively. The vacuum set point was 201.1mtorr and the oxygen flow rate was 5 sccm. With the implementation of this tuning scheme, fabrications of nanohole arrays with different hole diameters were possible with the same master mold. The results are shown in the next section. In the next section, this technique is used to fabricate nanohole samples with different plasmon resonances, by simply tuning the size of the nanoholes and depositing metal on top of the structures. Changes in the interactions between light and organic molecules for different plasmon responses were also studied.

5.4 Results and discussion

5.4.1 Coupling Enhancement and Giant Rabi-Splitting in Large Arrays of Tunable Plexcitonic Substrates

When two oscillators are placed in the same vicinity with a mean to exchange their energies, they can become coupled. One of the obvious cases is the case of coupled pendula. The dynamics of the coupled system does not only depend on the original dynamics of the oscillators but also the energy exchange process, in other words, the coupling strength. In the frequency domain, the frequency spectrum of the system is modified and does not resemble the original frequencies. Also, the shape of the spectrum is highly dependent on the coupling strength. When the resonance frequencies of the two oscillators are matched and the coupling strength is stronger than the mean of their decay rates, one can observe an anti-crossing behavior or splitting in the energy spectrum analogously to the bonding and anti-bonding in molecular orbital theory. In this so-called strong coupling regime, there exist two new eigenmodes separated by a certain splitting energy. These new modes are only described by both properties of the original modes. In a sense, they are hybrid states of the two original modes. The magnitude of the splitting is determined by the coupling strength and the splitting is sometimes referred to as Rabi splitting in the case of photon-exciton coupling. Photon-exciton coupling is of scientific interest since controlling interaction between them can result in fascinating new physics. For example, emission spectrum of an atom in a microcavity can be significantly altered³¹⁶⁻³¹⁸. Bose–Einstein condensation at standard cryogenic temperatures can be observed with photon-exciton coupling in semiconductor microcavity³¹⁹. Early reports pertaining photon-exciton coupling deal with atoms, and inorganic semiconductors in microcavity system with Rabi splitting in the order of tens meV³²⁰⁻³²². Strong photon coupling with organic molecules had not been observed until

1998 by the work of Lid zey et al.³²³ In general, organic molecules have very broad spectral linewidths due to inhomogeneous broadening, which make strong coupling difficult to observe. However, this is not always the case. Lid zey et al. integrated organic semiconductor, which has a narrow line width, with a microcavity and observed Rabi splitting as high as 110 meV. Such large splitting was attributed to the high oscillator strength of the organic molecules. The ability to achieve strong coupling with organic semiconductors is very fascinating and has a lot of practical implications since organic semiconductors have used extensively in applications such as electronics, displays, as well as gain media in laser systems. As already mentioned, In order to be in a strong coupling regime and able to observed the splitting, the coupling strength has to be large compared to the spectral line width of the individual oscillators. Therefore, one can achieve strong coupling by decreasing the line width and/or increasing the oscillator strength. In the former case, this is typically done with inorganic semiconductor materials by cooling the samples to decrease the line widths so that Rabi splitting becomes observable. Inorganic semiconductor materials, on the other hand, room temperature strong coupling can be easily achieved because of their large dipole moment. In the latter case, modifying the coupling strength is possible. The coupling strength between light and matter primarily depends on two factors: (1) the dipole moment or the oscillator strength of the matter and (2) the mode volume of the light. The larger the dipole moment and the more confined the mode volume result in the larger coupling strength. For a particular matter, increasing the dipole moment can be done by increasing the number of molecules that are coupled to the light field, resulting in a larger effective dipole moment. This is evident in the case of stronger coupling in semiconductors than single atoms. Confining the mode volume, on the other hand, is achievable with the use of photonic structures such as microcavity, photonic crystals, and plasmonic structures.

Plasmonic structures are very promising candidate for light confinement with regards to photon-exciton coupling. This is because nanoscale light confinement is possible with plasmonic structures. Moreover, plasmonic structures are usually an open cavity. Accessing the mode volume in which the coupling take place is relatively easy, thus enabling probing or measuring physical/chemical properties of the hybrid states. Nevertheless, in order to couple light to matter with the use of plasmonic structures, it is important to have an ability to design and fabricate a structure that has matched optical response to the matter of interest. In this section, the developed fabrication technique for tunable plasmonic substrates will be exploited in photon-exciton coupling to enhance Raman scattering detection.

A series of square lattice nanohole arrays of polyacrylonitrile (PAN) with different diameters were fabricated following the recipe in the Experimental methods. AFM images of the fabricated nanohole arrays with increasing plasma etching time up to 5 min are shown in Figure 5.2(a-f).

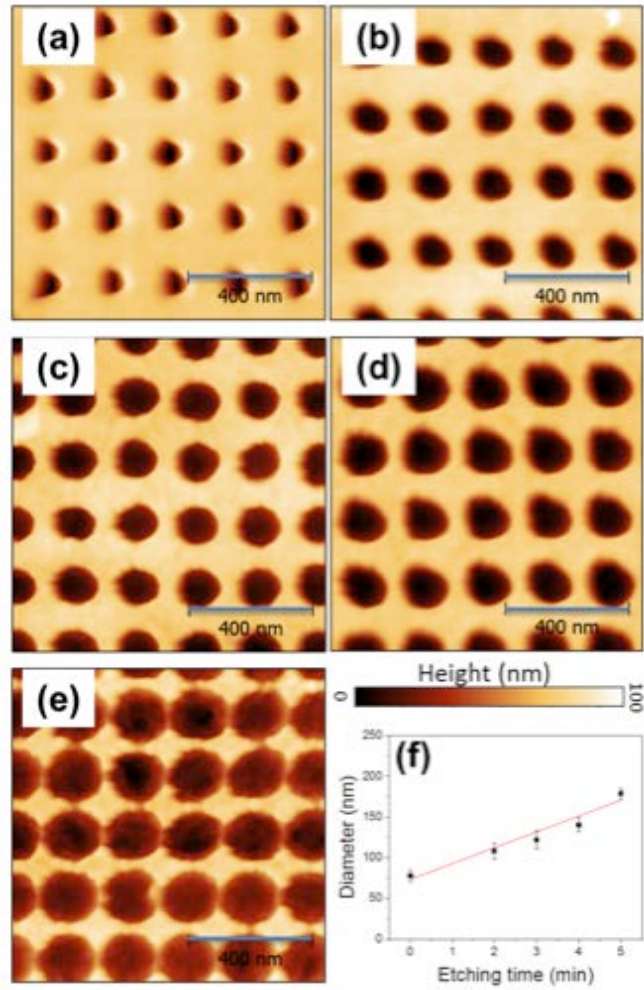


Figure 5.2 AFM images of nanohole structures at etching time of (a) 0min (b) 2min(c) 3min (d) 4min and (e) 5min. Hole diameter vs etching time is plotted in (f)

To develop plasmonic structures, a silver metal thin film of 35 nm thickness was evaporated on the samples with a deposition rate of 0.06 Å/s. The thickness of the silver was monitored using quartz crystal microbalance. A fiber-coupled spectrophotometer (Ocean optics) was used for light extinction measurements, Figure5.3(a).

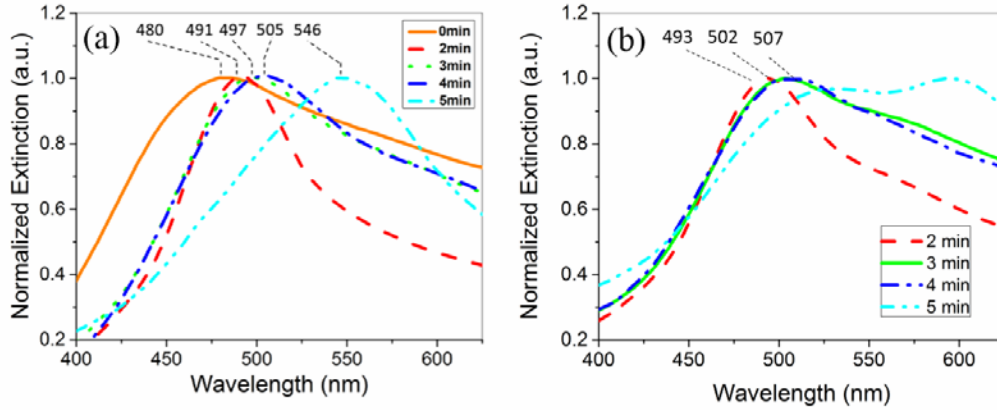


Figure 5.3 (a) Normalized extinction of the plasmonic nanohole samples at different etching time as a function of illumination wavelength. (b) Extinction vs wavelength of plasmonic nanohole samples coated with 1mM of R6G

As can be seen in Figure 5.3(a), the resonance peak of the nanohole arrays is red-shifted with increasing hole diameters. A large red-shift was observed with the 5 minutes etched plasmonic sample. FDTD simulation of the structures was also performed, using commercially available software, Lumerical FDTD Solutions. The nano hole depth profile was modeled by a fourth order super Gaussian curve of the form:

$$z = A \exp(-|r/w|^4) \quad (5.19)$$

where A is the depth of the hole and $2w$ is full width at $1/e$ maximum (FW1/eM). Measured AFM profiles were fit to the function and the fitting parameters were used for FDTD simulations. An example of fitted curves is shown in Figure 5.4(a). The simulated unit cell is shown in Figure 5.4(b). The simulation results are shown in Figure 5.4(c).

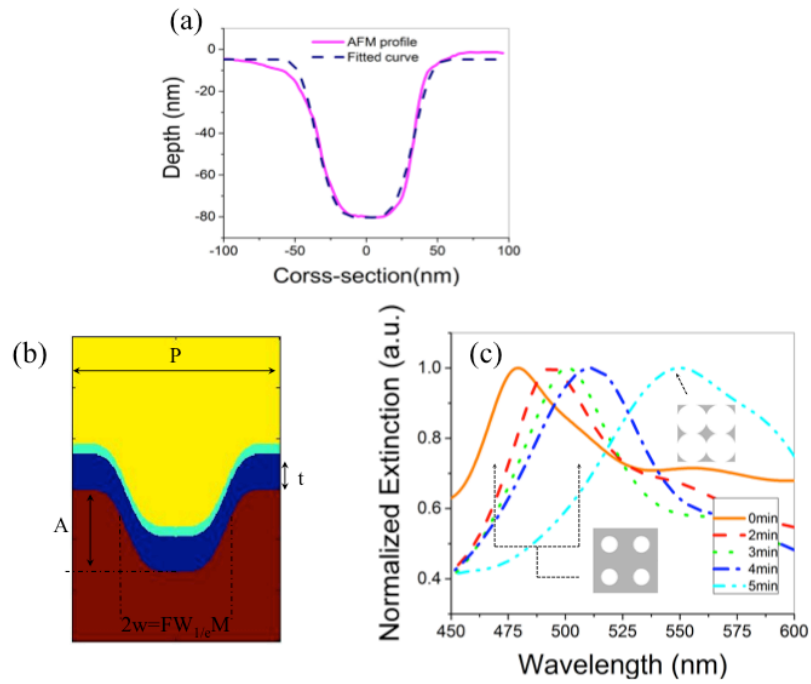


Figure 5.4 (a) AFM profile fitted with fourth order Gaussian function (b) Unit cell for simulation (c) FDTD simulated extinction spectra.

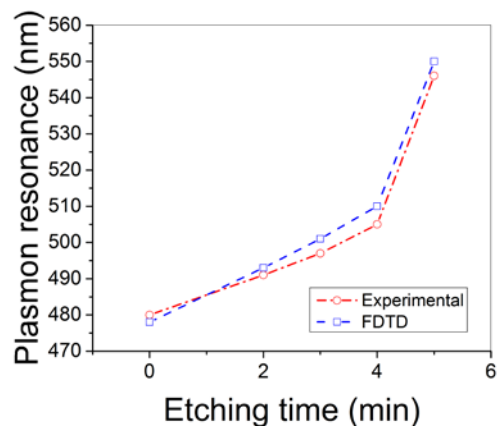


Figure 5.5 Comparison between experimental and simulated plasmon peak for samples with varied etching time

From the FDTD simulations and experimental measurements of our structures, the larger shift at 5 min treatment is attributed to partial merging of adjacent holes, resulting in larger features.

Our FDTD simulations of the plasmon resonance with varied nanohole diameter are in close agreement with the experimental data, Figure 5.4(c) and Figure 5.5. To this point, it is clear that, with this tuning scheme, direct applications such as tunable color filters³⁷⁻³⁸ could easily be derived from this fabrication technique.

By geometrically tuning the optical properties of the substrates, we intend to enhance the Raman signal of the analyte. Several studies have shown the importance of geometry optimization for detection enhancement³⁹⁻⁴⁴. These studies substantiate the importance of optimizing the geometry of the nanostructure in Surface Enhanced Raman Scattering (SERS) applications as well as other optical enhancement processes that involve plasmons and molecular excitons.

To further demonstrate the advanced optical properties of our easy-to-fabricate plasmonic substrates, we measured extinction and Raman scattering of the nanostructures with an overlayer of Rhodamine 6G (R6G) molecules. Only plasma-etched samples were used in this study to ensure that all samples under study have the same surface absorption properties. R6G was used as the analyte because of its excitonic absorption within our tuning range of the substrates.

The extinction spectra of the 1mM R6G coated nanohole samples are shown in Figure 5.3(b). When compared to their corresponding extinction spectra before R6G deposition, the extinction curves of the nanohole samples with the over layer of R6G dyes are not only spectrally shifted but also altered. These observations indicate a coupling between the plasmon mode in the nanosized cavities and molecular excitons of R6G. The coupling of the photon and exciton states can be classified into two distinct regimes, namely weak and strong couplings⁴⁵. In the former regime, the spectral and spatial distributions are modified but the exciton dynamics is only slightly altered. In the latter regime, however, mixing of the states results in strongly

modified excitonic dynamics. From our measurements, we found that the samples with etching time from 2-4 minutes showed a red-shift in their plasmon resonance. In fact, the interaction between plasmon resonance and molecular resonance has been previously studied with nanoparticle systems⁴⁶⁻⁴⁷. Three local maxima were observed when plotting the plasmon shift of R6G coated nanoparticles versus plasmon resonances without the dye (bare plasmon resonance) due to formation of dimers on the metal surface. Local maxima in plasmon shift were observed when bare plasmon resonances were close to the molecular resonance energy. To investigate the properties of R6G films on our plasmonic samples, evolution of absorption spectra of R6G coated on planar silver substrate was studied. Glass slides coated with 20nm thick silver layer were used as substrates in this study. R6G with different concentrations (1-11mM) were spun coated on the substrates at 3000 rpm for 10s. The absorption spectra acquired for each concentration are shown in Figure 5.6 (a). All samples showed increasing absorption from blue to red region due to the presence of the silver layer. Absorption shoulders within the wavelength range of 500-600nm were found. Two absorption peaks at around 518 and 555 nm could clearly be distinguished for the 6 mM and 11 mM sample. The features can be attributed to dimer and monomer absorption²⁰. By subtracting the silver baseline, the spectral profiles of R6G species could be better visualized for low concentration samples. From this concentration dependent study, it was found that all of our R6G samples show two absorption features [Appendix C, Figure C1]. Furthermore, it is known that R6G can form both J-type (head-to-tail dipole moment) and H-type (parallel dipole moment) dimers. Head-to-tail geometry in J-type dimers leads to a decrease in energy whereas parallel geometry in H-type dimer leads to an increase in energy. As a result, the absorption of H-type and J-type dimers is expected to blue shift and red shift from the monomer peak respectively. However, in the case of (silver) surface adsorption, the H-type

conformer is more likely to form due to the adsorption of R6G through one of its N atoms⁴⁸. This supports our observation that H-type dimers are predominantly present in our samples. Similar absorption profile of solid R6G film was previously reported^{20, 49}.

When investigating the effect of R6G on extinction profile of the plasmonic substrates, with 2-4min samples, only small plasmon shifts were observed. Such small shifts are possibly due to the fact that only a few nm thin layer of R6G was coated onto the substrates. However, among these samples, the plasmon shift is the highest with the 3 min sample (497nm bare plasmon resonance). The shift then decreases when the bare plasmon resonance is at a higher wavelength before observing a curve splitting for the 5 min sample. This local maximum of plasmon shift might be due to interaction of plasmon with R6G dimers similar to previous study

46

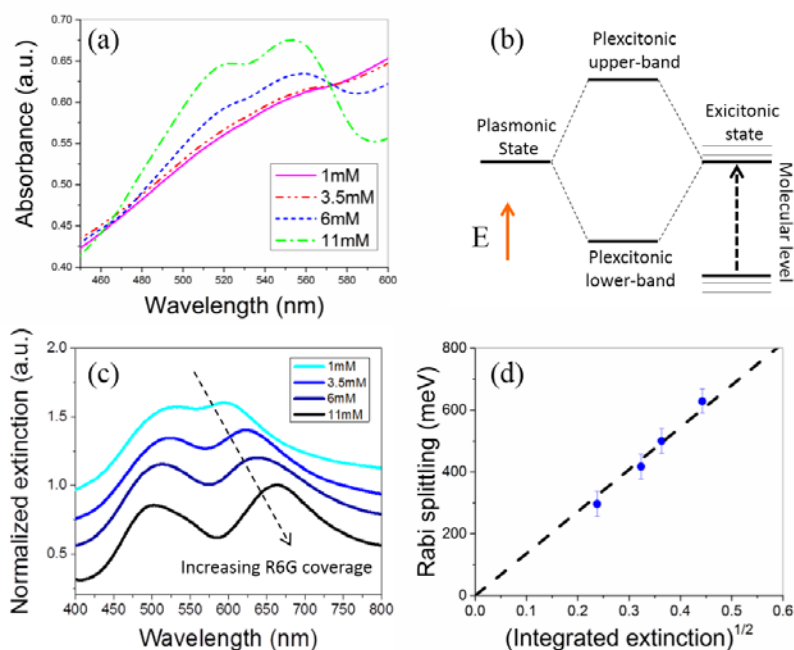


Figure 5.6 (a) Evolution of absorption of 1-11mM R6G deposited on a planar silver film (b) Hybridization diagram of plexcitonic modes (c) Extinction of 5 min etched sample with increasing R6G coverage from 1mM to 11mM (d) The magnitudes of the observed Rabi splitting

versus the square root of the integrated R6G extinction on glass (arbitrary unit). The dash line is a guide to the eyes.

In addition, the 2-4 min samples also show a shoulder at around 550 nm, Figure 5.3(b). The observed shoulders are close to the monomer absorption peak of the R6G dyes (555 nm)²⁰. These absorption shoulders cannot be attributed to the dye absorption alone since they are too intense for the amount of dye molecule used in this experiment. Moreover, their magnitudes vary and do not satisfy Beer's law. However, it was previously found that in a weak coupling regime where the resonance of the photon mode is far from the exciton mode, the spectra of the coupled modes appear similar to the sum of the individual spectrum^{45, 50}. Therefore, we attribute this observed absorption shoulder to weak coupling between plasmon mode in our structures and exciton mode of molecular transition of the dye. On the contrary, the spectrum of the sample with 5 minute etching exhibits a strong anti-crossing behavior with the R6G dye overlayer; the composite spectrum no longer resembles the sum of plasmon resonance and dye absorption. When the optical mode frequency is tuned to the exciton resonance frequency, the two states interact. The splitting at resonance, in analogy with the case of atoms in a microwave cavity, is referred to as the Rabi splitting. When the splitting is large compared to the natural line widths of the optical mode and of the exciton, the strong coupling regime holds and two separate modes are produced⁵¹. Anti-crossing of the coupled modes and the occurrence of two equal intensity transition separated by the vacuum Rabi splitting are indications of a strong coupling. The resulting two new modes in the strong coupling regime can be explained in term of mode hybridization, analogous to the molecular orbital theory, and hybridization diagrams as shown in Figure 5.6(b).

According to the spectrum of the 5 min etched sample without dye (Figure 5.3(a)), the sample has a plasmon resonance at about 547 nm, which is the closest to the R6G monomer peak at 555 nm. It is also possible that the presence of the dye overlayer red shifts the plasmon resonance of the structure such that the energy of the pure plasmon state of the structure is closer to the excitonic state of the dye, resulting in the observed anti-crossing behavior. However, this curve splitting behavior was only observed when plasmon resonance overlaps with the monomer resonance. In the case of dimer resonance, local maximum in plasmon shift was observed.

To prove that the observed splitting is truly caused by Rabi splitting, we measured optical extinction of the 5 min etched film with increasing R6G coverage; in the case of the strong coupling, the coupling strength may depend on the square root of the molecular absorption^{45, 52}. We have also found that the magnitude of the splitting increases with the concentration of R6G deposited, as shown in Figure 5.6(c). The magnitude of the observed splitting occurring in the 5 min etched sample displays a linear dependence with respect to the square root of the integrated extinction of the R6G deposited on glass (Figure 5.6(d)). Thus the results confirm that the observed splitting is in fact due to a strong coupling and is in agreement with previous studies^{11, 53}. In fact, coupling between R6G and nanostructured metal have been previously reported with subsequent Rabi splitting of up to 380 meV⁵⁴⁻⁵⁷. D. Richard et al. reported a Rabi splitting of 380meV in extinction profile of R6G coupled silver nanostructured film at square root integrated extinction of 2.5. P Torma et. al. performed reflectometry measurements in the Kretschmann configuration to study coupling between surface plasmon polaritons and R6G. Maximum Rabi splitting of 200meV was reported. In our measurement, with 11mM deposited R6G or a square root integrated extinction of 0.44, Rabi splitting of 600meV was achieved.

We also performed FDTD simulations of our 5 min sample (180nm diameter) with an overlayer of R6G molecules. In order to account for R6G exciton, its dielectric permittivity was described by the following Lorentz oscillator model:

$$\epsilon_{R6G}(\omega) = \epsilon_{\infty} + \frac{f\omega_0^2}{(\omega_0^2 - \omega^2 - i\gamma_0\omega)} \quad (5.19)$$

where the high frequency component $\epsilon_{\infty}=2.5$, f is the oscillator strength, ω_0 is the resonance frequency of 3.392×10^{15} rad/s, and γ_0 is the exciton line width of 2.14×10^{14} rad/s, derived from the resolved spectra of R6G on silver. Geometrical parameters of the samples and thicknesses of the coatings used in the simulation were measured using AFM. Rabi splitting is also observed with simulations and in very well agreement with the experimental results [Appendix B, Figure B2].

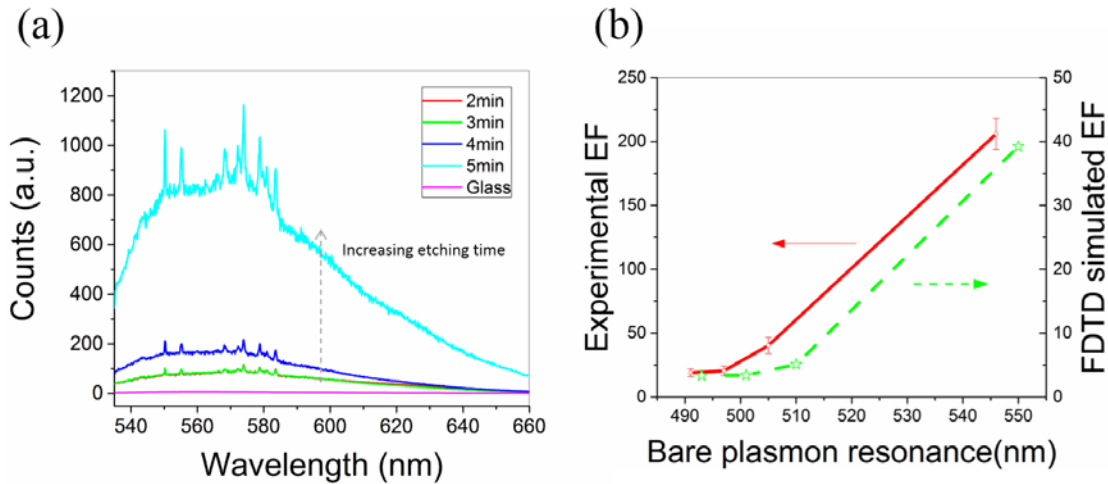


Figure 5.7 (a) Emission spectra of the samples excited with laser wavelength of 532 nm. Both Raman and fluorescence signals are present. (b) Measured and calculated enhancement factor vs. hole diameter.

To deepen our understanding of the effect of hybridization, we measured Raman scatterings from the plexcitonic samples. Raman signals of the samples deposited with the same

concentration of R6G (1 mM) are shown in Figure 5.6 (a). All samples exhibit signal enhancement when compared to sample on bare glass. The samples with 2-3 minutes etching time presented similar intensities of Raman signals and fluorescence background originating from the fluorescence of R6G dye centered at 560 nm⁵⁸. With 4 min etching time, slight increases in Raman intensities as well as the fluorescence intensity were measured. These enhancements can be due to: (1) the bare plasmon resonance peak of this sample is closer to the laser excitation and Stoke shift wavelengths of the dye⁴⁰, and (2) the coupling is stronger than the other two samples since its plasmonic state is closer in energy to the molecular exciton. The sample with 5 minute etching time, however, showed the largest Raman intensities as well as fluorescence background, which is in agreement with the observed strong coupling between the excitonic mode of the dye and the plasmon resonance of the structure. To calculate the enhancement factor, R6G adsorbed on a planar silver substrate is used as a reference to take into account the effect of surface adsorption on the properties of R6G. The analytical enhancement factor (EF) was calculated for these samples from the following equation:

$$EF = \frac{I_s / c_s}{I_{ref} / c_{ref}} \quad (5.20)$$

Where, at any given frequency, I_s is the signal intensity from the plasmon substrate, I_{ref} is the signal intensity from the reference, c_s is the concentration of the dye deposited on the substrate, and c_{ref} is the concentration of the dye deposited on the reference. These experimental enhancement factors of Raman peak at 555.152 nm (775cm⁻¹ Raman shift) are plotted against bare plasmon resonance of the structure in Figure 5.6(b). Finite difference time domain (FDTD) simulation was used to evaluate the expected enhancement factor from our R6G coated 5min sample. Since the Raman enhancement factor is the product of the enhancements in excitation

intensity and scattering intensity due to the presence of metal nanostructures, the FDTD computed EF was obtained using:

$$EF_{FDTD} = |g(\omega_{ex})|^2 |g(\omega_{sca})|^2 \quad (5.21)$$

where $g(\omega) = E_{loc}(\omega)/E_0(\omega)$ with E_{loc} and E_0 being the local and incident field at frequency ω respectively, ω_{exc} is the excitation frequency of 532 nm, and ω_{sca} is the scattering frequency of 555nm. The oscillator strength of R6G of $f=1$ was used since, in simulation, it produces similar peak positions and Rabi splitting magnitude to the experimental values. An analytical approximation of the oscillator strength also gives a similar value [Appendix D]. Figure 5.7 illustrates FDTD calculated EF profiles of the structures at different cross-sections.

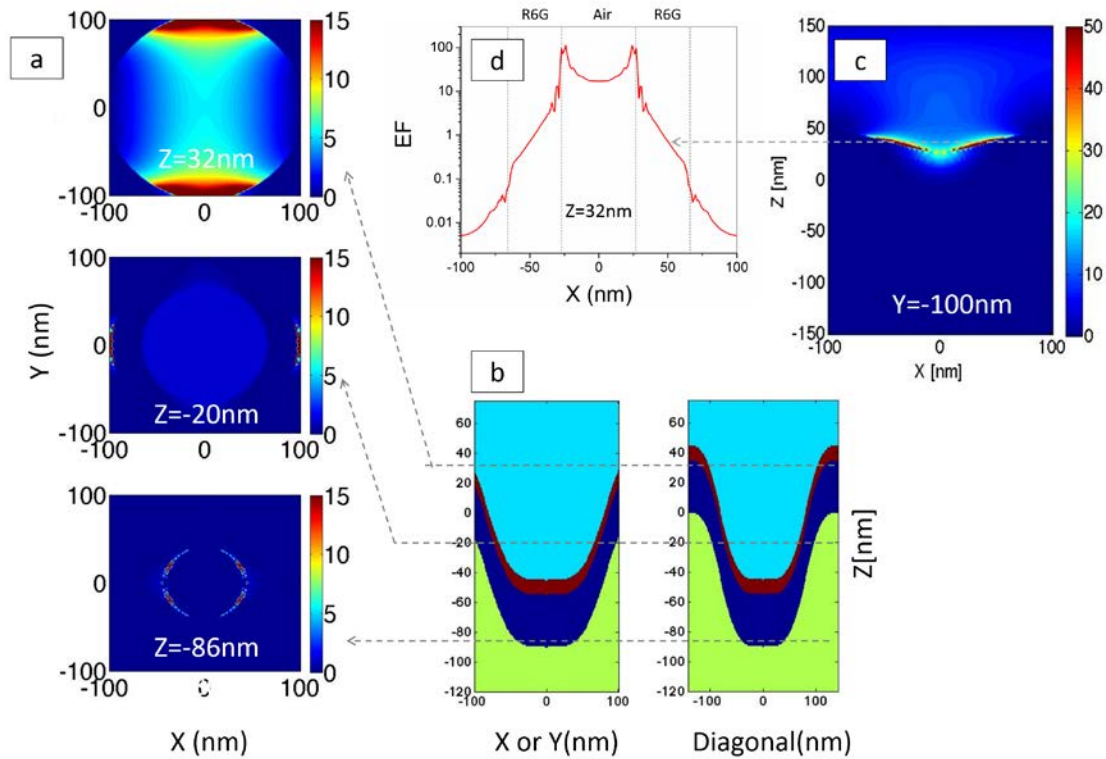


Figure 5.8 (a) EF profiles at different Z cross-sections. Color scales are kept uniform for better comparison (b) Schematic illustrations of the index profile of the simulated structure. (c) EF profile at the middle of the groove where two adjacent holes connect; largest EF within the R6G layer is located here. (d) EF of profile cut along x at z=32nm of the 2D profile in (c).

It has been found that the absolute maximum EF of the overall structure lies at the silver/polymer-substrate interface. Searching algorithm was used to find a local maximum EF with in R6G layer. In the case of 5 min sample, the local maximum EF is determined to be of only 38.87 and located in a groove where two adjacent holes merge. The cross-sectional plot of this hot spot is shown in Figure5.7 (d). The local maximum EFs of other samples were also calculated in the same fashion. These computationally derived maximum local EFs are plotted in Figure5.6(b) against their bare plasmon resonance for comparison. Albeit smaller, these experimentally obtained EFs follow the same trend as the theoretically calculated value. The sample that exhibits strong coupling shows the largest EF. This is because strong intensity enhancements both in the incident and the scattering frequencies are present in the sample. TableD1 in the Appendix D tabulates the calculated intensity enhancements of the incident and scattering frequencies for different etching time. The relative high intensity enhancements at both the incident and scattering frequencies might be due to the splitting and the resulted two resonance peaks that resonate with both frequencies. Increase in Raman intensity with double resonance plasmonic structures have been previously reported ⁵⁹⁻⁶⁰. However, in our case, the origin of the two resonance peaks is the coupling between plasmon and exciton.

One of the possible reasons for smaller calculated EFs might be the fact that only electromagnetic (EM) enhancement is considered in the simulation. In real samples, however, additional enhancement factors from other mechanisms, such as chemical enhancement might be responsible for the increase in the total enhancement factor. In general, three mechanisms are involved in the chemical enchantment, namely (1) ground state chemical interaction (2) resonance Raman enhancement and (3) Charge-transfer (CT) resonance Raman enhancement⁶¹. While, the first mechanism are not associated with any excitations of the nanometal–molecule

system, the latter two, however, require the excitation wavelength being resonant with either molecular transition or nanoparticle–molecule CT transitions for the case of (2) and (3) respectively. Molecules adsorbed at certain surface sites, for example atomic clusters, terraces, and steps, can couple electronically with the surface, leading to the chemical enhancement effect⁶². Experimentally observed chemical enhancements are within an order of magnitude⁶³⁻⁶⁴. However, we cannot neglect that the plasmon resonance and geometrical mismatches between the actual and modeled samples might as well result in the discrepancy. It is also possible that the plexitonic coupling alters Raman scattering cross section of the molecule since in the coupling regime the system is no longer composed of independent plasmon and excitons but rather described by the plexitonic states, similar to polaritons in semiconductor microcavities⁶⁵. Optical cross-sections are altered since electromagnetic enhancement and energy transfer rate between the molecule and metal can no longer be separately treated⁶⁶. Previous studies have shown altered Raman scattering with coupling systems⁶⁶⁻⁶⁷.

Nevertheless, these findings prove the feasibility of our fabrication technique for a tailored interaction between photonic and excitonic modes. Our technique can be used to tune the plasmonic resonance to match the excitonic resonance of the molecules of interest, leading to large enhancement in optical phenomena. This holds great potential for specific targeting of single or a few molecules. For example, the substrate can be tuned to match only the molecular absorption of a specific species, enabling low-level trace detections in sensors.

To summarize, in this section, the fabrication of resonance tunable plasmonic nanostructures in four simple steps: spin coating, peeling off, plasma etching and silver metal deposition was demonstrated. This approach allows high throughput, large area fabrication of plasmonic optical enhancement devices with great versatility. By tuning the plasmon resonance of the nanoholes

arrays, strong plexcitonic coupling could be observed. The ability to tune the resonance wavelength with simple fabrication process can be beneficial for applications such as surface enhanced Raman scattering and surface plasmon enhanced fluorescence. Finally, the largest enhancement in the Raman signals are the result of a strong coupling of the plasmonic states and molecular excitons, unveiling anti-crossing behavior when the resonance of the structure overlaps with the excitonic transition of the dye. Such behavior is believed to be an important step towards active control of all-optical devices and sensors at the nanoscale.

6 CONCLUSION

In this dissertation, the uses of nano and nanostructured materials in optical applications, including laser protection, 3D displays, and sensing, are discussed. In chapter 2, optical limiting properties of various nanomaterials are detailed. In the case of zinc ferrite nanoparticles, it was found that the optical limiting action was improved when Zn atoms in the tetrahedral sites was substituted by other transitional metals such as Cu and Ni. In the case of gold nanoclusters, its effective nonlinear absorption coefficient increases with the cluster size in the nanocluster regime. The value however reduces when the size of the particle make a transition from the nanocluster to nanocrystal. Onset of optical saturation due to surface plasmon resonance was observed in the gold clusters with the number of gold atoms as small as 144. Graphene oxide, on the other hand, showed larger nonlinear optical absorption when functionalized with highly electronegative fluorine atoms. Nonlinear scattering was also increased with the fluorinated samples. Inspired by the F-GO experiment, PA based characterization technique was developed in Chapter 3. It was found that similar nonlinear parameters could be obtained from photoacoustic and optical measurement in the case of nonlinear absorbers. However, nonlinear scatterers show non-complementary behaviors and when these two sets of information are collected simultaneously, erroneous conclusions can be avoided in the case of nonlinear scattering samples. In addition, more rigorous formulation for fitting the PA z-scan data was also introduced. In Chapter 4 of this dissertation, the use of graphenes as light sensitizers in PR polymer composite was studied. It was found that the addition of graphenes led to increase in the fast time constant of the PR composite. These findings make graphene very promising sensitizers for developing fast-response 3D holographic media. Facile nanofabrication technique for

producing metallic nanostructures with tunable plasmon resonance was introduced, in Chapter 5. Enhancing light-matter interaction, i.e. Raman scattering, with the developed platform was demonstrated. All in all, this dissertation demonstrates the versatility of nano and nanostructured materials in various optical applications. In terms of material engineering, unique properties of newly developed or unexplored nanomaterials might open the way for new applications as well as advancing the existing ones.

**APPENDIX A: COPYRIGHT PERMISSIONS FOR RELEVANT
PUBLICATIONS UPON WHICH THIS DISSERTATION IS BASED ON IN
PART**

**AIP PUBLISHING LLC LICENSE
TERMS AND CONDITIONS**

Feb 15, 2015

All payments must be made in full to CCC. For payment instructions, please see information listed at the bottom of this form.

License Number	3570370624847
Order Date	Feb 15, 2015
Publisher	AIP Publishing LLC
Publication	Applied Physics Letters
Article Title	Enhanced optical limiting in nanosized mixed zinc ferrites
Author	Panit Chantharasupawong, Reji Philip, Tamio Endo, et al.
Online Publication Date	May 30, 2012
Volume number	100
Issue number	22
Type of Use	Thesis/Dissertation
Requestor type	Author (original article)
Format	Print and electronic
Portion	Figure/Table
Number of figures/tables	5
Title of your thesis / dissertation	Nano and nanostructured materials for optical applications
Expected completion date	Apr 2015
Estimated size (number of pages)	200
Total	0.00 USD

Terms and Conditions

AIP Publishing LLC — Terms and Conditions: Permissions Uses

AIP Publishing LLC ("AIPP") hereby grants to you the non-exclusive right and license to use and/or distribute the Material according to the use specified in your order, on a one-time basis, for the specified term, with a maximum distribution equal to the number that you have ordered. Any links or other content accompanying the Material are not the subject of this license.

1. You agree to include the following copyright and permission notice with the reproduction of the Material: "Reprinted with permission from [FULL CITATION]. Copyright [PUBLICATION YEAR], AIP Publishing LLC." For an article, the copyright and permission notice must be printed on the first page of the article or book chapter. For photographs, covers, or tables, the copyright and permission notice may appear with the Material, in a footnote, or in the reference list.
2. If you have licensed reuse of a figure, photograph, cover, or table, it is your responsibility to ensure that the material is original to AIPP and does not contain the copyright of another entity, and that the copyright notice of the figure, photograph, cover, or table does not indicate that it was reprinted by AIPP, with permission, from another source. Under no circumstances does AIPP, purport or intend to grant permission to reuse material to which it does not hold copyright.
3. You may not alter or modify the Material in any manner. You may translate the Material into another language only if you have licensed translation rights. You may not use the Material for promotional purposes. AIPP reserves all rights not specifically granted herein.
4. The foregoing license shall not take effect unless and until AIPP or its agent, Copyright Clearance Center, receives the Payment in accordance with Copyright Clearance Center Billing and Payment Terms and Conditions, which are incorporated herein by reference.
5. AIPP or the Copyright Clearance Center may, within two business days of granting this

<https://s100.copyright.com/App/PrintableLicenseFrame.jsp?publisherID=43&publisherName=aip&publication=APPLAB&publicationID=1840&rightID=1&typ...> 1/2

license, revoke the license for any reason whatsoever, with a full refund payable to you. Should you violate the terms of this license at any time, AIPP, AIP Publishing LLC, or Copyright Clearance Center may revoke the license with no refund to you. Notice of such revocation will be made using the contact information provided by you. Failure to receive such notice will not nullify the revocation.

6. AIPP makes no representations or warranties with respect to the Material. You agree to indemnify and hold harmless AIPP, AIP Publishing LLC, and their officers, directors, employees or agents from and against any and all claims arising out of your use of the Material other than as specifically authorized herein.
7. The permission granted herein is personal to you and is not transferable or assignable without the prior written permission of AIPP. This license may not be amended except in a writing signed by the party to be charged.
8. If purchase orders, acknowledgments or check endorsements are issued on any forms containing terms and conditions which are inconsistent with these provisions, such inconsistent terms and conditions shall be of no force and effect. This document, including the CCC Billing and Payment Terms and Conditions, shall be the entire agreement between the parties relating to the subject matter hereof.

This Agreement shall be governed by and construed in accordance with the laws of the State of New York. Both parties hereby submit to the jurisdiction of the courts of New York County for purposes of resolving any disputes that may arise hereunder.

Questions? customercare@copyright.com or +1-855-239-3415 (toll free in the US) or +1-978-646-2777.

Gratis licenses (referencing \$0 in the Total field) are free. Please retain this printable license for your reference. No payment is required.

**AIP PUBLISHING LLC LICENSE
TERMS AND CONDITIONS**

Feb 15, 2015

All payments must be made in full to CCC. For payment instructions, please see information listed at the bottom of this form.

License Number	3570370782680
Order Date	Feb 15, 2015
Publisher	AIP Publishing LLC
Publication	Applied Physics Letters
Article Title	Enhanced optical limiting in nanosized mixed zinc ferrites
Author	Panit Chantharasupawong, Reji Philip, Tamio Endo, et al.
Online Publication Date	May 30, 2012
Volume number	100
Issue number	22
Type of Use	Thesis/Dissertation
Requestor type	Author (original article)
Format	Print and electronic
Portion	Excerpt (> 800 words)
Will you be translating?	No
Title of your thesis / dissertation	Nano and nanostructured materials for optical applications
Expected completion date	Apr 2015
Estimated size (number of pages)	200
Total	0.00 USD

Terms and Conditions

AIP Publishing LLC — Terms and Conditions: Permissions Uses

AIP Publishing LLC ("AIPP") hereby grants to you the non-exclusive right and license to use and/or distribute the Material according to the use specified in your order, on a one-time basis, for the specified term, with a maximum distribution equal to the number that you have ordered. Any links or other content accompanying the Material are not the subject of this license.

1. You agree to include the following copyright and permission notice with the reproduction of the Material: "Reprinted with permission from [FULL CITATION]. Copyright [PUBLICATION YEAR], AIP Publishing LLC." For an article, the copyright and permission notice must be printed on the first page of the article or book chapter. For photographs, covers, or tables, the copyright and permission notice may appear with the Material, in a footnote, or in the reference list.
2. If you have licensed reuse of a figure, photograph, cover, or table, it is your responsibility to ensure that the material is original to AIPP and does not contain the copyright of another entity, and that the copyright notice of the figure, photograph, cover, or table does not indicate that it was reprinted by AIPP, with permission, from another source. Under no circumstances does AIPP, purport or intend to grant permission to reuse material to which it does not hold copyright.
3. You may not alter or modify the Material in any manner. You may translate the Material into another language only if you have licensed translation rights. You may not use the Material for promotional purposes. AIPP reserves all rights not specifically granted herein.
4. The foregoing license shall not take effect unless and until AIPP or its agent, Copyright Clearance Center, receives the Payment in accordance with Copyright Clearance Center Billing and Payment Terms and Conditions, which are incorporated herein by reference.
5. AIPP or the Copyright Clearance Center may, within two business days of granting this

<https://s100.copyright.com/App/PrintableLicenseFrame.jsp?publisherID=43&publisherName=aip&publication=APPLAB&publicationID=1840&rightID=1&typ...> 1/2

license, revoke the license for any reason whatsoever, with a full refund payable to you. Should you violate the terms of this license at any time, AIPP, AIP Publishing LLC, or Copyright Clearance Center may revoke the license with no refund to you. Notice of such revocation will be made using the contact information provided by you. Failure to receive such notice will not nullify the revocation.

6. AIPP makes no representations or warranties with respect to the Material. You agree to indemnify and hold harmless AIPP, AIP Publishing LLC, and their officers, directors, employees or agents from and against any and all claims arising out of your use of the Material other than as specifically authorized herein.
7. The permission granted herein is personal to you and is not transferable or assignable without the prior written permission of AIPP. This license may not be amended except in a writing signed by the party to be charged.
8. If purchase orders, acknowledgments or check endorsements are issued on any forms containing terms and conditions which are inconsistent with these provisions, such inconsistent terms and conditions shall be of no force and effect. This document, including the CCC Billing and Payment Terms and Conditions, shall be the entire agreement between the parties relating to the subject matter hereof.

This Agreement shall be governed by and construed in accordance with the laws of the State of New York. Both parties hereby submit to the jurisdiction of the courts of New York County for purposes of resolving any disputes that may arise hereunder.

Questions? customercare@copyright.com or +1-855-239-3415 (toll free in the US) or +1-978-646-2777.

Gratis licenses (referencing \$0 in the Total field) are free. Please retain this printable license for your reference. No payment is required.



RightsLink®

[Home](#)
[Create Account](#)
[Help](#)


ACS Publications
Most Trusted. Most Cited. Most Read.

Title: Optical Power Limiting in Fluorinated Graphene Oxide: An Insight into the Nonlinear Optical Properties

Author: Panit Chantharasupawong, Reji Philip, Narayanan T. Narayanan, et al

Publication: The Journal of Physical Chemistry C

Publisher: American Chemical Society

Date: Dec 1, 2012

Copyright © 2012, American Chemical Society

[LOGIN](#)

If you're a [copyright.com](#) user, you can login to RightsLink using your [copyright.com](#) credentials. Already a [RightsLink](#) user or want to [learn more?](#)

PERMISSION/LICENSE IS GRANTED FOR YOUR ORDER AT NO CHARGE

This type of permission/license, instead of the standard Terms & Conditions, is sent to you because no fee is being charged for your order. Please note the following:

- Permission is granted for your request in both print and electronic formats, and translations.
- If figures and/or tables were requested, they may be adapted or used in part.
- Please print this page for your records and send a copy of it to your publisher/graduate school.
- Appropriate credit for the requested material should be given as follows: "Reprinted (adapted) with permission from (COMPLETE REFERENCE CITATION). Copyright (YEAR) American Chemical Society." Insert appropriate information in place of the capitalized words.
- One-time permission is granted only for the use specified in your request. No additional uses are granted (such as derivative works or other editions). For any other uses, please submit a new request.

[BACK](#)
[CLOSE WINDOW](#)

Copyright © 2015 [Copyright Clearance Center, Inc.](#) All Rights Reserved. [Privacy statement.](#) Comments? We would like to hear from you. E-mail us at customercare@copyright.com



RightsLink®

[Home](#)
[Create Account](#)
[Help](#)


Title: Evolution of Nonlinear Optical Properties: From Gold Atomic Clusters to Plasmonic Nanocrystals

Author: Reji Philip, Panit Chantharasupawong, Huifeng Qian, et al

Publication: Nano Letters

Publisher: American Chemical Society

Date: Sep 1, 2012

Copyright © 2012, American Chemical Society

[LOGIN](#)

If you're a [copyright.com](#) user, you can login to RightsLink using your [copyright.com](#) credentials. Already a [RightsLink](#) user or want to [learn more?](#)

PERMISSION/LICENSE IS GRANTED FOR YOUR ORDER AT NO CHARGE

This type of permission/license, instead of the standard Terms & Conditions, is sent to you because no fee is being charged for your order. Please note the following:

- Permission is granted for your request in both print and electronic formats, and translations.
- If figures and/or tables were requested, they may be adapted or used in part.
- Please print this page for your records and send a copy of it to your publisher/graduate school.
- Appropriate credit for the requested material should be given as follows: "Reprinted (adapted) with permission from (COMPLETE REFERENCE CITATION). Copyright (YEAR) American Chemical Society." Insert appropriate information in place of the capitalized words.
- One-time permission is granted only for the use specified in your request. No additional uses are granted (such as derivative works or other editions). For any other uses, please submit a new request.

[BACK](#)
[CLOSE WINDOW](#)

Copyright © 2015 [Copyright Clearance Center, Inc.](#) All Rights Reserved. [Privacy statement.](#) Comments? We would like to hear from you. E-mail us at customercare@copyright.com

AIP PUBLISHING LLC LICENSE TERMS AND CONDITIONS

Feb 15, 2015

All payments must be made in full to CCC. For payment instructions, please see information listed at the bottom of this form.

License Number	3570370022248
Order Date	Feb 15, 2015
Publisher	AIP Publishing LLC
Publication	Applied Physics Letters
Article Title	Simultaneous optical and photoacoustic measurement of nonlinear absorption
Author	Panil Chantharasupawong,Reiji Philip,Jayan Thomas
Online Publication Date	Feb 1, 2013
Volume number	102
Issue number	4
Type of Use	Thesis/Dissertation
Requestor type	Author (original article)
Format	Print and electronic
Portion	Excerpt (> 800 words)
Will you be translating?	No
Title of your thesis / dissertation	Nano and nanostructured materials for optical applications
Expected completion date	Apr 2015
Estimated size (number of pages)	200
Total	0.00 USD

[Terms and Conditions](#)

AIP Publishing LLC -- Terms and Conditions: Permissions Uses

AIP Publishing LLC ("AIPP") hereby grants to you the non-exclusive right and license to use and/or distribute the Material according to the use specified in your order, on a one-time basis, for the specified term, with a maximum distribution equal to the number that you have ordered. Any links or other content accompanying the Material are not the subject of this license.

1. You agree to include the following copyright and permission notice with the reproduction of the Material: "Reprinted with permission from [FULL CITATION]. Copyright [PUBLICATION YEAR], AIP Publishing LLC." For an article, the copyright and permission notice must be printed on the first page of the article or book chapter. For photographs, covers, or tables, the copyright and permission notice may appear with the Material, in a footnote, or in the reference list.
2. If you have licensed reuse of a figure, photograph, cover, or table, it is your responsibility to ensure that the material is original to AIPP and does not contain the copyright of another entity, and that the copyright notice of the figure, photograph, cover, or table does not indicate that it was reprinted by AIPP, with permission, from another source. Under no circumstances does AIPP, purport or intend to grant permission to reuse material to which it does not hold copyright.
3. You may not alter or modify the Material in any manner. You may translate the Material into another language only if you have licensed translation rights. You may not use the Material for promotional purposes. AIPP reserves all rights not specifically granted herein.
4. The foregoing license shall not take effect unless and until AIPP or its agent, Copyright Clearance Center, receives the Payment in accordance with Copyright Clearance Center Billing and Payment Terms and Conditions, which are incorporated herein by reference.
5. AIPP or the Copyright Clearance Center may, within two business days of granting this license, revoke the license for any reason whatsoever, with a full refund payable to you. Should you violate the terms of this license at any time, AIPP, AIP Publishing LLC, or Copyright Clearance Center may revoke the license with no refund to you. Notice of such revocation will be made using the contact information provided by you. Failure to receive

2/15/2015

RightsLink - Your Account

- such notice will not nullify the revocation.
6. AIPP makes no representations or warranties with respect to the Material. You agree to indemnify and hold harmless AIPP, AIP Publishing LLC, and their officers, directors, employees or agents from and against any and all claims arising out of your use of the Material other than as specifically authorized herein.
 7. The permission granted herein is personal to you and is not transferable or assignable without the prior written permission of AIPP. This license may not be amended except in a writing signed by the party to be charged.
 8. If purchase orders, acknowledgments or check endorsements are issued on any forms containing terms and conditions which are inconsistent with these provisions, such inconsistent terms and conditions shall be of no force and effect. This document, including the CCC Billing and Payment Terms and Conditions, shall be the entire agreement between the parties relating to the subject matter hereof.

This Agreement shall be governed by and construed in accordance with the laws of the State of New York. Both parties hereby submit to the jurisdiction of the courts of New York County for purposes of resolving any disputes that may arise hereunder.

Questions? customercare@copyright.com or +1-855-239-3415 (toll free in the US) or +1-978-646-2777.

Gratis licenses (referencing \$0 in the Total field) are free. Please retain this printable license for your reference. No payment is required.

**AIP PUBLISHING LLC LICENSE
TERMS AND CONDITIONS**

Feb 15, 2015

All payments must be made in full to CCC. For payment instructions, please see information listed at the bottom of this form.

License Number	3570370309201
Order Date	Feb 15, 2015
Publisher	AIP Publishing LLC
Publication	Applied Physics Letters
Article Title	Simultaneous optical and photoacoustic measurement of nonlinear absorption
Author	Panit Chantharasupawong, Reji Philip, Jayan Thomas
Online Publication Date	Feb 1, 2013
Volume number	102
Issue number	4
Type of Use	Thesis/Dissertation
Requestor type	Author (original article)
Format	Print and electronic
Portion	Figure/Table
Number of figures/tables	4
Title of your thesis / dissertation	Nano and nanostructured materials for optical applications
Expected completion date	Apr 2015
Estimated size (number of pages)	200
Total	0.00 USD

Terms and Conditions

AIP Publishing LLC — Terms and Conditions: Permissions Uses

AIP Publishing LLC ("AIPP") hereby grants to you the non-exclusive right and license to use and/or distribute the Material according to the use specified in your order, on a one-time basis, for the specified term, with a maximum distribution equal to the number that you have ordered. Any links or other content accompanying the Material are not the subject of this license.

1. You agree to include the following copyright and permission notice with the reproduction of the Material: "Reprinted with permission from [FULL CITATION]. Copyright [PUBLICATION YEAR], AIP Publishing LLC." For an article, the copyright and permission notice must be printed on the first page of the article or book chapter. For photographs, covers, or tables, the copyright and permission notice may appear with the Material, in a footnote, or in the reference list.
2. If you have licensed reuse of a figure, photograph, cover, or table, it is your responsibility to ensure that the material is original to AIPP and does not contain the copyright of another entity, and that the copyright notice of the figure, photograph, cover, or table does not indicate that it was reprinted by AIPP, with permission, from another source. Under no circumstances does AIPP, purport or intend to grant permission to reuse material to which it does not hold copyright.
3. You may not alter or modify the Material in any manner. You may translate the Material into another language only if you have licensed translation rights. You may not use the Material for promotional purposes. AIPP reserves all rights not specifically granted herein.
4. The foregoing license shall not take effect unless and until AIPP or its agent, Copyright Clearance Center, receives the Payment in accordance with Copyright Clearance Center Billing and Payment Terms and Conditions, which are incorporated herein by reference.

<https://s100.copyright.com/App/PrintableLicenseFrame.jsp?publisherID=43&publisherName=aip&publication=APPLAB&publicationID=1840&rightID=1&typ...> 1/2

5. AIPP or the Copyright Clearance Center may, within two business days of granting this license, revoke the license for any reason whatsoever, with a full refund payable to you. Should you violate the terms of this license at any time, AIPP, AIP Publishing LLC, or Copyright Clearance Center may revoke the license with no refund to you. Notice of such revocation will be made using the contact information provided by you. Failure to receive such notice will not nullify the revocation.
6. AIPP makes no representations or warranties with respect to the Material. You agree to indemnify and hold harmless AIPP, AIP Publishing LLC, and their officers, directors, employees or agents from and against any and all claims arising out of your use of the Material other than as specifically authorized herein.
7. The permission granted herein is personal to you and is not transferable or assignable without the prior written permission of AIPP. This license may not be amended except in a writing signed by the party to be charged.
8. If purchase orders, acknowledgments or check endorsements are issued on any forms containing terms and conditions which are inconsistent with these provisions, such inconsistent terms and conditions shall be of no force and effect. This document, including the CCC Billing and Payment Terms and Conditions, shall be the entire agreement between the parties relating to the subject matter hereof.

This Agreement shall be governed by and construed in accordance with the laws of the State of New York. Both parties hereby submit to the jurisdiction of the courts of New York County for purposes of resolving any disputes that may arise hereunder.

Questions? customercare@copyright.com or +1-855-239-3415 (toll free in the US) or +1-978-646-2777.

Gratis licenses (referencing \$0 in the Total field) are free. Please retain this printable license for your reference. No payment is required.

Photorefractive performances of a graphene-doped PATPD/7-DCST/ECZ composite

P. Chantharasupawong, C. W. Christenson, R. Philip, L. Zhai, J. Winiarz, M. Yamamoto, L. Tetard, R. R. Nair and J. Thomas, *J. Mater. Chem. C*, 2014, **2**, 7639

DOI: 10.1039/C4TC00782D

If you are not the author of this article and you wish to reproduce material from it in a third party non-RSC publication you must [formally request permission](#) using RightsLink. Go to our [Instructions for using RightsLink page](#) for details.

Authors contributing to RSC publications (journal articles, books or book chapters) do not need to formally request permission to reproduce material contained in this article provided that the correct acknowledgement is given with the reproduced material.

Reproduced material should be attributed as follows:

- For reproduction of material from NJC:
Reproduced from Ref. XX with permission from the Centre National de la Recherche Scientifique (CNRS) and The Royal Society of Chemistry.
- For reproduction of material from PCCP:
Reproduced from Ref. XX with permission from the PCCP Owner Societies.
- For reproduction of material from PPS:
Reproduced from Ref. XX with permission from the European Society for Photobiology, the European Photochemistry Association, and The Royal Society of Chemistry.
- For reproduction of material from all other RSC journals and books:
Reproduced from Ref. XX with permission from The Royal Society of Chemistry.

If the material has been adapted instead of reproduced from the original RSC publication "Reproduced from" can be substituted with "Adapted from".

In all cases the Ref. XX is the XXth reference in the list of references.

If you are the author of this article you do not need to formally request permission to reproduce figures, diagrams etc. contained in this article in third party publications or in a thesis or dissertation provided that the correct acknowledgement is given with the reproduced material.

Reproduced material should be attributed as follows:

- For reproduction of material from NJC:
[Original citation] - Reproduced by permission of The Royal Society of Chemistry (RSC) on behalf of the Centre National de la Recherche Scientifique (CNRS) and the RSC
- For reproduction of material from PCCP:
[Original citation] - Reproduced by permission of the PCCP Owner Societies
- For reproduction of material from PPS:
[Original citation] - Reproduced by permission of The Royal Society of Chemistry (RSC) on behalf of the European Society for Photobiology, the European Photochemistry Association, and RSC
- For reproduction of material from all other RSC journals:
[Original citation] - Reproduced by permission of The Royal Society of Chemistry

If you are the author of this article you still need to obtain permission to reproduce the whole article in a third party publication with the exception of reproduction of the whole article in a thesis or dissertation.

Information about reproducing material from RSC articles with different licences is available on our

<http://pubs.rsc.org.ezproxy.net.ucf.edu/en/content/requestpermission?msid=c4tc00782d>

1/2

2/15/2015

Request Permission

[Permission Requests page.](#)

<http://pubs.rsc.org/ezproxy.net.ucf.edu/en/content/requestpermission?msid=c4c00782d>

2/2



RightsLink®

[Home](#)
[Create Account](#)
[Help](#)


Title: Coupling Enhancement and Giant Rabi-Splitting in Large Arrays of Tunable Plexcitonic Substrates

Author: Panit Chantharasupawong, Laurene Tetard, Jayan Thomas

Publication: The Journal of Physical Chemistry C

Publisher: American Chemical Society

Date: Oct 1, 2014

Copyright © 2014, American Chemical Society

[LOGIN](#)

If you're a [copyright.com](#) user, you can login to RightsLink using your [copyright.com](#) credentials. Already a [RightsLink](#) user or want to [learn more?](#)

PERMISSION/LICENSE IS GRANTED FOR YOUR ORDER AT NO CHARGE

This type of permission/license, instead of the standard Terms & Conditions, is sent to you because no fee is being charged for your order. Please note the following:

- Permission is granted for your request in both print and electronic formats, and translations.
- If figures and/or tables were requested, they may be adapted or used in part.
- Please print this page for your records and send a copy of it to your publisher/graduate school.
- Appropriate credit for the requested material should be given as follows: "Reprinted (adapted) with permission from (COMPLETE REFERENCE CITATION). Copyright (YEAR) American Chemical Society." Insert appropriate information in place of the capitalized words.
- One-time permission is granted only for the use specified in your request. No additional uses are granted (such as derivative works or other editions). For any other uses, please submit a new request.

If credit is given to another source for the material you requested, permission must be obtained from that source.

[BACK](#)
[CLOSE WINDOW](#)

Copyright © 2015 [Copyright Clearance Center, Inc.](#) All Rights Reserved. [Privacy statement.](#) Comments? We would like to hear from you. E-mail us at customercare@copyright.com

**APPENDIX B: STEADY STATE DIFFRACTION EFFICIENCIES OF
PATPD/7-DCST/ECZ COMPOSITES**

Steady state four wave mixing measurements

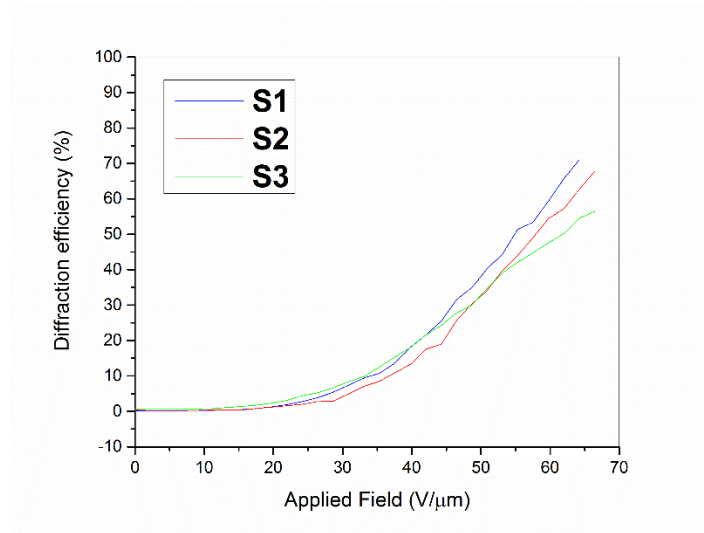
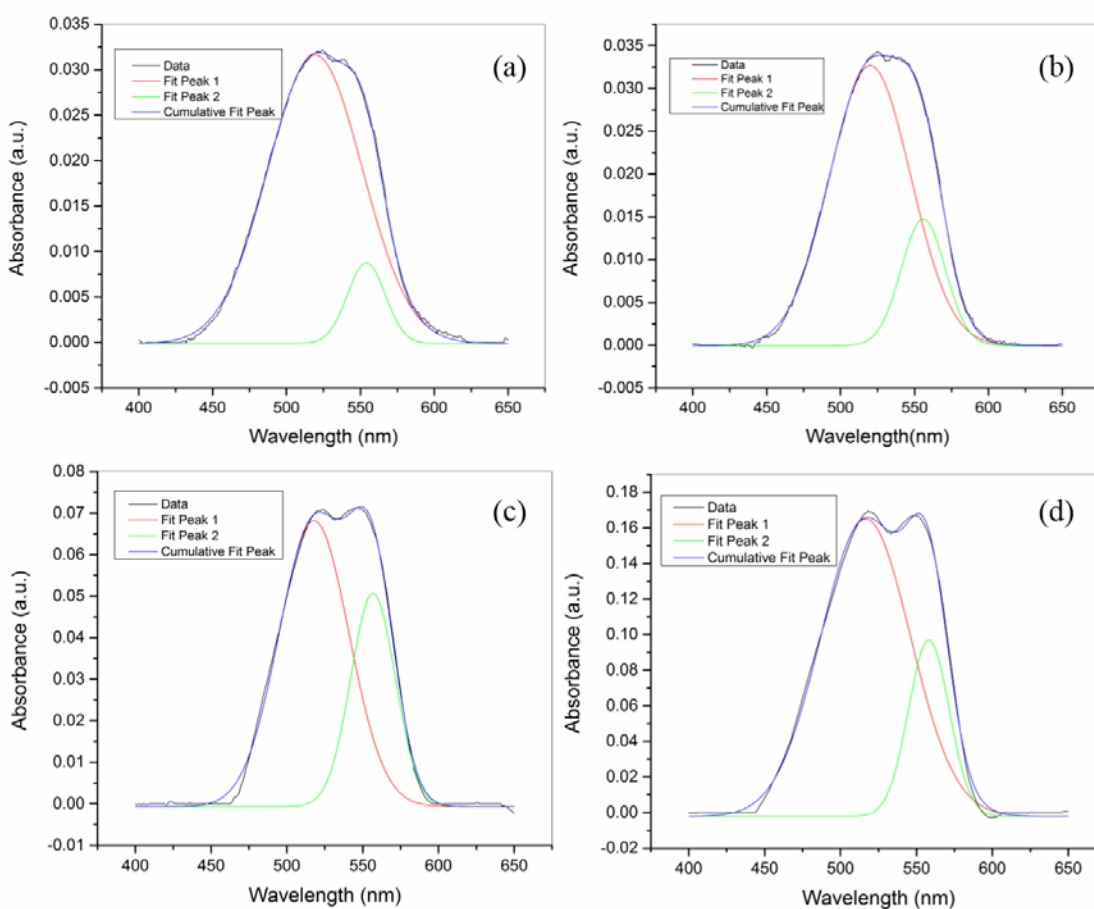


Figure B1. Steady state diffraction efficiencies of S1 (undoped) ,S2 (graphene-doped) and S3 (PCBM-doped). All samples show similar diffraction efficiencies.

**APPENDIX C: RESOLVED ABSORPTION SPECTRA OF R6G ON
PLANAR SILVER SURFACE**

R6G with concentration ranging from 1 to 11mM was deposited on a 20 nm silver coated glass slide using a spin coater at 3000rpm for 10s. The absorption spectra of the samples are plotted in Figure 5.6a. By subtracting the baseline of silver film, resolved R6G spectra were obtained. The result spectra are plotted in Figure C1(a-d). All samples show dimer and monomer absorption bands possibly due to surface induced aggregation at the silver surface.



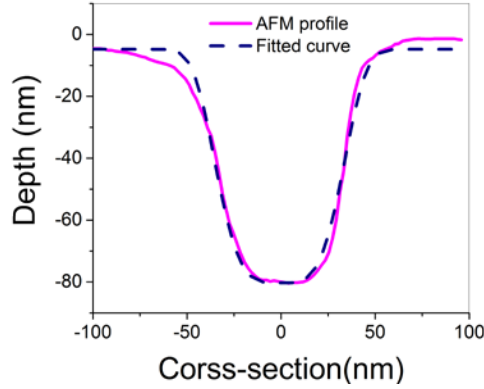
FigureC1. Resolved R6G spectra on silver surface for (a)1mM (b)3.5mM (c)6mM and (d) 11mM. The spectra are also deconvoluted with multiple Gaussian curves, showing both dimer and monomer bands.

**APPENDIX D: FDTD CALCULATION OF RAMAN ENHANCEMENT
FACTORS OF NANOIMPRINTED NANOHOLES**

We modeled our nano hole depth profile using a fourth order super Gaussian curve of the form:

$$z = A \exp(-|r/w|^4) \quad (D1)$$

where A is the depth of the hole and 2w is full width at 1/e maximum (FW1/eM). Measured AFM profiles were fit to the function and the fitting parameters were used for FDTD simulations. An example of fitted curves is shown in FigureB3.



FigureD1 Measured AFM profile and a best-fit curve to Equation(D1) for 0min sample

The simulated unit cell is shown in Figure D2(a). To check validity of our model, extinction spectra of our structures were simulated using the FDTD with parameters obtained from the AFM profile. The simulation results, Figure D2(b-c) is in close agreement with the experimental data. Large red-shift in the simulation is observed with the 5min sample as a result of partial merging of the holes, in very well agreement with the experimental measurement. Then, this model was used to simulate the Rabi splitting. In the simulation, a 10nm layer of R6G was coated on top of the structure. The R6G was modeled as a dispersive medium with dielectric permittivity described by Lorentz model:

$$\epsilon_{R6G}(\omega) = \epsilon_{\infty} + \frac{f\omega_0^2}{(\omega_0^2 - \omega^2 - i\gamma_0\omega)} \quad (D2)$$

where the high frequency component $\epsilon_\infty=2.5$, f is the oscillator strength, ω_0 is the resonance frequency of 3.392×10^{15} rad/s, and γ_0 is the exciton linewidth of 2.14×10^{14} rad/s. The line width is derived from the resolved absorption of 1mM R6G on silver using: $\eta = \sqrt{\epsilon}$ and $\alpha = 2k_0 \text{Im}(\eta)$ where η is the complex refractive index and α is the absorption coefficient. Figure D2(d) plots an extinction spectra of modeled 5min sample with increasing oscillator strength. The simulation results are in agreement with the experimental.

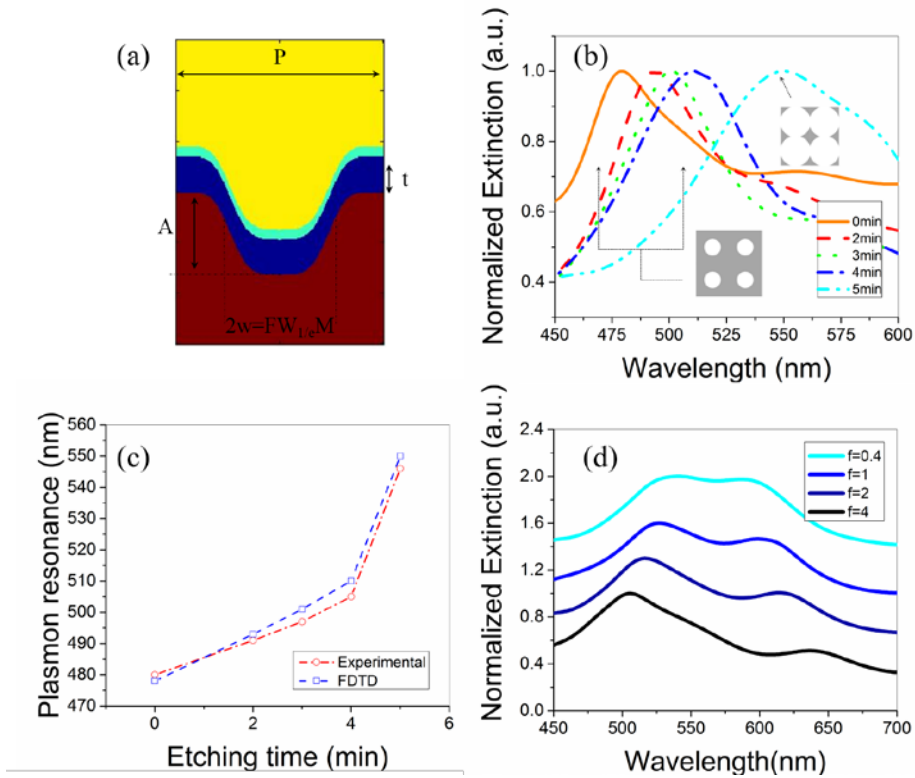


Figure D2 (a) Unit cell of the hole structure used in the simulation where w and A are obtained from fitting the AFM profile; t is the thickness of the silver layer (35nm); and P is the periodicity of the unit cell (200nm). (b) FDTD simulated extinction spectra of various hole sizes (c) Plasmon resonance vs etching time comparison between experimental and FDTD data. (d) Simulated extinction spectra of 5min sample with 10nm R6G over layer for different oscillator strength values ($f=0.4-4$).

In order to estimate the enhancement of our 5 min etched sample, the intensity enhancement factors (IEF) for both incident (532.24 nm) and scattering field (555.152nm) were calculated using the following relation:

$$IEF = |g(\omega)|^2 = |E_{loc}(\omega) / E_0(\omega)|^2 \quad (D3)$$

where $E_{loc}(\omega)$ is the local field at a given frequency ω . The Raman enhancement factor is then calculated by :

$$EF = IEF(\omega_{inc}) \times IEF(\omega_{sca}) \quad (D4)$$

where ω_{inc} and ω_{sca} are the incident and scattering frequency respectively. The oscillator strength of $f=1$ is used for the simulation since it gives similar peaks position and splitting to the experimental data. An analytical approximation of f was also done using:

$$f = 1.13 \times 10^{12} \text{ cm}^{-1} \times \frac{9n}{N(n^2 + 2)^2} \int \alpha dv \quad (D5)$$

$$\int \alpha dv \approx \frac{\pi}{2} \alpha_{max} \Delta v_{FWHM} \quad (D6)$$

where n is the index of refraction, α is the absorption coefficient, v is the wavenumber and N is the molecular density approximated from $\alpha = \sigma N$ with σ being the absorption cross-section. The literature value of $1.8 \times 10^{-16} \text{ cm}^2$ at 550nm was used for σ . This gives the oscillator strength of $f=1.106$ which is close to the assumed value.

Table D1: Summary of intensity and total enhancement factors from both the simulation and experiment. The simulation enhancement factors are taken from the local maximum within the R6G layer. Ratios between experimental and FDTD calculated EFs are also shown.

Sample	FDTD			Experimental EF	EF _{exp} /EF _{FDTD}
	E _{1oc} /E ₀ ² at 555.152nm	E _{1oc} /E ₀ ² at 532.24nm	EF		
2min	1.69	1.99	3.36	19.97	5.67
3min	1.71	2.00	3.43	20.55	5.99
4min	2.09	2.46	5.12	40.41	7.89
5min	5.34	7.35	39.22	206.04	5.25

APPENDIX E: MATLAB CODES

MATLAB code for simulating Z-scan curve.

```

% MATLAB code for simulating Z-scan curve
%Mesh in z-r space
X =[-20:0.05:20]*10^-2;
Y =[0:0.002:2]*10^-3;
[z,r]= (meshgrid(X,Y));

% Defining parameters
w0=33*10^-6;
lam=532*10^-9;
k=2*pi/lam;
z0=pi*w0^2/lam;
E=50*10^-6;
tp=5*10^-9;
wz=w0.*sqrt(1+z.^2./z0^2);
R=z.*(1+(z0./z).^2);
I00=((2*E)./((pi.*w0.^2)*sqrt(pi)*tp));
Iz0=I00.*(w0./wz).^2.*exp(-2*(r./wz).^2);
nwater=1.33;
nsol=1.3288;
inc_ang=0;
angle=asin(nwater*sin(inc_ang)/nsol);
L=1*10^-3./cos(angle);
slice=1000;
dL=L/slice;
linearT=0.06;
alp=-log(linearT)/L;
beta=10*10^-9*0; % nonlinear absorption coefficient [m/W]
I2=Iz0;
Isat= 6*10^11; % saturation intensity
% Calculate irradiance through sample
for j=1:length(X)
for p=1:slice
    dI=- (alp./ (1+I2(:,j)./Isat)+beta.*I2(:,j)).*I2(:,j).*dL;
    I2(:,j)=I2(:,j)+dI;
end
end

Pout=zeros(1,length(X));
Pin=zeros(1,length(X));
dY=Y(2)-Y(1);
% Calculate transmitted energy and transmission
for j=1:length(X)

    Pout(1,j)=2*pi*trapz(Y'.*I2(:,j))*dY; %radial integral
    Pin(1,j)=2*pi*trapz(Y'.*Iz0(:,j))*dY; %radial integral
end
Eout=Pout*sqrt(pi)*tp % time integral
Ein=Pin*sqrt(pi)*tp
T=Eout./Ein;
A1=T./linearT;
% Plot and write output txt file
plot(X,A1);

```

```
B=[X'*10^6,A1'];
dlmwrite('Plot.txt', B, 'delimiter', '\t','precision', 6)
```

MATLAB code for simulating PA Z-scan curve with k-space model

```
%MATLAB code for k space model
clear all
% loop parameter initialization(vary beam waist)
z= [0:8:80];%mm
w0=0.033%mm
lam=532*10^-6; %mm
z0= pi*w0^2/(lam);
wz= w0*sqrt(1+z.^2./z0^2);
qq=length(wz);
amp=zeros(1,qq);
% loop for the whole z scan range
for pp=1:qq
% initial pressure calculation
dot=1024;
gird=[-dot/2:dot/2-1]';
vel=1400; %mm/ms
dx=0.01;
dy=0.01;
[x,y]=meshgrid(gird*dx,gird*dy);
[kx,ky]= meshgrid(gird*2*pi/(dot*dx),gird*2*pi/(dot*dy));
ktot=sqrt(kx.^2+ky.^2);
w=wz(pp);
%input parameters
nwater=1.33;
nsol=1.5;
inc_ang=pi/4;
angle=asin(nwater*sin(inc_ang)/nsol);
L=1;%thin layer thickness in mm
alp=-log(0.22)./(L);
beta=.02*10^-5; % nonlinear absorption coefficient [mm/W]
Isat= 2*10^11000000000; % saturation intensity W/mm2
E=34*10^-6; % input energy J
tp=5*10^-9; % pulse width
I=zeros(dot,dot);
I00=((2*E)./(pi.*w^2)*sqrt(pi)*tp));
%%%%%%%%%%%%%%%%%%%%%%%%%%%%%%%%%%%%%%%%%%%%%%%%%%%%%%%%%%%%%%%%%%%%%%%%Solving beam irradiance through sample %%%%%%%%%%%%%%%%%%%%%%%%%%%%%%%%%%%%%%%%%%%%%%%%%%%%%%%%%%%%%%%%%%%%%%%%%
I=I00*exp(-2*(cos(angle)*x-(sin(angle)*y)).^2/w^2);
Inew=I;
A=zeros(size(I));
B=zeros(size(I));
start=dot/2;
stop=dot/2+100;
B(start,:)=Inew(start,:);
for p=start:stop
    dI=- (alp./(1+Inew(p,:)./Isat)+beta.*Inew(p,:)).*Inew(p,:).*dx./cos(angle);
    A(p+1,:)=(Inew(p,:)+dI);
    [a1 loc1]=max(I(p+1,:));
    [a2 loc2]=max(A(p+1,:));
    dl=loc1-loc2;
    for j=1:dot
        B(p+1,j+dl)=A(p+1,j);
    end
end
```

```

    end
    Inew(p+1,:) = A(p+1,:);
end

y = B(1:dot, 1:dot);
%%%%%%%%%%%%%%%%%%%%%%%%%%%%%%%%%%%%%%%%%%%%%%%%%%%%%%%%%%%%%%%%%%%%%%%%
% initial pressure
p_0 = (alp + beta.*y). * y;
%p0 = (alp ./ (1 + y ./ Isat)). * y; % for Isat

% calculate p0 in k domain
p_0fft = fftshift(fftn(p_0)). * 1; t = [0:0.005:1.5] * 1e-3; %ms
timesnap = zeros(dot, length(t));
%sensor_x = 0;
sensor_y = -0.8;
%nsx = round((N/2 + sensor_x/dx) + 1);
nsy = round((dot/2 + sensor_y/dy) + 1);
[a b] = size(p_0fft);
sensor_mask = zeros(a, b);
sensor_mask(nsy, :) = 1;
% Propagate the pressure in time with time propagator
for q = 1:length(t)
p = real(ifftn(fftshift(p_0fft.*cos(vel*ktot*t (q)))));
timesnap(:, q) = p(nsy, :);
end
f = 1/max(t) * [-length(t)/2:length(t)/2-1];
% apply transducer response
cf = 10e3 ; %kHz
wf = 0.6*cf;
filter = zeros(1, length(f));
for p = 1:length(f)
if f(p) >= 0;
filter(1, p) = exp(-(f(p)-cf).^2/wf^2);
else
filter(1, p) = 0*exp(-(f(p)+cf).^2/wf^2);
end
end
timesnapA = sum(timesnap)/a;
A = fftshift(fftn(timesnapA));
B = (A). * filter;
C = real(((ifftn(ifftshift(B)))));
amp(1, pp) = sqrt(pi) * w * (max(C) - min(C)); % integral for 3D case
end
% format output, compare to the simple model, and save
znew = zeros(1, 2*length(z)-1);
znew(1:length(z)) = sort(-z, 'ascend');
znew(length(z):2*length(z)-1) = sort(z, 'ascend');
ampnew = zeros(1, 2*length(z)-1);
ampnew(length(z):2*length(z)-1) = amp;
Iin = ((2*E) ./ ((pi.*wz.^2)*sqrt(pi)*tp));
PA = (alp + beta.*Iin);
PAnew = zeros(1, 2*length(z)-1);
PAnew(length(z):2*length(z)-1) = PA;
for r = 1:length(z);
ampnew(r) = ampnew(2*length(z)-r);
end

```

```
    PAnew(r)=PAnew(2*length(z)-r);  
end  
plot(znew,ampnew./min(ampnew(:)), 'b', znew,PAnew./min(PAnew(:)), 'g');  
P=[znew', ampnew'./min(ampnew(:)), PAnew'./min(PAnew(:))];  
dlmwrite('comaparePAfit.txt', P, 'delimiter', '\t', 'precision', 6);
```

APPENDIX F: LIST OF RELEVANT PUBLICATIONS

This dissertation is based in part on the following publications:

1. Chantharasupawong, P.; Philip, R.; Endo, T.; Thomas, J., Enhanced Optical Limiting in Nanosized Mixed Zinc Ferrites. *Applied Physics Letters* 2012, 100, 221108.
2. Philip, R.; Chantharasupawong, P.; Qian, H.; Jin, R.; Thomas, J., Evolution of Nonlinear Optical Properties: From Gold Atomic Clusters to Plasmonic Nanocrystals. *Nano letters* 2012, 12, 4661-4667.
3. Chantharasupawong, P.; Philip, R.; Narayanan, N. T.; Sudeep, P. M.; Mathkar, A.; Ajayan, P. M.; Thomas, J., Optical Power Limiting in Fluorinated Graphene Oxide: An Insight into the Nonlinear Optical Properties. *The Journal of Physical Chemistry C* 2012, 116, 25955-25961.
4. Chantharasupawong, P.; Philip, R.; Thomas, J., Simultaneous Optical and Photoacoustic Measurement of Nonlinear Absorption. *Applied Physics Letters* 2013, 102, 041116.
5. Chantharasupawong, P.; Christenson, C. W.; Philip, R.; Zhai, L.; Winiarz, J.; Yamamoto, M.; Tetard, L.; Nair, R. R.; Thomas, J., Photorefractive Performances of a Graphene-Doped Patpd/7-Dcst/Ecz Composite. *Journal of Materials Chemistry C* 2014, 2, 7639-7647.
6. Chantharasupawong, P.; Tetard, L.; Thomas, J., Coupling Enhancement and Giant Rabi-Splitting in Large Arrays of Tunable Plexcitonic Substrates. *The Journal of Physical Chemistry C* 2014.

LIST OF REFERENCES

1. Castellano, J. A., *Handbook of Display Technology*; Academic Press, 1992.
2. Chellappan, K. V.; Erden, E.; Urey, H., Laser-Based Displays: A Review. *Applied optics* **2010**, *49*, F79-F98.
3. Lee, B., Three-Dimensional Displays, Past and Present. *Phys. Today* **2013**, *66(4)*, 36.
4. Holliman, N. S.; Dodgson, N. A.; Favalora, G. E.; Pockett, L., Three-Dimensional Displays: A Review and Applications Analysis. *Broadcasting, IEEE Transactions on* **2011**, *57*, 362-371.
5. Kim, N.; Phan, A.-H.; Erdenebat, M.-U.; Alam, A.; Kwon, K.-C.; PIAO, M.; Lee, J.-H., 3d Display Technology. *Display and Imaging* **2013**, *1*, 73-95.
6. Blanche, P.-A.; Bablumian, A.; Voorakaranam, R.; Christenson, C.; Lin, W.; Gu, T.; Flores, D.; Wang, P.; Hsieh, W.-Y.; Kathaperumal, M., Holographic Three-Dimensional Telepresence Using Large-Area Photorefractive Polymer. *Nature* **2010**, *468*, 80-83.
7. Tay, S.; Blanche, P.-A.; Voorakaranam, R.; Tunç, A.; Lin, W.; Rokutanda, S.; Gu, T.; Flores, D.; Wang, P.; Li, G., An Updatable Holographic Three-Dimensional Display. *Nature* **2008**, *451*, 694-698.
8. Kauffman, D. R.; Star, A., Carbon Nanotube Gas and Vapor Sensors. *Angewandte Chemie International Edition* **2008**, *47*, 6550-6570.
9. Li, J.; Lu, Y.; Ye, Q.; Cinke, M.; Han, J.; Meyyappan, M., Carbon Nanotube Sensors for Gas and Organic Vapor Detection. *Nano Letters* **2003**, *3*, 929-933.
10. Bogue, R. W., Nanotechnology: What Are the Prospects for Sensors? *Sensor Review* **2004**, *24*, 253-260.
11. Walter, E. C.; Favier, F.; Penner, R. M., Palladium Mesowire Arrays for Fast Hydrogen Sensors and Hydrogen-Actuated Switches. *Analytical Chemistry* **2002**, *74*, 1546-1553.
12. Shi, J.; Zhu, Y.; Zhang, X.; Baeyens, W. R.; García-Campaña, A. M., Recent Developments in Nanomaterial Optical Sensors. *TrAC Trends in Analytical Chemistry* **2004**, *23*, 351-360.
13. Jaimes Salcedo, W.; Ramirez Fernandez, F. J.; Rubim, J. C., Photoluminescence Quenching Effect on Porous Silicon Films for Gas Sensors Application. *Spectrochimica Acta Part A: Molecular and Biomolecular Spectroscopy* **2004**, *60*, 1065-1070.
14. Murphy, C. J., Peer Reviewed: Optical Sensing with Quantum Dots. *Analytical Chemistry* **2002**, *74*, 520 A-526 A.

15. Lin, V. S.-Y.; Motesharei, K.; Dancil, K.-P. S.; Sailor, M. J.; Ghadiri, M. R., A Porous Silicon-Based Optical Interferometric Biosensor. *Science* **1997**, *278*, 840-843.
16. Wood, R. W., On a Remarkable Case of Uneven Distribution of Light in a Diffraction Grating Spectrum. *Proceedings of the Physical Society of London* **1902**, *18*, 269.
17. Fano, U., The Theory of Anomalous Diffraction Gratings and of Quasi-Stationary Waves on Metallic Surfaces (Sommerfeld's Waves). *JOSA* **1941**, *31*, 213-222.
18. Homola, J., Surface Plasmon Resonance Sensors for Detection of Chemical and Biological Species. *Chemical Reviews* **2008**, *108*, 462-493.
19. Fleischmann, M.; Hendra, P.; McQuillan, A., Raman Spectra of Pyridine Adsorbed at a Silver Electrode. *Chemical Physics Letters* **1974**, *26*, 163-166.
20. Kneipp, K.; Wang, Y.; Kneipp, H.; Perelman, L. T.; Itzkan, I.; Dasari, R. R.; Feld, M. S., Single Molecule Detection Using Surface-Enhanced Raman Scattering (Sers). *Physical review letters* **1997**, *78*, 1667.
21. Nie, S.; Emory, S. R., Probing Single Molecules and Single Nanoparticles by Surface-Enhanced Raman Scattering. *Science* **1997**, *275*, 1102-1106.
22. Anker, J. N.; Hall, W. P.; Lyandres, O.; Shah, N. C.; Zhao, J.; Van Duyne, R. P., Biosensing with Plasmonic Nanosensors. *Nature materials* **2008**, *7*, 442-453.
23. Nyokong, T.; Ahsen, V., *Photosensitizers in Medicine, Environment, and Security*; Springer, 2012.
24. Ebbesen, T. W.; Tanigaki, K.; Kuroshima, S., Excited-State Properties of C₆₀. *Chemical physics letters* **1991**, *181*, 501-504.
25. Arbogast, J. W.; Darmanyan, A. P.; Foote, C. S.; Diederich, F.; Whetten, R.; Rubin, Y.; Alvarez, M. M.; Anz, S. J., Photophysical Properties of Sixty Atom Carbon Molecule (C₆₀). *The Journal of Physical Chemistry* **1991**, *95*, 11-12.
26. Tutt, L. W.; Kost, A., Optical Limiting Performance of C₆₀ and C₇₀ Solutions. *Nature* **1992**, *356*, 225-226.
27. Brandelik, D.; McLean, D.; Schmitt, M.; Epling, B.; Colclasure, C.; Tondiglia, V.; Pachter, R.; Obermeier, K.; Crane, R. L. In *Nonlinear Optical Properties of Buckminsterfullerene Solutions*, MRS Proceedings, Cambridge Univ Press: 1992; p 361.
28. McLean, D.; Fleitz, P.; Pottenger, T.; Sutherland, R.; Brant, M.; Brandelik, D., Nonlinear Absorption Study of a C₆₀-Toluene Solution. *Optics letters* **1993**, *18*, 858-860.
29. Golovlev, V.; Garrett, W.; Chen, C., Reverse Saturable Absorption of C₆₀ in Liquids Irradiated by Picosecond and Nanosecond Laser Pulses. *JOSA B* **1996**, *13*, 2801-2806.

30. Li, C.; Zhang, L.; Wang, R.; Song, Y.; Wang, Y., Dynamics of Reverse Saturable Absorption and All-Optical Switching in C₆₀. *JOSA B* **1994**, *11*, 1356-1360.
31. Joshi, M. P.; Mishra, S.; Rawat, H.; Mehendale, S.; Rustagi, K., Investigation of Optical Limiting in C₆₀ Solution. *Applied physics letters* **1993**, *62*, 1763-1765.
32. Koudoumas, E., Solvent Effects on the Optical Limiting Action of C₆₀ Solutions. *Molecular Physics* **1996**, *88*, 125-133.
33. Kost, A.; Dougherty, T. K.; Elias, W. E.; Tutt, L.; Klein, M. B., Optical Limiting with C₆₀ in Polymethyl Methacrylate. *Optics letters* **1993**, *18*, 334-336.
34. Mishra, S.; Rawat, H.; Joshi, M.; Mehendale, S., On the Contribution of Nonlinear Scattering to Optical Limiting in C₆₀ Solution. *Applied Physics A* **1996**, *63*, 223-226.
35. Song, Y.; Fang, G.; Wang, Y.; Liu, S.; Li, C.; Song, L.; Zhu, Y.; Hu, Q., Excited-State Absorption and Optical-Limiting Properties of Organometallic Fullerene-C₆₀ Derivatives. *Applied physics letters* **1999**, *74*, 332-334.
36. Tang, B. Z., et al., Synthesis and Optical Properties of Fullerene-Functionalized Polycarbonates. *Macromolecules* **1998**, *31*, 103-108.
37. Tang, B.; Peng, H.; Leung, S.; Yu, N.-T.; Hiraoka, H.; Fok, W. In *Optical Limiting in Fullerene Materials*, MRS Proceedings, Cambridge Univ Press: 1997; p 69.
38. Ma, B.; Riggs, J. E.; Sun, Y.-P., Photophysical and Nonlinear Absorptive Optical Limiting Properties of [60]Fullerene Dimer and Poly[60]Fullerene Polymer. *The Journal of Physical Chemistry B* **1998**, *102*, 5999-6009.
39. Barroso, J.; Costela, A.; Garcia-Moreno, I.; Saiz, J., Wavelength Dependence of the Nonlinear Absorption of C₆₀-and C₇₀-Toluene Solutions. *The Journal of Physical Chemistry A* **1998**, *102*, 2527-2532.
40. Dini, D.; Barthel, M.; Hanack, M., Phthalocyanines as Active Materials for Optical Limiting. *European Journal of Organic Chemistry* **2001**, *2001*, 3759-3769.
41. Brannon, J. H.; Magde, D., Picosecond Laser Photophysics. Group 3a Phthalocyanines. *Journal of the American Chemical Society* **1980**, *102*, 62-65.
42. Perry, J. W.; Alvarez, D.; Choong, I.; Mansour, K.; Marder, S. R.; Perry, K. J., Enhanced Reverse Saturable Absorption and Optical Limiting in Heavy-Atom-Substituted Phthalocyanines. *Optics letters* **1994**, *19*, 625-627.
43. Shirk, J. S.; Lindle, J.; Bartoli, F.; Hoffman, C.; Kafafi, Z. H.; Snow, A. W., Off - Resonant Third - Order Optical Nonlinearities of Metal - Substituted Phthalocyanines. *Applied physics letters* **1989**, *55*, 1287-1288.

44. Calvete, M.; Yang, G. Y.; Hanack, M., Porphyrins and Phthalocyanines as Materials for Optical Limiting. *Synthetic Metals* **2004**, *141*, 231-243.
45. Mansour, K.; Alvarez Jr, D.; Perry, K. J.; Choong, I.; Marder, S. R.; Perry, J. W. In *Dynamics of Optical Limiting in Heavy-Atom Substituted Phthalocyanines*, OE/LASE'93: Optics, Electro-Optics, & Laser Applications in Science & Engineering, International Society for Optics and Photonics: 1993; pp 132-141.
46. Chen, Y.; Subramanian, L.; Fujitsuka, M.; Ito, O.; O'Flaherty, S.; Blau, W. J.; Schneider, T.; Dini, D.; Hanack, M., Synthesis and Optical Limiting Properties of Axially Bridged Phthalocyanines: [(Tbu4pcga) 2o] and [(Tbu4pcin) 2o]. *Chemistry-A European Journal* **2002**, *8*, 4248-4254.
47. Chen, Y.; Fujitsuka, M.; O'Flaherty, S. M.; Hanack, M.; Ito, O.; Blau, W. J., Strong Optical Limiting of Soluble Axially Substituted Gallium and Indium Phthalocyanines. *Advanced Materials* **2003**, *15*, 899-902.
48. Coulter, D. R.; Miskowski, V. M.; Perry, J. W.; Wei, T.-H.; Van Stryland, E. W.; Hagan, D. J. In *Optical Limiting in Solutions of Metallo-Phthalocyanines and Naphthalocyanines*, 1989 Orlando Symposium, International Society for Optics and Photonics: 1989; pp 42-51.
49. Hanack, M.; Schneider, T.; Barthel, M.; Shirk, J. S.; Flom, S. R.; Pong, R. G., Indium Phthalocyanines and Naphthalocyanines for Optical Limiting. *Coordination Chemistry Reviews* **2001**, *219*, 235-258.
50. Mansour, K.; Soileau, M.; Van Stryland, E. W., Nonlinear Optical Properties of Carbon-Black Suspensions (Ink). *JOSA B* **1992**, *9*, 1100-1109.
51. Nashold, K. M.; Walter, D. P., Investigations of Optical Limiting Mechanisms in Carbon Particle Suspensions and Fullerene Solutions. *Journal of the Optical Society of America B* **1995**, *12*, 1228-1237.
52. Goedert, R.; Becker, R.; Clements, A.; Whittaker, T., Time-Resolved Shadowgraphic Imaging of the Response of Dilute Suspensions to Laser Pulses. *Journal of the Optical Society of America B* **1998**, *15*, 1442-1462.
53. McEwan, K. J.; Milsom, P. K.; James, D. B. In *Nonlinear Optical Effects in Carbon Suspension*, 1998; pp 42-52.
54. Durand, O.; Grolier-Mazza, V.; Frey, R., Picosecond-Resolution Study of Nonlinear Scattering in Carbon Black Suspensions in Water and Ethanol. *Optics letters* **1998**, *23*, 1471-1473.
55. Tiwari, S.; Joshi, M.; Nath, S.; Mehendale, S., Salt-Induced Aggregation and Enhanced Optical Limiting in Carbon-Black Suspensions. *Journal of Nonlinear Optical Physics & Materials* **2003**, *12*, 335-339.

56. Neto, N. B.; Mendonca, C.; Misoguti, L.; Zilio, S., Optical Limiting of Ultrashort Pulses by Carbon Black Suspension. *Applied Physics B* **2004**, *78*, 1-3.
57. Sun, X.; Yu, R.; Xu, G.; Hor, T.; Ji, W., Broadband Optical Limiting with Multiwalled Carbon Nanotubes. *Applied Physics Letters* **1998**, *73*, 3632-3634.
58. Chen, P.; Wu, X.; Sun, X.; Lin, J.; Ji, W.; Tan, K., Electronic Structure and Optical Limiting Behavior of Carbon Nanotubes. *Physical review letters* **1999**, *82*, 2548.
59. Vivien, L.; Anglaret, E.; Riehl, D.; Bacou, F.; Journet, C.; Goze, C.; Andrieux, M.; Brunet, M.; Lafonta, F.; Bernier, P., Single-Wall Carbon Nanotubes for Optical Limiting. *Chemical Physics Letters* **1999**, *307*, 317-319.
60. Mishra, S.; Rawat, H.; Mehendale, S.; Rustagi, K.; Sood, A.; Bandyopadhyay, R.; Govindaraj, A.; Rao, C., Optical Limiting in Single-Walled Carbon Nanotube Suspensions. *Chemical Physics Letters* **2000**, *317*, 510-514.
61. Wang, J.; Blau, W. J., Solvent Effect on Optical Limiting Properties of Single-Walled Carbon Nanotube Dispersions. *The Journal of Physical Chemistry C* **2008**, *112*, 2298-2303.
62. Riggs, J. E.; Walker, D. B.; Carroll, D. L.; Sun, Y.-P., Optical Limiting Properties of Suspended and Solubilized Carbon Nanotubes §. *The Journal of Physical Chemistry B* **2000**, *104*, 7071-7076.
63. Jin, Z.; Sun, X.; Xu, G.; Goh, S. H.; Ji, W., Nonlinear Optical Properties of Some Polymer/Multi-Walled Carbon Nanotube Composites. *Chemical Physics Letters* **2000**, *318*, 505-510.
64. Vivien, L.; Riehl, D.; Lancon, P.; Hache, F.; Anglaret, E., Pulse Duration and Wavelength Effects on the Optical Limiting Behavior of Carbon Nanotube Suspensions. *Optics letters* **2001**, *26*, 223-225.
65. Liu, L.; Zhang, S.; Hu, T.; Guo, Z.-X.; Ye, C.; Dai, L.; Zhu, D., Solubilized Multi-Walled Carbon Nanotubes with Broadband Optical Limiting Effect. *Chemical physics letters* **2002**, *359*, 191-195.
66. O'Flaherty, S. M.; Hold, S. V.; Brennan, M. E.; Cadek, M.; Drury, A.; Coleman, J. N.; Blau, W. J., Nonlinear Optical Response of Multiwalled Carbon-Nanotube Dispersions. *JOSA B* **2003**, *20*, 49-58.
67. Chin, K. C.; Gohel, A.; Elim, H. I.; Chen, W.; Ji, W.; Chong, G. L.; Sow, C. H.; Wee, A. T., Modified Carbon Nanotubes as Broadband Optical Limiting Nanomaterials. *Journal of materials research* **2006**, *21*, 2758-2766.
68. Xu, J.; Xiao, M.; Czerw, R.; Carroll, D. L., Optical Limiting and Enhanced Optical Nonlinearity in Boron-Doped Carbon Nanotubes. *Chemical Physics Letters* **2004**, *389*, 247-250.

69. Izard, N.; Ménard, C.; Riehl, D.; Doris, E.; Mioskowski, C.; Anglaret, E., Combination of Carbon Nanotubes and Two-Photon Absorbers for Broadband Optical Limiting. *Chemical physics letters* **2004**, *391*, 124-128.
70. Webster, S.; Reyes-Reyes, M.; Pedron, X.; López-Sandoval, R.; Terrones, M.; Carroll, D. L., Enhanced Nonlinear Transmittance by Complementary Nonlinear Mechanisms: A Reverse-Saturable Absorbing Dye Blended with Nonlinear-Scattering Carbon Nanotubes. *Advanced Materials* **2005**, *17*, 1239-1243.
71. Guo, Z.; Du, F.; Ren, D.; Chen, Y.; Zheng, J.; Liu, Z.; Tian, J., Covalently Porphyrin-Functionalized Single-Walled Carbon Nanotubes: A Novel Photoactive and Optical Limiting Donor–Acceptor Nanohybrid. *Journal of Materials Chemistry* **2006**, *16*, 3021-3030.
72. Liu, Z. B.; Tian, J. G.; Guo, Z.; Ren, D. M.; Du, F.; Zheng, J. Y.; Chen, Y. S., Enhanced Optical Limiting Effects in Porphyrin-Covalently Functionalized Single-Walled Carbon Nanotubes. *Advanced Materials* **2008**, *20*, 511-515.
73. Sheik-Bahae, M.; Said, A. A.; Wei, T.-H.; Hagan, D. J.; Van Stryland, E. W., Sensitive Measurement of Optical Nonlinearities Using a Single Beam. *Quantum Electronics, IEEE Journal of* **1990**, *26*, 760-769.
74. Suzuki, Y.; Tachibana, A., Measurement of the Mm Sized Radius of Gaussian Laser Beam Using the Scanning Knife-Edge. *Applied Optics* **1975**, *14*, 2809-2810.
75. de Araújo, M. A.; Silva, R.; de Lima, E.; Pereira, D. P.; de Oliveira, P. C., Measurement of Gaussian Laser Beam Radius Using the Knife-Edge Technique: Improvement on Data Analysis. *Applied optics* **2009**, *48*, 393-396.
76. Joshi, H. M.; Lin, Y. P.; Aslam, M.; Prasad, P. V.; Schultz-Sikma, E. A.; Edelman, R.; Meade, T.; Dravid, V. P., Effects of Shape and Size of Cobalt Ferrite Nanostructures on Their Mri Contrast and Thermal Activation. *The Journal of Physical Chemistry C* **2009**, *113*, 17761-17767.
77. Hao, R.; Xing, R.; Xu, Z.; Hou, Y.; Gao, S.; Sun, S., Synthesis, Functionalization, and Biomedical Applications of Multifunctional Magnetic Nanoparticles. *Advanced Materials* **2010**, *22*, 2729-2742.
78. Arruebo, M.; Fernández-Pacheco, R.; Ibarra, M. R.; Santamaría, J., Magnetic Nanoparticles for Drug Delivery. *Nano Today* **2007**, *2*, 22-32.
79. Perez, J. M.; Simeone, F. J.; Saeki, Y.; Josephson, L.; Weissleder, R., Viral-Induced Self-Assembly of Magnetic Nanoparticles Allows the Detection of Viral Particles in Biological Media. *Journal of the American Chemical Society* **2003**, *125*, 10192-10193.
80. Hastings, J. M.; Corliss, L. M., Neutron Diffraction Studies of Zinc Ferrite and Nickel Ferrite. *Reviews of Modern Physics* **1953**, *25*, 114-119.

81. Ramirez, M. O., et al., Magnon Sidebands and Spin-Charge Coupling in Bismuth Ferrite Probed by Nonlinear Optical Spectroscopy. *Physical Review B* **2009**, *79*, 224106.
82. He, C.; Zou, B.; Wu, Z.; Nie, Y., Third Order Optical Nonlinearities in ZnFe₂O₄ Nanocrystals. *Optics Communications* **2008**, *281*, 851-854.
83. Joshi, M. P.; Mishra, S. R.; Rawat, H. S.; Mehendale, S. C.; Rustagi, K. C., Investigation of Optical Limiting in C60 Solution. *Applied Physics Letters* **1993**, *62*, 1763-1765.
84. Couris, S.; Koudoumas, E.; Ruth, A.; Leach, S., Concentration and Wavelength Dependence of the Effective Third-Order Susceptibility and Optical Limiting of C60 in Toluene Solution. *Journal of Physics B: Atomic, Molecular and Optical Physics* **1995**, *28*, 4537.
85. Guldi, D. M.; Prato, M., Excited-State Properties of C60 Fullerene Derivatives. *Accounts of Chemical Research* **2000**, *33*, 695-703.
86. Tauc, J.; Grigorovici, R.; Vancu, A., Optical Properties and Electronic Structure of Amorphous Germanium. *physica status solidi (b)* **1966**, *15*, 627-637.
87. Joshi, G. P.; Saxena, N. S.; Mangal, R.; Mishra, A.; Sharma, T. P., Band Gap Determination of Ni-Zn Ferrites. *Bulletin of Materials Science* **2003**, *26*, 387-389.
88. Stoneham, A. M.; Gavartin, J.; Shluger, A. L.; Kimmel, A. V.; Ramo, D. M.; Rønnow, H. M.; Aeppli, G.; Renner, C., Trapping, Self-Trapping and the Polaron Family. *Journal of Physics: Condensed Matter* **2007**, *19*, 255208.
89. Pisarev, R.; Moskvina, A.; Kalashnikova, A.; Rasing, T., Charge Transfer Transitions in Multiferroic Bifeo₃ and Related Ferrite Insulators. *Physical Review B* **2009**, *79*, 235128.
90. Wyrwas, R.; Alvarez, M.; Khoury, J.; Price, R.; Schaaff, T.; Whetten, R., The Colours of Nanometric Gold. *The European Physical Journal D-Atomic, Molecular, Optical and Plasma Physics* **2007**, *43*, 91-95.
91. Kelly, K. L.; Coronado, E.; Zhao, L. L.; Schatz, G. C., The Optical Properties of Metal Nanoparticles: The Influence of Size, Shape, and Dielectric Environment. *The Journal of Physical Chemistry B* **2002**, *107*, 668-677.
92. Thomas, J.; Anija, M.; Cyriac, J.; Pradeep, T.; Philip, R., Observation of a Fifth Order Optical Nonlinearity in 29kda Au@ Alkanethiol Clusters Excited in the Visible. *Chemical physics letters* **2005**, *403*, 308-313.
93. Del Fatti, N.; Voisin, C.; Achermann, M.; Tzortzakis, S.; Christofilos, D.; Vallée, F., Nonequilibrium Electron Dynamics in Noble Metals. *Physical Review B* **2000**, *61*, 16956.
94. Alvarez, M. M.; Khoury, J. T.; Schaaff, T. G.; Shafiqullin, M. N.; Vezmar, I.; Whetten, R. L., Optical Absorption Spectra of Nanocrystal Gold Molecules. *The Journal of Physical Chemistry B* **1997**, *101*, 3706-3712.

95. Philip, R.; Kumar, G. R.; Sandhyarani, N.; Pradeep, T., Picosecond Optical Nonlinearity in Monolayer-Protected Gold, Silver, and Gold-Silver Alloy Nanoclusters. *Physical Review B* **2000**, *62*, 13160.
96. Ramakrishna, G.; Varnavski, O.; Kim, J.; Lee, D.; Goodson, T., Quantum-Sized Gold Clusters as Efficient Two-Photon Absorbers. *Journal of the American Chemical Society* **2008**, *130*, 5032-5033.
97. Varnavski, O.; Ramakrishna, G.; Kim, J.; Lee, D.; Goodson, T., Critical Size for the Observation of Quantum Confinement in Optically Excited Gold Clusters. *Journal of the American Chemical Society* **2009**, *132*, 16-17.
98. Jin, R.; Qian, H.; Wu, Z.; Zhu, Y.; Zhu, M.; Mohanty, A.; Garg, N., Size Focusing: A Methodology for Synthesizing Atomically Precise Gold Nanoclusters. *The Journal of Physical Chemistry Letters* **2010**, *1*, 2903-2910.
99. Jin, R.; Qian, H.; Zhu, Y.; Das, A., Atomically Precise Nanoparticles: A New Frontier in Nanoscience. *J. Nanosci. Lett* **2011**, *1*, 72-86.
100. Tokizaki, T.; Nakamura, A.; Kaneko, S.; Uchida, K.; Omi, S.; Tanji, H.; Asahara, Y., Subpicosecond Time Response of Third - Order Optical Nonlinearity of Small Copper Particles in Glass. *Applied physics letters* **1994**, *65*, 941-943.
101. Walter, M.; Akola, J.; Lopez-Acevedo, O.; Jadzinsky, P. D.; Calero, G.; Ackerson, C. J.; Whetten, R. L.; Grönbeck, H.; Häkkinen, H., A Unified View of Ligand-Protected Gold Clusters as Superatom Complexes. *Proceedings of the National Academy of Sciences* **2008**, *105*, 9157-9162.
102. Zhu, M.; Aikens, C. M.; Hollander, F. J.; Schatz, G. C.; Jin, R., Correlating the Crystal Structure of a Thiol-Protected Au₂₅ Cluster and Optical Properties. *Journal of the American Chemical Society* **2008**, *130*, 5883-5885.
103. Aikens, C. M., Origin of Discrete Optical Absorption Spectra of M₂₅(Sh)₁₈-Nanoparticles (M = Au, Ag). *The Journal of Physical Chemistry C* **2008**, *112*, 19797-19800.
104. Ahmadi, T. S.; Logunov, S. L.; El-Sayed, M. A., Picosecond Dynamics of Colloidal Gold Nanoparticles. *The Journal of Physical Chemistry* **1996**, *100*, 8053-8056.
105. Brodie, B. C., On the Atomic Weight of Graphite. *Philosophical Transactions of the Royal Society of London* **1859**, *149*, 249-259.
106. Gao, W.; Alemany, L. B.; Ci, L.; Ajayan, P. M., New Insights into the Structure and Reduction of Graphite Oxide. *Nature Chemistry* **2009**, *1*, 403-408.
107. Chen, H.; Müller, M. B.; Gilmore, K. J.; Wallace, G. G.; Li, D., Mechanically Strong, Electrically Conductive, and Biocompatible Graphene Paper. *Advanced Materials* **2008**, *20*, 3557-3561.

108. Li, X.; Zhang, G.; Bai, X.; Sun, X.; Wang, X.; Wang, E.; Dai, H., Highly Conducting Graphene Sheets and Langmuir–Blodgett Films. *Nature nanotechnology* **2008**, *3*, 538-542.
109. Bae, S.; Kim, H.; Lee, Y.; Xu, X.; Park, J.-S.; Zheng, Y.; Balakrishnan, J.; Lei, T.; Kim, H. R.; Song, Y. I., Roll-to-Roll Production of 30-Inch Graphene Films for Transparent Electrodes. *Nature nanotechnology* **2010**, *5*, 574-578.
110. Balandin, A. A.; Ghosh, S.; Bao, W.; Calizo, I.; Teweldebrhan, D.; Miao, F.; Lau, C. N., Superior Thermal Conductivity of Single-Layer Graphene. *Nano Letters* **2008**, *8*, 902-907.
111. Sun, X.; Liu, Z.; Welsher, K.; Robinson, J.; Goodwin, A.; Zaric, S.; Dai, H., Nano-Graphene Oxide for Cellular Imaging and Drug Delivery. *Nano Research* **2008**, *1*, 203-212.
112. Yang, X.; Zhang, X.; Ma, Y.; Huang, Y.; Wang, Y.; Chen, Y., Superparamagnetic Graphene Oxide-Fe₃O₄ Nanoparticles Hybrid for Controlled Targeted Drug Carriers. *Journal of Materials Chemistry* **2009**, *19*, 2710-2714.
113. Ma, X.; Tao, H.; Yang, K.; Feng, L.; Cheng, L.; Shi, X.; Li, Y.; Guo, L.; Liu, Z., A Functionalized Graphene Oxide-Iron Oxide Nanocomposite for Magnetically Targeted Drug Delivery, Photothermal Therapy, and Magnetic Resonance Imaging. *Nano Research* **2012**, *5*, 199-212.
114. Zhuang, X.-D.; Chen, Y.; Liu, G.; Li, P.-P.; Zhu, C.-X.; Kang, E.-T.; Noeh, K.-G.; Zhang, B.; Zhu, J.-H.; Li, Y.-X., Conjugated-Polymer-Functionalized Graphene Oxide: Synthesis and Nonvolatile Rewritable Memory Effect. *Advanced Materials* **2010**, *22*, 1731-1735.
115. Wang, H.; Hao, Q.; Yang, X.; Lu, L.; Wang, X., Graphene Oxide Doped Polyaniline for Supercapacitors. *Electrochemistry Communications* **2009**, *11*, 1158-1161.
116. Chen, S.; Zhu, J.; Wu, X.; Han, Q.; Wang, X., Graphene Oxide–MnO₂ Nanocomposites for Supercapacitors. *ACS Nano* **2010**, *4*, 2822-2830.
117. Liu, Z.; Liu, Q.; Huang, Y.; Ma, Y.; Yin, S.; Zhang, X.; Sun, W.; Chen, Y., Organic Photovoltaic Devices Based on a Novel Acceptor Material: Graphene. *Advanced Materials* **2008**, *20*, 3924-3930.
118. Yu, D.; Yang, Y.; Durstock, M.; Baek, J.-B.; Dai, L., Soluble P3ht-Grafted Graphene for Efficient Bilayer–Heterojunction Photovoltaic Devices. *ACS Nano* **2010**, *4*, 5633-5640.
119. Liu, Y.; Zhou, J.; Zhang, X.; Liu, Z.; Wan, X.; Tian, J.; Wang, T.; Chen, Y., Synthesis, Characterization and Optical Limiting Property of Covalently Oligothiophene-Functionalized Graphene Material. *Carbon* **2009**, *47*, 3113-3121.
120. Xu, Y.; Liu, Z.; Zhang, X.; Wang, Y.; Tian, J.; Huang, Y.; Ma, Y.; Zhang, X.; Chen, Y., A Graphene Hybrid Material Covalently Functionalized with Porphyrin: Synthesis and Optical Limiting Property. *Advanced Materials* **2009**, *21*, 1275-1279.

121. Balapanuru, J.; Yang, J.-X.; Xiao, S.; Bao, Q.; Jahan, M.; Polavarapu, L.; Wei, J.; Xu, Q.-H.; Loh, K. P., A Graphene Oxide–Organic Dye Ionic Complex with DNA-Sensing and Optical-Limiting Properties. *Angewandte Chemie* **2010**, *122*, 6699-6703.
122. Johns, I.; McElhill, E.; Smith, J., Thermal Stability of Some Organic Compounds. *Journal of Chemical and Engineering Data* **1962**, *7*, 277-281.
123. Mathkar, A.; Narayanan, T.; Alemany, L. B.; Cox, P.; Nguyen, P.; Gao, G.; Chang, P.; Romero - Aburto, R.; Mani, S. A.; Ajayan, P., Synthesis of Fluorinated Graphene Oxide and Its Amphiphobic Properties. *Particle & Particle Systems Characterization* **2013**, *30*, 266-272.
124. Marcano, D. C.; Kosynkin, D. V.; Berlin, J. M.; Sinitiskii, A.; Sun, Z.; Slesarev, A.; Alemany, L. B.; Lu, W.; Tour, J. M., Improved Synthesis of Graphene Oxide. *ACS nano* **2010**, *4*, 4806-4814.
125. Mathkar, A.; Tozier, D.; Cox, P.; Ong, P.; Galande, C.; Balakrishnan, K.; Leela Mohana Reddy, A.; Ajayan, P. M., Controlled, Stepwise Reduction and Band Gap Manipulation of Graphene Oxide. *The Journal of Physical Chemistry Letters* **2012**, *3*, 986-991.
126. Zhang, X.-L.; Zhao, X.; Liu, Z.-B.; Shi, S.; Zhou, W.-Y.; Tian, J.-G.; Xu, Y.-F.; Chen, Y.-S., Nonlinear Optical and Optical Limiting Properties of Graphene Oxide–Fe₃O₄ Hybrid Material. *Journal of Optics* **2011**, *13*, 075202.
127. Kneisl, P.; Zondlo, J. W., Vapor Pressure, Liquid Density, and the Latent Heat of Vaporization as Functions of Temperature for Four Dipolar Aprotic Solvents. *Journal of Chemical and Engineering Data* **1987**, *32*, 11-13.
128. Justus, B. L.; Kafafi, Z.; Huston, A., Excited-State Absorption-Enhanced Thermal Optical Limiting in C₆₀. *Optics letters* **1993**, *18*, 1603-1605.
129. Sun, Y.-P.; Riggs, J. E.; Liu, B., Optical Limiting Properties of [60] Fullerene Derivatives. *Chemistry of materials* **1997**, *9*, 1268-1272.
130. Liu, Z.; Wang, Y.; Zhang, X.; Xu, Y.; Chen, Y.; Tian, J., Nonlinear Optical Properties of Graphene Oxide in Nanosecond and Picosecond Regimes. *Applied Physics Letters* **2009**, *94*, 021902.
131. Jiang, X.-F.; Polavarapu, L.; Neo, S. T.; Venkatesan, T.; Xu, Q.-H., Graphene Oxides as Tunable Broadband Nonlinear Optical Materials for Femtosecond Laser Pulses. *The Journal of Physical Chemistry Letters* **2012**, *3*, 785-790.
132. Tam, A.; Coufal, H., Pulsed Opto-Acoustics: Theory and Applications. *Le Journal de Physique Colloques* **1983**, *44*, C6-9-C6-20.
133. Patel, C.; Tam, A., Pulsed Optoacoustic Spectroscopy of Condensed Matter. *Reviews of Modern Physics* **1981**, *53*, 517.

134. Tam, A. C., Applications of Photoacoustic Sensing Techniques. *Reviews of Modern Physics* **1986**, 58, 381.
135. Rosencwaig, A.; Gersho, A., Theory of the Photoacoustic Effect with Solids. *Journal of Applied Physics* **1976**, 47, 64-69.
136. Stryland, E. W. V.; Sheik-Bahae, M., Z-Scan. In *Characterization Techniques and Tabulations for Organic Nonlinear Materials*, M. G. Kuzyk and C. W. Dirk, E., Ed. Marcel Dekker, Inc.: 1998; pp 655-692.
137. Gu, B.; Fan, Y.-X.; Wang, J.; Chen, J.; Ding, J.; Wang, H.-T.; Guo, B., Characterization of Saturable Absorbers Using an Open-Aperture Gaussian-Beam Z Scan. *Physical Review A* **2006**, 73, 065803.
138. Sheik-Bahae, M.; Said, A. A.; Wei, T. H.; Hagan, D. J.; Van Stryland, E. W., Sensitive Measurement of Optical Nonlinearities Using a Single Beam. *Quantum Electronics, IEEE Journal of* **1990**, 26, 760-769.
139. Tam, A. C., Applications of Photoacoustic Sensing Techniques. *Reviews of Modern Physics* **1986**, 58, 381-431.
140. Taheri, B.; Liu, H.; Jassemnejad, B.; Appling, D.; Powell, R. C.; Song, J., Intensity Scan and Two Photon Absorption and Nonlinear Refraction of C60 in Toluene. *Applied physics letters* **1996**, 68, 1317-1319.
141. Mansour, K.; Soileau, M. J.; Stryland, E. W. V., Nonlinear Optical Properties of Carbon-Black Suspensions (Ink). *J. Opt. Soc. Am. B* **1992**, 9, 1100-1109.
142. Cox, B.; Beard, P., Fast Calculation of Pulsed Photoacoustic Fields in Fluids Using K-Space Methods. *The Journal of the Acoustical Society of America* **2005**, 117, 3616-3627.
143. Bruder, F.-K.; Hagen, R.; Rölle, T.; Weiser, M.-S.; Fäcke, T., From the Surface to Volume: Concepts for the Next Generation of Optical–Holographic Data-Storage Materials. *Angewandte Chemie International Edition* **2011**, 50, 4552-4573.
144. Winiarz, J.; Ghebremichael, F.; Thomas, J.; Meredith, G.; Peyghambarian, N., Dynamic Correction of a Distorted Image Using a Photorefractive Polymeric Composite. *Opt. Express* **2004**, 12, 2517-2528.
145. Castro, J. M.; de Leon, E.; Barton, J. K.; Kostuk, R. K., Analysis of Diffracted Image Patterns from Volume Holographic Imaging Systems and Applications to Image Processing. *Appl. Opt.* **2011**, 50, 170-176.
146. Tay, S., et al., An Updatable Holographic Three-Dimensional Display. *Nature* **2008**, 451, 694-698.

147. Oh, J.-W.; Choi, J.; Kim, N., Tunable Color Filter with Surface Plasmon Resonance Using Organic Photorefractive Composite. *Appl. Opt.* **2009**, *48*, 3160-3164.
148. Suzuki, K.; Okamoto, A.; Takabayashi, M.; Honma, S., High Sensitive and Efficient Photorefractive Tunable Optical Wavelength Filter with Applied External Field. **2009**, 72120W-72120W.
149. Nolte, D. D.; Jeong, K.; French, P. M. W.; Turek, J., Holographic Optical Coherence Imaging. In *Optical Coherence Tomography*, Drexler, W.; Fujimoto, J., Eds. Springer Berlin Heidelberg: 2008; pp 593-617.
150. Linde, D.; Glass, A. M., Photorefractive Effects for Reversible Holographic Storage of Information. *Appl. Phys.* **1975**, *8*, 85-100.
151. Chen, F. S.; LaMacchia, J. T.; Fraser, D. B., Holographic Storage in Lithium Niobate. *Applied Physics Letters* **1968**, *13*, 223-225.
152. Chen, F. S., Optically Induced Change of Refractive Indices in Linbo[Sub 3] and Litao[Sub 3]. *Journal of Applied Physics* **1969**, *40*, 3389-3396.
153. Townsend, R. L.; LaMacchia, J. T., Optically Induced Refractive Index Changes in Batio[Sub 3]. *Journal of Applied Physics* **1970**, *41*, 5188-5192.
154. Günter, P.; Flückiger, U.; Huignard, J. P.; Micheron, F., Optically Induced Refractive Index Changes in Knbo3:Fe. *Ferroelectrics* **1976**, *13*, 297-299.
155. Mullen, R. A.; Hellwarth, R. W., Optical Measurement of the Photorefractive Parameters of Bi[Sub 12]Sio[Sub 20]. *Journal of Applied Physics* **1985**, *58*, 40-44.
156. Klein, M. B., Beam Coupling in Undoped Gaas at 1.06 Mm Using the Photorefractive Effect. *Opt. Lett.* **1984**, *9*, 350-352.
157. Sutter, K.; Günter, P., Photorefractive Gratings in the Organic Crystal 2-Cyclooctylamino-5-Nitropyridine Doped with 7,7,8,8-Tetracyanoquinodimethane. *J. Opt. Soc. Am. B* **1990**, *7*, 2274-2278.
158. Ducharme, S.; Scott, J. C.; Twieg, R. J.; Moerner, W. E., Observation of the Photorefractive Effect in a Polymer. *Physical Review Letters* **1991**, *66*, 1846-1849.
159. Salvador, M.; Prauzner, J.; Köber, S.; Meerholz, K.; Turek, J. J.; Jeong, K.; Nolte, D. D., Three-Dimensional Holographic Imaging of Living Tissue Using a Highly Sensitive Photorefractive Polymer Device. *Opt. Express* **2009**, *17*, 11834-11849.
160. Blanche, P. A., et al., Holographic Three-Dimensional Telepresence Using Large-Area Photorefractive Polymer. *Nature* **2010**, *468*, 80-83.

161. Silence, S. M.; Walsh, C. A.; Scott, J. C.; Moerner, W. E., C[Sub 60] Sensitization of a Photorefractive Polymer. *Applied Physics Letters* **1992**, *61*, 2967-2969.
162. Meerholz, K.; Volodin, B. L.; Sandalphon; Kippelen, B.; Peyghambarian, N., A Photorefractive Polymer with High Optical Gain and Diffraction Efficiency near 100%. *Nature* **1994**, *371*, 497-500.
163. Bittner, R.; Meerholz, K., Amorphous Organic Photorefractive Materials. In *Photorefractive Materials and Their Applications 2*, Günter, P.; Huignard, J.-P., Eds. Springer New York: 2007; Vol. 114, pp 419-486.
164. Thomas, J., et al., Bistriarylamine Polymer-Based Composites for Photorefractive Applications. *Advanced Materials* **2004**, *16*, 2032-2036.
165. Herlocker, J. A.; Fuentes-Hernandez, C.; Ferrio, K. B.; Hendrickx, E.; Blanche, P. A.; Peyghambarian, N.; Kippelen, B.; Zhang, Y.; Wang, J. F.; Marder, S. R., Stabilization of the Response Time in Photorefractive Polymers. *Applied Physics Letters* **2000**, *77*, 2292-2294.
166. Mecher, E.; Brauchle, C.; H. Horhold, H.; C. Hummelen, J.; Meerholz, K., Comparison of New Photorefractive Composites Based on a Poly(Phenylene Vinylene) Derivative with Traditional Poly(N-Vinylcarbazole) Composites. *Physical Chemistry Chemical Physics* **1999**, *1*, 1749-1756.
167. Grunnet-Jepsen, A.; Thompson, C. L.; Twieg, R. J.; Moerner, W. E., High Performance Photorefractive Polymer with Improved Stability. *Applied Physics Letters* **1997**, *70*, 1515-1517.
168. Wright, D.; Gubler, U.; Roh, Y.; Moerner, W. E.; He, M.; Twieg, R. J., High-Performance Photorefractive Polymer Composite with 2-Dicyanomethylen-3-Cyano-2,5-Dihydrofuran Chromophore. *Applied Physics Letters* **2001**, *79*, 4274-4276.
169. Kinashi, K.; Wang, Y.; Nonomura, A.; Tsujimura, S.; Sakai, W.; Tsutsumi, N., Dynamic Holographic Images Using Poly(N-Vinylcarbazole)-Based Photorefractive Composites. *Polym J* **2013**, *45*, 665-670.
170. Wortmann, R., et al., Design of Optimized Photorefractive Polymers: A Novel Class of Chromophores. *The Journal of Chemical Physics* **1996**, *105*, 10637-10647.
171. Moerner, W. E.; Silence, S. M.; Hache, F.; Bjorklund, G. C., Orientationally Enhanced Photorefractive Effect in Polymers. *J. Opt. Soc. Am. B* **1994**, *11*, 320-330.
172. Thomas, J.; Norwood, R. A.; Peyghambarian, N., Non-Linear Optical Polymers for Photorefractive Applications. *Journal of Materials Chemistry* **2009**, *19*, 7476-7489.
173. Goonesekera, A.; Ducharme, S., Effect of Dipolar Molecules on Carrier Mobilities in Photorefractive Polymers. *Journal of Applied Physics* **1999**, *85*, 6506-6514.

174. Quintana, J. A.; Boj, P. G.; Villalvilla, J. M.; Ortiz, J.; Fernandez-Lazaro, F.; Sastre-Santos, A.; Diaz-Garcia, M. A., Photorefractive Properties of an Unsensitized Polymer Composite Based on a Dicyanostyrene Derivative as Nonlinear Optical Chromophore. *Applied Physics Letters* **2005**, *87*, 261111-3.
175. Moon, I. K.; Choi, C.-S.; Kim, N., Synthesis and Characterization of Novel Photoconducting Carbazole Derivatives in Main-Chain Polymers for Photorefractive Applications. *Polymer* **2007**, *48*, 3461-3467.
176. Onsager, L., Initial Recombination of Ions. *Physical Review* **1938**, *54*, 554-557.
177. Mozumder, A., Effect of an External Electric Field on the Yield of Free Ions. I General Results from the Onsager Theory. *The Journal of Chemical Physics* **1974**, *60*, 4300-4304.
178. Ostroverkhova, O.; Moerner, W. E.; He, M.; Twieg, R. J., High-Performance Photorefractive Organic Glass with near-Infrared Sensitivity. *Applied Physics Letters* **2003**, *82*, 3602-3604.
179. Hendrickx, E.; Zhang, Y.; B. Ferrio, K.; A. Herlocker, J.; Anderson, J.; R. Armstrong, N.; A. Mash, E.; P. Persoons, A.; Peyghambarian, N.; Kippelen, B., Photoconductive Properties of Pvk-Based Photorefractive Polymer Composites Doped with Fluorinated Styrene Chromophores. *Journal of Materials Chemistry* **1999**, *9*, 2251-2258.
180. Conwell, E. M., Impurity Band Conduction in Germanium and Silicon. *Physical Review* **1956**, *103*, 51-61.
181. Blom, P. W. M.; Vissenberg, M. C. J. M., Charge Transport in Poly(P-Phenylene Vinylene) Light-Emitting Diodes. *Materials Science and Engineering: R: Reports* **2000**, *27*, 53-94.
182. Visser, S. A.; Gruenbaum, W. T.; Magin, E. H.; Borsenberger, P. M., Hole Transport in Arylamine Doped Polymers. *Chemical Physics* **1999**, *240*, 197-203.
183. Amodei, J., Analysis of Transport Processes During Holographic Recording in Insulators. *RCA review* **1971**, *32*, 185-198.
184. Staebler, D. L.; Amodei, J. J., Coupled-Wave Analysis of Holographic Storage in Linbo[Sub 3]. *Journal of Applied Physics* **1972**, *43*, 1042-1049.
185. Kukhtarev, N. V.; Markov, V. B.; Odulov, S. G.; Soskin, M. S.; Vinetskii, V. L., Holographic Storage in Electrooptic Crystals. I. Steady State. *Ferroelectrics* **1978**, *22*, 949-960.
186. Schildkraut, J. S.; Buettner, A. V., Theory and Simulation of the Formation and Erasure of Space-Charge Gratings in Photoconductive Polymers. *Journal of Applied Physics* **1992**, *72*, 1888-1893.

187. Schildkraut, J. S.; Cui, Y., Zero-Order and First-Order Theory of the Formation of Space-Charge Gratings in Photoconductive Polymers. *Journal of Applied Physics* **1992**, *72*, 5055-5060.
188. Ostroverkhova, O.; Singer, K. D., Space-Charge Dynamics in Photorefractive Polymers. *Journal of Applied Physics* **2002**, *92*, 1727-1743.
189. Kippelen, B.; Sandalphon; Meerholz, K.; Peyghambarian, N., Birefringence, Pockels, and Kerr Effects in Photorefractive Polymers. *Applied Physics Letters* **1996**, *68*, 1748-1750.
190. Wu, J. W., Birefringent and Electro-Optic Effects in Poled Polymer Films: Steady-State and Transient Properties. *J. Opt. Soc. Am. B* **1991**, *8*, 142-152.
191. Singer, K. D.; Kuzyk, M. G.; Sohn, J. E., Second-Order Nonlinear-Optical Processes in Orientationally Ordered Materials: Relationship between Molecular and Macroscopic Properties. *J. Opt. Soc. Am. B* **1987**, *4*, 968-976.
192. Binks, D. J.; West, D. P., Derivation of the Analytical Form for Holographic Contrast Growth in Photorefractive Polymers. *J. Opt. Soc. Am. B* **2002**, *19*, 2349-2356.
193. Kogelnik, H., Imaging of Optical Modes- Resonators with Internal Lenses(Gaussian Light Beam Propagation Modes and Transformation Upon Passage through Lenses between Resonators Explained by Fresnel Diffraction Theory). *Bell System Technical Journal* **1965**, *44*, 455-494.
194. Moharam, M. G.; Gaylord, T. K., Rigorous Coupled-Wave Analysis of Planar-Grating Diffraction. *J. Opt. Soc. Am.* **1981**, *71*, 811-818.
195. Pochi, Y., Two-Wave Mixing in Nonlinear Media. *Quantum Electronics, IEEE Journal of* **1989**, *25*, 484-519.
196. Herlocker, J. A.; Ferrio, K. B.; Hendrickx, E.; Guenther, B. D.; Mery, S.; Kippelen, B.; Peyghambarian, N., Direct Observation of Orientation Limit in a Fast Photorefractive Polymer Composite. *Applied Physics Letters* **1999**, *74*, 2253-2255.
197. Wright, D.; Diaz-Garcia, M. A.; Casperson, J. D.; DeClue, M.; Moerner, W. E.; Twieg, R. J., High-Speed Photorefractive Polymer Composites. *Applied Physics Letters* **1998**, *73*, 1490-1492.
198. Chung, S. H.; Stevens, J. R., Time-Dependent Correlation and the Evaluation of the Stretched Exponential or Kohlrausch--Williams--Watts Function. *American Journal of Physics* **1991**, *59*, 1024-1030.
199. Mecher, E.; Gallego-Gomez, F.; Tillmann, H.; Horhold, H.-H.; Hummelen, J. C.; Meerholz, K., Near-Infrared Sensitivity Enhancement of Photorefractive Polymer Composites by Pre-Illumination. *Nature* **2002**, *418*, 959-964.

200. Refregier, P.; Solymar, L.; Rajbenbach, H.; Huignard, J. P., Two-Beam Coupling in Photorefractive Bi[Sub 12]Sio[Sub 20] Crystals with Moving Grating: Theory and Experiments. *Journal of Applied Physics* **1985**, *58*, 45-57.
201. Sandalphon; Kippelen, B.; Meerholz, K.; Peyghambarian, N., Ellipsometric Measurements of Poling Birefringence, the Pockels Effect, and the Kerr Effect in High-Performance Photorefractive Polymer Composites. *Appl. Opt.* **1996**, *35*, 2346-2354.
202. Kamanina, N. V.; Shurpo, N. A.; Zubtsova, Y. A.; Prokhorenkov, A. V.; Serov, S. V.; Vasilyev, P. Y.; Studeonov, V. I.; Kajzar, F., Photorefractive and Photoconductive Properties of the Organic Materials Doped with Fullerenes, Quantum Dots, and Nanotubes. **2010**, 78381G-78381G.
203. Geim, A. K.; Novoselov, K. S., The Rise of Graphene. *Nat Mater* **2007**, *6*, 183-191.
204. Castro Neto, A. H.; Guinea, F.; Peres, N. M. R.; Novoselov, K. S.; Geim, A. K., The Electronic Properties of Graphene. *Reviews of Modern Physics* **2009**, *81*, 109-162.
205. Li, X.; Zhang, G.; Bai, X.; Sun, X.; Wang, X.; Wang, E.; Dai, H., Highly Conducting Graphene Sheets and Langmuir-Blodgett Films. *Nat Nano* **2008**, *3*, 538-542.
206. Bae, S., et al., Roll-to-Roll Production of 30-Inch Graphene Films for Transparent Electrodes. *Nat Nano* **2010**, *5*, 574-578.
207. Freitag, M.; Low, T.; Xia, F.; Avouris, P., Photoconductivity of Biased Graphene. *Nat Photon* **2013**, *7*, 53-59.
208. Xu, X.; Gabor, N. M.; Alden, J. S.; van der Zande, A. M.; McEuen, P. L., Photo-Thermoelectric Effect at a Graphene Interface Junction. *Nano Letters* **2009**, *10*, 562-566.
209. Stankovich, S.; Dikin, D. A.; Dommett, G. H. B.; Kohlhaas, K. M.; Zimney, E. J.; Stach, E. A.; Piner, R. D.; Nguyen, S. T.; Ruoff, R. S., Graphene-Based Composite Materials. *Nature* **2006**, *442*, 282-286.
210. Pang, H.; Chen, T.; Zhang, G.; Zeng, B.; Li, Z.-M., An Electrically Conducting Polymer/Graphene Composite with a Very Low Percolation Threshold. *Materials Letters* **2010**, *64*, 2226-2229.
211. Salavagione, H. J.; Martinez, G.; Gomez, M. A., Synthesis of Poly(Vinyl Alcohol)/Reduced Graphite Oxide Nanocomposites with Improved Thermal and Electrical Properties. *Journal of Materials Chemistry* **2009**, *19*, 5027-5032.
212. Yang, N.; Zhai, J.; Wang, D.; Chen, Y.; Jiang, L., Two-Dimensional Graphene Bridges Enhanced Photoinduced Charge Transport in Dye-Sensitized Solar Cells. *ACS Nano* **2010**, *4*, 887-894.

213. Kamat, P. V., Graphene-Based Nanoassemblies for Energy Conversion. *The Journal of Physical Chemistry Letters* **2011**, *2*, 242-251.
214. Yan, X.; Cui, X.; Li, L.-s., Synthesis of Large, Stable Colloidal Graphene Quantum Dots with Tunable Size. *Journal of the American Chemical Society* **2010**, *132*, 5944-5945.
215. Yan, X.; Cui, X.; Li, B.; Li, L.-s., Large, Solution-Processable Graphene Quantum Dots as Light Absorbers for Photovoltaics. *Nano Letters* **2010**, *10*, 1869-1873.
216. Moerner, W. E.; Silence, S. M.; Hache, F.; Bjorklund, G. C., Orientationally Enhanced Photorefractive Effect in Polymers. *J. Opt. Soc. Am. B* **1994**, *11*, 320-330.
217. Köber, S.; Salvador, M.; Meerholz, K., Organic Photorefractive Materials and Applications. *Advanced Materials* **2011**, *23*, 4725-4763.
218. Ditte, K.; Jiang, W.; Schemme, T.; Denz, C.; Wang, Z., Innovative Sensitizer Dipbi Outperforms Pcbm. *Advanced Materials* **2012**, *24*, 2104-2108.
219. Binks, D. J.; Bant, S. P.; West, D. P.; O'Brien, P.; Malik, M. A., Cdse/Cds Core/Shell Quantum Dots as Sensitizer of a Photorefractive Polymer Composite. *Journal of Modern Optics* **2003**, *50*, 299-310.
220. Li, X.; Van Embden, J.; Chon, J. W. M.; Evans, R. A.; Gu, M., Enhanced Photorefractive Performance in Cdse Quantum-Dot-Dispersed Poly(Styrene-Co-Acrylonitrile) Polymers. *Applied Physics Letters* **2010**, *96*, 253302-253302-3.
221. Gallego-Gómez, F.; Quintana, J. A.; Villalvilla, J. M.; Díaz-García, M. a. A.; Martín-Gomis, L.; Fernández-Lázaro, F.; Sastre-Santos, A. n., Phthalocyanines as Efficient Sensitizers in Low-Tg Hole-Conducting Photorefractive Polymer Composites. *Chemistry of Materials* **2009**, *21*, 2714-2720.
222. Kober, S.; Gallego-Gomez, F.; Salvador, M.; Kooistra, F. B.; Hummelen, J. C.; Aleman, K.; Mansurova, S.; Meerholz, K., Influence of the Sensitizer Reduction Potential on the Sensitivity of Photorefractive Polymer Composites. *Journal of Materials Chemistry* **2010**, *20*, 6170-6175.
223. Vannikov, A. V.; Rychwalski, R. W.; Grishina, A. D.; Pereshivko, L. Y.; Krivenko, T. V.; Savel'ev, V. V.; Zolotarevskii, V. I., Photorefractive Polymer Composites for the Ir Region Based on Carbon Nanotubes. *Opt. Spectrosc.* **2005**, *99*, 643-648.
224. Grishina, A. D.; Pereshivko, L. Y.; Licea-Jiménez, L.; Krivenko, T. V.; Savel'ev, V. V.; Rychwalski, R. W.; Vannikov, A. V., Carbon Nanotube-Containing Photorefractive Polymer Composites Operating at Telecommunication Wavelengths. *High Energy Chem* **2007**, *41*, 267-273.

225. Grishina, A. D.; Licea-Jimenez, L.; Pereshivko, L. Y.; Krivenko, T. V.; Savel'ev, V. V.; Rychwalski, R. W.; Vannikov, A. V., Infrared Photorefractive Composites Based on Polyvinylcarbazole and Carbon Nanotubes. *High Energy Chem* **2006**, *40*, 341-347.
226. Licea-Jiménez, L.; Grishina, A. D.; Pereshivko, L. Y.; Krivenko, T. V.; Savelyev, V. V.; Rychwalski, R. W.; Vannikov, A. V., Near-Infrared Photorefractive Polymer Composites Based on Carbon Nanotubes. *Carbon* **2006**, *44*, 113-120.
227. Lingam, N. K.; Kalghatgi, S.; Winiarz, J. G., Enhanced Photorefractivity in a Polymeric Composite Photosensitized with Carbon Nanotubes Grafted to a Photoconductive Polymer. *Journal of Applied Physics* **2011**, *109*, 023106-10.
228. Cao, L.; Chen, H.; Wang, M.; Sun, J.; Zhang, X.; Kong, F., Photoconductivity Study of Modified Carbon Nanotube/Oxotitanium Phthalocyanine Composites. *The Journal of Physical Chemistry B* **2002**, *106*, 8971-8975.
229. Grishina, A. D.; Krivenko, T. V.; Savel'ev, V. V.; Rychwalski, R. W.; Vannikov, A. V., Photoelectric, Nonlinear Optical, and Photorefractive Properties of Polyvinylcarbazole Composites with Graphene. *High Energy Chem* **2013**, *47*, 46-52.
230. Grishina, A. D.; Krivenko, T. V.; Savel'ev, V. V.; Rychwalski, R. W.; Vannikov, A. V., Photoelectric and Photorefractive Properties of Polyvinylcarbazole Composites with Graphene in the Visible Spectral Range. *High Energy Chem* **2013**, *47*, 187-191.
231. Blake, P., et al., Graphene-Based Liquid Crystal Device. *Nano Letters* **2008**, *8*, 1704-1708.
232. Hernandez, Y., et al., High-Yield Production of Graphene by Liquid-Phase Exfoliation of Graphite. *Nat Nano* **2008**, *3*, 563-568.
233. Kravets, V. G.; Grigorenko, A. N.; Nair, R. R.; Blake, P.; Anissimova, S.; Novoselov, K. S.; Geim, A. K., Spectroscopic Ellipsometry of Graphene and an Exciton-Shifted Van Hove Peak in Absorption. *Physical Review B* **2010**, *81*, 155413.
234. Mak, K. F.; Sfeir, M. Y.; Wu, Y.; Lui, C. H.; Misewich, J. A.; Heinz, T. F., Measurement of the Optical Conductivity of Graphene. *Physical Review Letters* **2008**, *101*, 196405.
235. Nair, R. R.; Blake, P.; Grigorenko, A. N.; Novoselov, K. S.; Booth, T. J.; Stauber, T.; Peres, N. M. R.; Geim, A. K., Fine Structure Constant Defines Visual Transparency of Graphene. *Science* **2008**, *320*, 1308.
236. Grunnet-Jepsen, A.; Wright, D.; Smith, B.; Bratcher, M.; DeClue, M.; Siegel, J.; Moerner, W., Spectroscopic Determination of Trap Density in C₆₀-Sensitized Photorefractive Polymers. *Chemical physics letters* **1998**, *291*, 553-561.

237. Bolink, H.; Krasnikov, V.; Malliaras, G.; Hadziioannou, G., Effect of Plasticization on the Performance of a Photorefractive Polymer. *The Journal of Physical Chemistry* **1996**, *100*, 16356-16360.
238. Batt, R. H.; Braun, C. L.; Hornig, J. F., Electric-Field and Temperature Dependence of Photoconductivity. *The Journal of Chemical Physics* **1968**, *49*, 1967-1968.
239. Braun, C. L., Electric Field Assisted Dissociation of Charge Transfer States as a Mechanism of Photocarrier Production. *The Journal of Chemical Physics* **1984**, *80*, 4157-4161.
240. Melz, P. J., Photogeneration in Trinitrofluorenone-Poly(N-Vinylcarbazole). *The Journal of Chemical Physics* **1972**, *57*, 1694-1699.
241. Peumans, P.; Forrest, S. R., Separation of Geminate Charge-Pairs at Donor-Acceptor Interfaces in Disordered Solids. *Chemical Physics Letters* **2004**, *398*, 27-31.
242. Grunnet-Jepsen, A.; Wright, D.; Smith, B.; Bratcher, M. S.; DeClue, M. S.; Siegel, J. S.; Moerner, W. E., Spectroscopic Determination of Trap Density in C60-Sensitized Photorefractive Polymers. *Chemical Physics Letters* **1998**, *291*, 553-561.
243. Garrett, M. H.; Chang, J. Y.; Jenssen, H. P.; Warde, C., High Beam-Coupling Gain and Deep- and Shallow-Trap Effects in Cobalt-Doped Barium Titanate, Batio3:Co. *J. Opt. Soc. Am. B* **1992**, *9*, 1407-1415.
244. Grunnet-Jepsen, A.; Thompson, C. L.; Moerner, W. E., Systematics of Two-Wave Mixing in a Photorefractive Polymer. *J. Opt. Soc. Am. B* **1998**, *15*, 905-913.
245. Christenson, C. W., et al., Materials for an Updatable Holographic 3d Display. *J. Display Technol.* **2010**, *6*, 510-516.
246. Bonaccorso, F.; Sun, Z.; Hasan, T.; Ferrari, A. C., Graphene Photonics and Optoelectronics. *Nat Photon* **2010**, *4*, 611-622.
247. Liu, Z.; He, D.; Wang, Y.; Wu, H.; Wang, J., Graphene Doping of P3ht:Pcbm Photovoltaic Devices. *Synthetic Metals* **2010**, *160*, 1036-1039.
248. Wu, Q.-H.; Hong, G.; Ng, T. W.; Lee, S. T., Substrate Effect on the Electronic Structures of Cupc/Graphene Interfaces. *Applied Physics Letters* **2012**, *100*, 161603-4.
249. Liu, Q.; Liu, Z.; Zhang, X.; Yang, L.; Zhang, N.; Pan, G.; Yin, S.; Chen, Y.; Wei, J., Polymer Photovoltaic Cells Based on Solution-Processable Graphene and P3ht. *Advanced Functional Materials* **2009**, *19*, 894-904.
250. Potts, J. R.; Dreyer, D. R.; Bielawski, C. W.; Ruoff, R. S., Graphene-Based Polymer Nanocomposites. *Polymer* **2011**, *52*, 5-25.

251. Anker, J. N.; Hall, W. P.; Lyandres, O.; Shah, N. C.; Zhao, J.; Van Duyne, R. P., Biosensing with Plasmonic Nanosensors. *Nat Mater* **2008**, *7*, 442-453.
252. Kabashin, A. V.; Evans, P.; Pastkovsky, S.; Hendren, W.; Wurtz, G. A.; Atkinson, R.; Pollard, R.; Podolskiy, V. A.; Zayats, A. V., Plasmonic Nanorod Metamaterials for Biosensing. *Nat Mater* **2009**, *8*, 867-871.
253. Lal, S.; Clare, S. E.; Halas, N. J., Nanoshell-Enabled Photothermal Cancer Therapy: Impending Clinical Impact. *Accounts of Chemical Research* **2008**, *41*, 1842-1851.
254. Huang, X.; Jain, P.; El-Sayed, I.; El-Sayed, M., Plasmonic Photothermal Therapy (Pptt) Using Gold Nanoparticles. *Lasers Med Sci* **2008**, *23*, 217-228.
255. Pillai, S.; Catchpole, K. R.; Trupke, T.; Green, M. A., Surface Plasmon Enhanced Silicon Solar Cells. *Journal of Applied Physics* **2007**, *101*, 093105-093105-8.
256. Thomann, I.; Pinaud, B. A.; Chen, Z.; Clemens, B. M.; Jaramillo, T. F.; Brongersma, M. L., Plasmon Enhanced Solar-to-Fuel Energy Conversion. *Nano Letters* **2011**, *11*, 3440-3446.
257. Oulton, R. F.; Sorger, V. J.; Genov, D. A.; Pile, D. F. P.; Zhang, X., A Hybrid Plasmonic Waveguide for Subwavelength Confinement and Long-Range Propagation. *Nat Photon* **2008**, *2*, 496-500.
258. Hecker, N. E.; Hopfel, R. A.; Sawaki, N.; Maier, T.; Strasser, G., Surface Plasmon-Enhanced Photoluminescence from a Single Quantum Well. *Applied Physics Letters* **1999**, *75*, 1577-1579.
259. Park, H.-J.; Doojin, V.; Noh, Y.-Y.; Lim, B.; Kim, D.-Y., Surface Plasmon Enhanced Photoluminescence of Conjugated Polymers. *Applied Physics Letters* **2007**, *90*, 161107-161107-3.
260. Senanayake, P.; Hung, C.-H.; Shapiro, J.; Lin, A.; Liang, B.; Williams, B. S.; Huffaker, D. L., Surface Plasmon-Enhanced Nanopillar Photodetectors. *Nano Letters* **2011**, *11*, 5279-5283.
261. Hagglund, C.; Zach, M.; Kasemo, B., Enhanced Charge Carrier Generation in Dye Sensitized Solar Cells by Nanoparticle Plasmons. *Applied Physics Letters* **2008**, *92*, 013113-013113-3.
262. Kulkarni, A. P.; Noone, K. M.; Munechika, K.; Guyer, S. R.; Ginger, D. S., Plasmon-Enhanced Charge Carrier Generation in Organic Photovoltaic Films Using Silver Nanoprisms. *Nano Letters* **2010**, *10*, 1501-1505.
263. Hung, W. H.; Aykol, M.; Valley, D.; Hou, W.; Cronin, S. B., Plasmon Resonant Enhancement of Carbon Monoxide Catalysis. *Nano Letters* **2010**, *10*, 1314-1318.

264. Liu, Z.; Hou, W.; Pavaskar, P.; Aykol, M.; Cronin, S. B., Plasmon Resonant Enhancement of Photocatalytic Water Splitting under Visible Illumination. *Nano Letters* **2011**, *11*, 1111-1116.
265. Nahata, A.; Linke, R. A.; Ishi, T.; Ohashi, K., Enhanced Nonlinear Optical Conversion from a Periodically Nanostructured Metal Film. *Opt. Lett.* **2003**, *28*, 423-425.
266. Verhagen, E.; Kuipers, L.; Polman, A., Enhanced Nonlinear Optical Effects with a Tapered Plasmonic Waveguide. *Nano Letters* **2006**, *7*, 334-337.
267. Jain, P. K.; Xiao, Y.; Walsworth, R.; Cohen, A. E., Surface Plasmon Resonance Enhanced Magneto-Optics (Supremo): Faraday Rotation Enhancement in Gold-Coated Iron Oxide Nanocrystals. *Nano Letters* **2009**, *9*, 1644-1650.
268. Tseng, A. A.; Kuan, C.; Chen, C. D.; Ma, K. J., Electron Beam Lithography in Nanoscale Fabrication: Recent Development. *Electronics Packaging Manufacturing, IEEE Transactions on* **2003**, *26*, 141-149.
269. Shinji, M.; Yukinori, O., Focused Ion Beam Applications to Solid State Devices. *Nanotechnology* **1996**, *7*, 247.
270. Dickey, M. D.; Weiss, E. A.; Smythe, E. J.; Chiechi, R. C.; Capasso, F.; Whitesides, G. M., Fabrication of Arrays of Metal and Metal Oxide Nanotubes by Shadow Evaporation. *ACS Nano* **2008**, *2*, 800-808.
271. Haynes, C. L.; Van Duyne, R. P., Nanosphere Lithography: A Versatile Nanofabrication Tool for Studies of Size-Dependent Nanoparticle Optics. *The Journal of Physical Chemistry B* **2001**, *105*, 5599-5611.
272. Jensen, T. R.; Schatz, G. C.; Van Duyne, R. P., Nanosphere Lithography: Surface Plasmon Resonance Spectrum of a Periodic Array of Silver Nanoparticles by Ultraviolet-Visible Extinction Spectroscopy and Electrodynamics Modeling. *The Journal of Physical Chemistry B* **1999**, *103*, 2394-2401.
273. Guo, L. J., Nanoimprint Lithography: Methods and Material Requirements. *Advanced Materials* **2007**, *19*, 495-513.
274. Link, S.; El-Sayed, M. A., Size and Temperature Dependence of the Plasmon Absorption of Colloidal Gold Nanoparticles. *The Journal of Physical Chemistry B* **1999**, *103*, 4212-4217.
275. Grand, J.; Adam, P.-M.; Grimault, A.-S.; Vial, A.; Lamy de la Chapelle, M.; Bijeon, J.-L.; Kostcheev, S.; Royer, P., Optical Extinction Spectroscopy of Oblate, Prolate and Ellipsoid Shaped Gold Nanoparticles: Experiments and Theory. *Plasmonics* **2006**, *1*, 135-140.
276. Mertens, H.; Biteen, J. S.; Atwater, H. A.; Polman, A., Polarization-Selective Plasmon-Enhanced Silicon Quantum-Dot Luminescence. *Nano Letters* **2006**, *6*, 2622-2625.

277. Wurtz, G. A.; Pollard, R.; Hendren, W.; Wiederrecht, G. P.; Gosztola, D. J.; Podolskiy, V. A.; Zayats, A. V., Designed Ultrafast Optical Nonlinearity in a Plasmonic Nanorod Metamaterial Enhanced by Nonlocality. *Nat Nano* **2011**, *6*, 107-111.
278. Lucas, B. D.; Kim, J.-S.; Chin, C.; Guo, L. J., Nanoimprint Lithography Based Approach for the Fabrication of Large-Area, Uniformly-Oriented Plasmonic Arrays. *Advanced Materials* **2008**, *20*, 1129-1134.
279. Park, H. J.; Kang, M.-G.; Guo, L. J., Large Area High Density Sub-20 Nm SiO₂ Nanostructures Fabricated by Block Copolymer Template for Nanoimprint Lithography. *ACS Nano* **2009**, *3*, 2601-2608.
280. Kooy, N.; Mohamed, K.; Pin, L. T.; Guan, O. S., A Review of Roll-to-Roll Nanoimprint Lithography. *Nanoscale research letters* **2014**, *9*, 1-13.
281. Gates, B. D.; Xu, Q.; Stewart, M.; Ryan, D.; Willson, C. G.; Whitesides, G. M., New Approaches to Nanofabrication: Molding, Printing, and Other Techniques. *Chemical reviews* **2005**, *105*, 1171-1196.
282. Pease, R. F.; Chou, S. Y., Lithography and Other Patterning Techniques for Future Electronics. *Proceedings of the IEEE* **2008**, *96*, 248-270.
283. Pelton, M.; Bryant, G. W., *Introduction to Metal-Nanoparticle Plasmonics*; Wiley, 2013.
284. Cooper, Stevenson, P., A Study of the Nucleation and Growth Processes in the Synthesis of Colloidal Gold. *Discussions of the Faraday Society* **1951**, *11*, 55-75.
285. Tao, A.; Sinsersuksakul, P.; Yang, P., Polyhedral Silver Nanocrystals with Distinct Scattering Signatures. *Angewandte Chemie International Edition* **2006**, *45*, 4597-4601.
286. Sun, Y.; Xia, Y., Shape-Controlled Synthesis of Gold and Silver Nanoparticles. *Science* **2002**, *298*, 2176-2179.
287. Wang, Z. L., Transmission Electron Microscopy of Shape-Controlled Nanocrystals and Their Assemblies. *The Journal of Physical Chemistry B* **2000**, *104*, 1153-1175.
288. Sun, Y.; Mayers, B.; Xia, Y., Metal Nanostructures with Hollow Interiors. *Advanced Materials* **2003**, *15*, 641-646.
289. Oldenburg, S. J.; Averitt, R. D.; Westcott, S. L.; Halas, N. J., Nanoengineering of Optical Resonances. *Chemical Physics Letters* **1998**, *288*, 243-247.
290. Lung, J.-K.; Huang, J.-C.; Tien, D.-C.; Liao, C.-Y.; Tseng, K.-H.; Tsung, T.-T.; Kao, W.-S.; Tsai, T.-H.; Jwo, C.-S.; Lin, H.-M., Preparation of Gold Nanoparticles by Arc Discharge in Water. *Journal of alloys and compounds* **2007**, *434*, 655-658.

291. Mafuné, F.; Kohno, J.-y.; Takeda, Y.; Kondow, T., Full Physical Preparation of Size-Selected Gold Nanoparticles in Solution: Laser Ablation and Laser-Induced Size Control. *The Journal of Physical Chemistry B* **2002**, *106*, 7575-7577.
292. Mulvaney, P.; Giersig, M.; Henglein, A., Electrochemistry of Multilayer Colloids: Preparation and Absorption Spectrum of Gold-Coated Silver Particles. *The Journal of Physical Chemistry* **1993**, *97*, 7061-7064.
293. Huang, S.; Tsutsui, G.; Sakaue, H.; Shingubara, S.; Takahagi, T., Experimental Conditions for a Highly Ordered Monolayer of Gold Nanoparticles Fabricated by the Langmuir–Blodgett Method. *Journal of Vacuum Science & Technology B* **2001**, *19*, 2045-2049.
294. Chen, S., Langmuir–Blodgett Fabrication of Two-Dimensional Robust Cross-Linked Nanoparticle Assemblies. *Langmuir* **2001**, *17*, 2878-2884.
295. Liu, S.; Zhu, T.; Hu, R.; Liu, Z., Evaporation-Induced Self-Assembly of Gold Nanoparticles into a Highly Organized Two-Dimensional Array. *Phys. Chem. Chem. Phys.* **2002**, *4*, 6059-6062.
296. Sau, T. K.; Murphy, C. J., Self-Assembly Patterns Formed Upon Solvent Evaporation of Aqueous Cetyltrimethylammonium Bromide-Coated Gold Nanoparticles of Various Shapes. *Langmuir* **2005**, *21*, 2923-2929.
297. Jensen, T. R.; Malinsky, M. D.; Haynes, C. L.; Van Duyne, R. P., Nanosphere Lithography: Tunable Localized Surface Plasmon Resonance Spectra of Silver Nanoparticles. *The Journal of Physical Chemistry B* **2000**, *104*, 10549-10556.
298. Choi, J.; Sauer, G.; Nielsch, K.; Wehrspohn, R. B.; Gösele, U., Hexagonally Arranged Monodisperse Silver Nanowires with Adjustable Diameter and High Aspect Ratio. *Chemistry of Materials* **2003**, *15*, 776-779.
299. van der Zande, B. M. I.; Böhmer, M. R.; Fokkink, L. G. J.; Schönenberger, C., Colloidal Dispersions of Gold Rods: Synthesis and Optical Properties. *Langmuir* **1999**, *16*, 451-458.
300. Shingubara, S., Fabrication of Nanomaterials Using Porous Alumina Templates. *Journal of Nanoparticle Research* **2003**, *5*, 17-30.
301. Haynes, C. L.; McFarland, A. D.; Smith, M. T.; Hulteen, J. C.; Van Duyne, R. P., Angle-Resolved Nanosphere Lithography: Manipulation of Nanoparticle Size, Shape, and Interparticle Spacing. *The Journal of Physical Chemistry B* **2002**, *106*, 1898-1902.
302. Liu, S.; Maoz, R.; Schmid, G.; Sagiv, J., Template Guided Self-Assembly of [Au₅₅] Clusters on Nanolithographically Defined Monolayer Patterns. *Nano Letters* **2002**, *2*, 1055-1060.
303. Fresco, Z. M.; Fréchet, J. M. J., Selective Surface Activation of a Functional Monolayer for the Fabrication of Nanometer Scale Thiol Patterns and Directed Self-Assembly of Gold Nanoparticles. *Journal of the American Chemical Society* **2005**, *127*, 8302-8303.

304. Kuzyk, A.; Schreiber, R.; Fan, Z.; Pardatscher, G.; Roller, E.-M.; Hoge, A.; Simmel, F. C.; Govorov, A. O.; Liedl, T., DNA-Based Self-Assembly of Chiral Plasmonic Nanostructures with Tailored Optical Response. *Nature* **2012**, *483*, 311-314.
305. Pal, S.; Deng, Z.; Ding, B.; Yan, H.; Liu, Y., DNA - Origami - Directed Self - Assembly of Discrete Silver - Nanoparticle Architectures. *Angewandte Chemie* **2010**, *122*, 2760-2764.
306. Chou, S. Y.; Krauss, P. R.; Renstrom, P. J., Imprint of Sub - 25 Nm Vias and Trenches in Polymers. *Applied physics letters* **1995**, *67*, 3114-3116.
307. Boltasseva, A., Plasmonic Components Fabrication Via Nanoimprint. *Journal of Optics A: Pure and Applied Optics* **2009**, *11*, 114001.
308. Mie, G., Beiträge Zur Optik Trüber Medien, Speziell Kolloidaler Metallösungen. *Annalen der physik* **1908**, *330*, 377-445.
309. Bohren, C. F.; Huffman, D. R., *Absorption and Scattering of Light by Small Particles*; Wiley, 2008.
310. Link, S.; El-Sayed, M. A., Shape and Size Dependence of Radiative, Non-Radiative and Photothermal Properties of Gold Nanocrystals. *International Reviews in Physical Chemistry* **2000**, *19*, 409-453.
311. Sprünken, D. P.; Omi, H.; Furukawa, K.; Nakashima, H.; Sychugov, I.; Kobayashi, Y.; Torimitsu, K., Influence of the Local Environment on Determining Aspect-Ratio Distributions of Gold Nanorods in Solution Using Gans Theory. *The Journal of Physical Chemistry C* **2007**, *111*, 14299-14306.
312. Quinten, M., *Optical Properties of Nanoparticle Systems: Mie and Beyond*; Wiley, 2010.
313. Weiland, T., A Discretization Model for the Solution of Maxwell's Equations for Six-Component Fields. *Electronics and Communications AEU* **1977**, *31*, 116-120.
314. Yee, K. S., Numerical Solution of Initial Boundary Value Problems Involving Maxwell's Equations in Isotropic Media. *IEEE Trans. Antennas Propag* **1966**, *14*, 302-307.
315. Inan, U. S.; Marshall, R. A., *Numerical Electromagnetics: The FDTD Method*; Cambridge University Press, 2011.
316. Agarwal, G. S., Vacuum-Field Rabi Splittings in Microwave Absorption by Rydberg Atoms in a Cavity. *Physical Review Letters* **1984**, *53*, 1732-1734.
317. Kleppner, D., Inhibited Spontaneous Emission. *Physical Review Letters* **1981**, *47*, 233-236.
318. Sanchez-Mondragon, J. J.; Narozhny, N. B.; Eberly, J. H., Theory of Spontaneous-Emission Line Shape in an Ideal Cavity. *Physical Review Letters* **1983**, *51*, 550-553.

319. Kasprzak, J., et al., Bose-Einstein Condensation of Exciton Polaritons. *Nature* **2006**, *443*, 409-414.
320. Zhu, Y.; Gauthier, D. J.; Morin, S. E.; Wu, Q.; Carmichael, H. J.; Mossberg, T. W., Vacuum Rabi Splitting as a Feature of Linear-Dispersion Theory: Analysis and Experimental Observations. *Physical Review Letters* **1990**, *64*, 2499-2502.
321. Nelson, T. R., et al., Room - Temperature Normal - Mode Coupling in a Semiconductor Microcavity Utilizing Native - Oxide AlAl/GaAs Mirrors. *Applied Physics Letters* **1996**, *69*, 3031-3033.
322. Kelkar, P.; Kozlov, V.; Jeon, H.; Nurmikko, A. V.; Chu, C. C.; Grillo, D. C.; Han, J.; Hua, C. G.; Gunshor, R. L., Excitons in a II-VI Semiconductor Microcavity in the Strong-Coupling Regime. *Physical Review B* **1995**, *52*, R5491-R5494.
323. Lidzey, D. G.; Bradley, D.; Skolnick, M.; Virgili, T.; Walker, S.; Whittaker, D., Strong Exciton-Photon Coupling in an Organic Semiconductor Microcavity. *Nature* **1998**, *395*, 53-55.